SAINT-PETERSBURG STATE UNIVERSITY

Chen Ruiqi

Natural and synthetic oxide phases with f-elements: recrystallization, crystal chemistry and properties

Scientific specialty 1.6.4. Mineralogy, Crystallography.
Geochemistry, geochemical methods of mineral exploration

DISSERTATION
submitted for the degree of
Candidate of Geological and Mineralogical Sciences

Translation from Russian

Supervisors:
Doctor of Geological and Mineralogical Sciences,
Oleg I. Siidra
Doctor of Chemistry, Associate Professor,
Marie Colmont

Saint Petersburg
2024

Contents

Acknowledgments

The work was carried out under the supervision of Dr. **Oleg Iohannesovich Siidra** (Professor, Department of Crystallography, St. Petersburg State University) and Dr. **Marie Colmont** (Associate Professor, Unité de Catalyse et Chimie du Solide (UCCS), École centrale de Lille). Dr. **Angel M. Arevalo-Lopez** (researcher at Centre national de la recherche scientifique (CNRS)) also provided invaluable assistance. The author would like to express special acknowledgement to them for establishing the program, the proposed topic and their comprehensive help and support at all stages of the work.

The author also expresses deep gratitude to Vera A. Firsova (researcher of ISC RAS) for consultations on the processing of experimental HTXRD data in the RietToTensor software package, Valery L. Ugolkov (senior researcher of ISC RAS) for assistance and conducting combined thermal analysis, Vladimir N. Bocharov (specialist of Resouce center “Geomodel”, SPBU) for his assistance on Raman spectroscopic analysis, and Natalia S. Vlasenko (engineer of Resouce center “Geomodel”, SPBU) for her assistance on electron micro-probe analysis, Vladimir V. Shilovsky (assistant engineer of Resouce center “Geomodel”, SPBU) for conducting electron back scatter diffraction experiments, Maria G. Krzhizhanovskaya (Department of Crystallography, St. Petersburg State University) and Natalia V. Platonova (assistant director of Resouce center “XRD”, SPBU) for conducting HTXRD experiments and consultation on X-ray phase analysis.

The author is also grateful to José Luis Rosas-Huerta (postdoc of Unité de Catalyse et Chimie du Solide (UCCS), Université de Lille) for consultation and assistance in the synthesis of crichtonite compounds and processing of measurement data, Frédéric CAPET and Laurence BURYLO (technician-researchers of the X-ray Diffraction and Diffusion Department, Institute Chevreul) for assistance on X-ray analysis, Claire MINAUD (assistant engineer, Institute Chevreul) for conducting magnetic property measurements, Clemens RITTER (instrument scientist, Institute Laue-Langevin) for advice and neutron diffraction for synthetic samples.

The author is grateful to the employees of RC SPBU: “X-ray diffraction research methods”, “Geomodel”, “Microscopy and Microanalysis”; as well as “Institute Chevraul” and “Institute Laue-Langevin” in France for technical support during this work. The author also thanks the Region Hauts-de-France for financial support and the Chevreul Institute (FR 2638), the Region Hauts-de-France and FEDER for funding the X-ray diffractometers.

The journey of this joint doctoral program has not been without its challenges, much like the myriad obstacles faced by many PhD students. Without the encouragement and assistance of friends, the author could not have started and completed these three years. Therefore, the author is very thankful to them: Artem S. Borisov, Victoria A. Ginga (Vladimirovna), Irina A. Volkova (Chernyshova), José Luis Rosas-Huerta, Jonas Wolber, Mingwei Tang, Qi Yang, Diana O. Nekrasova,

and Xudong Shen.

The author also expresses her heartfelt gratitude to her family. They have been always the strong backing and their support is invaluable in achieving this success.

Thesis summary

This is a joint program between Saint-Petersburg State University and École Centrale de Lille. The first part was mostly done in Saint-Petersburg and related to the studies on natural minerals, while the second part of work was conducted in Lille and related to synthetic materials.

Background and state of the art

1. *Study of recrystallization processes and properties of metamict minerals.*

The ever-growing amount of radioactive waste originating from the use of nuclear power for energy production, medicine, industry and research, underscores the great environment concern of immobilization of long-lived radionuclide wastes. Deep geological disposal of nuclear waste stands out as the most reliable and sustainable long-term solution world-wide [Chapman, Hooper, 2012; Ringwood, 1985]. Various inorganic waste forms have been developed, ranging from glasses (borosilicates, phosphates and sintered glasses), cements (Portland cement, cast stone/saltstone, hydroceramics, and geopolymers) to synthetic crystalline matrix (e.g. SYNROC – known as synthetic rock, is composed of hollandite, zirconolite, and perovskite) and ceramics (titanates, sodalite, apatite, monazites and goethite/magnetite). The design of suitable matrices is continuously required to ensure the safe disposal and effective immobilization of radioactive wastes [Caurant, Majérus, 2021; Glagovskii et al., 1999].

While borosilicate glass remains the preferred waste form for many countries dealing with nuclear waste, significant efforts have been directed towards developing alternative crystalline ceramic nuclear waste forms [Ewing, Lutze, 1991]. The stability of crystalline forms is exemplified by minerals, which contain radioactive elements and persist in geological bodies for millions of years. Despite enduring self-irradiation over vast periods, these minerals remain solid, stable, and resistant to decomposition, meeting the requirements for radionuclide immobilization. Moreover, previous research has demonstrated that crystalline forms exhibit greater resistance compared to glasses [Hatch, 1953; Yudintsev et al., 2001]. The idea of SYNROC, namely synthetic rock, came out in the 1970s' [Ringwood, 1985]. The major phases in synroc are zirconolite, perovskite, pyrochlore, brannerite, crichtonite, monazite, etc [Lumpkin, 2006; McCarthy, White, Pfoertsch, 1978].

Ideally, the ceramic should satisfy certain criteria: high durability, stability and resistivity to various physical and chemical conditions (temperature, pressure, radiation, acidity/alkalinity, etc.) [Weber et al., 2009]. Since radioactive waste deposition in deep geological formation should be designed to isolate the waste over a long period of time, it is necessary to predict possible changes in the main properties of engineered safety barriers based on the analysis of the influence of many factors, such as: the effect of high temperatures and radiation doses, typical for high heat generating high-level radioactive waste [Tyupina, Kozlov, Krupskaya, 2023]. From a risk assessment perspective, it is crucial to understand the matrix properties for material development in waste

management [Ringwood, 1985].

The composition and amount of high-level waste (HLW) can heat both the waste package and surrounding rock and cause temperatures to rise to 800-900 °C [Gibb, 1999]. Heat-induced expansion of matrices can cause distortions and stress in ceramic waste containers, highlighting the importance of studying thermo-physical properties like linear and volume thermal expansion.

In this light of the above, minerals present a valuable avenue for research. With their rich content of radioactive elements, they offer a means to mimic crystalline counterparts of waste materials. Moreover, they have undergone irradiation for millions of years, a condition that cannot be replicated in laboratory experiments involving heavy ion bombardment. Natural phases provide a means for testing the hypothesized long-term behavior of waste-form phases in specific geochemical environments [Omel'yanenko et al., 2007; Yudintsev, 2021].

2. *Synthesis and study of synthetic analogs of crichtonite group minerals to obtain new magnetic materials*.

This work exemplifies the "from mineral to material" approach. Studying minerals not only offers solutions to intricate problems but also sparks innovation in the development of functional materials. In the second part of the work, synthesis and characterization of properties of a number of new compounds belonging to the structural type of crictonite were carried out. The relevance of this study lies in its potential application as a magnetic functional material.

To date, the priority tasks in science and industry include the search for and production of cost-effective, resource-efficient functional materials characterized by various useful physical and chemical properties. For instance, extensive research has been conducted on the magnetic properties of monazite- and zircon-like compounds. Among these, perovskite stands out as a prime example, attracting significant scientific attention due to its variable formulas, flexible structures, unique properties, and broad applications. The magnetic properties of perovskite materials have been extensively explored [Mtougui et al., 2018]. Magnetic perovskites are applied in magnetic refrigeration [Xu et al., 2002], information storage and other fields.

Standard manganese-based perovskites have been intensively researched due to metal-insulator transitions and colossal magnetoresistance amongst their properties. The interesting behavior has been attributed in part to the competition between a ferromagnetic metallic state and an antiferromagnetic insulating state with phase separation and the presence of charge-ordering. Manganites are also well known due to other structural, electronic, and magnetic characteristics [Jadli et al., 2021; Markovich, Wisniewski, Szymczak, 2014].

This has inspired us to explore novel frameworks for complex compounds exhibiting intriguing magnetic properties. One such promising research target is the crichtonite group, which we delve into in our study. This mineral group boasts a highly adaptable structure capable of accommodating a diverse range of elements, thus holding potential for functional materials. Despite this, its magnetic

properties remain relatively understudied.

The degree of scientific development of the topic.

Studies devoted to developing a concept for immobilizing high-level waste on the basis of actinide-containing minerals include the work of Ringwood A. E., Ewing R.C., Lumpkin G. R., Yudintsev S. V., Burakov B. E., Gieré, R., Zhang Y. etc. Various types of multiphase ceramic waste forms, often based on the structures of these minerals, have been studied for their potential in waste immobilization. These host-phases include hollandite [Tumurugoti et al., 2017; Yudintsev, 2021], pyrochlore [Omel'yanenko et al., 2007], monazite [McCarthy, White, Pfoertsch, 1978; Omel'yanenko et al., 2007], zirconolite [Ringwood, 1985], perovskite [Kesson, Ringwood, 1981], brannerite [Zhang, Mir, 2023], crichtonite [Gong et al., 1994], murataite [Yudintsev et al., 2022] and so on [Burakov, Ojovan, Lee, 2011]. Their chemical compatibility [Kessoft, Sinclair, Ringwood, 1983], durability [Lumpkin, 2006; Lumpkin et al., 2014; Ringwood, 1985; Smith et al., 1992], radiation resistance [los Reyes de et al., 2020; Meldrum et al., 1999a; Wang et al., 1999b; Wang et al., 1999a; Yudintsev et al., 2001] were investigated to assess their potential for waste immobilization.

The design and development of these ceramics have been influenced by important results obtained from studies of so-called "natural-analogue materials" [Gieré, Lumpkin, Smith, 2018].

To begin with, the decay of radioactive components induces a transition from periodic to aperiodic structures in crystalline materials [Ewing et al., 1987; Ewing, 1994; Pabst, 1952]. This radiation-induced structural damage, known as metamictization, is observed in natural minerals [Murakami, 1993] and is similarly manifested in synthetic ceramics designed for the immobilization of radioactive elements. In laboratory settings, heavy ion irradiation is commonly employed to assess the radiation resistance of these materials [Lumpkin, Smith, Blackford, 2001; Meldrum et al., 1999b]. Given that minerals with actinides undergo self-irradiation over geological timescales—a timescale that cannot be replicated under laboratory conditions—studies on the radiation damage in natural minerals are conducted to evaluate the long-term stability of waste forms [Lumpkin, Blackford, Colella, 2013; Lumpkin, Chakoumakos, 1988; Lumpkin, Leung, Ferenczy, 2012].

Next, the annealing of radiation damage has been studied through the thermal recrystallization of metamict minerals [Eyal, Lumpkin, Ewing, 1986; Lumpkin, Ewing, Foltyn, 1986; Zhang et al., 2006]. This recrystallization has been investigated using various techniques, with the most employed method being powder X-ray diffraction (pXRD) [Tomašić et al., 2004]. Numerous studies have utilized pXRD in combination with other methods, such as transmission electron microscopy (TEM) [Seydoux-Guillaume et al., 2002; Tomašić et al., 2006; Tomašić et al., 2008; Zhang et al., 2006], spectroscopic methods like Raman spectroscopy [Frost, Reddy, 2011a; Frost, Reddy, 2011b; Tomašić et al., 2008; Tomašić et al., 2011], and X-ray photoelectron spectroscopy (XPS) [Colella et al., 2005].

The mechanism of metamictization has been widely discussed [Ewing, 1975; Graham, Thornber, 1974]. However, the mechanisms underlying the recrystallization of metamict minerals

remain not completely unclear [Tomašić et al., 2006]. Some mineral species with close composition can recrystallize, while others cannot. In relatively recent work, samarskite was reported to recrystallize completely in a study published by Britvin et al. [2019], but not in the work by Cao et al. [2015]. Therefore, it is necessary to expand thermal recrystallization studies to a broader range of mineral samples to better understand the factors influencing recrystallization.

Finally, the thermal expansion coefficients of synthetic materials with abovementioned structures have been calculated in various studies to provide a database for ceramic waste immobilization [Asuvathraman, Kutty, 2014; Ball, Thorogood, Vance, 1992; Bobiński, Ziółkowski, 1991; Zhang et al., 2020]. Given the limited research on the thermophysical properties of minerals, six minerals containing lanthanides and actinides were selected in this study to add significantly to the existing information on the behavior of such minerals with increasing temperature.

The second part of this work focused on magnetic research. Fergusonite-type [Kawakami et al., 2013], brannerite-type [Kimber, Attfield, 2007; Markkula, Arevalo-Lopez, Paul Attfield, 2012], and pyrochlore-type [Taira et al., 2003] compounds have been extensively studied for their magnetic properties. However, there is a relative lack of research on the magnetic properties of crichtonite-structure-based compounds. Therefore, this study aims to synthesize and investigate the magnetic properties of crichtonite-structure compounds.

Goal and tasks of the dissertation research:

The subject of this study are samples of metamict minerals containing lanthanides and actinides from the collection of the former museum of the Department of Mineral Deposits (Saint-Petersburg State University), as well as synthetic compounds of crichtonite with lanthanides and a range of optional cations.

The purpose of this research is to study the behavior of metamict minerals with increasing temperature, rationally design the material based on structure type of crichtonite and study their magnetic properties.

The objectives of the dissertation research are determined by the stated purpose and include:

1. The mineralogical characterization (composition analysis) of selected metamict minerals – fergusonite-(Y), davidite-(La), brannerite, zirconolite, samarskite and thorite[1].
2. Investigating metamict samples under thermal treatment, employing combined technologies to monitor the samples at various stages: before, during, and after the treatment.
3. Reapply the heat treatment under different heating conditions (for metamict minerals with a sufficient sample size).
4. Identification of crystallized phases in heat-treated samples through a combination of

[1] To make it easier for the readers, the crystal structures of selected minerals are outlined in appendix, see page 140.

methods.

5. Evaluating the thermal expansion tensor of recrystallized minerals through method of High-temperature X-ray diffraction.
6. Comparison and analysis of the results obtained and conclusion about the most promising mineral-like matrices for high-level waste (HLW).
7. Synthesis of the crichtonite-group minerals analogs and rational substitution of cations.
8. Examination of the magnetic behavior of synthesized crichtonite-structure materials.
9. Determination of the crystalline and magnetic structures (X-ray and Neutron diffraction) of new synthetic compounds.

Methods of research

The localized composition and morphology of minerals were studied using scanning electron microscopy (SEM). The chemical composition of the mineral samples was determined by energy dispersive spectroscopy (EDS) and wave-dispersive spectroscopy (WDS). Characterization of the functional groups of the mineral samples by Raman spectroscopy.

Powder X-ray analysis (PXRD) of metamict samples before and after heat treatment to determine the degree of crystallinity and phase purity. The phase content of heated products of minerals was obtained through the Rietveld method.

High-temperature X-ray diffraction experiments were carried out, combined with complex thermal analysis (Thermal Gravimetric Analysis and Differential Scanning Calorimetry TG-DSC) to investigate the recrystallization process *in-situ*.

The syntheses of the compounds presented in the work were carried out by solid-state reactions. Magnetic properties characterization of the samples was performed through temperature-dependent susceptibility, field dependent magnetization measurements.

Identification and refinement of the crystalline and magnetic structure of the synthesized compounds were carried out by X-ray diffraction and neutron diffraction at Institute Laue-Langevin in city Grenoble.

Reliability of the results

The reliability of the results of this work is based on complementary experimental data obtained using modern physical and chemical independent research methods, reproducibility of experiments and comparison of results with data published by other researchers.

In total, during the exploration of 6 natural minerals, the author collected 1170 energy dispersive spectra, 395 Raman spectra, 9 sets of DSC and TG data, and 485 powder thermal X-ray diffraction patterns.

Additionally, in the investigation of synthetic compounds, 27 systems were synthesized, resulting in 19 DC magnetic measurements, 10 AC magnetic measurements, 1 heat-capacity measurement, and 7 neutron diffraction datasets.

Approbation of the study

On the topic of the dissertation, four articles were published in scientific journals indexed in the systems Web of Science and Scopus. There are four more articles being prepared for submission to journals. The main results of the work within the framework of this thesis were presented in the form of an oral report at two Russian conferences and poster presentations at one international conference.

Scope and the structure of the thesis

The dissertation consists of an introduction, four chapters, a conclusion, a list of references and an appendix.The total volume of the work is 159 pages, including 99 figures, 76 tables and a bibliography of 255 titles. Chapter 1 provides an overview of the mineralogical characteristics of the natural minerals under study. It also explores the crystallographic structure of mineral specimens and covers essential information about the physical properties of solid materials, including thermal expansion and magnetic properties. In Chapter 2, the methods of studying the compounds and the calculations used in this work are given. Chapter 3 presents in detail the results of complex mineralogical analyses of natural samples and explore the thermal evolution these minerals undergo. Chapter 4 discusses thermal expansion behavior with calculation of thermal expansion coefficients of 6 structures. Chapter 5 discusses the syntheses conducted on novel crichtonite-like compounds, along with their physical properties. An explanation of the synthesis procedures for each compound, as well as the results of X-ray powder diffraction analysis, are given in the appendices.

Scientific novelty

This work investigated the evolution with increasing temperature of six mineral samples, which contributes to a comprehensive understanding of recrystallization of minerals from metamict state. In this work, it has been observed for the first time the temperature induced recrystallization of 2 metamict minerals *in-situ*. These minerals serve as valuable subjects to study the thermal expansion properties, yielding data on the coefficient of thermal expansion for 6 minerals, with potential applications in waste management. The study on synthetic compounds completed a route that from mineral to material. Their magnetic properties were explored. Therefore, there are three thesis statements containing elements of novelty submitted for defense:

Thesis statements to be defended:

1. When metamict davidite-(La) and brannerite are annealed in the temperature range 650–1200 °C, their crystal structures are completely restored. The process of recrystallization of thorite and fergusonite is accompanied by the crystallization of their polymorphs, huttonite and fergusonite-α, respectively. The process of recrystallization of thorite and huttonite is accompanied by the crystallization of various fluorite-type oxides and calcium uranates, depending on the composition of the primary metamict samples. Metamict zirconolite restores the crystal structure as the 3*T* polytype at 1050 ºC.
2. For the first time, the coefficients of thermal expansion were calculated on mineral samples

of davidite-(La), brannerite, zirconolite-3*T*, fergusonite-(Y), thorite and huttonite. The most isotropic behavior of thermal expansion with increasing temperature is exhibited by the structure of zirconolite-3*T*, and the lowest value of volumetric thermal expansion $\bar{\alpha}_V$ = 12.49(12) × 10^{-6} °C^{-1} was observed in thorite. *β*-Fergusonite shows the highest volumetric thermal expansion with increasing temperature, $\bar{\alpha}_V$ = 32.1(5) × 10^{-6} °C^{-1}, which significantly exceeds the values previously obtained on synthetic pure samples. At a temperature of 825 °C, *β*-fergusonite reversibly transforms into α-fergusonite. Fergusonite-(Y) of complex composition is the least preferred for use as ceramics for the immobilization of radioactive elements.

3. A series of compounds with a crichtonite structure have been synthesized with the most notable framework being *Ln*MTO and *A*MTO[2], where *Ln* represents the trivalent lanthanides (La, Ce, Nd) and *A* is divalent cations, specially, Ca, Sr, or Ba. Titanium is in 3+/4+ mix-valence state. The compounds *A*MTO exhibit similar magnetism and are characterized by ferrimagnetic arrangement of Mn^{2+} and Ti^{3+} spins. In the samples CaFTO and SrFTO[3], even with the full replacement of Mn^{2+} by Fe^{2+}, the ferrimagnetic arrangement persists between spins located at different sites. In contrast, the partial substitution of Ti^{3+} with Fe^{3+} in samples SrMTFO and LaMTFO[4] is confirmed to leading to spin glass behavior. The observation on samples *Ln*$Mn_3Ti_{18}O_{38}$ suggests that rare earth ions also disrupt the magnetic ordering.

Brief introduction of main research results:

1. Metamict davidite-(La) from Radium Hill deposit in Australia successfully recrystallized through heat treatment[5]. The evolution of this mineral with increasing temperature was investigated, and the coefficients of thermal expansion (CTE) for the crystalline sample were determined. The results show that davidite has relatively low CTE, demonstrating thermophysical stability, with almost isotropic thermal expansion. The author made a significant contribution to this publication, including conducting experiments, analyzing results, and drafting the manuscript. These contributions are detailed in the author contributions section at the end of the published article.
2. Two compounds $SrMn_3Ti_{18}O_{38}$ and $SrMn_3Ti_{14}Fe_4O_{38}$ with crichtonite structure, which is isostructural with davidite, were successfully synthesized and reported[6]. The magnetic

[2] *Ln*MTO and *A*MTO: short name for crichtonite compounds with composition of *Ln*$Mn_3Ti_{18}O_{38}$ and *A*$Mn_3Ti_{18}O_{38}$, see 4.2 and 4.3.
[3] CaFTO and SrFTO: short name for crichtonite compounds with composition of $Ca_2Fe_2Ti_{18}O_{38}$ and $SrFe_3Ti_{18}O_{38}$, see 4.3.2 and 4.3.5.
[4] SrMTFO and LaMTFO: short name for crichtonite compounds with composition of $SrMn_3Ti_{14}Fe_4O_{38}$ and $LaMn_3Ti_{14}Fe_4O_{38}$, see 4.3.4 and 4.2.2.
[5] Chen R., Siidra O. I., Ugolkov V. L., Firsova V. A., Vlasenko N. S., Arevalo-Lopez A. M., Colmont M., Bocharov V. N. Thermal evolution of metamict davidite-(La) from the Radium Hill, Australia: recrystallization and thermal expansion // Physics and Chemistry of Minerals. 2024. Vol. 51. № 2. P. 12. https://doi.org/10.1007/s00269-024-01274-9
[6] Rosas-Huerta J. L., Chen R., Ritter C., Siidra O., Colmont M., Arévalo-López A. M. Ferrimagnetic and spin glass behaviour in $SrMn^{2+}{}_3Ti^{4+}{}_{14}M^{3+}{}_4O_{38}$ (M = Ti and Fe) synthetic crichtonites // Chemical Communications. 2023. Vol. 59. № 88. P. 13199–13202. https://doi.org/10.1039/D3CC04336C

measurements and neutron powder diffraction were used to exam the ferrimagnetic behavior in $SrMn_3Ti_{18}O_{38}$, while $SrMn_3Ti_{14}Fe_4O_{38}$ shows spin-glass behavior. The author performed the synthesis and analyzed the results, processed the primary data, and participated in writing the manuscript of the article.

3. The thermal expansion of natural metamict brannerite from Akchatau, Kazakhstan was studied, with it thermal expansion determined[7]. The author made major contributions to this publication, including conducting experiments, analyzing results, and drafting the manuscript.
4. The fergusonite-(Y) from the Ilmeny Mountains has been studied. After crystallization, fergusonite undergoes a reversible alpha-beta polymorphic transition. The thermal expansion of both tetragonal (α-fergusonite) and monoclinic (β-fergusonite) polymorphs was examed, finding that β-fergusonite has anisotropic expansion, while α-fergusonite expands less[8]. The author made significant contributions to this publication, including conducting experiments, analyzing results, and drafting the manuscript. This contribution is detailed in the author's section at the end of the published article.

[7] Chen R., Siidra O. I., Firsova V. A., Arevalo-Lopez A., Colmont M., Ugolkov V. L., Bocharov V. N. The Chemistry, Recrystallization and Thermal Expansion of Brannerite from Akchatau, Kazakhstan // Materials. 2023. Vol. 16. № 4. P. 1719. https://doi.org/10.3390/ma16041719

[8] Chen R., Siidra O. I., Firsova V. A., Ugolkov V. L., Vlasenko N. S., Bocharov V. N., Arevalo-Lopez A. M., Colmont M., Tokarev I. V. Thermal evolution of the metamict fergusonite-(Y) // Physics and Chemistry of Minerals. 2024. Vol. 51. № 1. P. 8.. https://doi.org/10.1007/s00269-023-01263-4

Chapter 1. Literature review

The primary focus of the first chapter is on the geological and crystallographic characteristics of six mineral specimens, including previous research on their metamictization and temperature induced recrystallization. Additionally, it briefly covers the fundamental principles of thermal expansion properties in solid substances and introduces the magnetism of materials.

1.1 Geological fingerprints and crystallographic structure of studied minerals

1.1.1 Brannerite UTi_2O_6

Brannerite is an uranium titanate mineral with UTi_2O_6 ideal formula. It contains 62.8 wt.% of UO_2 [Lumpkin, Leung, Ferenczy, 2012; Szymanski, Scott, 1982]. The high content of uranium makes brannerite an exploitable uranium resource. It contains uranium in a multivalent state due to its origin [Turuani et al., 2020] and redox reactions are caused by the radioactive decay. Therefore, tetra-, penta- and hexavalent uranium are able to incorporate into the natural and synthetic brannerite [Colella et al., 2005; Vance et al., 2001]. ThO_2 is a common component of the natural brannerite, along with up to 8 wt.% of rare earth elements (REE) and a small amount of CaO, Fe_2O_3, PbO and Al_2O_3 [Pabst, 1954; Turuani et al., 2020]. Due to the hydration and alteration, the significant amounts of Si and other elements are able to be incorporated into the structure [Charalambous et al., 2012]. Thus, the mineral has the general formula of AB_2O_6, where the *A* site can be occupied by U, Ca, Th, Y and REE, and the *B* site is mainly occupied by Ti, Nb, Si, Fe and Al [Charalambous et al., 2012; Lumpkin, Leung, Ferenczy, 2012; Turuani et al., 2020].

Natural brannerite specimens are often metamict because of the radiation damage. However, Szymanski and Scott [1982] successfully determined the crystal structure of the synthetic UTi_2O_6, indicating the monoclinic symmetry and *C*2/*m* space group. Both the U and Ti atoms are in distorted octahedral coordination. TiO_6 octahedra are linked one with each other via a common edge, thus forming a TiO_2 layer parallel to the *ab* plane. Layers are interconnected via UO_6 octahedra, as shown in Figure 1.

The highly radioactive, uranium-bearing mineral was first found in a gold placer in Idaho, USA [Hess, Wells, 1920]. As an accessory mineral, brannerite is widely reported in various geological environments, including granites, granitic pegmatites and hydrothermally altered sedimentary rocks. Turuani et al. [2020] have studied brannerite samples from five hydrothermal and five pegmatitic localities across the world and revealed the difference in element content correlated with the geological environments. Aluminum, for instance, is hardly observed in hydrothermal brannerite, while brannerite in pegmatite shows a wider range of Al-content. Low-temperature Au deposits may also be a source of brannerite. In the Witwatersrand (South Africa), brannerite is considered as a secondary uranium mineral, it also appears as inclusion in detrital minerals, linings around pyrobitumen nodules and micro veins in gold-bearing horizons [Fuchs et al., 2021]. The uranium

mineralization in the Central African Orogenic Belt is related to post-magmatic metamorphism, and the minerals associated with brannerite are monazite, uraninite, zircon, albite, calcite, chlorite, apatite, U-silicates, and iron oxides [Olivier et al., 2021]. A Cretaceous siderite deposit in Eastern Alps underwent metamorphism also caused U-metamorphization, brannerite in the Hüttenberg deposit exhibit euhedral prismatic crystals, and shows the evidence of hydration, metamictization, and alteration to anatase/leucoxene [Waitzinger et al., 2021]. Brannerite is reported also in altered ores at the uranium deposit Komsomolskoye, Central Kazakhstan [Chernikov, Dorfman, 2004].

In this work, the brannerite sample (Figure 1) originates from the Akchatau, Kazakhstan, where the W-Mo deposits are hosted within leucocratic granites of the Permian age [Yefimov et al., 1990].

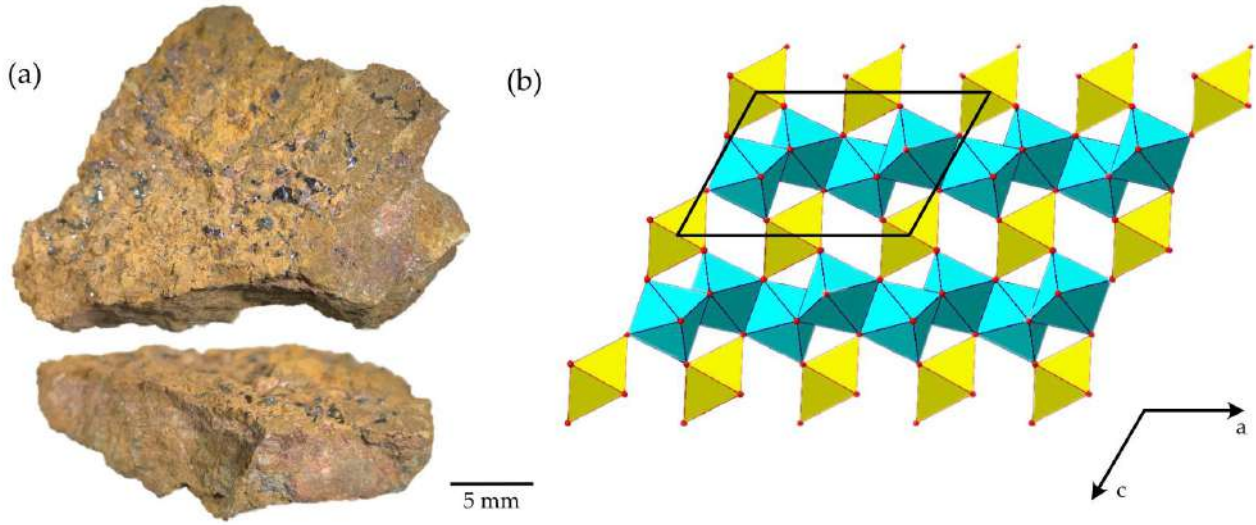

Figure 1. Brannerite in a host rock from Akchatau (Kazakhstan), black massive grains are brannerite (a); General projection of the crystal structure of brannerite along the *b* axis (b) (UO_6 = yellow octahedra; TiO_6 = blue octahedra; structure drawn after Szymanski and Scott [1982], SG: *C*2/*m*, *a*=9.8, *b*=3.8, *c*=6.9 Å, *β*= 119.0°).

1.1.2 Thorite and huttonite $ThSiO_4$

Thorite and huttonite, two dimorphs of $ThSiO_4$, are well-known naturally occurring actinide orthosilicates. Thorite is often found in a metamict (radiation-damaged) state, while huttonite is often crystalline [Ewing, Haaker, 1980; Förster, Harlov, Milke, 2000. Both minerals have a structure composed of isolated SiO_4 tetrahedra and ThO_8 (in thorite) or ThO_9 (in huttonite) edge-sharing polyhedra [George, 1951; Pabst, Hutton, 1951]. The crystal structures of huttonite and thorite are demonstrated in Figure 2. The density of huttonite is 7.1 g/cm^3, while it is 6.7 g/cm^3 for thorite, both ideally $ThSiO_4$. The primary structural distinction is the presence of large voids in the structure of thorite [Taylor, Ewing, 1978]. These voids form channels parallel to the *c* axis and may contain water [Strzelecki et al., 2021]. Metamict thorite may contain up to 70 mol % of waters [Ewing, 1994]. "Thorogummite" $(Th,U)(SiO_4)_{1-x}(OH)_{4x}$, which is a term for hydrated thorite, was discredited a decade ago [Piilonen et al., 2014].

The phase transition of thorite (zircon-type $I4_1/amd$) into huttonite (monazite-type $P2/c$) in natural and synthetic system Th-Si-O is reported in the range of 715-1225 °C [Finch, Harris, Clark, 1964; Mazeina et al., 2005; Pabst, 1952; Seydoux-Guillaume, Montel, 1997]. Synthesis studies for

the thorite-huttonite system have determined the temperature of the phase transition (thorite to huttonite) at 1 atm, 1210 ± 10°C [Seydoux-Guillaume, Montel, 1997], is in a good agreement with [Finch, Harris, Clark, 1964] (1225 ± 10°C) and disagrees with [Dachille, Roy, 1964] (1000°C). Mazeina et al., [2005] have determined the phase diagram in dependence of pressure and temperature. Huttonite is more stable at high-pressures and high-temperatures [Mazeina et al., 2005].

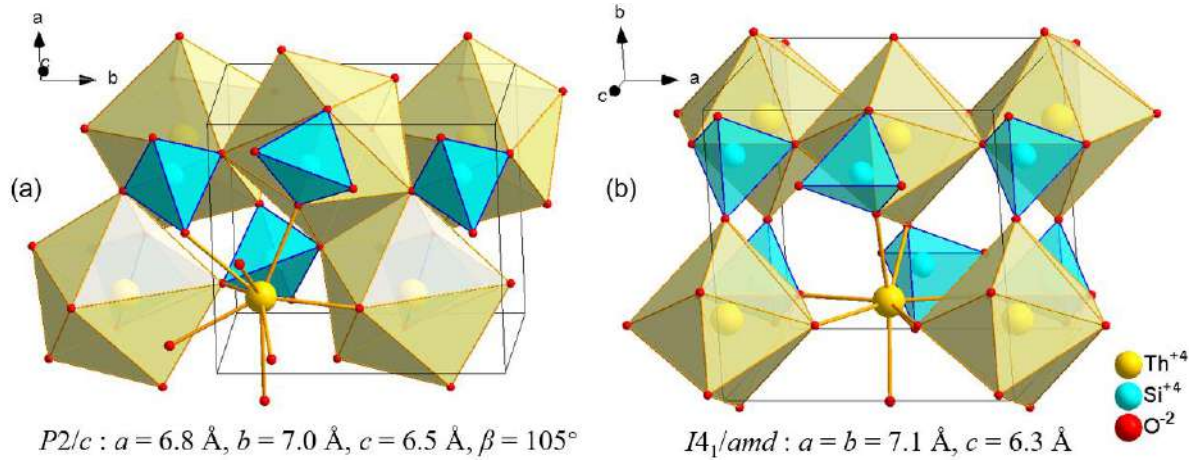

Figure 2. Crystal structure of (a) huttonite and (b) thorite, their space group are *P*2/*c* and *I*4$_1$/*amd*, respectively (drawn after Taylor, Ewing [1978]).

Many publications provide virous results on the recrystallization of the metamict thorium silicates. Huttonite was reported to crystallize from the metamict thorite upon heating above 1000 °C [Robinson, Abbey, 1957]. In the examination of five thorium silicate metamict specimens, as detailed by Pabst [1952], thorite and huttonite phases can crystallize simultaneously at 715°C. In certain specimen, thorite predominates over huttonite at range of 850-935°C. The thorium silicate phase in all samples eventually converted to the huttonite upon the heat treatment to 1400 °C. Staartz [1976] heated thorite at 1000 °C for 1 h, which led to the crystallization of thorite and cubic (Th,U)O_2. Applying pressure lowers the crystallization temperature: natural crystalline Hedonite from Gillespies Beach in New Zealand has been shown to form at relatively low temperatures and pressures (500 °C and 7 kbar) [Förster, Harlov, Milke, 2000].

The study of thorium silicate minerals can enhance our understanding of the long-term behaviour of these actinide bearing phases [Yudintsev et al., 2022]. Thorite and huttonite are known as actinide-bearing phases in multi-phase ceramic waste forms [Lumpkin et al., 2014; Shelyug et al., 2021]. In ion irradiation experiments conducted on hydrothermally synthesized huttonite and thorite, the former exhibits lower critical amorphization temperature [Meldrum et al., 1999b]. It was observed that the area of the radiation damage in huttonite was smaller than in thorite, which was tentatively attributed to the higher density of the former [Cartz, Karioris, Gowda, 1982]. That also explained why huttonite more often exhibits as crystalline in nature.

This research on metamict thorite is driven by the limited knowledge of the behavior of huttonite upon temperature rise. Huttonite is rarely encountered, necessitating further investigation with more samples of metamict thorium silicates.

1.1.3 Fergusonite-(Y) $YNbO_4$

Fergusonite, named after Robert Ferguson, is one of the most abundant metamict mineral [Haidinger, 1826]. It was even first described before the term Metamict was coined to refer to an amorphous mineral [Ewing et al., 1987].

Fergusonite, a natural concentrator of rare-earth elements, occurs primarily as an accessory mineral in pegmatites and granites [Guastoni, Cámara, Nestola, 2010; Tomašić et al., 2006]. It can also be found in carbonatites and skarn deposits [Kapustin, 1976]. The formation of fergusonite is believed to occur at the late stage of mineralization [Zozulya, Macdonald, Bagiński, 2020]. It is often associated with REE minerals such as aeschynite, samarskite, yttrotantalite, pyrochlore, columbite, allanite, monazite, etc. Fergusonite is hardly distinguished from other "*ABO*" niobates and tantalate minerals without detailed chemical and structural analyses.

Three eponymous species of the fergusonite group are approved by the International Mineral Association (IMA) with the general formula of ABO_4. They are classified according to the dominant *A* site cation: Y, Ce, or Nd. *B* site stands mainly for Nb except for the formanite-(Y) containing solely Ta. The bigger *A* site can be replaced by U, Th, Ca, and Pb, while Ta, Ti, and W are likely occupying the Nb site. The most common natural representative is fergusonite-(Y).

Two polymorphs of fergusonite are reported to occur naturally, the tetragonal α-fergusonite and the monoclinic *β*-fergusonite. The monoclinic polymorph (*C2/c*) is named *β*-fergusonite to distinguish it from tetragonal ($I4_1/a$) *α*-form. Ferguson [1955] examined the monoclinic structure in both natural fergusonite and synthetic $YTaO_4$. The tetragonal structure was first determined by Komkov on the mineral sample [Komkov, 1959]. Both structures contain isolated NbO_4-tetrahedra interlinked with yttrium in eight-fold coordination (Figure 3). *I*2/*a* is also commonly used in the literature to describe *β*-fergusonite, having a different setting from *C*2/*c* via the transformation matrix ($00\bar{1}/010/101$) [Guastoni, Cámara, Nestola, 2010], which is used for *β*-fergusonite refinement in this work. A third polymorph, *M'*-fergusonite, which crystallizes in a space group *P*2/*a* has been determined by Wolten [1967]. In addition, a fourth triclinic polymorph of fergusonite ($P\bar{1}$) was observed recently in high-pressure experiments [Garg et al., 2022].

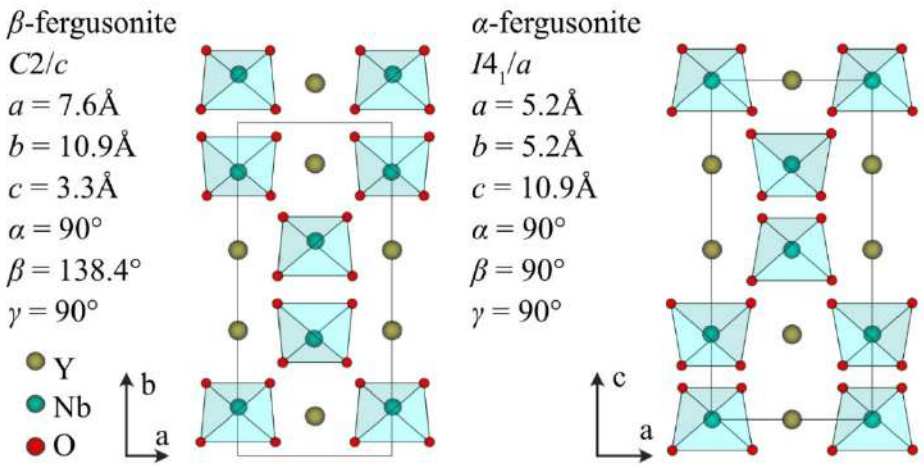

Figure 3. Projections of the crystal structures of *β*- and *α*-fergusonites on (001) and (010), respectively. Also see Figure 39.

1.1.4 Samarskite $YFeNb_2O_8$

Samarskite-(Y) is one of the most famous rare earth minerals. Samarskite was named in honor of V.E. Samarsky-Bykhovets [Britvin et al., 2019]. Samarskite-(Y) is a typical accessory mineral in niobium-yttrium-fluorine pegmatites (NYF) and their parent granites [Černý, London, Novák, 2012; Dill, 2015; Guastoni et al., 2019]; therefore, variations in its chemical composition have been carefully studied see for instance [Ercit, 2005; Hanson, Simmons, Falster, 1998; Papoutsa, Pe-Piper, 2013; Pieczka et al., 2014; Uher, Ondrejka, Konečný, 2009]. However, the crystal structure of samarskite remained unclear for long time because the mineral is often found in a metamict state [Capitani, Mugnaioli, Guastoni, 2016; Ewing, 1975]. The first experiment aimed at restoring the crystalline state of samarskite by annealing showed that the structure formed when samarskite is heated in air to 660 °C corresponds to a wolframite-type structure [Lima-de-Faria, 1958]. Further studies [Hanson et al., 1999; Simmons, Hanson, Falster, 2006; Sugitani, Suzuki, Nagashima, 1985; Tomašić et al., 2010] revealed the sequential transformation of orthorhombic (low temperature) and monoclinic (high temperature) oxide phases during the annealing of metamict samarskite.

The chemical formula of samarskite-(Y) was firstly accepted as ABO_4, where A = (Y, Ln, Ca, Fe, U) and B = (Nb, Ti, Ta) [Hanson et al., 1999]. However, the redetermination of the structure of natural crystalline samples has led to a revision of the general formula of samarskite. The updated formula is AMB_2O_8 [Britvin et al., 2019], where A = Y, Ln, Th, U^{4+}, Ca; M = Fe^{3+}, Mn^{2+}; B = Nb, Ta, Ti, Si. The monoclinic structure (Space group: $P2/c$) can be described as comprising three distinct layers. The A layer consists of square antiprisms (AO_8), united through common edges, the B layer consists of chains of octahedra (BO_8), and the M layer comprises octahedra chains of (MO_8). These three layers stack sequentially along the a-axis in the order ABMB (Figure 4).

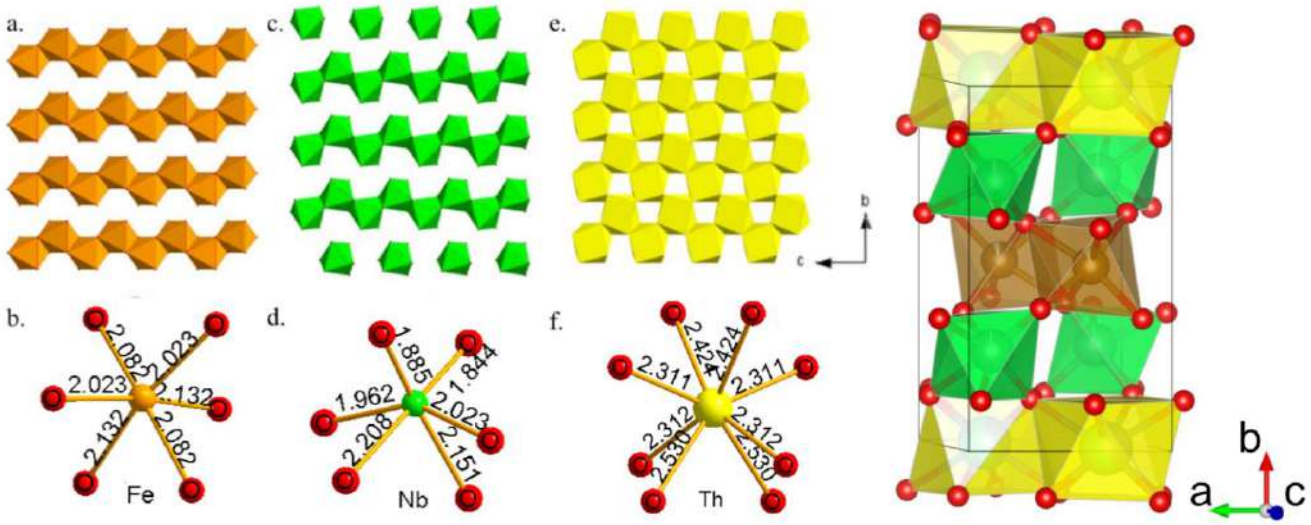

Figure 4. Crystal structure of samarskite. (MO_6) octahedrons form chains along the c-axis (a,b); (BO_6) octahedra chains (c,d); Layer consisting of square antiprisms (AO_8) (e,f) (drawn after Britvin et al., 2019). Space group: $P2/c$, a=9.8, b=5.6, c=5.2 Å, β= 93.4°. Distances are given in Angströms.

1.1.5 Zirconolite $CaZrTi_2O_7$

Zirconolite, ideally $CaZrTi_2O_7$, was first described by Borodin et al., [1956], see also Bulakh et al., [2006]. This mineral was discovered in calcite-amphibole-clinopyroxene rock found in the central part of the alkaline-ultrabasic Afrikanda complex located in the Kola alkaline province. [Chakhmouradian, Zaitsev, 1999; Chakhmouradian, Zaitsev, 2002; Chakhmouradian, Zaitsev, 2004; Kukharenko et al., 1965; Zaitsev, Chakhmouradian, 2002]. Subsequently, at Kola, the mineral was found in phoscorites and carbonatites from Kovdor, Vuoriyarvi, Seblyavr and Turiy Mys [Chakhmouradian, Williams, 2004]. Zirconolite occurrences, however, are not restricted to phoscorite / carbonatite complexes only. The mineral is now known from a wide range of silicate rocks, and even skarns [Pascal et al., 2009; Williams, Gieré, 1996; Zubkova et al., 2018].

Compositionally, zirconolite is characterized by wide element variations, and could contain significant amount of Nb, Fe, rare earth elements (REE), U and Th [Bellatreccia et al., 1999; Bellatreccia et al., 2002; Gieré, Williams, Lumpkin, 1998; Pascal et al., 2009; Sharygin, Doroshkevich, Khromova, 2016; Ventura Della, Bellatreccia, Williams, 2000; Williams, Gieré, 1996]. Presence of U and Th in zirconolite, particularly in geologically old rocks, led to damage of a crystal structure and mineral metamictization. Young zirconolite, however, is crystalline, even Th and U rich, and is suitable for a single-crystal analysis [Zubkova et al., 2018]. In addition to its significance as a host for high-field-strength and rare earth elements [Chakhmouradian, Williams, 2004] and mineral-geochronometer [Wu et al., 2010], synthetic zirconolite is regarded as a crucial component in Synroc materials [Lutze, Ewing, 1988].

Natural and synthetic zirconolite fulfills the various requirements for a titanate ceramic matrix for HLW (high-level waste), such as the ability to include a wide range of elements, radiation tolerance, and mechanical durability [Kessoft, Sinclair, Ringwood, 1983; Yudintsev et al., 2022; Zhang et al., 2018]. The structure of a zirconolite framework is typically characterized by two distinct layers. One of these layers primarily composed of octahedrally coordinated cations (TiO_6) which approximate a hexagonal tungsten bronze (HTB) motif. Individual pyrochlore HTB layers are very similar to those of zirconolite (Figure 5, a). In between the HTB layers are layers of CaO_8 and ZrO_7 polyhedra. Depending on the composition and formation conditions, zirconolite may form distinct polytypes: 2*M*, 3*O*, 3*T*, and 4*M* [Cheary, Coelho, 1997; Chukanov et al., 2014; Chukanov et al., 2019; Coelho, Cheary, Smith, 1997; Gilbert et al., 2010; Vance et al., 2002]. In the nomenclature of polytypes, the numeral indicates the number of layers in the unit cell, while the letter denotes the crystal system, such as in the case of zirconolite-2*M*, which is a monoclinic crystal with two layers stacked along the *c*-axis of the unit cell (Figure 5, b). Zirconolite-3T is trigonal crystal with three layers in unit cell (Figure 5, c). Although numerous studies have been conducted to investigate the effect of cation doping on polytype crystallization, the effect of polytype performance on high-level waste (HLW) immobilization has not been thoroughly investigated [Coelho, Cheary, Smith, 1997; Gilbert et al., 2010; Ji et al., 2021; Vance et al., 2002].

When natural minerals with complex chemical compositions are heated, recrystallization occurs. The knowledge gained about crystallized polytypes provides valuable insight into predicting the preferred polytype that may form in SYNROC when the temperature is increased. This study presents a comprehensive investigation of geologically old, ca. 370 Ma, metamict zirconolite from the Kovdor phoscorites and carbonatites (Kola Alkaline Province).

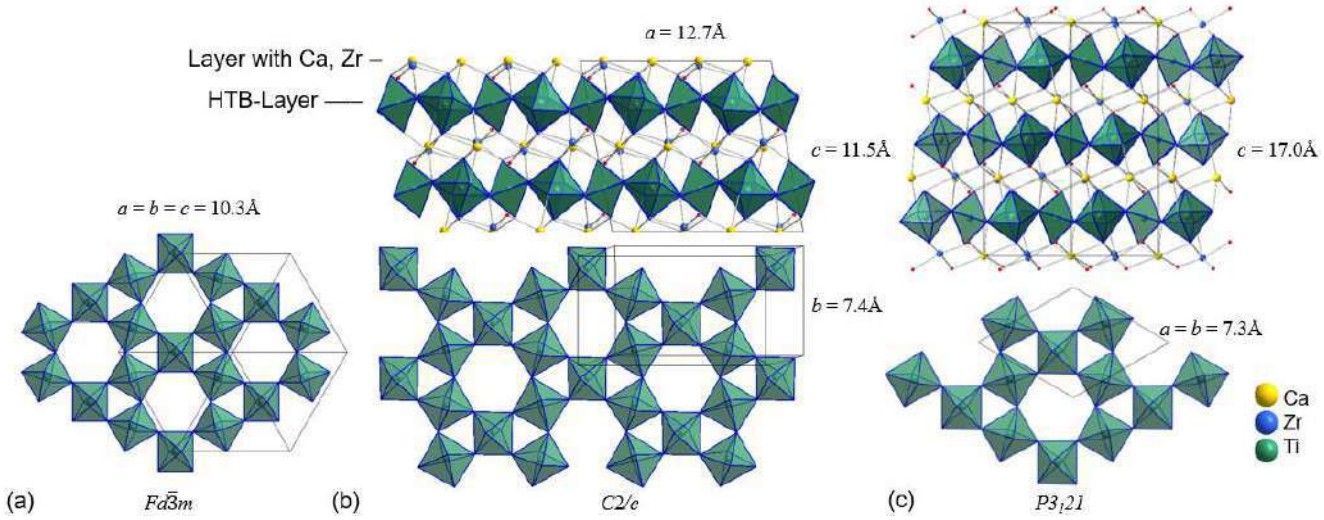

Figure 5. HTB-type layer on (111) of pyrochlore (a). The HTB-layers in zirconolite-2*M* (b) and zirconolite-3*T* (c). Drawn after Sameera et al., [2011b], Gatehouse et al., [1981] and Zubkova [2018], respectively.

1.1.6 Minerals of the crichtonite group $ABT_2C_{18}O_{38}$

Davidite is a rare earth mineral known for its high uranium content, was mined for uranium in the Radium Hill area in Australia [Ludwig, Cooper, 1984]. It is estimated that ~ 970 tons of davidite ore were mined between 1906 and 1944, producing 852 tons of U_3O_8 [Lottermoser, Ashley, 2005].

Davidite-(La) belongs to the crichtonite group, which crystallizes in a trigonal symmetry, space group $R\bar{3}$. Crichtonite group is classified as complex oxide mineral with general formula $^{XII}A\,^{VI}B\,^{IV}T_2\,^{VI}C1_6\,^{VI}C2_6\,^{VI}C3_6\,O_{38}$, where *A*, B_i, *T* and C_i stand for six different metal positions [Rastsvetaeva, 2020]. Nomenclature within this mineral group depends mainly on the compositions at the *A*, *B* and *T* positions, since the compositions at these sites can be determined accurately. For *C*1-*C*3, however, the distribution of titanium and some other cations is rather problematic. In octahedra with close values of ionic radii, they have similar scattering factors and almost identical M-O distances (from rV^{5+} = 0.54 to rTi^{4+} = 0.605 Å)[Shannon, 1976]. Therefore, the compositions of the *C*1-*C*3 positions are usually given as a total.

Large *A*-cations are placed in a dodecahedron and considered to be the key cations. *B*-, *T*- and *C*- are small cations, which lie in octahedra and tetrahedra. Comparative data for the new minerals and related species of the crichtonite group in terms of site occupancies are given in Table 1. The general structure of crichtonite comprises two distinct layers, denoted as R and O (Figure 6). The O layers are characterized by larger C1 octahedra, which form 12-membered rings. In contrast, the R layers consist of 6-membered rings formed by smaller C2 and C3 octahedra. Additionally, the third layer, R*, is related to the R layer by an inversion center. Each layer is shifted within the *ab* plane, resulting in the formation of three sets of layers. These nine derived layers are stacked in a $(ROR^*)^3$

rhombohedral sequence. In davidite-(La), sites can vary with *A* site = La, Ce and Ca, *B* = U, Y, La, *T* = Fe^{2+}, *C*1 = Fe^{3+}, Ti, Cr, while *C*2 and *C*3 sites are predominantly occupied by Ti. This coordination polyhedral condense into layers stacked in a nine-layer sequence (Figure 6).

Table 1. Dominant compositions of crichtonite-group minerals.

Mineral	Key sites				Reference
Metal site	^{XII}A	^{VI}B	$^{IV}T_2$	$^{VI}C_{18}$ *	
Crichtonite	Sr	Mn^{2+},Y,U	Fe^{2+}	Ti,Fe^{3+},Cr,V	[Grey, Lloyd, White, 1976]
Senaite	Pb	Mn^{2+},Y,U	Fe^{2+}	Ti,Fe^{3+},Cr,V	[Grey, Lloyd, 1976]
Landauite	Na,Pb	Mn^{2+},Y	Zn,Fe	Ti,Fe^{3+},Nb	[Grey, Gatehouse, 1978]
Loveringite	Ca,Ce,La	Zr,Fe	Mg,Fe	Ti,Fe^{3+},Cr,Al	[Gatehouse et al., 1978]
Davidite-(La)	La	Y,U	Fe^{2+}	Ti,Fe^{3+},Cr,V	[Gatehouse, Grey, Kelly, 1979]
Davidite-(Ce)	Ce	Y,U	Fe^{2+}	Ti,Fe^{3+},Cr,V	[Gatehouse, Grey, Kelly, 1979]
Lindsleyite	Ba,Sr	Zr,Ca	Mg,Fe	Ti,Cr^{3+},Fe	[Haggerty et al., 1983]
Mathiasite	K,Ba,Sr	Zr,Fe	Mg,Fe	Ti,Cr^{3+},Fe	[Gatehouse, Grey, Smyth, 1983]
Dessauite	Sr	Y,U,Mn	Fe^{2+}	Ti,Fe^{3+},Cr,V	[Orlandi et al., 1997]
Gramaccioliite-(Y)	Pb,Sr	Y,Mn	Fe^{2+}	Ti,Fe^{3+}	[Orlandi et al., 2004]
Cleusonite,	Pb	U^{4+},U^{6+}	Fe^{2+}	Ti,Fe^{2+},Fe^{3+}	[Wülser et al., 2006]
Paseroite	Pb	Mn^{2+},□	Fe^{2+},□	V^{5+},Ti^{4+},□	[Mills et al., 2012]
Mapiquiroite	Sr,Pb	U^{4+},Y	Fe^{2+}	Ti,Fe^{3+}	[Biagioni et al., 2014]
Almeidaite	Pb	Mn^{2+},Y	Zn	Ti,Fe^{3+}	[Filho et al., 2015; Rastsvetaeva et al., 2014]
Mianningite	□,Pb,Ce	U,Mn	Fe^{3+}	Ti,Fe^{3+}	[Ge et al., 2017]
Saranovskite	Sr,Ba	Ca,Y,Fe	Fe^{2+}	Ti,Cr^{3+},Fe,Sc	[Chukanov et al., 2020]
Haitaite-(La)	La	U^{4+}	Fe^{3+}	Ti,Fe^{2+},Fe^{3+}	[Wang et al., 2022]
Botuobinskite	Sr	Fe,Zr	Mg	Ti,Cr,Fe,Al	[Rezvukhin et al., 2023]
Mirnyite	Sr	Zr,Fe	Mg	Ti,Cr,Fe,Al	[Rezvukhin et al., 2023]

* Note: C positions in all minerals of crichtonite group is occupied by predominantly Ti.

Variable formula expressed by crichtonite group minerals reveal their potential applications in materials science. The crichtonite group minerals, including davidite-(La), possess unique properties that make them attractive candidates for nuclear waste immobilization [Lumpkin, 2006; Yudintsev et al., 2001]. They have been found to exhibit extraordinarily high chemical capacity and resistance to radiation, which validate the powerful waste loading of crichtonite structure [Gong et al., 1994]. As a host phase for radioactive wastes, crichtonite may form in multi-phase ceramics [Yudintsev et al., 2022]. The thermal behavior of different phases in these ceramics can cause strains and cracks, which reduces the material's effectiveness. Hence, it is essential to investigate the thermal properties of different phases, including crichtonite, to avoid a severe mismatch between phases.

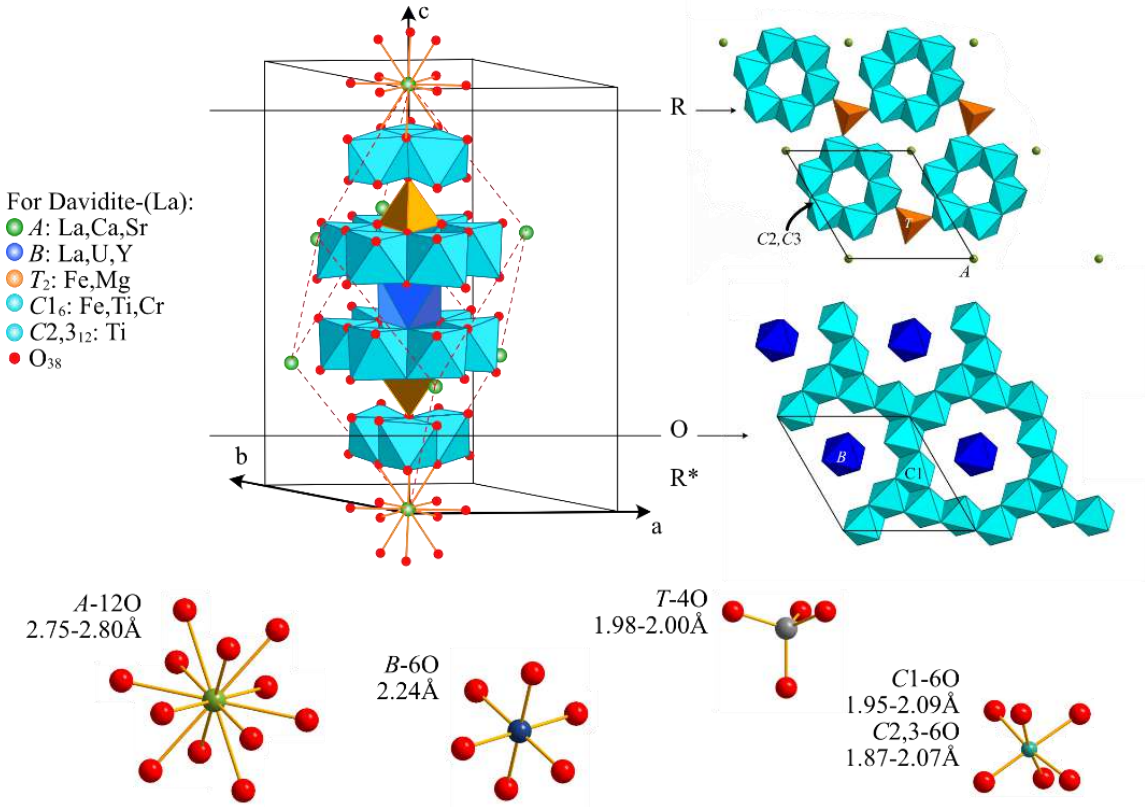

Figure 6. The crystal structure of davidite-(La) – a specie of crichtonite group (drawn after [Gatehouse, Grey, Kelly, 1979]). Its rhombohedral and hexagonal unit cell are illustrated by red dashed and black solid lines, respectively. The general structure is characterized by a nine-layer stacking sequence $(ROR^*)^3$.

1.2 Thermal expansion of inorganic compounds and minerals

Thermal expansion is one important parameter for the physical characterization of the temperature dependent behavior of materials and is of relevance for both Earth and materials science. Thermal expansion is caused by the anharmonicity of the thermal oscillation of atoms and is determined by the atomic molecular composition of the substance [Bubnova, Firsova, Filatov, 2013]. The weaker the chemical bonds between the atoms the larger the expansion. The quantitative characteristic of the expansion is represented by coefficient α, which is the relative increment of the value of a measured parameter i under the temperature T increasing by 1 K: $\alpha_i\ (K^{-1}) = \frac{1}{i} \cdot \frac{di}{dT}$, where the parameter i is any linear or angular parameter of crystal lattice, atomic spacing, the length or angle of the chemical bond in the structure, or the length of the product [Filatov, 1990]. Thermal expansion of a crystal lattice is a homogeneous deformation and, therefore, is described by a symmetric tensor of the second rank.

For anisotropic compounds such as crystalline phases which are uniformly heated or cooled the resulting homogeneous strain x_{ij} can be described by the following relationship: $x_{ij} = \alpha_{ij}\Delta T$, where α_{ij} are the thermal expansion coefficients defining a symmetrically second rank tensor and ΔT is the temperature change [Langreiter, Kahlenberg, 2015]. Most oxides, for example, have ambient temperature thermal expansion coefficients in the order of 10^{-6}/K.

One of the oldest and most frequently used methods for thermal expansion measurement is mechanical dilatometry [James et al., 2001]. The displacement that results from a specimen with

increasing temperature is mechanically transmitted to a sensor located away from the heat, yielding a plot of displacement against temperature from which the coefficients of thermal expansion (CTE) can be calculated. As discussed by Paufler and Weber [1999], however, this methodology has the disadvantage that the consideration of finite temperature differences will always produce “average values”.

In addition, there is a growing interest in using the method of diffraction to evaluate the thermal expansion data. This technique has been frequently employed for temperature dependent investigations on single-crystals or polycrystalline compounds using X-rays or neutrons [Asuvathraman, Kutty, 2014; Ball, Thorogood, Vance, 1992; Kutty et al., 1994a; Momin, Mirza, Mathews, 1991; Paufler, Weber, 1999; Sarin et al., 2014].

The program “RietToTensor” [Bubnova et al., 2018; Firsova et al., 2015] includes the following steps to process the thermal expansion data: 1. Rietveld analysis of the diffraction data; 2. Calculation of unit cell parameters; 3. Approximation of the temperature dependence of the elementary cell parameters; 4. Determination of the coefficients α along the principal axes of the tensor and the orientation of these axes with respect to the crystallographic axes.

The temperature dependences of the relative parameters are firstly approximated by the polynomials of degree from 1 to 3: $a(T)=p_0 + p_1 \cdot T + p_2 \cdot T^2 + p_3 \cdot T^3$. The quality of the fitting can be determined by the least squares method with weight coefficients.

The components of the tensor are determined for all crystal systems in the crystallographic coordinate system as the solution of the system of six equations of the following form: $\alpha_d = \alpha_{11}x_d^2 + \alpha_{22}y_d^2 + \alpha_{33}z_d^2 + 2\alpha_{12}x_dy_d + 2\alpha_{23}y_dz_d + 2\alpha_{13}x_dz_d$, where α_{ij} are the tensor components and x_d, y_d, and z_d are the directional cosines of the normal with respect to the crystal physical axes xyz. The thermal expansion along the interplanar distance d:

$$\alpha_d = \frac{-d_{hkl}^2}{2} \cdot \left(\frac{\partial f}{\partial a} \cdot \frac{da}{dT} + \frac{\partial f}{\partial b} \cdot \frac{db}{dT} + \frac{\partial f}{\partial c} \cdot \frac{dc}{dT} + \frac{\partial f}{\partial \alpha} \cdot \frac{d\alpha}{dT} + \frac{\partial f}{\partial \beta} \cdot \frac{d\beta}{dT} + \frac{\partial f}{\partial \gamma} \cdot \frac{d\gamma}{dT}\right) \quad , \quad \text{where} \quad d_{hkl} = f(h,k,l,a,b,c,\alpha,\beta,\gamma),$$

is a function of indices hkl and the cell parameters. The system of equations is written for planes (100), (010), (001), (110), (101), and (011).

Multiphase ceramics were designed for the immobilization and disposal of high-level radioactive wastes (HLW) [Ringwood, 1985]. To understand the thermophysical properties of ceramics, it is necessary to study their constituent components [Yudintsev et al., 2022]. The material's expansion at elevated temperatures and radiation is the crucial feature for HLW ceramics.

Previously, numerous studies were conducted to examine the thermal characteristics of the phases proposed for such applications. The $Ln_2Zr_2O_7$ and $Ln_2Hf_2O_7$ pyrochlores have volumetric expansion coefficients of 23.4-31.8 $\times$ 10^{-6} °C^{-1} in the range 25-1400 °C [Kutty et al., 1994]. The $CePO_4$ monazite expands very weak, and its α_v varies from 21.0-27.4 $\times$ 10^{-6} °C^{-1} in the range 25-700 °C [Asuvathraman, Kutty, 2014]. Perovskite $CaTiO_3$ expands in a broader range: 37.87 - 55.37

$\times$ 10^{-6} °C^{-1} in the range 25-1000 °C [Ball, Thorogood, Vance, 1992]. The volumetric coefficients of the thermal expansion of zirconolite-3*T* $CaZrTi_2O_7$ are 29.49 - 31.99 $\times$ 10^{-6} °C^{-1} in the same temperature range [Ball, Thorogood, Vance, 1992].

Considering that the waste immobilization form is usually a ceramic with various complex oxides, we can neglect the expansion anisotropy of single crystals when discussing the thermal expansion of the material. It is therefore reasonable to compare the volumetric CTE in brannerite with the available data for the other oxide materials.

1.3 Magnetic properties

For a complete representation of the magnetic phenomena in various structures, it is necessary to understand the general aspects of magnetic properties. The important properties to characterize substance are magnetic susceptibility χ, with units $emu.mol^{-1}$ in cgs (centimeter-gram-second) or $m^3.K.mol^{-1}$ in SI (international system). Magnetic susceptibility χ is the quantity that relates a material's magnetization, *M* (emu), in response to an applied magnetic field, *H* (Tesla):

$$\chi = \frac{M}{H}$$

Magnetic susceptibility measurement is a classic and effective method used to unveil the magnetic identity of material. Susceptibility measurements can be performed in a direct current (DC) field, giving insights on the static magnetic properties, or an alternating current (AC) field in order to probe the dynamic properties. The contributions to the magnetic susceptibility of a substance generally divides them into diamagnetic and paramagnetic. Diamagnetic substances (containing no unpaired electrons) are repelled by an applied magnetic field, whereas paramagnetic materials are attracted to the externally applied magnetic field (via unpaired electrons).

Beginning with the fundamental property of any material – **diamagnetism**, always present, even when it is masked by a stronger paramagnetic contribution. When this is the only response, these substances are composed of atoms which have no net magnetic moments because all the orbitals are filled with electrons, which, because of the Pauli exclusion principle, must have different spin directions. When a magnetic field is applied, a negative magnetisation is produced, and the susceptibility is negative. This phenomenon arises from the interaction between the magnetic field and the movement of electrons within their orbitals, hence it is also referred to as "orbital diamagnetism".

In many cases, the diamagnetic susceptibility, χ_D, is so small that it can simply be ignored. In addition, it is usually independent of the temperature and the strength of the applied field. However, in certain situations, it may be desirable to correct the measured data by subtracting off the diamagnetic term. This is a relatively straightforward task because the diamagnetic contribution is temperature independent and can be accurately approximated using tabulated values for the constituent ions [Bain, Berry, 2008].

In contrast to diamagnetism, **paramagnetism** is exclusive to materials possessing unpaired electrons. When a paramagnet is in the absence of an external magnetic field, it behaves as a magnetically disordered gas-like state where the magnetic moments are oriented with equal probability in all directions. Under the influence of temperature, the equilibrium of the system can shift, and because of the thermal motion of particles, the directions of magnetic moments can also change continuously, but in this case the resulting average magnetic moment of the paramagnetic substance will always be equal to zero in the absence of an external magnetic field. Pierre Curie in 1895 found that the magnetic susceptibility is inversely proportional to the temperature. The temperature dependence of the susceptibility was further developed by incorporating the Weiss field, resulting in the well-known Curie-Weiss law:

$$\chi = \frac{C}{T - \theta_{\mathrm{CW}}}$$

where C is Curie constant (with emu K.mol^{-1} units in cgs or m^3.K.mol^{-1} in SI), and θ_{CW} (in Kelvin) is often referred to as the Curie–Weiss temperature. The Curie constant C is directly related to the number of unpaired electrons and once determined, can be used to calculate the effective magnetic moment per ion, μ_{eff}, in units of Bohr magnetons, μ_{B},

[in cgs], $\mu_{\mathrm{eff}} = \sqrt{8C}$, μ_{B}

The magnitude of the Curie–Weiss temperature θ_{CW} is related to the strength of the molecular field, which can be taken as an approximate indicator of the strength of the magnetic correlations between ions. Positive values of θ_{CW} occur when the molecular field aligns with the external field, indicating **ferromagnetic** interactions, whereas negative values of θ_{CW} imply **antiferromagnetic** interactions. In ferromagnetic materials, within regions known as "Weiss-domains", all spins are aligned parallel. On applying an external magnetic field, this alignment persists as long as it remains below the critical temperature T_{C}, which is the Curie temperature. Conversely, in antiferromagnetic substances, the spins are aligned antiparallel. The temperature below which cooperative coupling operates is known as the Néel temperature, T_{N}.

As the temperature approaches to $|\theta_{\mathrm{CW}}|$, deviations from the Curie–Weiss law are expected, which could include a transition to a magnetically ordered or frozen state. For ferromagnets, one often finds that $T_{\mathrm{C}} \approx \theta_{\mathrm{CW}}$ whereas larger deviations are typically observed for antiferromagnets, $T_{\mathrm{N}} < |\theta_{\mathrm{CW}}|$, due to an oversimplification of how the molecular field is defined. In some cases, the value is even further suppressed because of frustration.

Describing the relative arrangement of magnetic moments, **ferrimagnetism** represents the third type of collective magnetic behavior. Ferrimagnetic (FiM) materials are characterized by a domain structure, which can consist of two or more sublattices arranged antiparallel relative to each other. Ferrimagnets have a susceptibility that qualitatively resembles a ferromagnet, particularly in the vicinity of T_{C}. Ferrimagnetic transitions can be distinguished from ferromagnetic transitions by the saturation value of their susceptibility, which will be smaller than the full magnetic moment. Figure

7 shows examples of the described magnetic orderings.

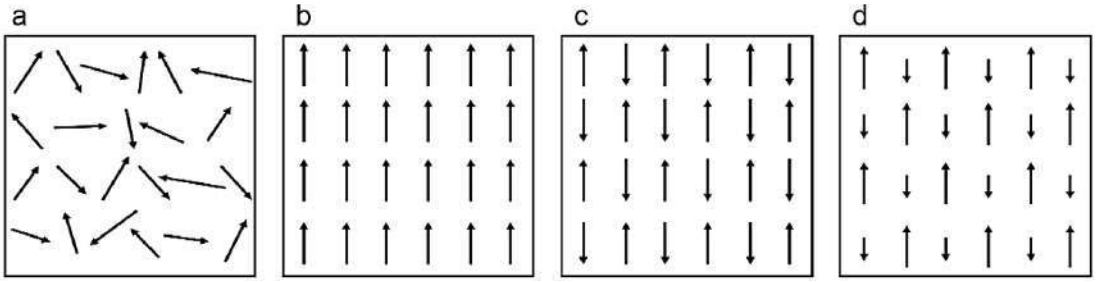

Figure 7. Schematic examples of paramagnet (a), ferromagneti (b), antiferromagneti (c) and ferrimagnets (d).

Unlike the preceding three types of magnetic ordering, some categories of substances freeze into a magnetic disordered state, like an aperiodic glass, thus termed "**spin-glass**." The freezing temperature of spin-glass, T_f, is usually marked by a cusp in susceptibility closely resembling the cusps seen in antiferromagnets, measured under zero-field-cooled (ZFC) conditions. However, when measured under field-cooled (FC) conditions the susceptibility of a spin glass will be temperature independent below T_f, producing a large FC-ZFC splitting. The key sign of the transition to the spin-glass state comes from measurements of frequency-dependent AC susceptibility, where the transition should shift to higher temperatures with increasing field oscillation frequency [Mugiraneza, Hallas, 2022].

Chapter 2. Research methodology and experimental conditions

2.1 Scanning electron microscopy (SEM), energy dispersive X-ray spectroscopy (EDXS) and wavelength-dispersive spectroscopy (WDS)

Sample grains (size 0.5–2 mm) of mineral samples were hand-picked and mounted in an epoxy resin. The sample grains were investigated by the scanning electron microscope Hitachi S-3400N, equipped with a spectrometer Oxford Instruments X-Max 20. Photos of the samples were taken in the backscattered electron mode (BSE), the contrast of the BSE image depicts the atomic number of the element. Quantitative analyses were performed with an accelerating voltage of 20 kV to ensure X-rays from all important elements can be detected, with a resolution of up to 4 nm. A beam current of 1.8 nA was used, with acquisition times ranging from 30 s for brief characterization and 60 s for detailed analysis. The standards from MAC (Micro Analysis Consultants Ltd., United Kingdom) and Geller reference standards (Geller microanalytical laboratory) were used for quantification.

Metamict zirconolite grains (see 3.5.1) were studied by scanning electron microscopy, using a JEOL 5900LV SEM at the Natural History Museum (London). Zirconolite has been analyzed using the wavelength-dispersive Camera SX-100 electron microprobe (NHM, London). 138 spot analyses were acquired under following analytical conditions: 20 kV accelerating voltage, 20 nA beam current and 1 μm beam diameter. As probe standards well-characterized natural minerals and synthetic compounds were used.

2.2 Electron backscatter diffraction analysis (EBSD)

Electron Backscatter Diffraction (EBSD) analyses of the thorite grains (see 3.2) were performed by the means of a Scanning Electron Microscope (SEM) Hitachi S-3400N equipped with Nordlys Nano EBSD detector. The composition and structural data, including EDX and EBSD single-point measurements and mapping, are collected and processed with Oxford AzTec and Channel5 software packages. The thorite reference data from Fuchs, Gebert, [1958] and monazite structure data [Ni, Hughes, Mariano, 1995] for huttonite were used for diffraction pattern indexing and phase identification.

2.3 Raman spectroscopy

Raman spectroscopy was implemented to investigate the features of the metamict and annealed mineral samples, employing a Horiba Jobin–Yvon LabRam HR800 Raman spectrometer in combination with an Olympus BX41 microscope. Raman spectra were excited by an Ar+ laser (514 nm), solid-state laser (532 nm), and He-Cd laser (325 nm) in the range between 100 and 4000 cm^{-1}. The laser beam spot size was 5 μm. The spectra were processed using software Labspec and Origin. The spectral resolution was 2 cm^{-1}.

2.4 Thermal analyses

The thermal analysis is conducted using a NETZSCH STA 429 thermal analyzer in the laboratory of the Institute of Silicate Chemistry of the RAS, located in Saint Petersburg. Powder samples ranging from 10 to 40 mg were compressed into pellets (with pressing pressure of about 8 kg/mm^2) and positioned within aluminum crucibles for experimentation. The maximum experiment temperature can reach up to 1500°C, with a controlled heating rate not exceeding 20°C per minute. The experimental atmosphere can be either air or argon, depending on the requirements.

2.5 X-ray diffraction

In Saint-Petersburg. Powder X-ray diffraction was carried out to analyze the crystal structure of natural samples. The diffractometer Miniflex II from Rigaku, in Resource center "XRD", Saint-Petersburg State University, was used for PXRD on mineral samples at room temperature. The Miniflex II diffractometers at the Resource Center are equipped with a copper and cobalt anode. The cobalt anode was used to reduce the fluorescence of copper X-rays from Co, Fe, and Mn samples. Because the mineral samples do not contain large amounts of Fe and Mn, and because of equipment availability, a copper anode was also used in the experiments.

Additionally, High-temperature X-ray diffraction was performed using diffractometer Ultima IV from Rigaku, in Resource Center "XRD" as well. Copper and cobalt anodes were employed in diffraction experiments based on availability, resulted in wavelengths of Kα-Cu (λ=1.54 Å) and Kα-Co (λ=1.79 Å).

In Lille. Powder X-Ray diffraction was conducted at room temperature to examine the crystal structure of synthetic compounds. The analysis was performed using the diffractometer D8 Advance from Bruker, situated at the Institute Chevreul, Lille, with an X-ray wavelength of Kα-Cu (λ=1.54 Å).

2.6 Solid-state synthesis in vacuum

Solid-phase synthesis was employed to produce samples of novel crichtonite-like compounds. The principle of the solid-state reaction is that the chemical phase that minimizes the free energy is most favorable to nucleate and grow. In general, solid-state method requires high temperatures and controlled atmosphere for preparation. In these experiments, a vacuum at a level of 1×10^{-2} KPa was used to avoid oxidation of Mn and V.

First, the precursors are mixed in stoichiometric ratios and ground thoroughly in an agate mortar. Ethanol is added for better mixing and grinding. The mixture is then dried at 100°C to remove ethanol. After drying, the precursors are pressed into 80 mg pellets and enclosed within a vacuum-sealed quartz tube with a diameter of 6-8 mm. This tube is then heated in a furnace at the required temperatures. The stoichiometry used is presented in Table 2. Out of 27 systems attempted, 12 systems exhibited the desired crichtonite phase with a purity exceeding 90 wt.%, which are detailed in Table 3.

Table 2. Stoichiometry of successfully synthesized compounds.

Compounds	Sample name	Ratio of reactants									
$LaMn_3Ti_{18}O_{38}$	LaMTO	0.5	La_2O_3	16.25	TiO_2	1.75	Ti	3	MnO		
$LaMn_3Ti_{13}Fe_5O_{38}$	LaMTFO	0.5	La_2O_3	13	TiO_2	2	Fe	1.5	Fe_2O_3	3	MnO_2
$CeMn_3Ti_{18}O_{38}$	CeMTO	1	CeO_2	16.5	TiO_2	1.5	Ti	3	MnO		
$NdMn_3Ti_{18}O_{38}$	NdMTO	0.5	Nd_2O_3	16.75	TiO_2	1.25	Ti	3	MnO		
$CaMn_3Ti_{18}O_{38}$	CaMTO	1	$CaCO_3$	17	TiO_2	1	Ti	3	MnO		
$Ca_2Fe_2Ti_{18}O_{38}$	CaFTO	1	$SrCO_3$	17	TiO_2	1	Ti	1	Fe_2O_3	1	Fe
$SrMn_3Ti_{18}O_{38}$	SrMTO	1	$SrCO_3$	17	TiO_2	1	Ti	3	MnO		
$SrMn_3Ti_{14}Fe_4O_{38}$	SrMTFO	1	$SrCO_3$	14	TiO_2	2	Fe	1	Fe_2O_3	3	MnO_2
$SrFe_3Ti_{18}O_{38}$	SrFTO	1	$SrCO_3$	17	TiO_2	1	Ti	1	Fe_2O_3	1	Fe
$BaMn_3Ti_{18}O_{38}$	BaMTO	1	$BaCO_3$	17	TiO_2	1	Ti	3	MnO		

Table 3. Synthesized crichtonite compounds and its purities.

Sample No.	$^{XII}A_1$	$^{VI}B_1$	$^{IV}B2_2$	$^{VI}C1_6{}^{VI}C2_6{}^{VI}C3_6$	O_{38}	Wt.% of crichtonite phase
33	Na^+	Mn^{2+}	$Mn^{2+}{}_2$	$Ti^{4+}{}_{10}$ $Ti^{3+}{}_8$	O_{38}	85%
1	Ba^{2+}	Mn^{2+}	$Mn^{2+}{}_2$	$Ti^{4+}{}_{14}$ $Ti^{3+}{}_4$	O_{38}	95%
2	Ba^{2+}	Mn^{2+}	$Mn^{2+}{}_3$	$Ti^{4+}{}_{14}$ $Fe^{3+}{}_4$	O_{38}	94%
3	Ca^{2+}	Mn^{2+}	$Mn^{2+}{}_2$	$Ti^{4+}{}_{14}$ $Ti^{3+}{}_4$	O_{38}	91%
4	Ca^{2+}	Mn^{2+}	$Mn^{2+}{}_3$	$Ti^{4+}{}_{14}$ $Fe^{3+}{}_4$	O_{38}	67%
5	Sr^{2+}	Mn^{2+}	$Mn^{2+}{}_2$	$Ti^{4+}{}_{14}$ $Ti^{3+}{}_4$	O_{38}	94%
6	Sr^{2+}	Mn^{2+}	$Mn^{2+}{}_2$	$Ti^{4+}{}_{14}$ $Fe^{3+}{}_4$	O_{38}	100%
17	Sr^{2+}	Mn^{2+}	$Mn^{2+}{}_2$	$Ti^{4+}{}_{14}$ $Cr^{3+}{}_4$	O_{38}	93%
27 (MAW157)	Sr^{2+}	Mn^{2+}	$Mn^{2+}{}_2$	$V^{4+}{}_{14}$ $V^{3+}{}_4$	$O_{37.5}$	92%
28-jl	Sr^{2+}	Fe^{2+}	$Fe^{2+}{}_2$	$Ti^{4+}{}_{14}$ $Ti^{3+}{}_4$	$O_{37.5}$	95%
30	Sr^{2+}	Mn^{2+}	$Mn^{2+}{}_2$	$Ti^{4+}{}_{14}$ $Sc^{3+}{}_4$	O_{38}	64%
8	Bi^{3+}	Mg^{2+}	$Mg^{2+}{}_2$	$V^{4+}{}_{13}$ $V^{3+}{}_5$	$O_{37.5}$	96%
9	Bi^{3+}	Mg^{2+}	$Mg^{2+}{}_2$	$V^{4+}{}_{13}$ $V^{3+}{}_5$	O_{38}	60%
14	Y^{3+}	Mg^{2+}	$Mg^{2+}{}_2$	$V^{4+}{}_{13}$ $V^{3+}{}_5$	O_{37}	50%
12	Y^{3+}	Ce^{3+}	$Mg^{2+}{}_2$	$V^{4+}{}_{12}$ $V^{3+}{}_6$	O_{38}	30%
13	Y^{3+}	Y^{3+}	$Mg^{2+}{}_2$	$V^{4+}{}_{12}$ $V^{3+}{}_6$	O_{38}	No
15	Ce^{3+}	Mg^{2+}	$Mg^{2+}{}_2$	$V^{4+}{}_{13}$ $V^{3+}{}_5$	O_{38}	50%
37	Y^{3+}	Mn^{2+}	$Mn^{2+}{}_2$	$Ti^{4+}{}_{13}$ $Ti^{3+}{}_5$	O_{38}	10%
16	La^{3+}	Mn^{2+}	$Mn^{2+}{}_2$	$Ti^{4+}{}_{13}$ $Fe^{3+}{}_5$	O_{38}	92%
18	La^{3+}	Mn^{2+}	$Mn^{2+}{}_2$	$Ti^{4+}{}_{13}$ $Ti^{3+}{}_5$	O_{38}	96%
31	La^{3+}	Fe^{3+}	$Fe^{3+}{}_2$	$Ti^{4+}{}_{10}$ $Ti^{3+}{}_8$	O_{38}	80%
32	La^{3+}	Fe^{3+}	$Fe^{3+}{}_2$	$Ti^{4+}{}_{10}$ $Fe^{3+}{}_8$	O_{38}	30%
34	Ce^{3+}	Mn^{2+}	$Mn^{2+}{}_2$	$Ti^{4+}{}_{13}$ $Ti^{3+}{}_5$	O_{38}	97%
23	Nd^{3+}	Mn^{2+}	$Mn^{2+}{}_2$	$Ti^{4+}{}_{13}$ $Ti^{3+}{}_5$	$O_{37.5}$	91%
24	Nd^{3+}	Mn^{2+}	$Mn^{2+}{}_2$	$Ti^{4+}{}_{13}$ $Fe^{3+}{}_5$	$O_{37.5}$	74%
38	Sm^{3+}	Mn^{2+}	$Mn^{2+}{}_2$	$Ti^{4+}{}_{13}$ $Ti^{3+}{}_5$	O_{38}	85%
36	Gd^{3+}	Mn^{2+}	$Mn^{2+}{}_2$	$Ti^{4+}{}_{13}$ $Ti^{3+}{}_5$	O_{38}	62%

For crichtonites containing divalent cation in the A-site such as system of Sr-Mn-Ti(Fe)-O, an extra step was employed to decarbonate the reactant $SrCO_3$. In the first step, precursors $SrTi^{4+}{}_{16.5}O_{34}$ and $SrTi^{4+}{}_{14}O_{29}$ were obtained by heating stoichiometric amounts of $SrCO_3$ and TiO_2 in air at 900 °C for 12 h. Afterwards, they were mixed with MnO, Ti metal and TiO_2 for $SrMn^{3+}{}_3Ti^{4+}{}_{14}Ti^{3+}{}_4O_{38}$ and

with MnO_2, Fe and Fe_2O_3 for $SrMn^{3+}{}_3Ti^{4+}{}_{14}Fe^{3+}{}_4O_{38}$. The temperature in furnace was increased to 950 °Cover 3 h and held for 12 h before further increasing to 1100 °C over 1.5 hours with a dwell time of 48 h. Finally, the samples were cooled to room temperature by turning off the furnace.

2.7 Magnetic properties measurements

Investigation of magnetic properties is essential to understand these materials. The macroscopic magnetization in general depends on the magnetic field *H* and the temperature *T*. The term magnetization is preferred for measurements performed at fixed temperature with varying applied field while susceptibility is more often used to refer to measurements performed with varying temperature and fixed applied field, but colloquially, these terms are often used interchangeably.

Measurements of magnetic susceptibility can be collected with a DC (direct current) or AC (alternating current) applied field. In a DC measurement, the field is held constant and the measurement is obtained under equilibrium conditions. Conversely, in an AC susceptibility measurement, the field oscillates inducing a time-dependent magnetization that provides insights on the material's dynamics. In an AC measurement, the response can also depend upon the frequency at which the field is alternated.

In this work, the magnetic susceptibility and magnetization measurements were carried out using Dynacool-PPMS (Physical Property Measurement System) from Quantum Design (Chevreul Institute, University of Lille). This apparatus measures changes in the magnetic flux as the sample moves through the detection coil. The set up can reach up to 9 Tesla in magnetic field and perform temperature scans from 1.8 K to 400 K.

Susceptibility measurements were performed in Zero-Field cooling (ZFC) mode where the sample is cooled through the magnetic ordering temperature without the application of external field and then the required magnetic field is switched on at the lowest temperature and the magnetization is measured during warming. The subsequent measurement is performed while cooling under magnetic field and it is called Field–Cooled (FC) mode. The initial state of a material in susceptibility measurement depends on whether the sample was measured under FC or ZFC conditions. Divergence between measurements performed in FC and ZFC conditions, often termed splitting, indicates hysteresis (dependence on the magnetic field history), which can be indicative of various ordered and frozen magnetic states.

After gathering susceptibility measurement data, one can analyze the temperature dependence of susceptibility and its inverse. By fitting the temperature dependence, it is possible to derive both the Curie constant and the Curie-Weiss temperature.

$$\frac{1}{\chi} = \frac{T - \theta_{\mathrm{CW}}}{C}$$

Once the Curie constant is determined, it can be used to calculate the effective magnetic moment per ion in units of Bohr magnetons, $\mu_{\mathrm{eff,exp}} = \sqrt{8C}\ \mu_{\mathrm{B}}$. This effective moment can be

directly compared to the calculated theoretical value. The effective magnetic moment for an ion is given by $\mu_{\text{eff,theo}} = g_J \cdot \sqrt{J(J+1)}\ \mu_B$, which depends only on its total angular momentum J and its g-tensor g_J. In compounds containing multiple magnetic ions per formula unit, the total effective moment is determined by summing the squares of the individual effective moments.

2.8 Neutron powder diffraction

The detection of a magnetic ordering or spin freezing transition via magnetic susceptibility is generally straightforward, as they are typically marked by a sharp discontinuity. The qualitative appearance of the discontinuity, its field dependence, and its response to field-cooled (FC) and zero field-cooled (ZFC) conditions provides key insights that can be used to deduce the nature of the ordered or frozen state. However, in all but the simplest cases, determining the exact spin configuration requires additional experimentation— e.g. neutron diffraction.

Similar to X-rays, a neutron beam can detect the structural information of materials since its wavelength is comparable with the interatomic space in solids and liquids. However, neutrons also have some unique advantages: Neutrons interact with the atomic nucleus via the strong nuclear force, while X-rays interact with the electrons via an electromagnetic interaction. Therefore, the response of neutrons from light atoms is much higher than that of X-rays. The neutron has a large penetration depth that can benefit the investigation of materials under extreme conditions such as low/high temperatures, high pressures, high magnetic and electric fields since these experiments all require shields which prevent the application of X-rays. The neutron also carries a magnetic moment which can interact with the spins of electrons. This makes neutrons an excellent probe to determine the magnetic properties of matter, such as magnetic ordering, magnetic excitations, and spin fluctuations.

The crystal structure of NdMTO, CaMTO, CaFTO, BaMTO, SrMTO, SrFTO and SrMTFO were characterized by neutron powder diffraction. High-resolution NPD was carried out at the Institut Laue Langevin (ILL) in the D20 beamline with λ =1.36-1.54 Å (118° take-off angle) for an accurate crystal structure determination since the different scattering factor between Ti (-3.43 fm), Mn (-3.73 fm) and Fe (-9.45 fm) allows the identification of a possible cation ordering (see table 2.3 in Hutchings et al., 2005). NPD analyses were made through the Fullprof suite [Rodríguez-Carvajal, 1993].

Chapter 3. Evolution of metamict minerals with increasing temperature

This chapter provides comprehensive studies on six natural minerals, progressing from the simplest to the most complex structures. Beginning with brannerite (UTi_2O_6) and thorite ($ThSiO_4$), two actinide minerals known for their radioactive resistance, the discussion then moves to fergusonite-(Y) ($YNbO_4$) and samarskite-(Y) ($YFeNb_2O_8$), niobate minerals that incorporate rare earth elements. The chapter continues with zirconolite ($CaZrTi_2O_7$) and davidite-(La) ($ABT_2C_{18}O_{38}$), titanite mineral notable for its capacity to accommodate substantial amounts of rare earth elements. The final section focuses on davidite-(La), which features the most complex structure among the minerals examined.

3.1 Brannerite[9]

3.1.1 Chemical composition and phase purity

Initial grains of **M**etamict **B**rannerite (labled as **MB1** and **MB2**) and **H**eated calcined grain of Brannerite (**HB3**) were investigated by EPMA, the BSE image is shown in Figure 8.

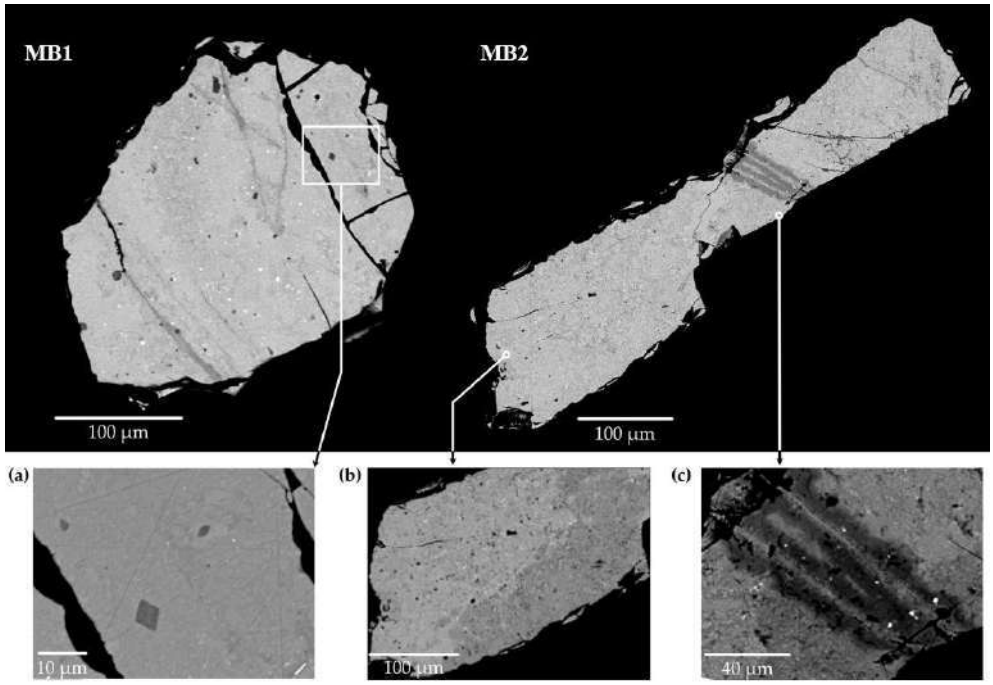

Figure 8. Two unheated grains of brannerite contain some impurities, enlarged areas of grains are shown in (a-c). The rhombic crystal of pyrochlore can be seen in (c). The altered region is well-represented in grain "**MB2**".

The unheated samples exhibit the following compositional ranges: 51.9-58.3 wt.% UO_2, 32.8-36.6 wt.% TiO_2, 3.9-6.6 wt.% ThO_2. Additional constituents include on average of 0.8 wt.% Fe_2O_3, 0.8 wt.% CaO, 0.9 wt.% PbO, 0.8 wt.% SiO_2, 0.5 wt.% Na_2O. The chemical analyses (average of 5 analyses for **MB1**, 15 analyses for **MB2** and 7 analyses for **MB3**), the ranges and atom per formula unit (*apfu*) are given in Table 4. The calculation of the formula coefficients (*apfu*) was performed using two approaches: first by assuming that the total cations in the *B*-site sum to 2, and second by assuming that the *apfu* for the oxygen ion is 6. By assuming the *apfu* of a certain ion, one can obtain

[9] Brannerite: ideal formula UTi_2O_6. Space group: *C*2/*m*, see 1.1.1.

the *apfu* of other ions according to the proportion.

Table 4. Chemical composition of unheated and heated brannerite (**MB1**, **MB2** and **HB3**). Mineral formula coefficients for each grain were calculated by two methods: "*B*"=2 or "O"=6.

	MB1-*unheated*			**MB2-*unheated***			**HB3-*heated***		
Oxides (Wt.%)	Average	Range	Deviation	Average	Range	Deviation	Average	Range	Deviation
TiO_2	35.66	35.36-36.02	0.2	35.35	32.78-36.17	0.76	37.28	36.2-37.89	0.68
Fe_2O_3	0.68	0.25-0.75	0.21	0.86	0.25-1.37	0.53	0.26	0.11-0.36	0.09
Nb_2O_5							0.47	0.37-0.54	0.09
SiO_2	0.3	0.3-0.3	/	1.45	0.77-1.73	0.39	0.14	0-0.22	0.07
UO_2	56.22	55.35-57.55	0.97	56.11	51.88-58.29	2.05	57.07	51.44-59.38	2.92
ThO_2	5.35	3.86-6.17	0.74	4.89	3.86-6.53	0.62	6.2	4.04-12.51	3.21
CaO	0.67	0.37-1.02	0.2	0.87	0.37-1.57	0.37	1.02	0.78-1.21	0.19
Na_2O				0.52	0.46-0.56	0.05			
PbO	1.06	0.64-1.43	0.22	0.72	0.33-1.17	0.26	0.45	0.36-0.68	0.12
Total	99.56	99-100.26		98.89	97.08-100.11		102.65	101.28-104.47	

Formula coefficient	"*B*"=2	"O"=6	"*B*"=2	"O"=6	"*B*"=2	"O"=6
Ti	1.94	1.92	1.86	1.86	1.97	1.95
Fe^{3+}*	0.04	0.02	0.04	0.02	0.01	0.01
Nb					0.01	0
Si	0.02	0.02	0.1	0.1	0.01	0.01
Σ	2	1.96	2	1.98	2	1.97
U	0.91	0.9	0.87	0.87	0.89	0.88
Th	0.09	0.09	0.08	0.08	0.09	0.09
Ca	0.05	0.05	0.06	0.06	0.07	0.07
Na			0.07	0.03		
Pb	0.02	0.02	0.01	0.01	0.01	0.01
Σ	1.06	1.05	1.09	1.06	1.07	1.06
O	6.06	6	5.99	6	5.2	6
□+	/	0.12	/	0.28	/	0.05

* All iron is calculated as trivalent

According to the analysis, the Akchatau brannerite is close to the stoichiometric brannerite, and contains a significant amount of thorium to form a solid solution with thorutite, ThTi2O6. Surprisingly, rare earth elements are not detected in studied samples. Total measured contents are close to 100%, water was not detected. The presence of small amounts of lead may originate as a decay product of the uranium series.

MB1 is a heterogenous brannerite, Figure 8 shows the contrast in BSE intensity indicating that the elements are unevenly distributed. Some areas show evidence of the alteration. The elongated section, spreading along the fracture, appears as “darker” BSE intensity in comparison with the overall grain. The analytic total of this area is reduced to ~95%. The low amount shows that some lightweight, undetectable components concentrate here, in the meanwhile, the weight percentage of SiO_2 increases up to 0.5 %. Other areas in **MB1** do not contain SiO_2. Several rhombic crystals (5-8 μm) were identified as uranium-rich pyrochlore with ~10 % H_2O.

In addition to inclusions, little “bright white” spots of 0.4-3 μm in size can be seen in both

grains (Figure 8). Their composition cannot be determined unambiguously due to the capture of other elements from the surrounding brannerite matrix. Table 5 shows their average chemical composition with totals normalized to a hundred percent. High contents of PbO and S suggest it to be galena, PbS.

Table 5. The chemical composition of inclusions, which are presumably galena in **MB1** and **MB2**.

Average contents of inclusions	S	CaO	TiO_2	PbO	ThO_2	UO_2	Nomalized total
MB1	17.05	0.25	9.66	50.29	2.69	20.06	100
MB2	20.88	0.21	5.88	60.35	0.91	12.15	100

The grain **MB2** is even less homogeneous compared to **MB1**, Table 4 demonstrates its chemical composition based on 15 spot analyses. The grain **MB2** is characterized by the linearly altered zones, where the content of SiO_2 reaches 1.5-1.7 wt.% (Figure 8, **MB2**).

The resulting formula for **MB1** was initially calculated by assuming that the *apfu* for the oxygen ion is 6: $(U_{0.90}, Th_{0.09}, Ca_{0.05}, Pb_{0.02})_{\Sigma=1.05}(Ti_{1.92}, Fe_{0.02}, Si_{0.02})_{\Sigma=1.96}O_6\square^{+}_{0.12}$. Considering the presence of the alteration zones with hydroxyl, the calculation accuracy based on 6 O *apfu* is rather poor. Herein another formula, calculated based on *B*=2 *apfu*: $(U_{0.91}, Th_{0.09}, Ca_{0.05}, Pb_{0.02})_{\Sigma=1.06}(Ti_{1.94}, Fe_{0.04}, Si_{0.02})_{\Sigma=2}O_{6.06}$.

Formulas for **MB2** are: $(U_{0.87}, Th_{0.08}, Na_{0.07}, Ca_{0.06}, Pb_{0.01})_{\Sigma=1.09}(Ti_{1.86}, Fe_{0.04}, Si_{0.10})_{\Sigma=2}O_{5.99}$ and $(U_{0.87}, Th_{0.09}, Na_{0.03}, Ca_{0.06}, Pb_{0.01})_{\Sigma=1.06}(Ti_{1.86}, Fe_{0.02}, Si_{0.10})_{\Sigma=1,06}O_6\square^{+}_{0.28}$, calculated by the same methods described above, respectively.

The chemical composition of brannerite fulfills the stoichiometry AB_2O_6, where *A* = U and Th; *B* = Ti and Fe. The localization of Si is not clear yet. It is presumed to occupy part of the *B* site as its atomic radius is closer to that of Ti, rather than U.

Another grain **HB3** was calcined in the atmosphere at 1200 °C for 4 hours to ensure crystallization. Its chemical composition is also listed in Table 4 for comparison. The chemical composition of annealed brannerite is like that of the metamict grain. Calcined brannerite apparently becomes homogeneous although the texture shows increased porosity typical for recrystallized metamict minerals. Numerous bright spots (0.2-1μm) are observed in the enlarged BSE image. But their chemical content has not been successfully determined due to their small size.

3.1.2 Raman spectroscopy

Raman spectroscopy was used to investigate the molecule structure of the metamict and annealed brannerite. Frost and Beddy [Frost, Reddy, 2011b] compared the Raman spectra of brannerite and uranyl oxyhydroxide hydrates; they attributed the observed Raman bands to the $(UO_2)^{2+}$ and TiO stretching and bending vibrations as well as U–OH and O-Ti-O bending vibrations. Charalambous and coauthors [2012] examined partially-metamict brannerite, the Raman spectra of metamict minerals exhibited broad bands in the range of 50-1100 cm^{-1}. Zhang and coauthors [2013] obtained Raman spectra of natural and synthetic brannerite, identified 12 vibrational modes, set up the relationship between spectra and the structure, and recognized some incorrect Raman assignments

done in previous works.

We obtained Raman spectra in a range of 90–3500 cm^{-1} for both metamict and annealed samples. As the BSE image shows, the metamict mineral is heterogeneous. The Raman spectrum of metamict brannerite shows only a few broad and overlapping bands (Figure 9 a). Raman bands are concentrated in the range 90-1200 cm^{-1}.

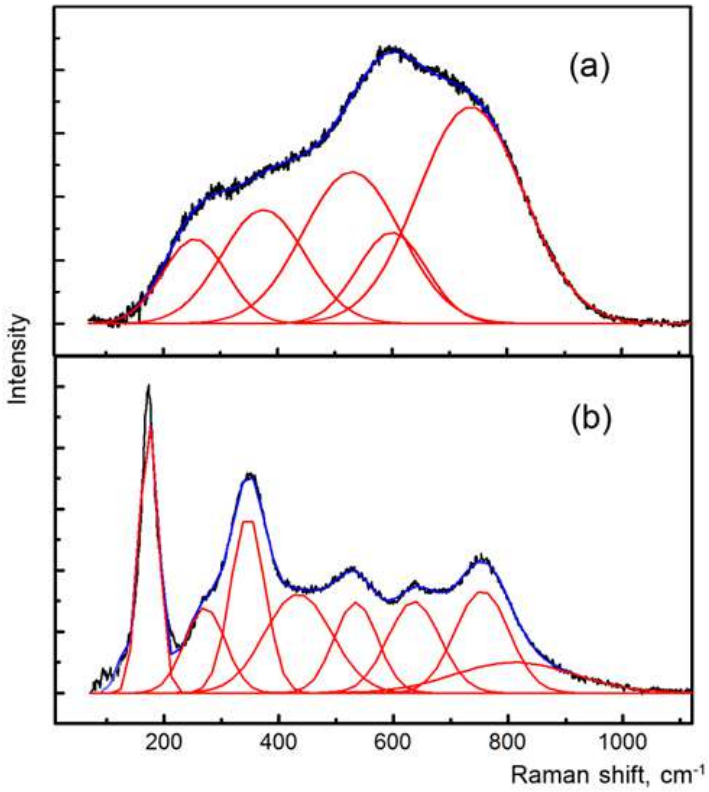

Figure 9. Raman spectra of metamict (**a**) and annealed brannerite (**b**).

The mineral structure is heavily damaged. However, the Raman spectra of most areas perform neither O-H stretching of water molecules and hydroxyl groups at approximately 3500 cm^{-1} nor the O-H-O bending bands at around 1600 cm^{-1}. O-H bands are observed only in the areas close to the cracks (Figure 8 c), indicating the partial hydration and alteration.

Annealed brannerite grains are more homogeneous. The vibrational modes are very intense and sharp in their Raman spectra (Figure 9 b). The brannerite spectrum is in excellent agreement with the Raman spectrum of annealed brannerite provided in the previous work of Zhang et al. [2013]. The comparison of obtained data with the reference data is provided in Table 6.

The different Raman spectra of the sample before and after heating are indicative of a change in its crystal structure. The damaged crystal structure of metamict brannerite shows vibrational bands of low intensity in Raman spectra, where the heated mineral crystals have recrystallized and give more intense Raman peaks. The Raman bands of metamict brannerite overlaps, making identification and correlation very difficult.

Table 6. Raman bands and its assignment in annealed studied brannerite sample and the reference data from [Frost, Reddy, 2011b; Zhang et al., 2013].

This study	Reference data			
Annealed **HB3**	Annealed brannerite [Frost, Reddy, 2011b]		Natural and synthetic brannerite [Zhang et al., 2013]	
Raman shift (cm^{-1})	Raman shift (cm^{-1})	Assignment	Raman shift (cm^{-1})	Assignment
174	171	O–Ti–O bending modes	~171	Ti–O bending modes
284	269	$U_3(OH)_3$ out-of-plane bending vibrations	~265	O–Ti–O vibrations
348	356	$U_3(OH)_3$ or $U_2O(OH)$ group elongation vibrations	~356	O–Ti–O vibrations
517	400-600	Ti–O vibrations or U–O vibrations	400-600	U–O vibrations
			~490	O–Ti–O vibrations
641	641	Ti–O symmetric stretching vibration	~640	Ti–O asymmetric stretching vibration
769	766	$(UO_2)^{2+}$ symmetric stretching vibrations	~760	O–Ti–O symmetric stretching vibrations, not $(UO_2)^{2+}$ symmetric stretching vibrations

3.1.3 High-temperature X-ray powder diffraction

To identify the recrystallization temperature and to observe in-situ the crystallization of brannerite, X-ray powder diffraction was performed for the metamict sample. Figure 10 demonstrates the structural evolution of the metamict brannerite with increasing temperature. Pt holder diffraction peaks and unknown impurity were observed during the entire heating process.

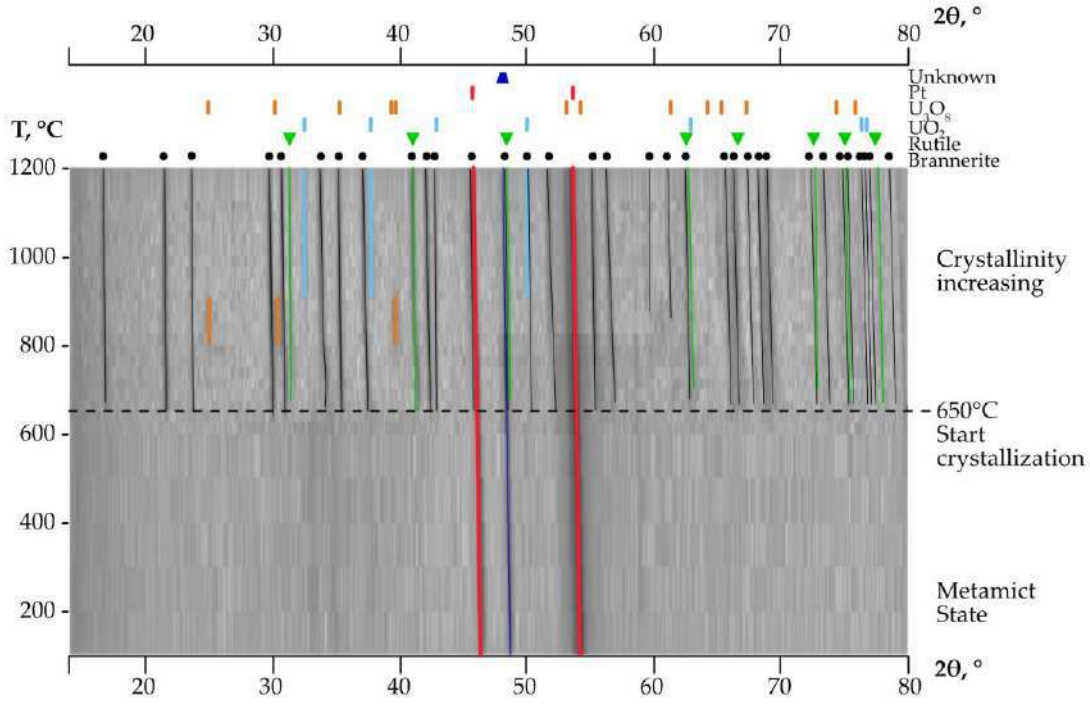

Figure 10. Evolution of X-ray powder diffraction patterns of metamict brannerite at temperatures from 100 to 1200 °C. There is no evidence of recrystallization until 625 °C.

Previous research shows that the temperature of the brannerite from Crocker Well (South Australia) recrystallization is in the range of 800-900°C [Charalambous et al., 2012]. Adler and Puig

[Adler, Puig, 1961] determined the start of brannerite recrystallization above 550 °C. The brannerite from El Cabril mine (Spain) completely recrystallizes between 900 °C and 1100 °C, but the crystallization process starts earlier in the range 500°C -700°C [Balek et al., 2007]. However, our in-situ studies reveal that brannerite from Akchatau recrystallizes at a temperature as low as 625-650°C. At the temperature above 625 °C, several diffraction peaks quickly evolve, indicating the start of the recrystallization process.

There are some previously published data showing that TiO_2 and U_3O_8 can be produced during the recrystallization of the brannerite-type material, when the stoichiometric material is heated in the air [Dixon Wilkins et al., 2021]. Uranium oxides appear at ~800 °C: diffraction lines 25°, 31.5° and 40° 2θ — can be assigned to U_3O_8 (ICSD-51525). This phase, however, disappears at ~ 900 °C and evolves into the uraninite-type structure UO_2 (ICSD-61576). It is known, that U_3O_8 decomposes into UO_2 with the temperature increase even under mildly reducing conditions [Kim et al., 2012; Lin et al., 2014].

Figure 11 shows the ratio of thus formed U_3O_8 and UO_2 with the temperature increase. The diffraction pattern of the sample after cooling shows that the oxides may present only at the levels below the detection limits. In addition, the rutile phase is also noted in the annealed sample. Rutile, TiO_2 is typically associated with brannerite-rich ores in natural environments. The R-factors calculated by the Rietveld refinement increase with temperature, and fluctuate in the range of 6.2-12.6%.

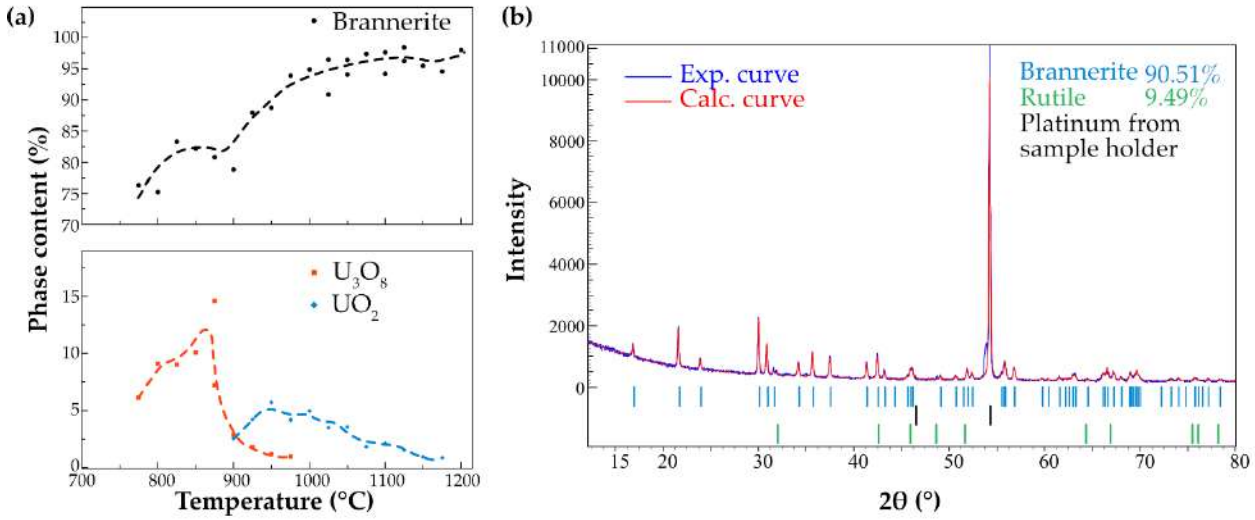

Figure 11. The content of the uranium oxide phases formed during the heating of metamict brannerite (**a**). The refinement on XRD date obtained after cooling (**b**) demonstrates excellent refinement quality, with values of Rexp = 4.10, Rwp = 4.98, Rp = 3.70.

3.1.4 Thermal expansion

High-temperature powder diffraction experiments were performed on annealed brannerite. The program “Rietveld to tensor” was used to analyze the XRD data and to calculate the thermal expansion [Bubnova et al., 2018].

Lattice parameters of brannerite were calculated using the Rietveld Method. The structure

expands mostly along the *a* axis, while along the *b* axis the changes are very minor. Unit-cell parameters *a*, *b* and *c* increase in the range 9.82-9.92 Å, 3.74-3.77 Å, and 6.88 to 6.94 Å, respectively. The *β* angle decreases slightly between 118.6 and 118.1°. The unit-cell volume increases from 221.0 to 227.8 Å^3 (Figure 12).

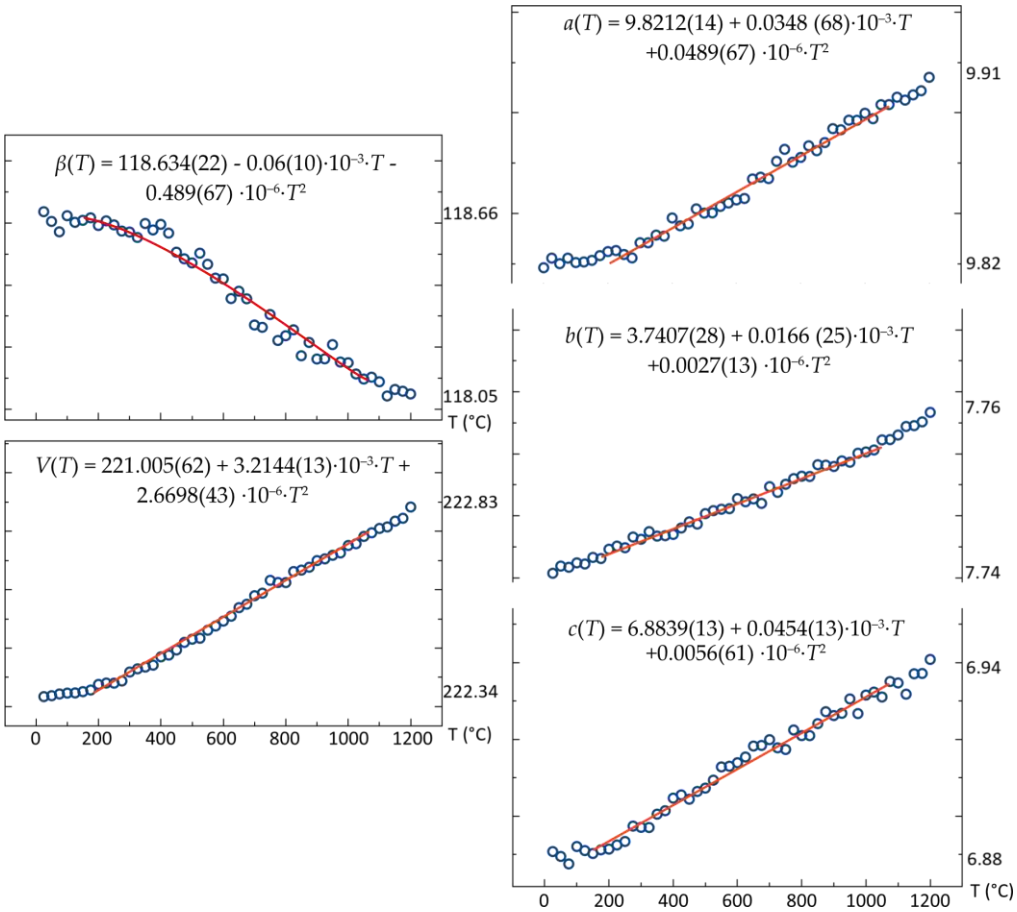

Figure 12. Unit cell parameters of crystallized brannerite in relation to temperature.

The temperature dependence of the unit-cell parameters was approximated by polynomials of the second order:

$a(T) = 9.8212(14) + 0.0348\ (68)\cdot10^{-3}\cdot T + 0.0489(67)\cdot10^{-6}\cdot T^2$

$b(T) = 3.7407(28) + 0.0166\ (25)\cdot10^{-3}\cdot T + 0.0027(13)\cdot10^{-6}\cdot T^2$

$c(T) = 6.8839(13) + 0.0454(13)\cdot10^{-3}\cdot T + 0.0056(61)\cdot10^{-6}\cdot T^2$

$\beta(T) = 118.634(22) - 0.06(10)\cdot10^{-3}\cdot T - 0.489(67)\cdot10^{-6}\cdot T^2$

$V(T) = 221.005(62) + 3.2144(13)\cdot10^{-3}\cdot T + 2.6698(43)\cdot10^{-6}\cdot T^2$

Table 7 shows the obtained values. The value of the volumetric expansion α_v is the sum of the eigenvalues α_{11}, α_{22}, and α_{33}. The linear expansion along the crystallographic axis *b* is α_{22}. All the thermal expansion coefficients are positive except for α_β. Decreasing parameter beta indicates a "shear structural deformation". This type of thermal deformation is typical for monoclinic crystals as its thermal expansion is determined primarily by the change of the *β* angle. The angle between the 1-st axis of the tensor and the crystallographic *a* axis decreases with the increase of the temperature; as a result, the structure expands mostly in the α_{11} direction approaching the bisector of the *β* angle (Figure 13b). Thermal expansion tensors of brannerite at different temperatures are shown in

Figure 13a. The decreasing β angle value is demonstrated by the rotation of the crystallographic *a* axis towards the *c* axis.

Table 7. Principal values of the thermal expansion tensor and volumetric expansion of brannerite. α_{11}, α_{22}, and α_{33} are tensor components along the principal axes; $\angle(\alpha_{11}, \alpha_a)$ is the angle between the 1-st axis of the tensor and the crystallographic axis *a*; α_a, α_b, α_c, α_β, α_V are CTE of the corresponding parameter.

	$\alpha \times 10^6$ °C^{-1}				
T, °C	100	300	600	900	1100
α_{11}	8.39(67)	12.03(42)	18.19(33)	24.44(93)	28.6(1.4)
$\alpha_{22} = \alpha_b$	4.59(37)	4.88(17)	5.304(95)	5.73(22)	6.01(30)
α_{33}	4.38(35)	4.94(17)	5.013(89)	4.91(19)	4.79(24)
$\angle(\alpha_{11}, \alpha_a)$	78.9°	61.8°	54.4°	51.7°	50.6°
$\angle(\alpha_{33}, \alpha_c)$	129.8°	33.2°	26.0°	23.5°	22.7°
α_a	4.53(56)	6.52(31)	9.48(21)	12.42(57)	14.36(83)
α_c	6.75(74)	7.07(41)	7.54(28)	8.01(74)	8.3(1)
α_β	-1.32(70)	-3.00(40)	-5.53(23)	-8.07(63)	-9.78(94)
α_V	17.4(1.3)	21.85(75)	28.51(51)	35.1(1.3)	39.4(1.9)

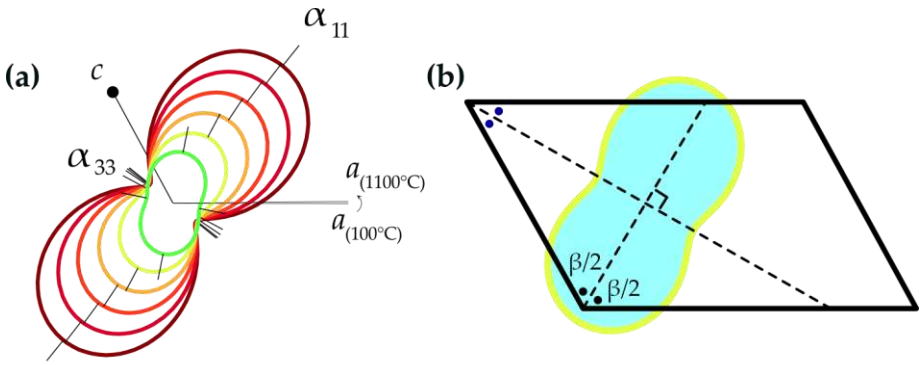

Figure 13. Spherical diagram of the thermal expansion tensors of brannerite (a) and the projection on the unit cell. The β angle decrease is accompanied by the expansion along the α_{11} direction, which is a bisector of an obtuse angle.

Note, that the expansion along the *a* axis is higher, compared to α_c, at temperatures below 500 °C; afterwards, α_c exceeds α_a in the range 500°C-1100°C. The maximum expansion occurs along or close to the direction of the longer (weaker) bonds. The U-O bond is more sensitive to the temperature increase. The expansion of the UO_6 octahedra is more pronounced at the first stages of the heating. Its expansion drives the enlargement of the interlayer distance as UO_6 octahedra link two TiO_6 octahedral layers [Chen et al., 2023].

3.1.5 Thermal analysis

The results of the Differential Scanning Calorimetric (DSC) experiment and Thermal Gravimetric Analysis (TGA) of the metamict brannerite are shown in Figure 14. DSC curve indicates two thermal transitions in the studied temperature range. With the temperature increases, metamict brannerite starts to recrystallize, which results in an exothermic peak at 670 °C. The endothermic peak at 1082 °C shows that the sample undergoes partial melting. X-ray diffraction pattern of the studied sample after the thermal analysis and complete cooling indicates the formation of rutile.

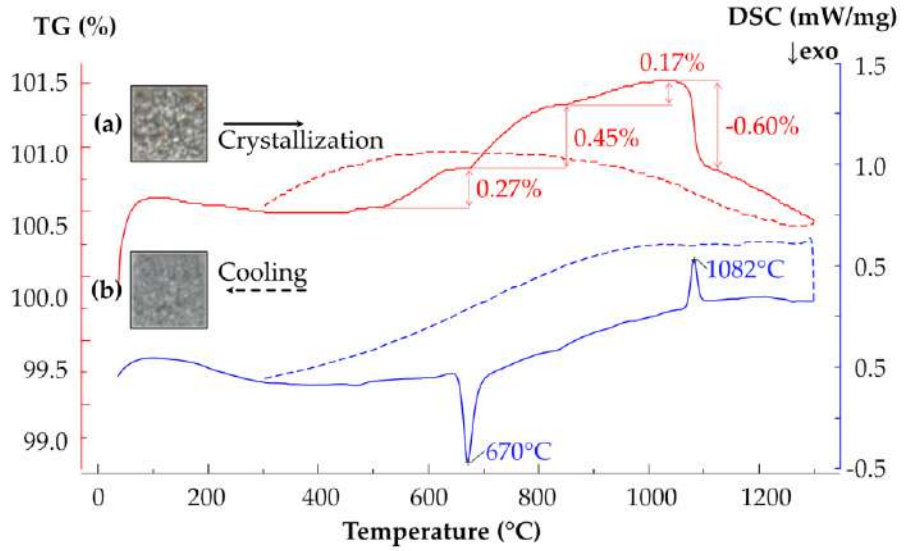

Figure 14. DTA and DSC curves of metamict brannerite heated to 1300 °C. Photographs of the powder sample before (a) and after (b) thermal analysis are shown (field of view of each frame is 0.5×0.5 mm).

The TG curve shows a mass decrease of 0.11% from 99 to 307 °C, corresponding to the loss of adsorbed water from the sample surface. The partial oxidation of Fe and U results in the TG curve upward trend from 444 to 1055 °C. The mass of the sample increases by 0.27 % and 0.45 % in the temperature intervals 444-643 °C and 670-834 °C respectively. A pause in the mass increase is observed in the range of 643-670 °C, which implies several oxidation stages. The TG curve also demonstrates a slow mass increase by 0.17 % in the range 834-1055 °C. Between 1055 and 1115 °C, a mass loss of 0.60 % is observed, which corresponds to the endothermic effect with a maximum at 1082 °C.

To conclude, there is an increase in a sample mass due to the oxidation between 444 and 1055 °C. A strong exothermic process associated with the crystallization of brannerite is observed at 670 °C. The mass increase almost stops at the same time and continues only after the completion of the crystallization of brannerite. Brannerite starts partially to decompose after 1000 °C.

3.1.6 Remarks for subsection

Natural metamict brannerite from Akchatau, Kazakhstan, and its annealed sample were studied by EPMA and Raman spectroscopy to determine its chemical composition. The XRD and Raman spectra of the metamict brannerite indicated its structure to be heavily damaged. Iron and uranium are heterogeneously distributed in the mineral due to the radiation damage. The studied metamict mineral grains show some zones enriched by the hydroxyl and SiO_2. Pyrochlore and galena are found as inclusions. The crystal structure of brannerite is restored after annealing. The thermally processed brannerite's texture is porous and homogeneous.

The radioactivity of pristine and annealed samples of brannerite was measured. The specific activity of ^{226}Ra accounts for up to 96% of the total radioactivity, which indicates that the main type of decay in the mineral sample belongs to the uranium series.

XRD at high temperatures was performed for the metamict sample to investigate the

recrystallization process in situ. It has been reported previously in several works that brannerite recrystallizes in the temperature range of 800-1000 °C [Balek et al., 2007; Charalambous et al., 2012; Patchett, Nuffield, 1960; Zhang et al., 2018]. In contrast, the studied brannerite from Akchatau regains its structure at a temperature ~650 °C, approved also by the DSC measurements. We suggest that the recrystallization temperature is dependent mainly on the chemistry and homogeneity of the sample; but also depends on the degree of the radiation damage of the sample. Brannerite from Akchatau is characterized by the absence of the significant amounts of REE and yttrium, typically observed at many other localities. The experimental conditions, such as heating rate, and annealing step, may also affect the recrystallization temperature.

HTXRD was also performed on the annealed recrystallized brannerite. Thermal expansion of brannerite has been determined for the first time. The brannerite structure expands anisotropically with the temperature increase. The anisotropy is determined mainly by the change of the unit cell angles typical for monoclinic crystals. Despite its anisotropy, thermal expansion in brannerite is rather weak. Brannerite has a low CTE at room temperature - α_v=16 × 10^{-6} °C^{-1}, which increases up to 39.4 × 10^{-6} °C^{-1} at 1100 °C.

3.2 Thorite[10]

Three mineral samples from the collection of Saint-Petersburg State university mineralogy museum were studied. They originate from Vestfold og Telemark, Norway. **MTS1** (initial collection number 183/9) is an orange crystal embedded in the felspar from pegmatite. **MTS2** and **MTS3** are fragments with a greasy luster, with initial collection numbers k-191/4 and 183/5, respectively. In the text below, we refer to the metamict thorium silicate samples as **MTS**, and recrystallized thorium silicate samples obtained by heating metamict samples as **HTS**.

3.2.1 Mineralogy of samples

The **MTS1** sample is represented by a color-zoned metamict thorium silicate with preserved tetragonal shape embedded in an albite matrix. Samples **MTS2** and **MTS3** are massive, irregularly shaped metamict thorium silicate samples ~ 2 cm wide each (Figure 15).

Three regions can be identified from the back scatter electron (BSE) image of MTS1 based on BSE color: **MTS1-core, MTS1-midst** and **MTS1-rim**. They are discernible by their BSE contrast from core to rim: brightest grey, light grey, and dark grey. These regions intriguingly correspond to the macroscopically visible colors observed—yellow opaque, yellow translucent, and black—as illustrated in Figure 16a. BSE images of the enlarged area are shown in the insets of Figure 16b, c.

Figure 16d, e, and f display the element distribution maps of Si, Th, and Ca, respectively. Si exhibits uniform distribution across three regions. In addition, **MTS1-core** shows elevated Th levels and reduced Ca content, contrasting **MTS1-midst** and **MTS1-rim**.

[10] Thorite and huttonite, two dimorphs of $ThSiO_4$. Space group (SG) of thorite: $I4_1/amd$, SG of huttonite: $P2/c$. Their structures are demonstrated in Figure 2.

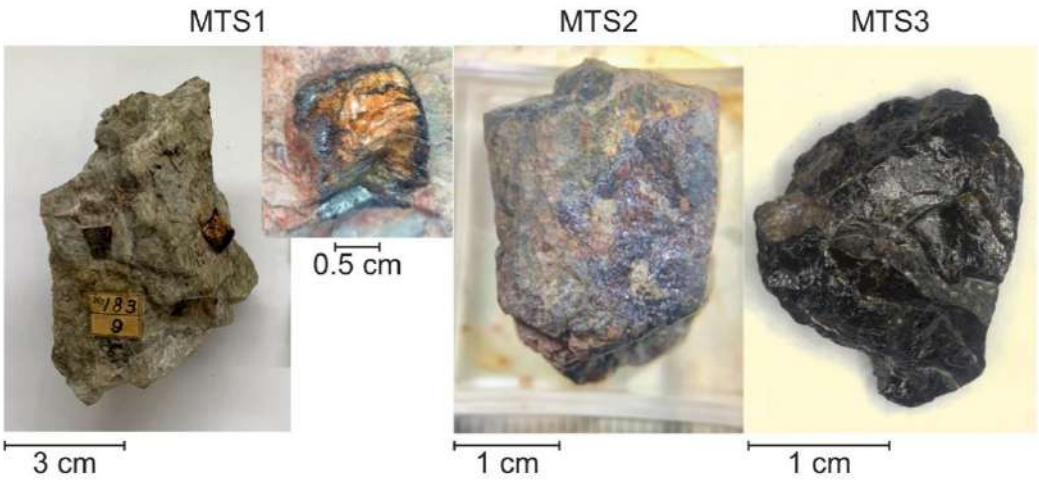

Figure 15. Mineral sample of **MTS1**, **MTS2** and **MTS3**.

The grain from the sample **MTS2** is heterogeneous featuring irregularly distributed dark-grey and brown areas (Figure 17c). These areas match the lighter and darker BSE colors, known as **MTS2-high-U** and **MTS2-high-Fe**, respectively, corresponding to the lighter and darker regions in the BSE image (Figure 17d). Detailed chemical analyses of these areas will be discussed in the next chapter. The narrow white vein, less than 2 μm wide as observed in the BSE image of **MTS2** (Figure 17d), consists of a high lead-containing silicate uranium phase (32 wt.% PbO and 46 wt.% UO_2, see Table 8 (point 166). In addition, in the BSE image of **MTS2**, white dots of 1-2 μm size can also be observed spread throughout the volume. These white dots have a higher Uranium content than the thorium silicate substrate (up to 25 wt.% UO_2), see Table 8 (point 175).

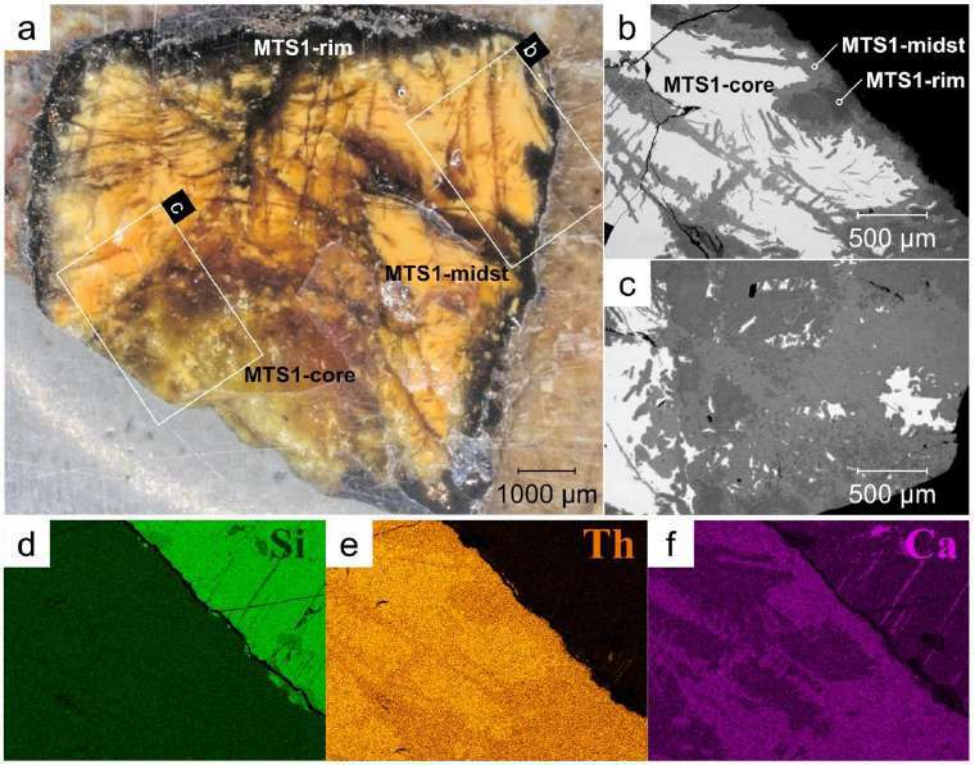

Figure 16.Polished color-zoned metamict thorium silicate (**MTS1** sample) with preserved tetragonal shape embedded in albite matrix. Three zones/areas are distinguished by their BSE color: **MTS1-bright**, **MTS1-grey** and **MTS1-dark**, which correspond to the macroscopically visible color respectively (from the core to the rim): opaque yellow, translucent yellow, and opaque black (a). The areas highlighted with white rectangles indicate areas for BSE images further shown in (b) and (c) insets. The element maps of (b) inset are shown in (d), (e) and (f) for Si, Th and Ca, respectively.

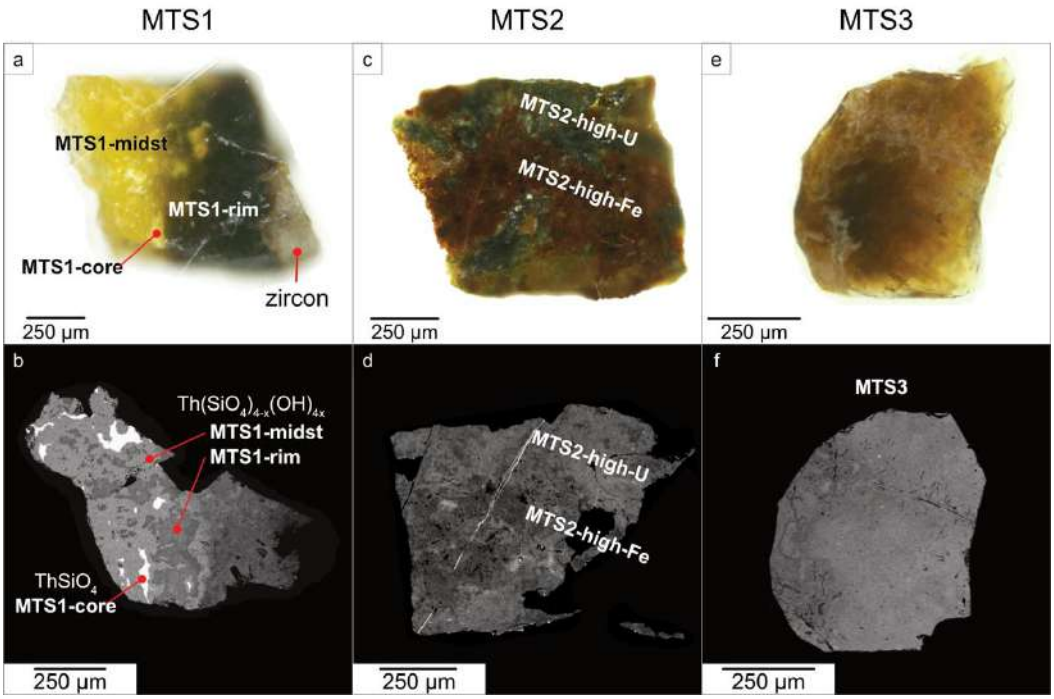

Figure 17. Photographs and BSE images depicting the selected grains from **MTS1**, **MTS2** and **MTS3** samples. **MTS1** is represented by a grain consisting of yellow opaque (**MTS1-core**), yellow translucent (**MTS1-midst**) and black areas (**MTS1-rim**) (a). The grain consists of both almost anhydrous $ThSiO_4$ (yellow opaque areas) and heavily hydroxylated silicate thorium (b). A grain from the **MTS2** sample consists of black (**MTS2-high-U**) and brown areas (**MTS2-high-Fe**) irregularly distributed over the sample (c). Brown areas are characterized by high Fe content, whereas black areas are rich in U (d). A tan grain from the **MTS3** sample (e) has medium brightness in BSE (f).

Table 8. Chemical composition (wt. %) of inclusions observed in metamict minerals MTS.

Sample	**MTS1**	**MTS2**	**MTS2**	**MTS3**	**MTS3**
Point №	263	166	175	224	209
Regions	Zircon	U veins	Bright spots	Pb veins	Bright spots
SiO_2	32.05	11.05	13.94		17.55
CaO			0.82	0.13	3.56
Fe_2O_3		0.7			
ZrO_2	61.79				
HfO_2	1.56				
PbO		28.99	5.65	99.29	2.01
ThO_2	0.35	10.49	36.51		61.83
UO_2		45.53	25.58		2.65
Total	95.74	96.76	82.49	99.43	87.6

The tan (yellow in the thin section) **MTS3** sample is relatively homogeneous and has medium brightness in BSE (Figure 17 e, f). A set of bright spots are visible in the thorium silicate matrix, showing elevated uranium content (Table 8, point 209). The Pb veins are also observed in **MTS3** sample (Table 8, point 224).

3.2.2 Chemical composition of metamict thorium silicates

The results of an electron microprobe analysis of **MTS1**, **MTS2** and **MTS3** (Table 9) reveal a variable uranium (UO_2 = 0 - 25.68 wt.%) and thorium (ThO_2 = 36.67 - 78.05 wt.%) content. The metamict samples contains hydrated water, which is common for metamict thorite. The average

analysis total is therefore approximately ~86 wt.%, because hydroden is too light to be detected in electron micro-probe analyses.

Two diagrams, UO_2 vs ThO_2 and CaO vs SiO_2 (wt.%), are drawn in Figure 18 to distinguish MTS samples in terms of chemical composition. The **MTS1-core** analyses are similar to the composition of ideal $ThSiO_4$. In contrast, the **MTS1-midst**, **MTS1-rim**, **MTS2-high-U**, **MTS2-high-Fe** and **MTS3** are hydrated and altered thorium silicates.

The detailed chemical composition is given in Table 9. The **MTS1-core** group corresponds to the opaque yellow areas from the "core" of the **MTS1** sample correspond to the almost ideal and only slightly hydroxylated silicate thorium, with average total of 98 wt. %. Among the studied samples, **MTS1-core** has the highest ThO_2 content of 78.05 wt. % which corresponds to the brightest areas in BSE images shown in Figure 16 and Figure 17b. Although a minor hydroxylation for these areas is observed and confirmed by the Raman spectroscopy (see below).

Table 9. Chemical composition (wt. %) and atom per formula unit of metamict thorium silicate from Vestfold og Telemark (**MTS**).

Sample	**MTS1-core**	**MTS1-midst**	**MTS1-rim**	**MTS2-high-U**	**MTS2-high-Fe**	**MTS3**	
Visible color	Yellow, opaque	Yellow, translucent	Black	Black	Brown	Yellow	
Color in BSE	Bright-grey	Light-grey	Dark-grey	Light-grey	Dark-gtey	Light-grey	
Point No.	249	264	258	181	198	211	222
Wt.%							
SiO_2	18.24	17.30	17.38	16.68	19.24	18.45	18.93
CaO		3.33	4.03	1.24	2.55	4.11	5.15
MnO					0.33	0.57	0.46
Fe_2O_3					5.40	0.36	
PbO	1.86	1.36	0.82	4.25		0.79	0.96
ThO_2	76.83	63.62	63.00	51.68	55.60	58.56	59.12
UO_2	2.21	0.62	1.91	12.78		3.03	2.93
Total	99.14	86.23	87.14	86.62	83.13	85.89	87.56
Structural formulae calculated on the basis of 2 cations.							
Si^{4+}	0.99	0.97	0.95	0.99	0.99	0.98	0.97
Ca^{2+}		0.20	0.24	0.08	0.14	0.23	0.28
Mn^{2+}					0.01	0.03	0.02
Fe^{3+}					0.10	0.01	
Pb^{2+}	0.03	0.02	0.01	0.07		0.01	0.01
Th^{4+}	0.95	0.81	0.78	0.70	0.65	0.70	0.69
U^{4+}	0.03	0.01	0.02	0.17		0.04	0.03
$OH^-_{calc.}$	0.05	0.44	0.49	0.29	0.83	0.58	0.63
$O^{2-}_{calc.}$	3.95	3.56	3.51	3.71	3.17	3.42	3.37

Blanks in the Table – content of the element is below detection limit.
$OH^-_{calc.}$ and $O^{2-}_{calc.}$ – calculated from charge balance.

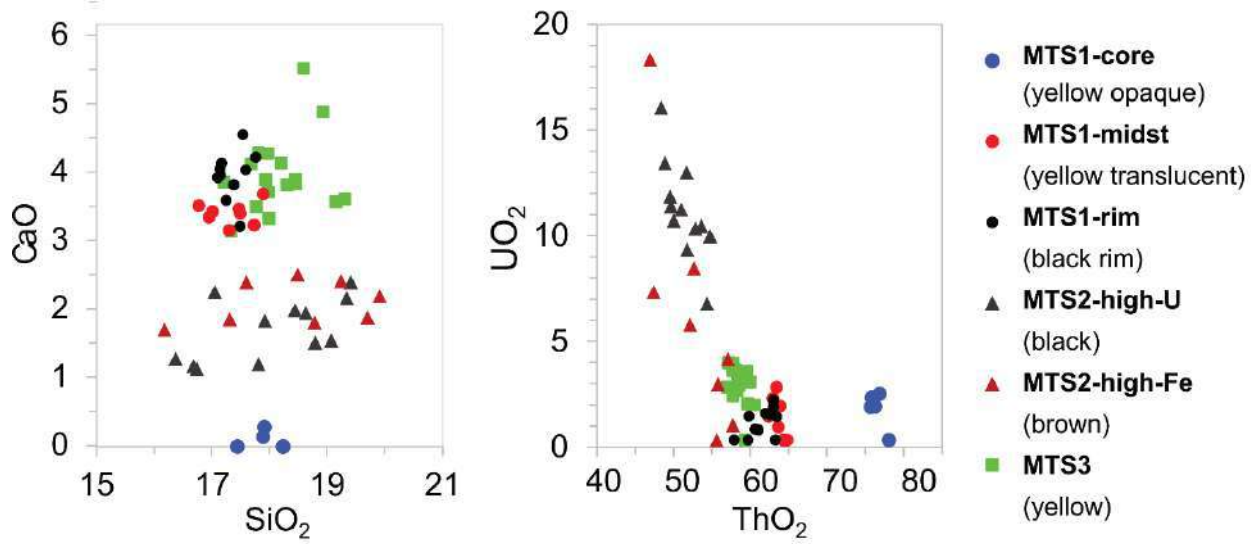

Figure 18. Diagrams UO_2 vs ThO_2 and CaO vs SiO_2 (wt.%) drawn for metamict samples.

The **MTS1-midst** and **MTS1-rim** groups match the translucent yellow and opaque black rim, respectively. These groups show a higher level of CaO, coupled with a reduced content of ThO_2 and a lower total, down to 57.89 wt. %. Black opaque rim (**MTS1-rim**) is also enriched by MnO, Fe_2O_3 and P_2O_5. Notably, **MTS1-rim** exhibits more significant alteration and hydroxylation than **MTS1-midst** does.

The general characteristic of heterogeneous sample **MTS2** is the increased uranium and iron content compared to **MTS1** and **3** (Table 9), which is manifested in a brown and dark-grey colors (Figure 17c). These regions correspond to variations in composition, with the black area (**MTS2-high-U**) being rich in uranium, as illustrated in Figure 18. The brown area (**MTS2-high-Fe**) are high in iron.

The sample **MTS3** (Figure 17e, f) is chemically homogeneous homogeneous and there is no need to subdivide it into regions. The plots from group **MTS3** in Figure 18 suggests a chemical similarity to the altered areas in **MTS1 (-midst** and **-rim)**, despite being from different samples. Additionally, the uranium content in **MTS3** is higher than **MTS1** (Table 9).

3.2.3 Chemical composition of recrystallized thorium silicates

Figure 19 shows heat-treated grains **HTS1**, **HTS2** and **HTS3**. After the heat treatment, all areas including the initially brown areas in **MTS1**(Figure 17a) turned yellow (Figure 19a). The Fe-rich **MTS2** (Figure 17c) sample turned black (Figure 19c). The **MTS3** grain acquired a uniform yellow color after the heating.

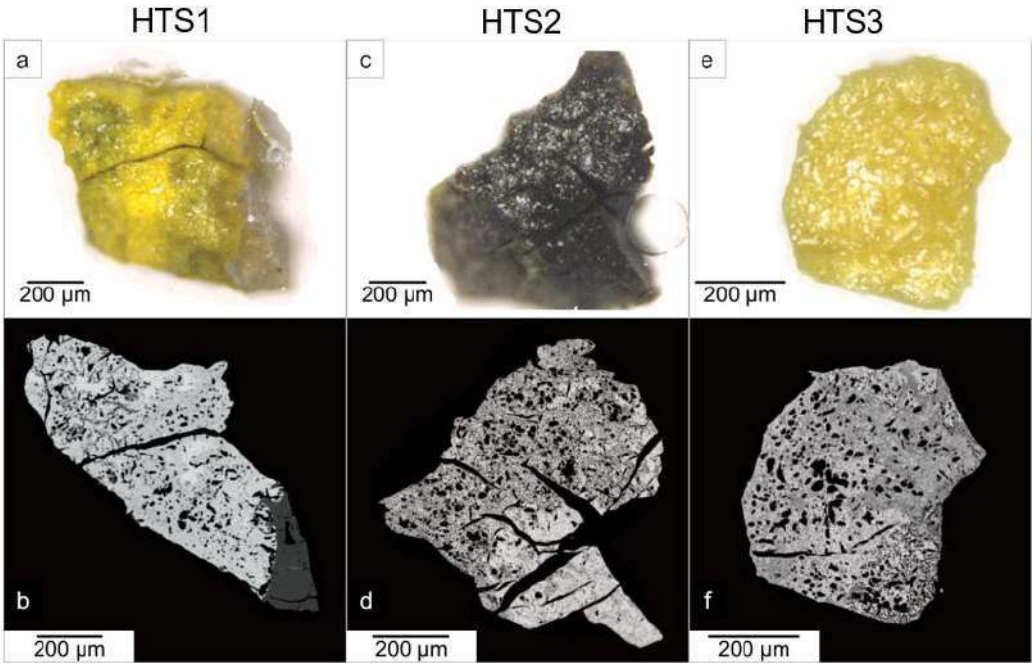

Figure 19. Photographs (a,c,e) and BSE images (b,d,f) depicting **HTS1**, **HTS2** and **HTS3** grains.

All the grains developed porous and fissured texture (Figure 19b, d, f) as a result of the dehydration and volume change. Thorium silicate has recrystallized in all samples without significant chemical variation, as confirmed by the chemical analyses in Table 10. However, two types of recrystallized thorium silicates can be seen in the BSE images: the first type is homogeneous with a grey BSE color (further **BSE-light**), while the second type displays a dark BSE color due to relatively fine granularity (further **BSE-dark**), as shown in Figure 20.

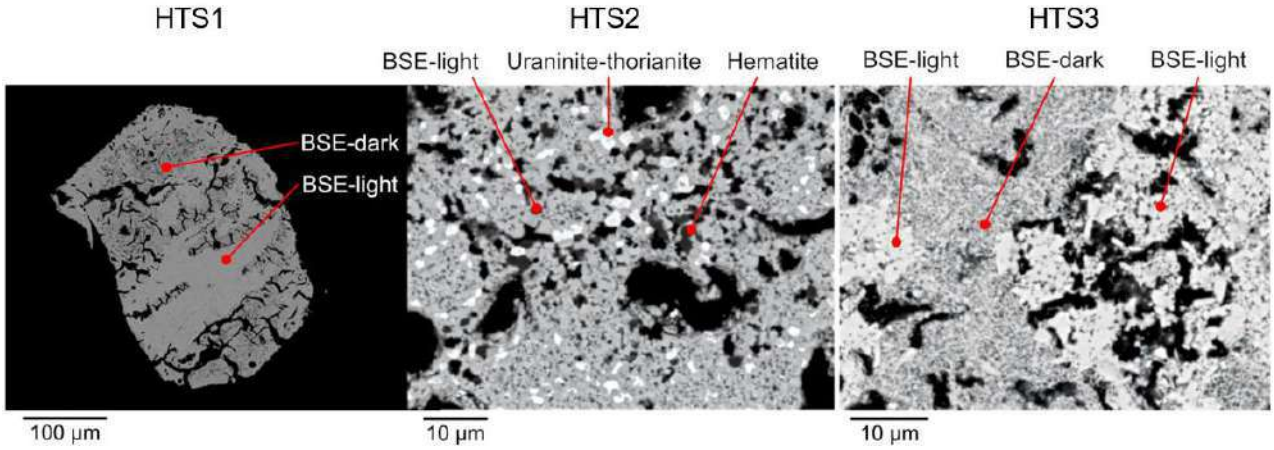

Figure 20. Thorium silicates in three samples have recrystallized with a similar texture. Two types of recrystallized thorium silicates can be observed in all samples – BSE-light and BSE-dark. The abundant uranium and iron are immobilized in phases such as uraninite and hematite.

The compositions of SiO_2 and ThO_2 are plotted in Figure 21, demonstrating that **BSE-grey** closely approximates the ideal composition of $ThSiO_4$. In Figure 21. , star-shaped symbols represent the ideal $ThSiO_4$ composition, with approximately 81.6 wt.% ThO_2 and 18.5 wt.% SiO_2 (Table 10, point 1089). The data points from the **BSE-grey** group cluster around these star-shaped symbols, whereas those from the **BSE-dark** group are more widely dispersed and show lower ThO_2 content.

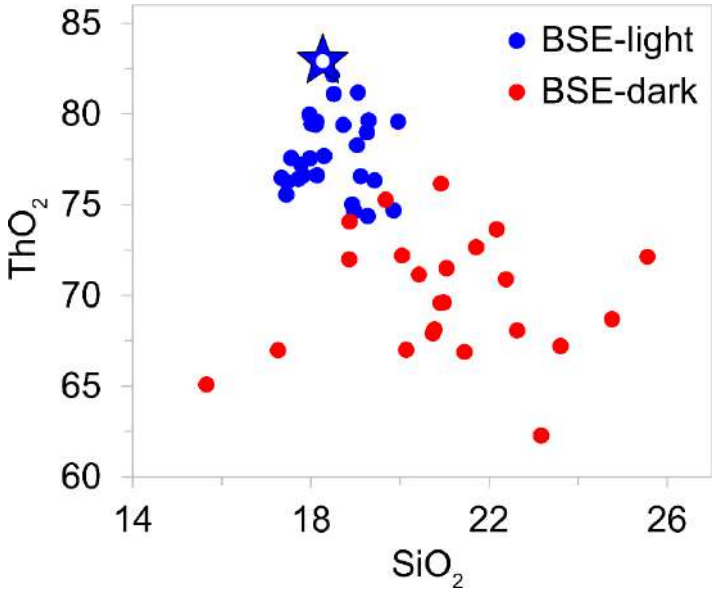

Figure 21. Compositional variations of thorium silicates in wt.% in **HTS** samples. Star-shaped symbols represent the ideal $ThSiO_4$ composition, see point 1089 in Table 10.

Table 10. Chemical composition (wt. %) and atoms per formula unit of the crystallized **HTS** samples.

Sample	**HTS1**		**HTS2**		**HTS3**		
Color and part of the crystal	Yellow		Black		Yellow		
Color in BSE	**BSE-light**	**BSE-dark**	**BSE-light**	**BSE-dark**	**BSE-light**	**BSE-dark**	**BSE-dark**
Point No.	1048	1047	1078	1069	☆ 1089	1086	1070
Wt.%							
SiO_2	18.14	22.38	18.49	25.56	18.52	20.78	21.45
CaO		4.87		0.86		3.35	2.13
MnO		1.10				0.29	0.94
Fe_2O_3						1.14	3.03
PbO	2.19			0.54			0.44
ThO_2	76.60	70.88	82.12	72.13	81.09	68.10	66.88
UO_2	2.54			1.19		5.89	3.07
Total	99.48	99.23	100.61	100.28	99.61	99.55	97.94
Structural formulae calculated based on 4 O.							
Si^{4+}	1.00	1.08	0.99	1.38	1.00	1.04	1.06
Ca^{2+}		0.25		0.05		0.18	0.11
Mn^{2+}		0.04				0.01	0.04
Fe^{3+}						0.04	0.11
Pb^{2+}	0.03			0.01			0.01
Th^{4+}	0.96	0.78	1.01	0.88	1.00	0.77	0.75
U^{4+}	0.03			0.01		0.07	0.03

Blanks in the Table – content of the element is below detection limit

MTS2 is characterized by high levels of uranium and iron, which do not fully incorporate into the thorium silicate phase after heat treatment. Alongside with the recrystallization of thorium silicate,

the abundant uranium oxides appear as white spots in the BSE image (Figure 20) and have crystallized in a fluorite structure, forming uraninite-thorianite solid solutions, as confirmed by X-ray diffraction analysis (see below). Meanwhile, the iron oxides, which exhibit a black BSE color (Figure 20), have crystallized separately into hematite, as identified by Raman spectroscopy (Figure 23).

3.2.4 Raman spectroscopy

Raman spectra for metamict grains are shown in Figure 22 and Figure 23. The spectra of the metamict samples lack well-defined peaks, showing only broad bands. Experimental bands are found concentrated at ~ 3500 cm^{-1} (Figure 22), which are assigned to stretching vibrations of OH group and/or H_2O molecular [Chukanov, Vigasina, 2020]. The bending modes of water molecular are usually located at about 1600 cm^{-1} [Kolesov, 2006; Strzelecki et al., 2021], they are not observed in the experimental spectra likely due to polarization direction.

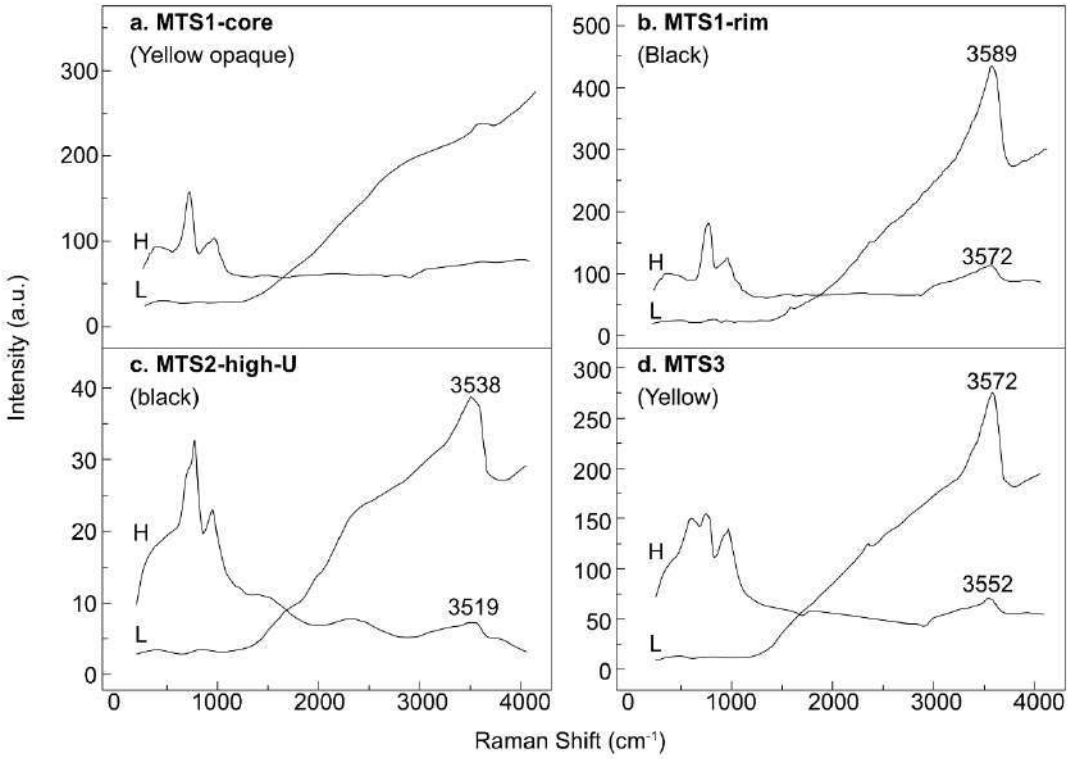

Figure 22. Raman spectra of **MTS1**, **MTS2** and **MTS3** obtained using 325 nm laser, the BSE brightness and macroscopic color of the sampling points are labeled. "H" Spectra designated "H" have enhanced intensity obtained after the application of the diffraction grating at 1800 gr/mm. "L" spectra are obtained at 600 gr/mm and have significantly lower intensities.

Reference spectra for uranium- and thorium-containing compounds are shown in Figure 23: huttonite (Jin and Soderholm, 2015, laser 532 nm, synthetic sample); thorite (Clavier et al., 2014, laser 532 nm, synthetic sample; hematite from heated goethite ([Faria de, Lopes, 2007] laser 632 nm); uranium-containing thorianite from Belafeno, Malagasy Republic (Jégou et al. , 2010, laser 532 nm); *R*-$CaUO_4$ (Liegeois, 1977, laser 633 nm, synthetic rhombohedral calcium uranate); uranophane from Grafton County, New Hampshire, USA (Stark and Noller, 2022, laser 514 nm, natural mineral sample).

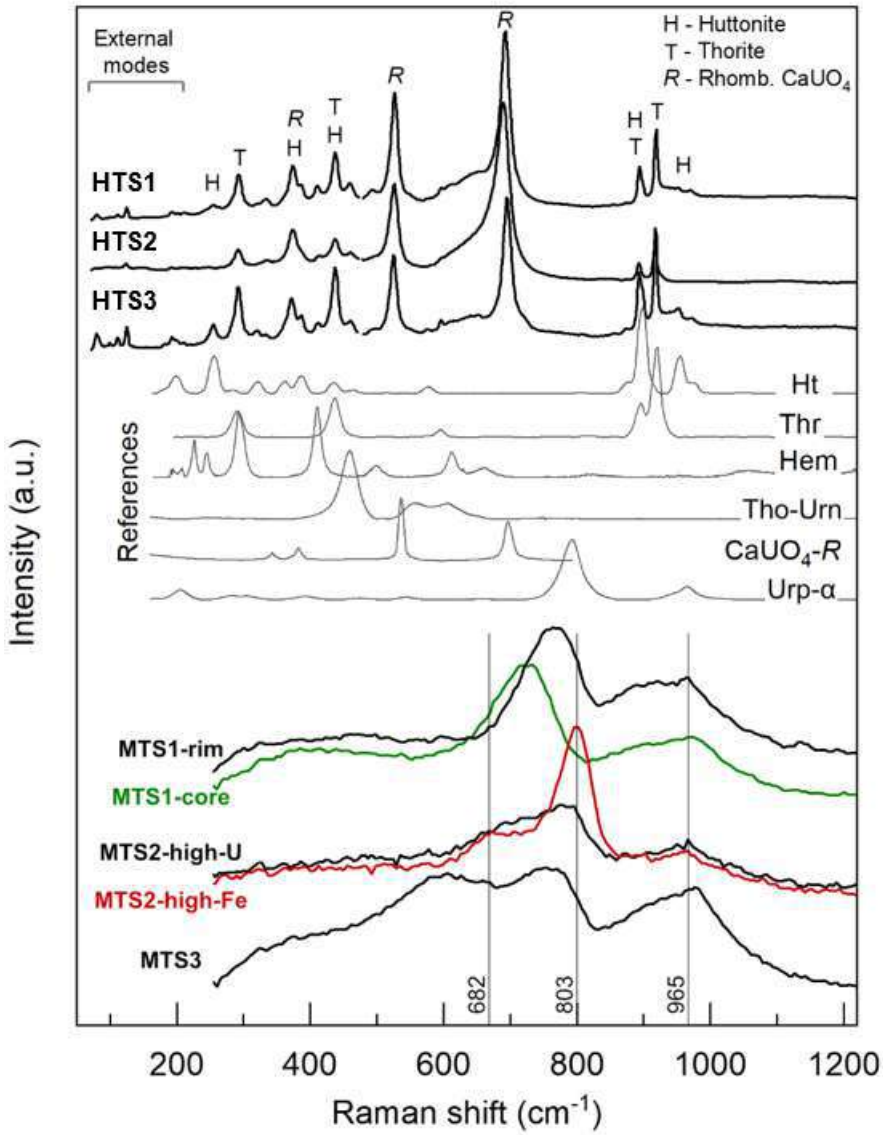

Figure 23. Raman spectra of metamict thorium silicate samples are presented below: almost anhydrous $ThSiO_4$ from **MTS1-core** (325 nm laser); $ThSi(O,OH)_4 \cdot nH_2O$ from **MTS1-rim** (325 nm laser); Hydrated $ThSi(O,OH)_4 \cdot nH_2O$ with high U-content from **MTS2-high-U** (325 nm laser); Fe-rich $ThSi(O,OH)_4 \cdot nH_2O$ from **MTS2-high-Fe** (325 nm laser); $ThSi(O,OH)_4 \cdot nH_2O$ from **MTS3** (325 nm laser). Above, the Raman spectra for the heated sample are shown: **RTS1** (532 nm laser); **RTS2** (532 nm laser); **RTS3** (532 nm laser). The reference spectra are detailed: Ht-huttonite, Thr-thorite, Hem-hematite, Tho-thorianite, Urn-uraninite, $CaUO_4$-*R* – rombhrdral calcium uranate, Urp-α – uranophane-α.

All vibrational bands in metamict samples heavily overlap due to low crystallinity, complicating spectral assignments. The main peaks are observed to be clustered around ~680, 800 and 960 cm^{-1} (Figure 23). The bands between 680 and 800 cm^{-1} are primarily attributed to symmetric stretching vibrations of $(UO_2)^{2+}$, commonly observed in uranophane at approximately 800 cm^{-1} [Frost et al., 2006]. This band may shift to a lower frequency due to elongation of the U-O bonds, similar to the symmetric stretch of the uranyl ion in rhombohedral uranate calcium at ~696 cm^{-1}, as noted by Liegeois-Duyckaerts [1977]. The bands near 960 cm^{-1} are ascribed to (SiO_4^{4-}) vibrations, typical in uranophane (symmetric stretching ν1 at 970 cm^{-1}), huttonite (asymmetric stretching ν3 at 900 cm^{-1}), and thorite (asymmetric stretching ν3 at 920 cm^{-1}), as documented by [Clavier et al., 2014; Frost et al., 2006; Jin, Soderholm, 2015].

Raman spectroscopy of heat-treated samples **HTS1**, **HTS2**, and **HTS3** reveals the presence of

multiple phases, notably huttonite, thorite, and rhombohedral $CaUO_4$ (Figure 23). Minor phases such as hematite and thorianite are also identified. Table 11 lists the experimental peak positions in comparison with reference data. Thorite is distinguished by Raman bands at 290, 430, 890, and 913 cm^{-1}, while huttonite phase exhibits characteristic bands at 436, 899, 953, and 971 cm^{-1}. Rhombohedral calcium uranate is recognized by intensive peaks at 534 and 690 cm^{-1}. Additionally, the peaks at 293 and 408 cm^{-1} in the Raman spectrum, which is characteristic for hematite (RRUFF record R050300. Lafuente et al., 2016 and Faria de, Lopes, 2007), imply the presence of this phase. Peaks at 409 cm^{-1} are attributed to hematite. Peak at 459 cm^{-1} is likely due vibration mode of the oxygen atoms coordinating actinide cations such as like Ce, Th, U, this peak is also observed in cerianite (Fig. 3 in Zaitsev et al., 2011), thorianite (RRUFF record R060849. Lafuente et al., 2016), uraninite (Fig. 3d in Pointurier and Marie, 2010).

Table 11. Observed bands (cm^{-1}) in Raman spectra of **HTS1**, **HTS2** and **HTS3** in the range 100-1000 cm^{-1} and the reference spectra for crystalline huttonite, thorite and rhombohedral $CaUO_4$.

HTS1	**HTS2**	**HTS3**	Huttonite [Jin, Soderholm, 2015]	Thorite [Clavier et al., 2014]	$CaUO_4$ [Liegeois-Duyckaerts, 1977]	Hematite [Faria de, Lopes, 2007]	U-containing Thorianite [Jégou et al., 2010]
124	125	125	120	125			
196	193	193	200	200			
255		256	257				
292	292	293	289	290		293	
319		320	322				
334	334	333			340		
373	373	372			379		
388		387	388				
412	413	411				408	
437	437	438	436	430			
459	460	461					459
492	496	491				498	
526	526	525			534		
596		596		590			
693	690	695			696		
895	892	892	899	890			
919	917	917		913			
950		952	953				
971		972	971				

3.2.5 High-temperature powder X-ray diffraction

High temperature X-ray diffraction was performed on four powder samples: **MTS1-midst**, **MTS1-rim**, **MTS2** and **MTS3**. This powder sample **MTS1-midst** is mixed with powder sampled from the core and midst areas of MTS1, so it is yellow in color. Likewise, sample **MTS2** has powders from both the high-U region and high-Fe region, and has an overall black color. **MTS1-rim** and **MTS3** are black and yellow, respectively.

Table 12 lists the crystallization temperatures of the main phases observed during heating. The crystallization of thorite starts in the range 420 – 480 °C, while the emergence of huttonite peaks occurs at 870 – 930 °C (Figure 24).

Several cubic phases with a common fluorite structure form upon heating. This correlates with chemical analysis results showing the formation of some uranium oxides post heat treatment, particularly as uraninite-thorianite solid solutions. For clarity, we refer to the cubic phase as 'fluorite'. Additionally, we differentiate these phases by labeling each with the value of the *a* parameter (Å).

The fluorite-type phases differ in unit cell size due to the substitution of larger cations such as Th and U with smaller cations, likely Ce, Pb, Ca, Fe, and Mn.

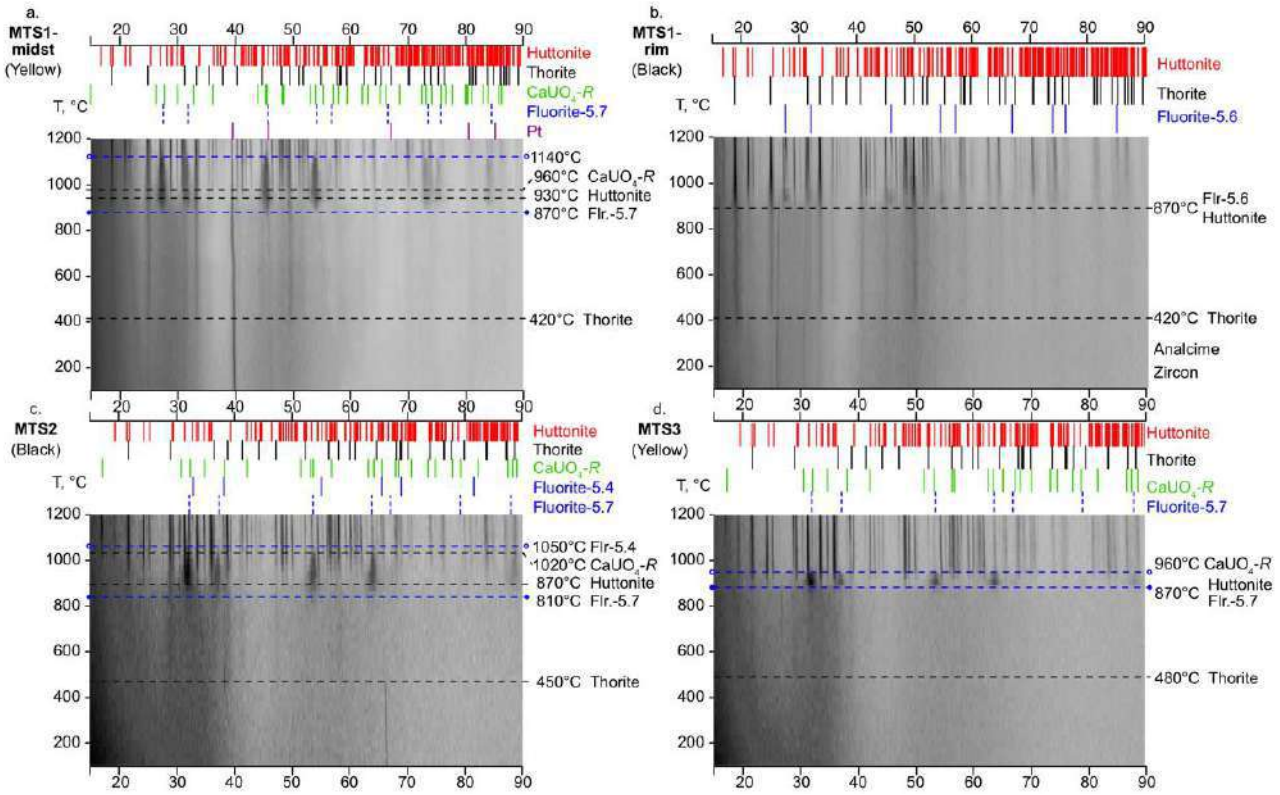

Figure 24. Evolution of the metamict thorium silicates (**MTS1-midst** – a, **MTS1-rim** – b, **MTS2** – c, **MTS3** – d) upon heating, the color of powder sample are given in brackets. Reference data utilized: huttonite [Taylor, Ewing, 1978], thorite [Taylor, Ewing, 1978], Pt [Davey, 1925], rhombohedral $CaUO_4$ [Loopstra, Rietveld, 1969], fluorite (Flr.)-5.7 [Clausen et al., 1983], fluorite (Flr.)-5.6 [Brauer, Gradinger, 1950], fluorite (Flr.)-5.4 [Shelly et al., 2023]. Temperatures of the appearance and decomposition of thorianite are indicated by blue dotted lines.

While 'fluorite-5.7' appears at ~ 810 – 870 °C in **MTS1-midst**, **MTS2** and **MTS3**, a smaller phase 'fluorite-5.6' starts to crystallize at 870 °C in **MTS1-rim** (Figure 24). These two phases are close to pure thorianite (*a* = 5.69 Å, [Clausen et al., 1983]) and $(Th_{0.8}La_{0.2})O_{1.90}$ (*a* = 5.62 Å, [Brauer, Gradinger, 1950]) in terms of unit cell size. In the **MTS2**, 'fluorite-5.4' emerges at ~ 1000 °C and persists throughout the heating process. The size of this phase is comparable [Shelly et al., 2023]. Upon further temperature rise up to 1200 °C, fluorite-5.7 decomposes in all samples studied, while Ca-containing oxide of uranium and thorium is detected in the crystallized sample after cooling (Table 13). No fluorite-type phases are detected in the **HTS1-midst** and **HTS3** samples after cooling.

Rhombohedral "$CaUO_4$" [Loopstra, Rietveld, 1969] forms in all samples, except for **MTS1rim**.

After subsequent cooling, the primary phases are huttonite and thorite. The total amount of the

crystallized $ThSiO_4$ (huttonite and thorite) is generally in agreement with the initial concentration of thorium oxide in the **MTS** samples (Table 9). The **MTS1-midst** has the highest content of thorium oxide, leading to the maximum amount of the crystallized $ThSiO_4$ phases (huttonite and thorite) upon the crystallization. In contrast, the **MTS2** exhibits the lowest thorium content and exhibits the smallest quantity of the crystallized $ThSiO_4$ phases, as listed in Table 13. **MTS1-rim** possesses the lowest amount of UO_2, resulting in the absence of rhombohedral $CaUO_4$ formation upon the crystallization process. And **MTS2** shows the highest uranium content, leading to the 15 wt. % of rhombohedral $CaUO_4$ formed upon heating.

Table 12. Crystallization temperatures of the main phases observed upon heating of the **MTS** samples by the means of powder X-ray diffraction. The observed fluorite-type phases are labeled with the value of the *a* unit-cell parameter.

Sample	**MTS1-midst**	**MTS1-rim**	**MTS2**	**MTS3**
Thorite	420 °C	420 °C	450 °C	480 °C
Fluorite -5.7	870 - 1140 °C	-	810 - 1050 °C	870 - 960 °C
Fluorite-5.6	-	870 °C	-	-
Huttonite	930 °C	870 °C	870 °C	870 °C
$CaUO_4$- rhombohedral	960 °C	-	1020 °C	960 °C
Fluorite-5.4	-	-	1050 °C	-

* The values of the temperature range at which Fluorite-5.7 exists are given.

Table 13. Phase composition of **HTS** samples after cooling. The amount of each phase is given in wt. %. E.s.d is ~ 3%.

Sample	**RTS1-midst**	**RTS1-rim**	**HTS2**	**HTS3**
R_{wp} (%)	10	12	8	9
Huttonite[1]	63	32	39	63
Thorite[1]	29	54	28	18
$CaUO_4$-rhombohedral [2]	8	-	15	19
Fluorite-type phase[3,4,5]	-	14	18	-

Reference data: [1] - Taylor and Ewing, 1978; [2] - Loopstra and Rietveld, 1969); [3,4,5] - Clausen et al., 1983 (thorianite ThO_2), Brauer and Gradinger, 1950 $(Th_{0.8}La_{0.2})O_{1.90}$, Shelly et al., 2023 $(Ce_{0.8}U_{0.2}O_2)$.

3.2.6 Electron backscatter diffraction (EBSD)

Grain from the **metamict** sample did not generate any diffraction as expected, while all heat-treated **HTS** grains produced EBSD patterns. Heat-treated grains **HTS1-midst** and **HTS1-rim** are initially yellow and black, respectively, which correspond to the **MTS1-core, -midst** and **MTS1-rim** regions before heating. The patterns show a good match for huttonite and thorite structures. The clearest recorded patterns are depicted on Figure 25c, e. Given patterns show a reasonable mean angle deviation (MAD) of 0.52° and 0.38°, respectively, with the highest possible number of matching bands, while the values less than 1º are considered a good match. In Figure 25d, f, the pole figures show the distribution density map projections of crystallographic direction of mineral orientation relative to the sample surface.

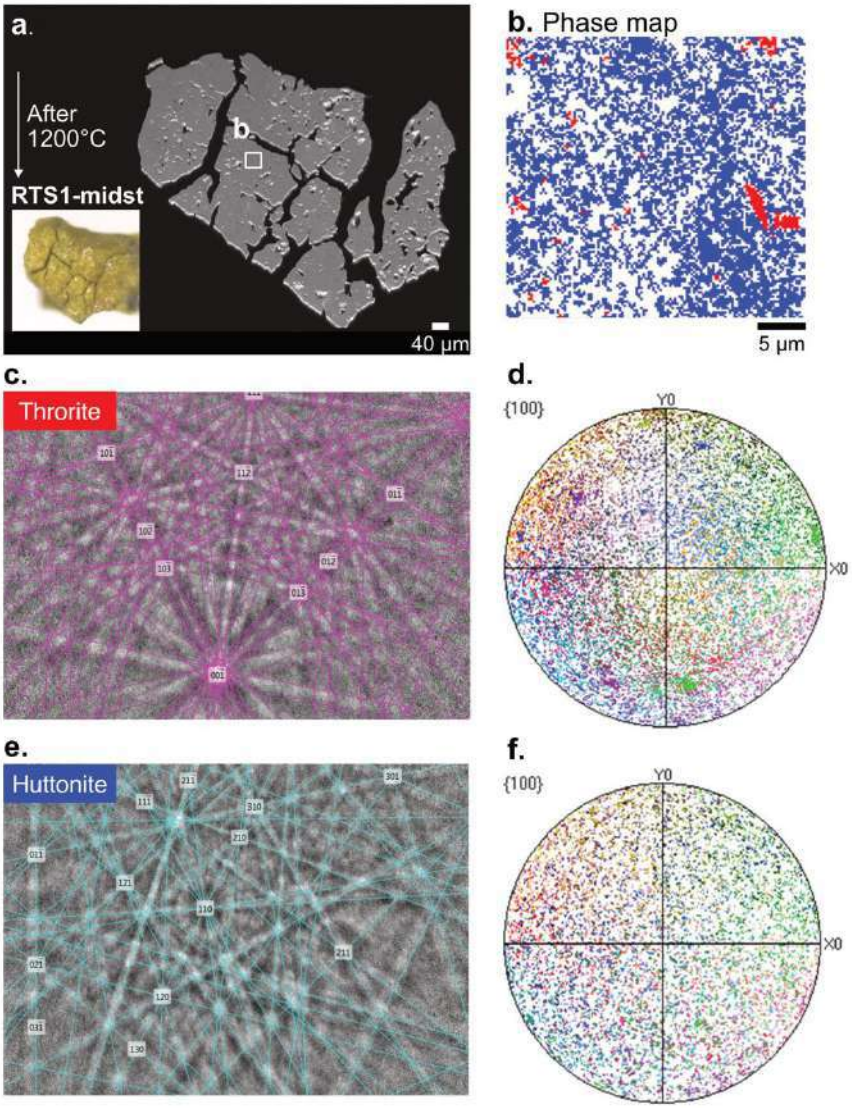

Figure 25. The photograph and BSE image of the **HTS1-midst** grain (a). Phase map of the selected area is shown to the right (b). Huttonite is blue, and thorite is red. EBSD patterns for thorite (c) and huttonite (e), and their pole figures (d,f).

Both **HTS1-midst** and **HTS1-rim** samples are fine-grained aggregates with the crystal size not exceeding 2 µm. The presence of both huttonite and thorite is evident in all samples (Figure 25 and Figure 26). EBSD phase analysis indicates a high prevalence of huttonite after heating within the **HTS1-midst** grain (Figure 25). In contrast, the **HTS1-rim** represents an intergrowth mixture of huttonite and thorite, with almost 50:50 ratio of both minerals crystallized (Figure 26). Additionally, element mapping revealed that the distribution of Ca overlaps with the undefined structure in the phase map (Figure 26c, d), suggesting the presence of Ca-rich phase in heated sample, which are possibly high-Ca-containing uraninite and rhombohedral $CaUO_4$ according to the results of XRD and Raman spectroscopy.

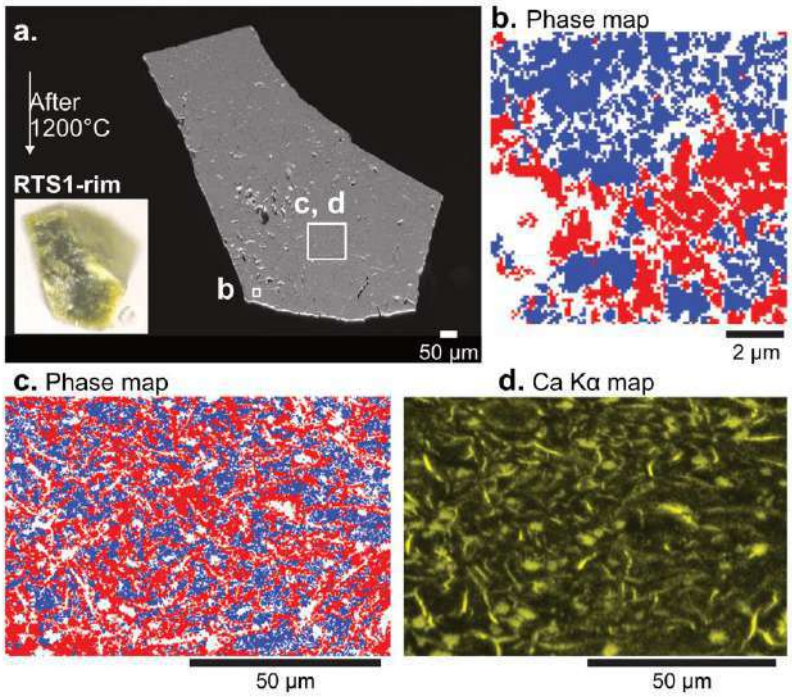

Figure 26. The photograph and BSE image of the **HTS1-rim** grain (a). The areas highlighted with white rectangles indicate areas for EBSD and elemental map. Phase maps of two selected areas (b,c). Huttonite is blue, and thorite is red. Ca*K*α elemental map of the selected area 'c' is shown in inset (d).

3.2.7 Differential scanning calorimetry (DSC)

Differential scanning calorimetry (DSC) was performed only for the most homogeneous specimen **MTS3**. DSC curves were first obtained for the metamict sample (1st cycle). After the crystallization, the thermal analysis was repeated (2nd cycle) using the same pellet (**HTS3**) (Figure 27). Observed effects are summarized in Table 14.

Table 14. Thermal effect observed in **MTS3** and subsequently in **HTS3** samples.

No.	Tentative assignment	1st Cycle (**MTS3**)			2nd Cycle (**HTS3**)			Thermal effect
		start	peak	end	start	peak	end	
Heating								
1	Surface water loss	79	161	272		-		endo
2	Water loss	466	494	584		-		endo
3	Crystallization of thorianite	829	871	906		-		exo
4	Crystallization of huttonite	906	952	1000		-		exo
5	Crystallization of rhombohedral $CaUO_4$	1039	1048	1089	~1040	1050	1068	exo
6	Partial melting	1167	1204	1222	1125	1214	1237	endo
Cooling								
7	Recrystallization	1205	1165	1088	1206	1167	1084	exo

Two endothermal peaks are observed in the temperature range below 600 °C, which can be attributed to dehydration and dehydroxylation. Subsequently, two exothermal peaks emerge at 871

°C and 952 °C, and correspond to the crystallization of thorianite and huttonite. The thermal effect observed at 1048 °C is due to the crystallization of rhombohedral $CaUO_4$. No peaks corresponding to the crystallization of thorite are observed. This phenomenon may be caused by several factors: 1. The exothermal annealing of thorite may be compensated by the endothermal dehydroxylation process; 2. The structural restoration process of the thorite phase begins after dehydration, but it proceeds very slow. This results in a lack of a prominent peak in the DSC curve.

The DSC curve for the **HTS3** sample does not exhibit any significant thermal effects.

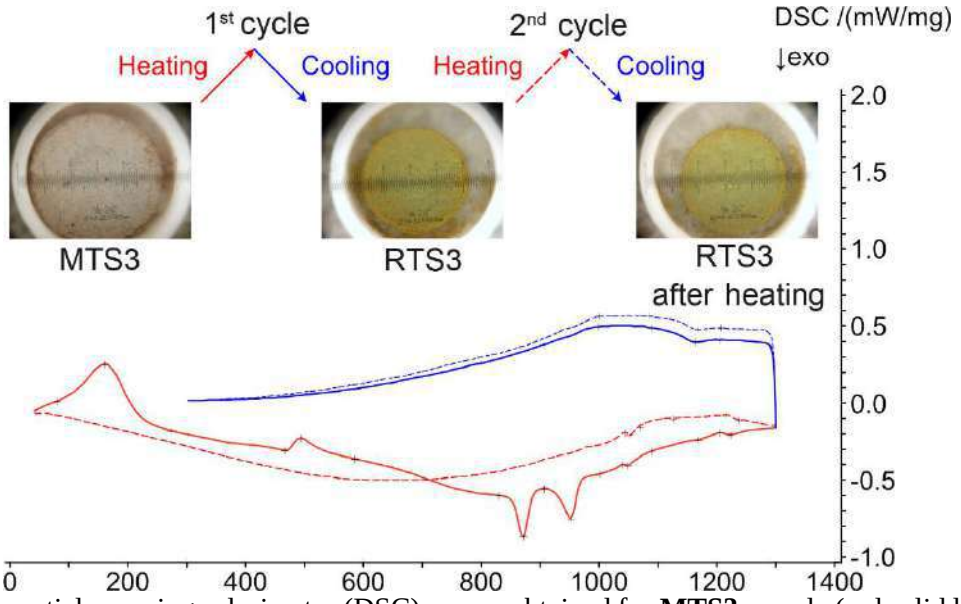

Figure 27. Differential scanning calorimetry (DSC) curves obtained for **MTS3** sample (red solid line) and **HTS3** sample (red dashed line) upon heating and corresponding curves obtained upon cooling (blue solid and dashed line, respectively. Color changes of pellets are shown in photographs above.

3.2.8 Thermal expansion of huttonite and thorite

High-temperature X-ray diffraction on crystalline samples **HTS1-midst** and **HTS3** was performed. Obtained coefficients of the thermal expansion (CTE) are listed in Table 15.

Table 15. CTE values for thorite and huttonite. Values are multiplied by 10^{-6}.

HTS1-midst				
Huttonite				
T, °C	50	400	800	1200
α_{11}	7.297(44)	7.899(19)	8.676(16)	9.564(41)
α_{22}	4.878(29)	5.414(13)	6.023(11)	6.627(28)
α_{33}	5.222(31)	6.087(15)	6.971(12)	7.728(33)
α_a	5.232(42)	6.094(19)	7.072(16)	8.042(41)
α_b	4.878(56)	5.414(25)	6.023(21)	6.627(55)
α_c	7.080(50)	7.828(23)	8.676(19)	9.514(49)
α_β	-0.423(23)	-0.130(10)	0.2050(90)	0.540(23)
α_V	17.40(11)	19.399(48)	21.670(40)	23.92(10)
Thorite				
T, °C	50	400	800	1200
$\alpha_{11}=\alpha_a$	2.471(56)	3.081(25)	3.776(21)	4.467(55)
$\alpha_{22}=\alpha_b$	2.471(47)	3.081(21)	3.776(18)	4.467(46)
$\alpha_{33}=\alpha_c$	4.646(47)	5.059(21)	5.529(18)	5.996(46)
α_V	9.59(12)	11.222(56)	13.081(47)	14.93(12)

Table 15. (Continued)

HTS3				
Huttonite				
T, °C	50	400	800	1200
α_{11}	6.771(93)	7.748(41)	8.895(38)	10.077(95)
α_{22}	5.042(69)	5.510(29)	6.042(26)	6.570(61)
α_{33}	4.692(64)	5.779(30)	6.971(30)	8.106(76)
α_a	4.692(69)	5.795(31)	7.047(28)	8.289(71)
α_b	5.04(14)	5.510(63)	6.042(59)	6.57(15)
α_c	6.634(56)	7.691(25)	8.888(23)	10.072(58)
α_β	-0.279(44)	-0.083(19)	0.141(18)	0.364(46)
α_V	16.51(23)	19.04(10)	21.909(94)	24.75(23)
Thorite				
T, °C	50	400	800	1200
$\alpha_{11}=\alpha_a$	2.980(84)	3.303(38)	3.672(31)	4.039(81)
$\alpha_{22}=\alpha_b$	2.980(95)	3.303(44)	3.672(36)	4.039(93)
$\alpha_{33}=\alpha_c$	4.910(95)	5.455(44)	6.074(36)	6.688(93)
α_V	10.87(22)	12.06(10)	13.418(83)	14.77(21)

Upon the temperature rise, the volume CTE increases from 9.47(13) to 14.93(12) × 10^{-6} °C^{-1} for thorite, and from 16.25(11) to 24.75(23) × 10^{-6} °C^{-1} for huttonite in the range of 25-1200 °C. Projections of the figures of CTE for huttonite and thorite are given in Figure 28.

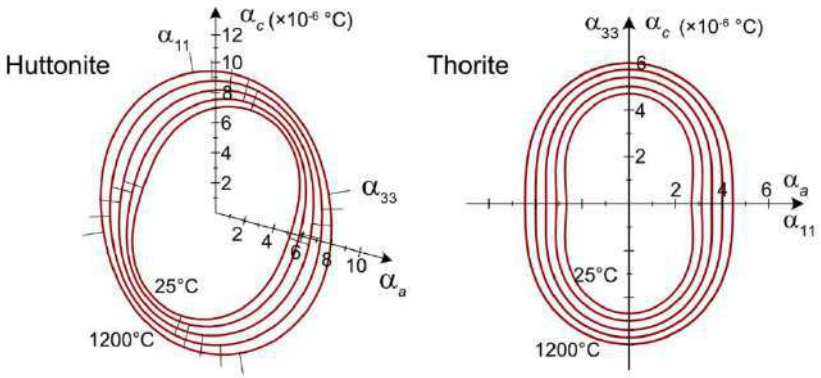

Figure 28. Projections of the CTE for huttonite and thorite in the temperature range 25 – 1200 °C.

3.2.9 Concluding remarks

Three metamict thorium silicate samples were studied employing Raman, EMPA, EBSD, DSC and HTXRD. It is worth noting that all metamict samples are heterogeneous. The chemical analyses show insufficient totals, implying that they are heavily hydrated and hydroxylated. Among all regions/grains of the metamict sample, **MTS1-core** shows the lowest degree of hydration and alteration, possibly being relics of a non-altered mineral. This assumption is also supported by its position in the cubic crystal, as **MTS1-core** is located in the core, surrounded by **MTS1-midst** and **MTS1-rim** in sequence. The composition variation indicates that the degree of alteration increases in the same sequence. **MTS3** appears as a hydrated and hydroxylated massive volume of yellow mineral, with a chemical composition similar to the altered regions of **MTS1**. Additionally, **MTS3** is visually similar to **MTS2-midst** areas. **MTS2** is differentiated from the other two samples by its elevated content of iron and uranium.

EMPA study reveals element redistributions after heating in all studied samples. **MTS2** is

characterized by the highest U content. Upon heating, the solid solution of $(Th,U)SiO_4$ exhibits a tendency to transform into uranium-depleted $ThSiO_4$, with the majority of the U concentration occurring in the fluorite-type phase. Powder X-ray diffraction patterns indicate the emergence of cubic fluorite-type phases at approximately 850 °C, followed by a decomposition and the emergence of the rhombohedral $CaUO_4$-type phase, which persists until 1200 °C and subsequent cooling. Rhombohedral $CaUO_4$-type phase, observed as a transformation product upon heating of the metamict sample, has not been reported to date as a mineral.

The proposed mechanism for the formation is that during heating, amorphous material undergoes recrystallization, which encompasses both the seeding stage and the crystal growth stage. This process results in the formation of chaotically oriented and fine-grained polycrystalline aggregates with elevated concentrations of Ca impurities on the grain boundaries.

The phase map of heat-treated grains shows a quenching texture. The main phases, thorite and huttonite, are proven to crystallize in fine sizes. Abundant elements crystallize in other phases, such as rhombohedral uranate calcium and uraninite-thorianite solid solution, filling the gaps between huttonite and thorite. Therefore, the crystallized thorium silicate does not show composition variation in between **HTS1**, **HTS2**, and **HTS3**. The elemental redistribution resulting from recrystallization indicates that the metamictization of these samples cannot be reversed by annealing.

During our *in situ* X-ray investigations, we observed the commencement of the crystallization process of thorite from the metamict sample at temperatures as low as ~400 °C. It is noteworthy that there is no thorite crystallization peak observed in the DSC curve, indicated that the process is sluggish. Thorite crystallization temperatures were previously reported in the range 715 – 950 °C for mineral samples [Eyal, Lumpkin, Ewing, 1986; Pabst, 1952]. The phase transition of thorite into huttonite was previously reported in the range 715 – 1400 °C [Finch, Harris, Clark, 1964; Mazeina et al., 2005; Pabst, 1952]. The crystallization temperature of huttonite revealed by in-situ HTXRD in this work is ~ 900 °C. the observed thorite-huttonite phase transition is slow, and both polymorphs can coexist in a wide temperature range. Impurities in the mineral samples may stabilize the thorite phase [Lumpkin, Chakoumakos, 1988; Meldrum et al., 1999b; Meldrum et al., 1999a]. Hence, it may potentially contribute to lowering the phase transition temperature.

The thermal expansion of huttonite crystallized from the natural metamict thorium silicate sample is comparable to that observed previously for the synthetic ones [Knyazev, Komshina, Savushkin, 2017]. In this study, we conducted HTXRD by employing a smaller temperature step of 30 °C. The increasing trend of the unit-cell parameters of huttonite (Figure 29) can be described by the second-order polynomials. The average $\alpha_{V,\text{huttonite}} = 20.66 \times 10^{-6}$ °C^{-1} for the temperature range 25-1200 °C. This value is significantly smaller than that observed for isostructural monazite ($\alpha_V = 27.4 \times 10^{-6}$ °C^{-1}, 25-700°C) [Asuvathraman, Kutty, 2014].

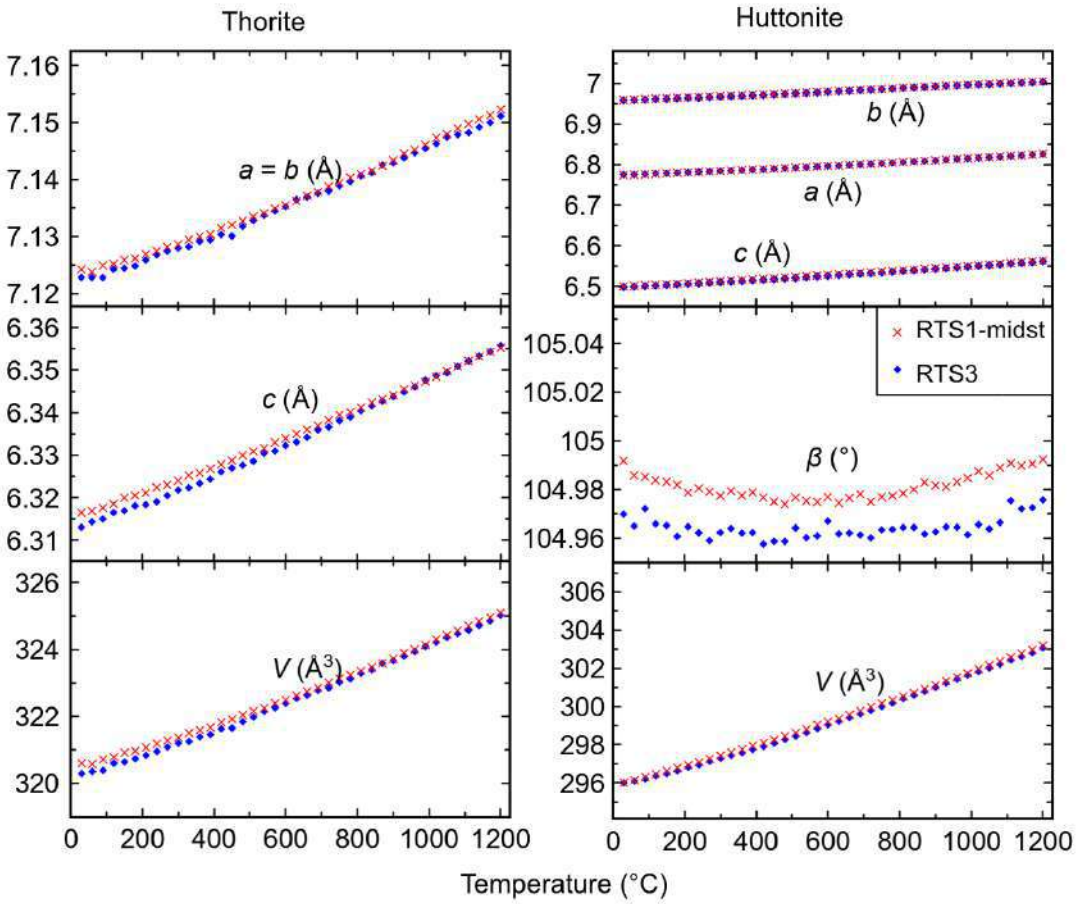

Figure 29. Temperature dependences of the unit-cell parameters and volume for thorite and huttonite from **HTS1-midst** and **HTS3** samples.

Recent calculations of the thermal expansion of synthetic thorite by Knyazev, Komshina, Savushkin [2017] and Strzelecki et al. [2021] exhibit some discrepancies with each other, possibly attributable to methodological variations. The unit-cell parameters of thorite (Figure 29) exhibit a linear trend upon heating. The thermal expansion of thorite shows the average $\alpha_{V,\text{thorite}} = 12.54 \times 10^{-6}$ °C^{-1} in the temperature range 25-1200 °C. It is similar to that one for the synthetic thorite ($\alpha_V = 12.1 \times 10^{-6}$ °C^{-1}, 25-900 °C) obtained earlier [Knyazev, Komshina, Savushkin, 2017]. Note, that the synthetic uranothorite has a significantly higher value of $\alpha_V = 17.21 \times 10^{-6}$ °C^{-1} in the temperature range 400-800 °C [Strzelecki et al., 2021]. The uranium in thorite structure increases the thermal expansion. In general, the thermal expansion of thorite is lesser than that of huttonite.

3.3 Fergusonite-(Y) [11]

The mineral sample originates from the Blyumovskaya Pit, Ilmeny Mountains, Southern Ural, Russia, previously existed collection of the radioactive minerals at the department of Mineral Deposits, Saint-Petersburg State University, Russia. The Blyumovskaya Pit is famous for its rare-earth mineralization. Fergusonite-(Y) in Blyumovskaya Pit, as well as other associated minerals like mica, samarskite, columbite, and monazite, is believed to form from metasomatic process [Belogub, Bazhenov, 1997].

[11] Fergusonite-(Y): $YNbO_4$, see 21.1.3. Space group (SG) of α-fergusonite: $I4_1/a$. SG of β-fergusonite: $C2/c$. Crystal structure see Figure 3.

Studied mineral sample was initially labeled as "yttrotantalite", but the chemical analyses proved that the dominant element is Nb, instead of Ta. The severe alteration of the sample also increased the difficulty for its identification. The sample investigated occurs as irregular grains with waxy to vitreous luster. The color is yellow-brown and the mineral shows conchoidal fracture (Figure 30). Mineral grains were hand-picked for the further investigation. After heating to 1200 °C the mineral turns bright yellow and opaque.

3.3.1 Chemical composition

Figure 31 shows the heterogeneity of an initial fergusonite grain, that is hydrated and heavily altered. The BSE images demonstrate the degree of the alteration; in the darker regions, the content of REE, Nb, and Ta is lower, while Si and Ca are incorporated into the matrix. Most of the bright dots revealed in BSE images can be identified as inclusions of galena PbS. Some larger irregularly shaped inclusions correspond to the uraninite UO_2.

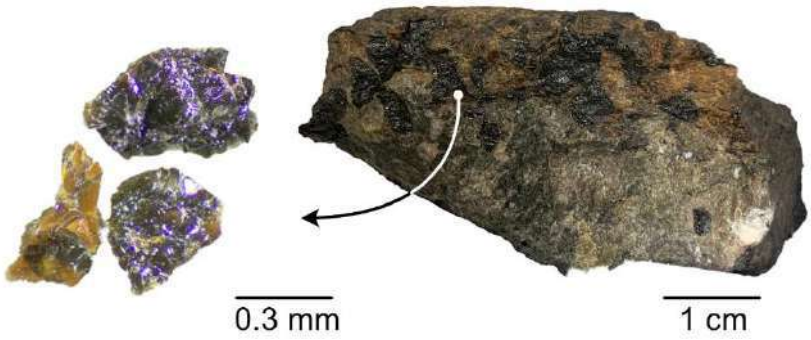

Figure 30. Fergusonite metamict grains and the rock sample.

Table 16 displays the chemical content of the metamict and heat treated fergusonite-(Y). The formula of metamict fergusonite is $(Y_{0.70}, Ln_{0.20}, Ca_{0.13}, U_{0.02}, Th_{0.02})_{\sum 1.07} (Nb_{0.72}, Ta_{0.17}, W_{0.06}, Ti_{0.04})_{\sum 1} (O_{3.97}, (OH)_{0.11}, F_{0.08}, Cl_{0.03}) \cdot 2.12H_2O$, calculated on the basis $B = 1$. The formula coefficient of hydroxyl group is calculated based on the charge balance. The content of water in the mineral is calculated from the results of the thermal analysis. TGA curve showed a 7.24 % weight loss, which corresponds to the average difference between the EMPA analytical total and 100%. After heating up to 1200 °C, the mineral grains became more homogeneous and porous, however many cracks appeared.

The heated sample has the formula $(Y_{0.64}Ln_{0.17}Ca_{0.14}U_{0.02}Th_{0.01})_{\sum 0.98} (Nb_{0.74}Ta_{0.13}W_{0.06}Ti_{0.05})_{\sum 1} O_{3.92}$, the metamict water, fluorine and chlorine was expelled from the structure after heating.

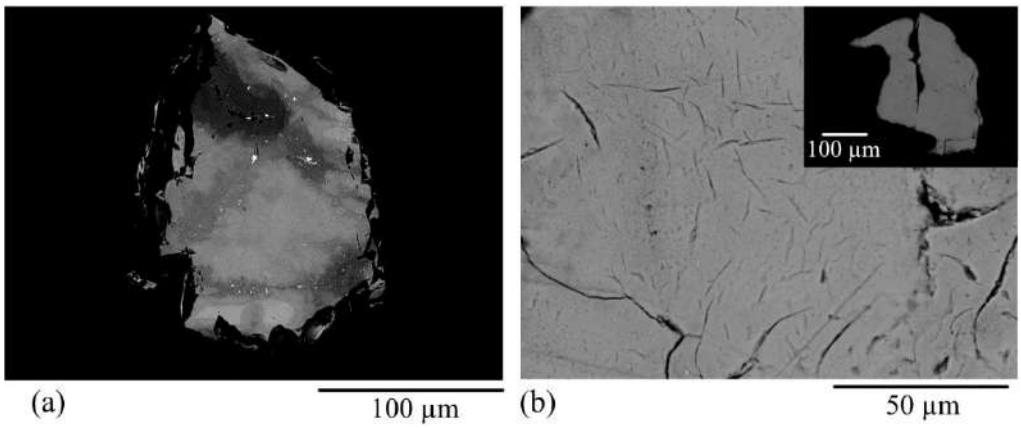

Figure 31. BSE images of two grains of (a) the metamict and (b) annealed fergusonite-(Y). The compositional zoning in metamict grains is significantly erased after heating. The induced volume changes produce fissures that can be observed at an enlarged scale of heated grains.

Table 16. Chemical composition of fergusonite-(Y) from the Blyumovskaya Pit, Urals, Russia.

Oxides wt. %	Metamict fergusonite			Heated fergusonite			*a.p.f.u*	Initial fgs.	Heated fgs.
	average	range	deviation	average	range	deviation			
CaO	2.28	2.04-2.44	0.15	2.09	1.79-2.68	0.35	Ca	0.13	0.14
TiO_2	1.13	0.96-1.41	0.17	1.21	0.93-1.68	0.28	Y	0.70	0.64
Y_2O_3	25.37	25.18-25.49	0.00	28.05	27.34-28.51	0.00	Th	0.02	0.01
Nb_2O_5	30.59	29.95-30.8	0.11	33.76	32.68-34.35	0.46	U	0.02	0.02
Nd_2O_3	0.19	0-0.34	0.32	0.19	0-0.38	0.67	Nd	0.00	0
Sm_2O_3	0.59	0-0.87	0.01	0.67	0.47-0.88	0.01	Sm	0.01	0.01
Gd_2O_3	1.71	1.49-1.82	0.01	1.77	1.51-2.06	0.01	Gd	0.03	0.02
Dy_2O_3	3.40	3.13-3.56	0.16	3.48	3.27-3.63	0.19	Dy	0.06	0.05
Er_2O_3	2.75	2.48-3.01	0.32	2.88	2.73-3.02	0.15	Er	0.05	0.04
Yb_2O_3	3.47	2.9-3.85	0.12	4.12	3.55-4.42	0.20	Yb	0.06	0.05
Ta_2O_5	11.97	11.54-12.6	0.15	12.58	11.71-13.11	0.14	$\sum A$ =	0.97	0.98
WO_3	4.80	3.99-5.98	0.21	5.47	4.12-6.38	0.12	Ti	0.04	0.05
ThO_2	1.78	1.17-2.37	0.36	1.54	1.22-1.71	0.34	Nb	0.72	0.74
UO_2	1.81	1.41-2.05	0.37	1.87	1.59-2.37	0.55	Ta	0.17	0.15
Total	91.83	90.58-93.07	0.74	99.66	99.13-100.59	0.91	W	0.06	0.06
F	0.49						$\sum B$ =	1	1
Cl	0.32						O	3.97	3.92
Total	99.07						F	0.08	-
H_2O(*)	6.42						Cl	0.03	-
$O=F_2$	0.65						(OH)	0.11	-
$O=Cl_2$	0.23						H_2O	2.12	-
Total	97.37								

* Water's weight percentage was determined via mass difference in the thermal gravity curve.

3.3.2 Raman spectroscopy

The Raman spectrum of the metamict fergusonite-(Y) is demonstrated in Figure 32. The observed intensive band at 814 cm^{-1} is attributed to the stretching modes of the NbO_4 tetrahedra [Blasse, 1973]. The modes observed at around 298 cm^{-1} can be assigned to the external vibrations of

a tetrahedral unit. The broad water bands in the range of 3000-3500 cm^{-1} indicate that the metamict fergusonite-(Y) is hydrated. The bands of H-O-H bending vibrations of H_2O molecules, often observed in the range 1600–1700 cm^{-1}, are not observed.

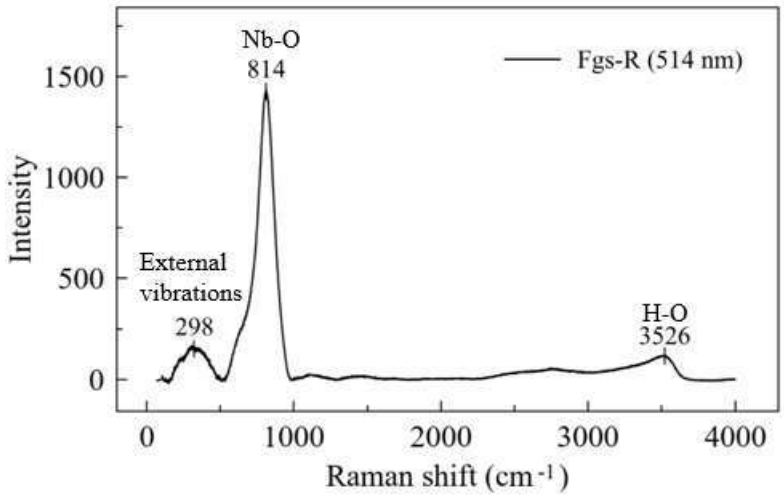

Figure 32. Raman spectra of the metamict fergusonite (laser wavelength 514 nm).

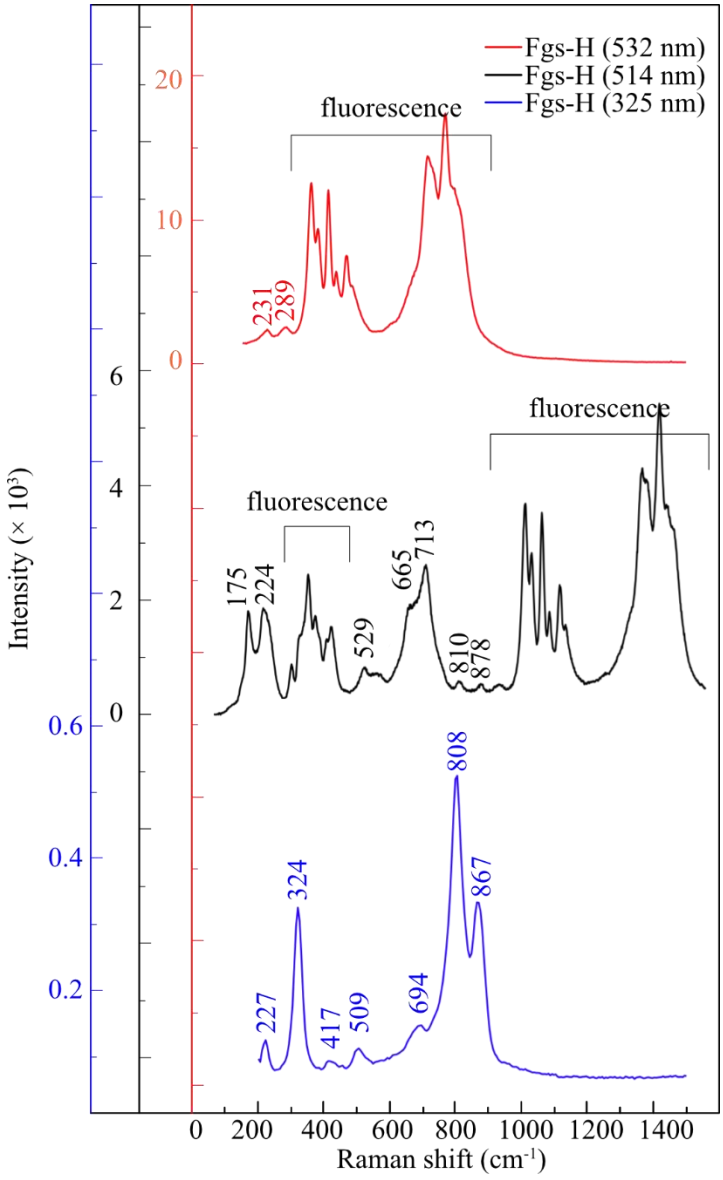

Figure 33. Raman spectra of ignited fergusonite measured with 325, 514, and 532 nm laser (down up).

The three Raman spectra of the heat treated fergusonite differ in intensity of the Raman bands

(Figure 33). We note that the obtained spectra of the crystalline fergusonite-(Y) are more susceptible to the excitation laser wavelength, compared with that of the metamict sample. Many luminescence lines are observed in the spectra of heated fergusonite. The luminescence lines are shifted by the difference between the frequencies of the excitation lasers. We avoided the luminescence lines by using a shorter wavelength – 325 nm laser, but the signal/noise ratio and the spectral resolution are simultaneously decreased.

Tomašić et al. [2006] recorded Raman spectra for the heat treated fergusonites from Norway and Sweden (Fer-BS and Fer-YT in Table 17). Yashima et al. [1997] also investigated the synthetic $YNbO_4$ by the Raman spectroscopy. The obtained Raman spectrum of fergusonite-(Y) from the Blyumovskaya Pit is generally in good agreement with the previously studied fergusonites from Norway and Sweden. Bands at 350-400 cm^{-1} are attributed to Y-O vibrations, and peaks at 540 cm^{-1} are assigned to Ta-O vibrations. The peaks at 100-230 cm^{-1} are due to the external vibrations. Bands in the region of 600-900 cm^{-1} can be assigned to Nb(Ti, Ta)-O internal vibrations.

Table 17. Raman bands excited by 325 nm, 514 nm and 532 nm lasers on metamict and heated fergusonite and comparison with literature data.

Raman shift (cm^{-1})						Assignment			
Fgs-R *325 nm*	**Fgs-R** *514.5 nm*	**Fgs-R** *532 nm*	**Fgs-H** *325 nm*	**Fgs-H** *514.5 nm*	**Fgs-H** *532 nm*	Fer-BS *514.5 nm*	Fer-YT *514.5 nm*	$YNbO_4$	
		93					105		External vibrations
						129		131	
				175		174	164	166	
	215		**227**	**224**	**231**	218	218	213	
297	**298**				**289**		296		
			324			326	324	324	symmetric bending
				331		335	331	336	
		365		**355**		356	350		Asymmetric bending
	392			**381**	**365**	374	370	381	
			417	**429**	**418**	426	425	420	
					475	462		465	Asymmetric stretching
			509	**529**		523			
		582		**567**		559	559		
	663			**665**		658	657	658	
				667		673			
						692			Symmetric stretching
			694	**713**	**719**	707	714		
				754	**774**				
802	**814**	**806**	**808**	**810**		810	816	811	
			867	**878**			878		
							924		
O–H stretching of water molecules:									
3489	**3526**	**3521**							

3.3.3 Recrystallization of fergusonite-(Y)

Figure 34 shows TG, DSC curves and the ion current curves from the ions of masses 18, 19 (H_2O and F). After the heating and the subsequent cooling, the sample was examined by XRD. The sample contained the following phases (R_{wp}=8.097%): 88.3% β-fergusonite (ICSD-100176), 5.7% pyrochlore (ICSD-173054), 2.6% fersmite (ICSD-77474), 1.9% α-fergusonite (ICSD-414675) and 1.6% uraninite (ICSD-160815). Residual α-fergusonite may present because of a quick cooling process that prevented complete conversion to the β-fergusonite.

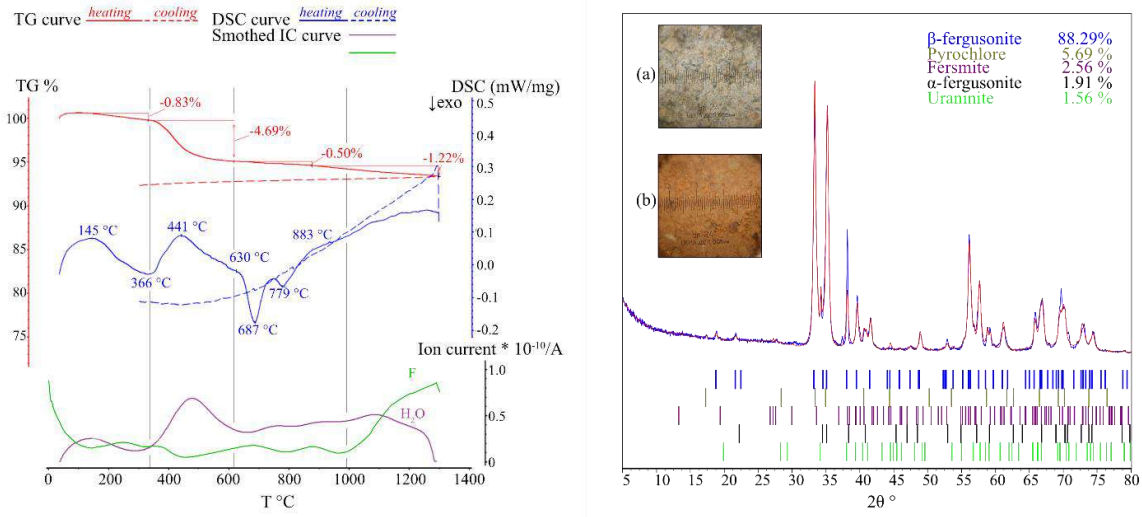

Figure 34. TG, DSC and ion current (IC of mass 18 and 19) curves of the metamict fergusonite-(Y) heated to 1300 °C (left). The XRD of sample after thermal analysis (right). Photographs (FOV 2 mm for each) of the powder sample before (a) and after (b) thermal analysis are shown as an inset to the right.

Due to the loss of the both adsorbed and crystallization water during the heating, the sample continuously loses its weight. The TG curve indicates 3 main steps of the mass loss: 25-350 °C, 350-650°C and 650-1300 °C. The main dehydration stage occurs at 350-650 °C, which corresponds to the ion spike of H_2O. The ion current of mass 18 bursts over the same temperature range.

The DSC curve demonstrates that endothermic reaction involving dehydration occurs at temperatures ranging from 25 °C to 366 °C and 366 °C to 630 °C. The exothermal peaks at 687 °C and 779 °C exhibit recrystallization of the metamict fergusonite and other minor associated phases (e.g. pyrochlore). This observation is in a very good agreement with the fergusonite crystallization temperature above 650 °C obtained by the powder HTXRD. The upward of the DSC curve after 883 °C suggests an endothermic process that may involve a decomposition reaction [Ho, Kuo, Hopper, 2000]. This observation related to decomposition and correlates with the explosion of the F ion after 1000 °C.

Figure 35 displays the recrystallization process of the metamict fergusonite at high temperatures. The crystallization starts above 400 °C, when some weak peaks appear on the X-ray diffraction pattern, however the overall crystallinity of the sample is still poor. The peaks rise significantly with the temperature. XRD pattern also reveals the crystallization of the impurity phase with pyrochlore structure. The sample crystallizes in a tetragonal scheelite-type (*α* [Komkov, 1959]) at high temperatures. However, the structure transforms into the monoclinic *β*-fergusonite after

cooling.

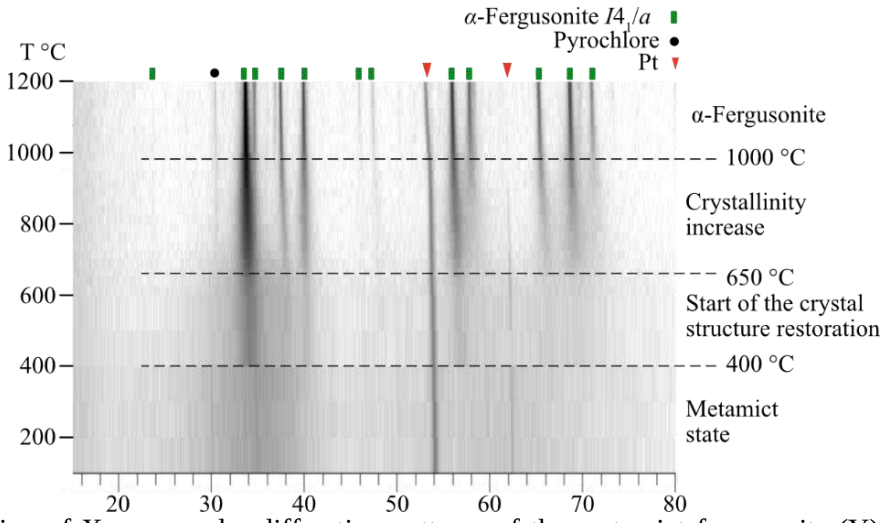

Figure 35. Evolution of X-ray powder diffraction patterns of the metamict fergusonite-(Y) in the range 100–1200 °C. There is no evidence of recrystallization until 400 °C. Four main stages of the transformation are bordered by the dashed lines.

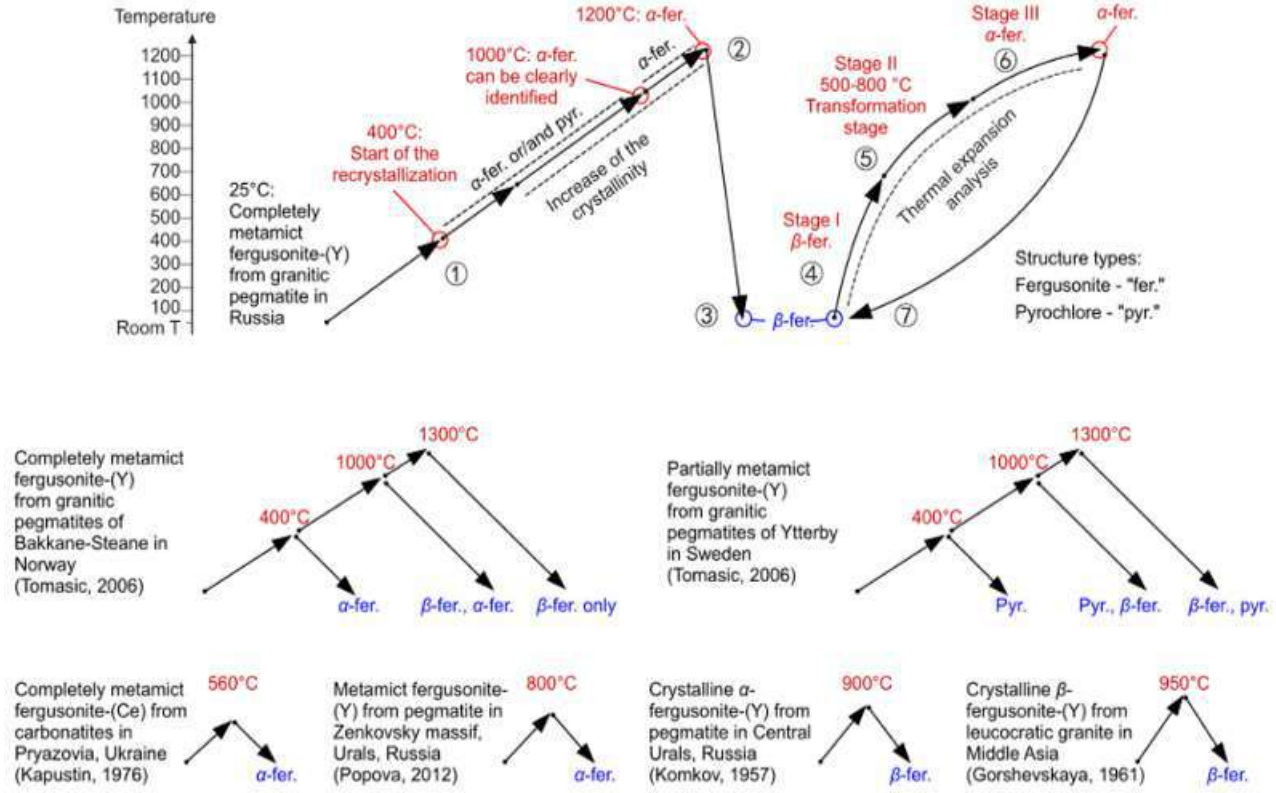

Figure 36**.** Schematic diagram of the thermal evolution of fergusonite-(Y) observed in this study (above): (1) When crystallization begins, the metamict sample is heated to 400 °C; (2) the temperature is raised to 1200 °C, and the "hot" sample is identified as α-fergusonite; (3) after cooling, only β-fergusonite is observed in the "cold" sample; (4) the "cold" β-fergusonite is gradually heated to (5) a 500-800 °C temperature range; (6) α-fergusonite was observed in the range of 800-1200°C; and (7) the cooling resulted in the transformation back to β-fergusonite. Previous studies are summarized below.

In previous research, totally or partially metamict fergusonites were annealed in the range 400-800 °C [Popova et al., 2012; Tomašić et al., 2006]. Some experiments were carried out on the mineral samples in the temperature range 900-1300 °C [Gorzhevskaya, Sidorenko, Smorchkov, 1961; Komkov, 1959; Tomašić et al., 2006]. The experimental conditions and annealed products are shown in Figure 36. Summarizing the results of these experiments, one can conclude that the final restored

structure depends on the employed temperature. At low temperatures, the tetragonal α-fergusonite is recovered. However, when heated to the higher temperatures 900-1300 °C the β-fergusonite is obtained.

3.3.4 Thermal expansion

The crystalline fergusonite-(Y), obtained after the heat treatment, was further investigated by the means of HTXRD to estimate the thermal expansion.

Figure 37 shows three stages of the structural transformation. At low temperatures, the *β*-fergusonite is dominant. The transformation starts at about 500 °C. This observation is also supported by the parametric curve's inflection point at 500 °C (Figure 38). The α-fergusonite is present in the XRD spectrum at temperatures above 850 °C. The phase transition between *β*- and *α*-fergusonites is reversible transformation of second order. The *β*-fergusonite reverts to being the dominant phase after cooling.

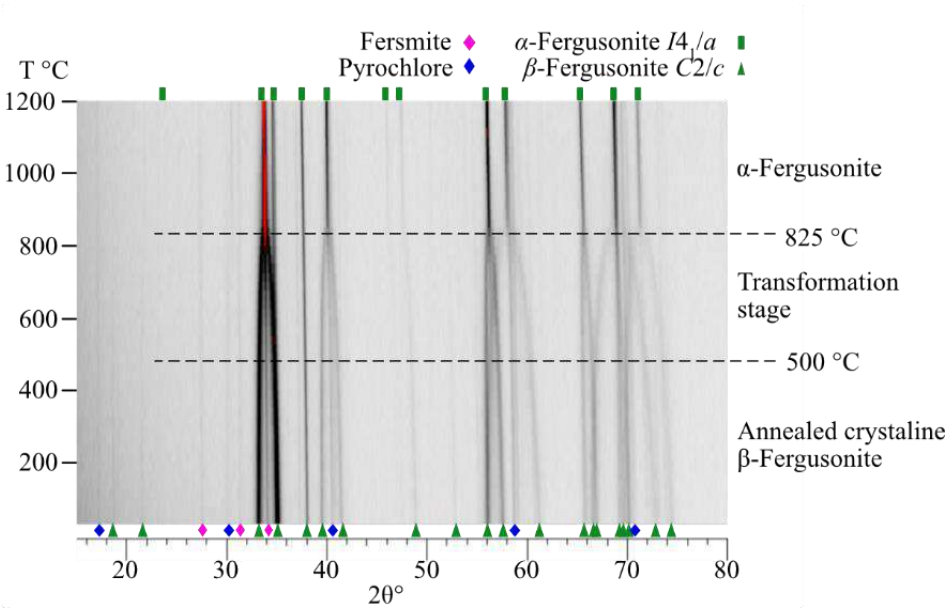

Figure 37. Evolution of X-ray powder diffraction patterns of the recrystallized β-fergusonite-(Y) in the range 100–1200 °C. The tetragonal structure appears above 800 °C, but the rearrangement process is assumed to start at ~ 500 °C. Some impurities – pyrochlore (ICSD-173054) and fersmite (ICSD-77474) are observed and remain intact throughout the heating.

Figure 38 displays the temperature dependence of the unit cell parameters for both phases. In accordance with the three stages of the structural transformation, these curves are split into three parts. The second-order polynomials were applied to fit these curves.

Stage I. In the temperature range of 25-500 °C, the sample has a monoclinic structure:

$a(T) = 7.03(38) + 0.\ 12(23)\cdot10^{-3}\cdot T + 0.17(28)\cdot10^{-6}\cdot T^2$

$b(T) = 10.96\ (21) + 0.\ 14(12)\cdot10^{-3}\cdot T - 0.01(14)\cdot10^{-6}\cdot T^2$

$c(T) = 5.30(12) + 0.03(35)\cdot10^{-3}\cdot T - 0.\ 06(86)\cdot10^{-6}\cdot T^2$

$\beta(T) = 134.12(74) + 0.46(41)\cdot10^{-3}\cdot T + 0.21(50)\cdot10^{-6}\cdot T^2$

$V(T) = 293.51(47) + 8.29(42)\cdot10^{-3}\cdot T + 2.28(76)\cdot10^{-6}\cdot T^2$

Stage II. At a temperature of 500-825 °C, phase transformation occurs, however the structure

is still considered as a monoclinic:

$a(T) = 7.40(33) - 1.\ 18(10)\cdot10^{-3}\cdot T + 0.32(79)\cdot10^{-6}\cdot T^2$

$b(T) = 11.06\ (23) - 0.\ 26\ (71)\cdot10^{-3}\cdot T + 0.39(54)\cdot10^{-6}\cdot T^2$

$c(T) = 5.16(95) + 0.49(29)\cdot10^{-3}\cdot T - 0.\ 44(22)\cdot10^{-6}\cdot T^2$

$\beta(T) = 134.38(14) - 0.74(43)\cdot10^{-3}\cdot T + 1.58(32)\cdot10^{-6}\cdot T^2$

$V(T) = 301.85(41) - 24.2(13)\cdot10^{-3}\cdot T + 32.3(96)\cdot10^{-6}\cdot T^2$

Stage III. In the temperature range 850-1200 °C, the sample is tetragonal:

$a(T) = 5.20\ (69) - 0.001(13)\cdot10^{-3}\cdot T + 0.02(65)\cdot10^{-6}\cdot T^2$

$c\ (T) = 10.93(12) + 0.16(24)\cdot10^{-3}\cdot T - 0.001(11)\cdot10^{-6}\cdot T^2$

$V(T) = 296.22(38) + 4.11(83)\cdot10^{-3}\cdot T + 2.32(26)\cdot10^{-6}\cdot T^2$

The schematic diagram of two-unit cells in Figure 38 shows their relationships. b_{mon} in the monoclinic unit cell can be taken as the height of a parallelogram prism placed vertically. As the volume increases (temperature increases), the b_{mon} increases and finally becomes the c_{tet} in a tetragonal lattice (the lattice type is indicated by the subscripts). The monoclinic angle β is expanding from 134.1 ° to almost 135° (=90°+45°); it is inherited by the diagonal of the square $a_{tet}\times\sqrt{2}$ in the tetragonal unit cell. The parameter a_{mon} increases with the decrease of the c_{mon} and finally becomes identical to the a_{tet} at the phase transition point.

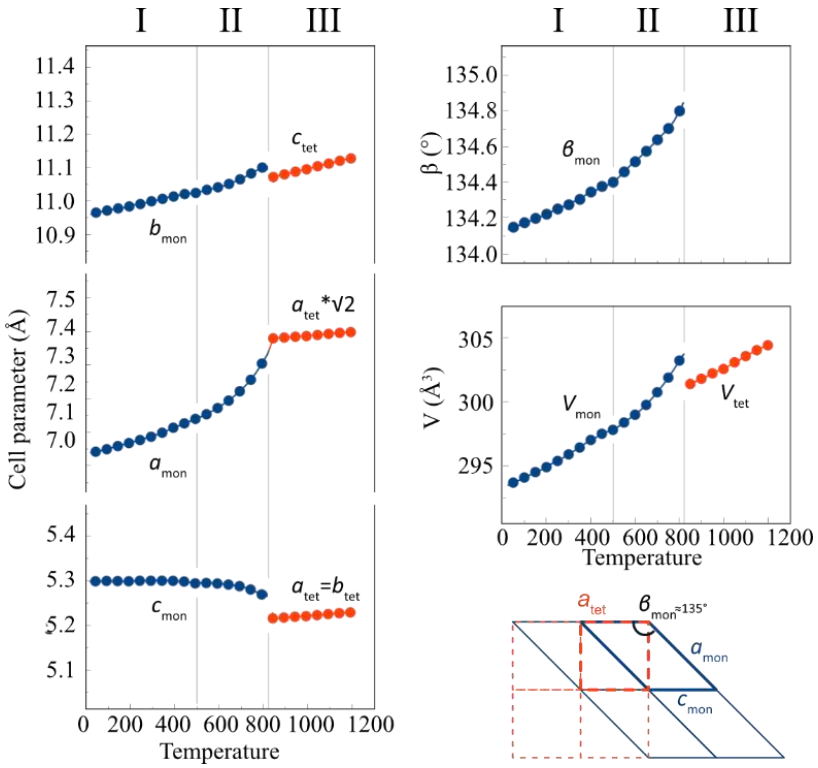

Figure 38. Temperature dependences of the unit-cell parameters and volume. The three stages of the transformation are highlighted by I, II, III. Blue and red colors indicate the monoclinic and tetragonal phases, respectively. The scheme below demonstrates the relationships between the tetragonal and monoclinic unit cells in α- and β-fergusonite-(Y).

The coefficients of the thermal expansion were also determined in the three temperature ranges 25-500, 500-825 and 850-1200 °C (Table 18, Table 19). And the figures of the coefficients of thermal expansion (CTE) are shown in Figure 39 [Chen et al., 2024a].

Table 18. The thermal expansion tensor parameters of monoclinic fergusonite at different temperatures, which are divided into two parts, correspond with the two-segment blue curves in Figure 38.

CTE (× 10^{-6} ºC^{-1})	in the temperature ranges of 25-500 ºC				and 500-850 ºC			
T,°C	25	200	400	500	525	650	750	850
α_{11}	19.07(86)	28.86(44)	40.24(92)	45.9(1.6)	29.24(82)	83.55(41)	127.3(1)	170.0(2)
$\alpha_{22} = \alpha_b$	12.90(58)	12.59(19)	12.24(28)	12.07(43)	13.18(37)	22.02(11)	29.03(23)	35.99(44)
α_{33}	-3.30(15)	-10.24(16)	-18.50(43)	-22.69(81)	-9.78(27)	-45.84(23)	-76.01(61)	-106.6(1)
α_a	18.75(58)	27.09(21)	36.48(36)	41.10(58)	29.0(3.1)	74.75(100)	110.5(2.2)	145.1(4.2)
α_c	4.9(1)	0.71(40)	-4.09(65)	-6.5(1)	6.1(1.1)	-14.54(38)	-31.16(84)	-47.9(1.6)
$\angle(\alpha_{11}, \alpha_a)$	6.9°	12.3°	14.6°	15.3°	4.7°	15.1°	16.7°	17.5°
$\angle(\alpha_{22}, \alpha_b)$	0°	0°	0°	0°	0°	0°	0°	0°
$\angle(\alpha_{33}, \alpha_c)$	37.3°	31.9°	29.7°	29.1°	39.7°	29.5°	28°	27.4°
α_V	28.7(1.2)	31.22(48)	33.98(78)	35.3(1.2)	32.64(92)	59.73(29)	80.30(64)	99.4(1.2)

Table 19. The thermal expansion tensor parameters of tetragonal polymorphs at different temperatures.

CTE of tetragonal fergusonite (× 10^{-6} ºC^{-1})					
T,°C	850	900	1000	1100	1200
$\alpha_{11} = \alpha_c$	14.56(48)	14.54(36)	14.51(15)	14.47(19)	14.44(42)
$\alpha_{22} = \alpha_b$	6.09(40)	6.46(30)	7.21(12)	7.95(16)	8.69(34)
$\alpha_{33} = \alpha_a$	6.09(40)	6.46(30)	7.21(12)	7.95(16)	8.69(34)
$\angle(\alpha_{11}, \alpha_a)$	90°	90°	90°	90°	90°
$\angle(\alpha_{22}, \alpha_b)$	0°	0°	0°	0°	0°
$\angle(\alpha_{33}, \alpha_c)$	90°	90°	90°	90°	90°
α_V	26.7(1.3)	27.47(100)	28.92(41)	30.37(53)	31.8(1.1)

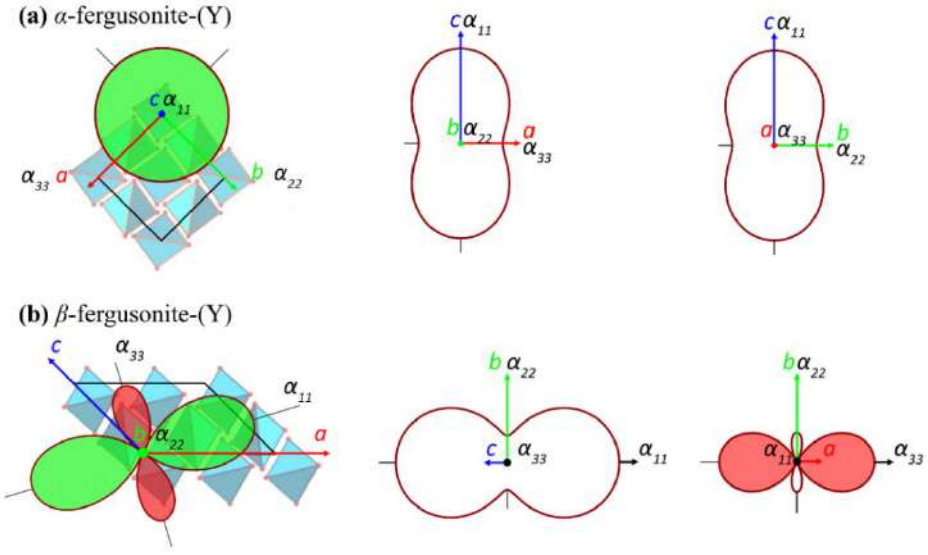

Figure 39. Pole figures of the thermal expansion coefficients of α- (a) and β-fergusonite-(Y) (b). Negative thermal expansion is highlighted in red.

The thermal expansion of *β*-fergusonite-(Y) is highly anisotropic. Along the α_{33} axis the expansion is negative, and along the α_{11} axis there is a significant expansion. This is due to the contraction of the lattice along the long diagonal and expansion along the short diagonal during the transformation of *β* into *α*-fergusonite Figure 39. In the tetragonal structure, in the range of 850-1200 °C, the main axes of the thermal expansion tensor coincide with the crystallographic axes (Table

19). The maximum thermal expansion occurs along the *c*-axis: $\alpha_{11} = \alpha_c$, while the thermal expansion in the *ab*-plane is isotropic: $\alpha_{22} = \alpha_b = \alpha_{33} = \alpha_a$.

3.3.5 Radioactivity of metamict and annealed fergusonite-(Y)

The measured specific activities of radionuclides in the metamict sample are: ^{232}Th - 72.2 Bq/g, ^{226}Ra - 347 Bq/g, and the total gamma-radioactivity is 452 Bq/g. The alpha-beta emission measurements revealed that the alpha activity of fergusonite-(Y) is 215.6±15, and the beta activity is 1061.8±33 Bq/g.

After heating the same sample in Nabertherm oven in air at 1100 °C for 24 hours, the radioactivity was measured again: the specific activity of ^{226}Ra decreased by the almost 37% down to 220 Bq/g, and the activity of ^{232}Th also decreased by 17% to 55.7 Bq/g. The total gamma radioactivity of the sample became 313 Bq/g. Alpha activity and beta activity of the annealed sample of fergusonite has also decreased by 21% and 9% down to 170.88 and 971.53 Bq/g, respectively.

The decrease in the radioactivity in a bulk mineral sample after heating may be caused by the loss of radioactive isotopes. At high temperatures, some of the radioactive elements may evaporate and escape from the sample [Yang et al., 2005]. We assume that some of the radioactive elements in the metamict mineral grains are adsorbed in the form of aqueous complexes in nanometer sized pores, which could not be detected by the electron microprobe analysis. Upon heating, such complexes are released. For instance, uranium[Ho, Kuo, Hopper, 2000], radon[Giletti, Kulp, 1955].

3.3.6 Remarks for subsection

A series of ceramics with fergusonite-type structure were described previously (Figure 40) [Sarin et al., 2014; Yang et al., 2020; Zhang et al., 2020]. These studies covered a temperature range including the phase transition from *β*- to *α*-fergusonite. Zhang et al., [2020] and Yang et al., [2020] used dilatometry and thermomechanical analysis, respectively, to obtain average CTE values for various fergusonite-type compounds. However, it should be noted that these methods may exhibit reduced accuracy when applied to crystal structures with low symmetry, especially those that exhibit negative thermal expansion as temperature increases. Our results are generally consistent with the results described in [Sarin et al., 2014].

In Figure 40, all $REENbO_4$ compounds (REE = Y, La, Nd, Sm, Gd, Dy, Er, Yb) show an increasing CTE of monoclinic structure, and then significantly lower values after the transformation. The phase transformation temperature depending on the REE type varies from 670 °C to 858 °C. The phase transformation temperature of our natural sample is 825 °C, which is slightly lower than for pure synthetic $YNbO_4$ (858 °C) [Sarin et al., 2014]. A general trend is observed indicating that CTE tends to decrease with decreasing REE radii.

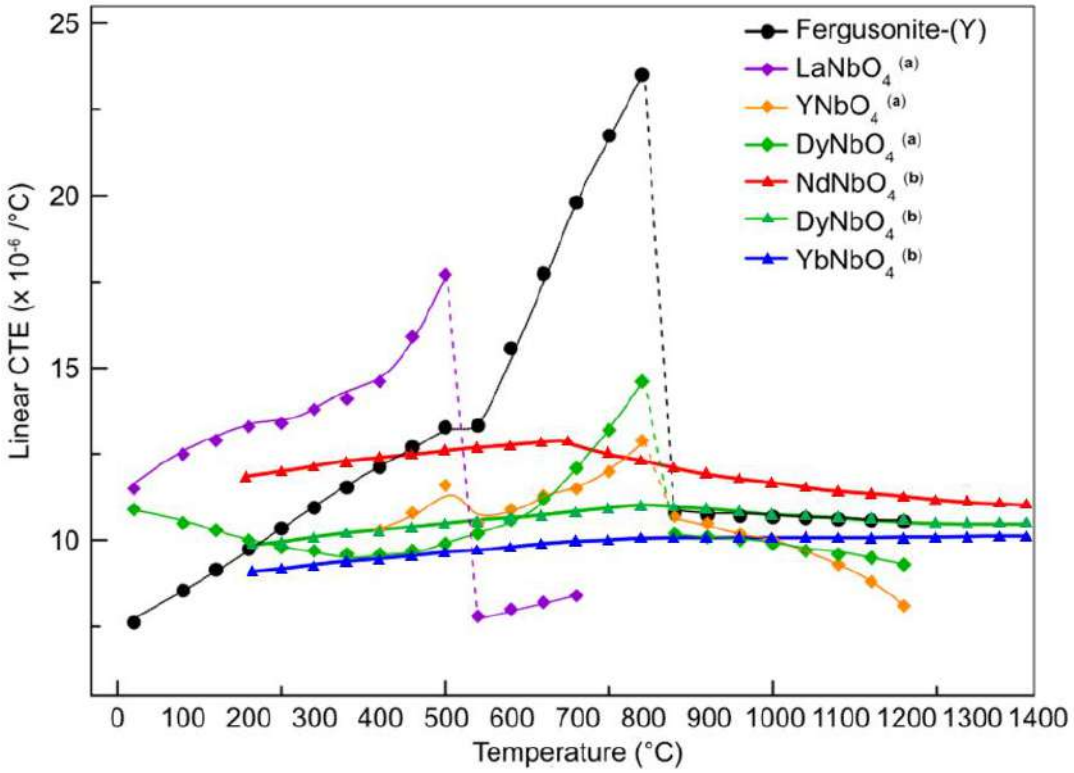

Figure 40**.** Temperature dependences of the average CTE (calculated as the average value of α_{11}, α_{22} and α_{33}) for the mineral sample of fergusonite-(Y) studied in this work (black) and the synthetic reference phases described in [Sarin et al., 2014] (a) and [Zhang et al., 2020] (b).

The expansion coefficient of volume of β-fergusonite-(Y), studied in this work, is more sensitive to the temperature rise and varies in a broader range of 28.7-99.4 $\cdot 10^{-6}$ °C^{-1} (50-850 °C). It is assumed that the CTEs are significantly enlarged due to the complex composition of the mineral sample, which introduces lattice anharmonicity [Zhang et al., 2020]. The increasing average atom radii also contributes to the increase of CTEs. The strong anisotropy of fergusonite's expansion may contribute to the mechanical stress in the container due to the mismatch of the thermal expansion coefficients of the ceramics and the canister.

The prevailing consensus is that the chemical stability of matrices based on Ti-Zr-Nb associations in oxides is higher. The thermal expansion of fergusonite is compared and assessed in this work. The thermal expansion coefficient of monoclinic fergusonite varied considerably. In contrast, fergusonite in scheelite type has a relatively constant thermal expansion coefficient, which suggests that the crystal structure significantly influences the material's thermal properties.

3.4 Samarskite-(Y)[12]

The studied sample is a massive rock consisting mainly of the black mineral samarskite. The unheated sample used in this study is a metamict rock called **MS**, which have a metallic luster and a conchoidal fracture (Figure 41). The sample is originated from the Black Cloud Mine, Colorado, USA.

[12] Samarskite-(Y): $YFeNb_2O_8$. Space group: *P*2/*c*. Crystal structure see Figure 4.

Figure 41. Rock sample of metamict samarskite-(Y), which is black with metallic luster and a conchoidal fracture, from the Black Cloud Mine, Colorado, USA.

3.4.1 Chemical analysis before heat-treatment

The Back Scattering Electron (BSE) images are shown in Figure 42. In comparison with samarskite from Lachersee, and samarskite from the Ilmeny Mountains [Britvin et al., 2019, the sample studied in this work demonstrate higher contents of scandium, calcium, but lower REE on average, see Table 20.

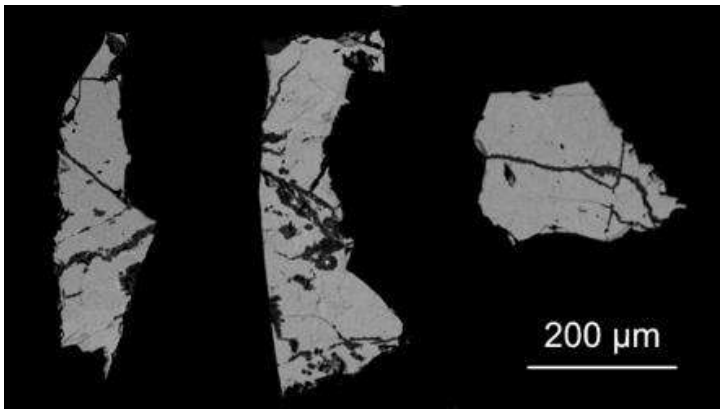

Figure 42. The Back Scattering Electron (BSE) images of unheated samarskite grains **MS**.

The analyses total ranges from 95 to 99%, with average value of 98% wt (Table 20). In Figure 43a, hydrothermal alteration can be observed along cracks of grains. The average contents of Ta_2O_5, Nb_2O_5, Fe_2O_3 and TiO_2 decrease from the main volume hydrothermal altered zone, and the average value of SiO_2, on the contrary, increases.

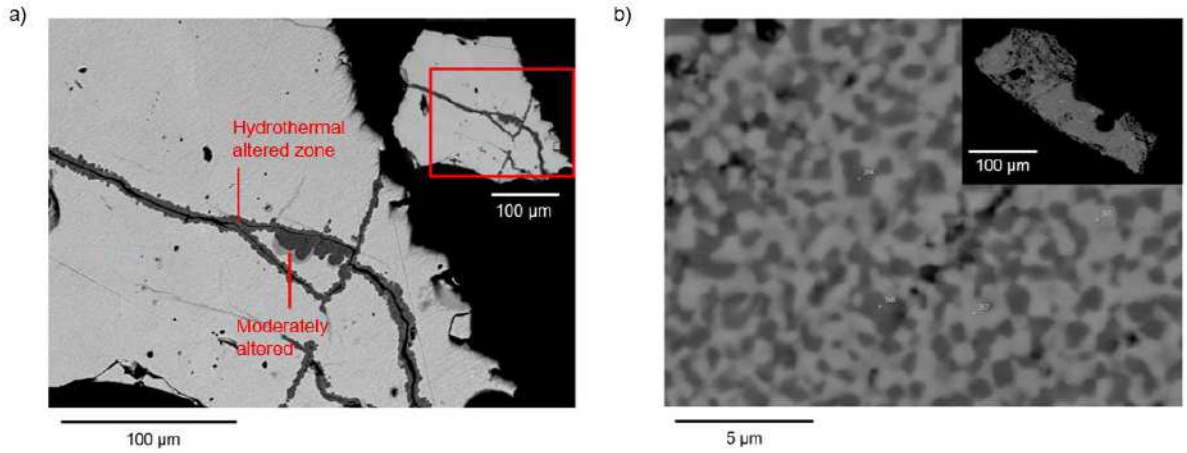

Figure 43. BSE images of a) metamict sample **MS** and b) heated sample **HS**.

Table 20. Chemical composition and atom per formula unit (*a.p.f.u.*) of **MS** and comparison with reference data: "Samarskite-1" taken from Lachersee, Germany, "Samarskite-2" from Blyumovskaya mine, Russia [Britvin et al., 2019].

	Samarskite1	Samarskite2	Sample **MS**			
Compounds	Wt.%	Wt.%	Av. wt.%	Deviation	Element	*a.p.f.u.*
CaO	0.36	-	0.22	0.06	Y	0.56
Sc_2O_3	-	-	0.67	0.09	Sc	0.05
Y_2O_3	5.3	6.42	13.06	0.29	Nd	0.01
La_2O_3	0.18	0.07	-		Sm	0.02
Ce_2O_3	0.88	0.22	-		Gd	0.03
Pr_2O_3	0.12	0.09	-		Dy	0.04
Nd_2O_3	0.66	0.29	0.51	0.08	Er	0.01
Sm_2O_3	0.34	0.49	0.72	0.12	Yb	0.02
Eu_2O_3	0.15	0.12	-		Th	0.06
Gd_2O_3	0.48	0.48	1.16	0.2	U	0.16
Tb_2O_3	-	0.1	-		Ca	0.02
Dy_2O_3	1.35	1.59	1.34	0.29	Σ	0.98
Ho_2O_3	0.29	0.79	-		Fe	0.71
Er_2O_3	0.84	0.9	0.46	0.17	Mn	0.06
Tm_2O_3	-	0.29	-		Σ	0.77
Yb_2O_3	1.25	1.14	0.71	0.16	Nb	1.56
Lu_2O_3	0.11	-	-		Ti	0.34
(ΣLn_2O_3)	6.64	6.57	4.9	0.07	Ta	0.1
ThO_2	18.11	1.39	3.3	0.21	Σ	2
UO_2	6.65	19.22	8.65	0.34	Si	0.09
MnO	2.34	0.97	0.87	0.11	O	7.7
Fe_2O_3	10.79	11.59	11.56	0.15		
SiO_2	-	-	1.14	0.16		
TiO_2	0.9	1.95	5.58	0.43		
ZrO_2	1.48	-	-			
Nb_2O_5	45.75	25.52	42.57	0.38		
Ta_2O_5	1.12	25.82	4.47	0.16		
WO_3	1.02	-	-			
Total	100.47	99.45	96.98			

3.4.2 Chemical analysis after heat-treatment

Heating the mineral in a vacuum to 1150 °C degrees caused an interesting change. In the BSE images of heated samarskite **HS**, one can see a mosaic picture - two new phases are formed, the crystals of which are evenly distributed over the grains and are expressed in a darker shade in the photographs (Figure 43, b).

Analyses of the formed phases were performed (Table 21). Comparing the average values of components for light and dark areas, it should be noted that uranium and rare earth elements (especially yttrium) are concentrated in the light region, while iron, titanium, and niobium are concentrated in the dark areas (Figure 43, b). Based on the results of X-ray phase analysis, these two phases are yttrium fergusonite ($YNbO_4$) (light areas), and tapiolite (general formula: $FeTa_2O_6$) (dark areas). The formulas of these two phases are calculated for "$B = 1$" and "$B = 2$", respectively.

Table 21. Average values of chemical components in dark and light zones. It is identified that the bright spots are yttrium fergusonite. Their a.p.f.u. are calculated according to "*B* = 1"; and the dark spots are tapiolite, its formula was calculated based on "*B* = 2".

Compounds	Av. wt.% Tapiolite (BSE dark)	Fergusonite (BSE bright)		Atoms	*a.p.f.u.* Tapiolite (BSE dark)	Fergusonite (BSE bright)
Y_2O_3	3.06	17.42		Y	0.1	0.38
Sc_2O_3	0.98	0.45		Sc	0.05	0.02
Nd_2O_3	0	0.75		Nd	0	0.01
Sm_2O_3	0	1.15		Sm	0	0.02
Gd_2O_3	0	1.97		Gd	0	0.03
Dy_2O_3	0.52	1.67		Dy	0.01	0.02
Er_2O_3	0	0.23		Er	0	0
Yb_2O_3	0	0.23		Yb	0	0
ThO_2	1.07	4.53		Th	0.02	0.04
UO_2	3.45	10.09		U	0.05	0.09
CaO	0	0.36		Ca	0	0.02
			Cation *A*	Σ=	0.23	0.63
Fe_2O_3	15.58	5.6		Fe	0.74	0.17
MnO	0.79	0.76		Mn	0.04	0.03
			Cation *M*	Σ=	0.79	0.2
Nb_2O_5	48.07	42.96		Nb	1.38	0.8
TiO_2	9.75	4.65		Ti	0.46	0.14
Ta_2O_5	9.18	4.98		Ta	0.16	0.06
			Cation *B*	Σ=	2	1
SiO_2	1.78	1.25		Si	0.11	0.05
				O=	6.53	3.82

3.4.3 Mössbauer spectroscopy

There was a study on the valency of iron in samarskite [Malczewski, Grabias, Dercz, 2010]. The Mössbauer spectrum of samarskite from Centennial Cone, Colorado shows that there are three quadrupole doublets assigned to Fe^{2+} and Fe^{3+} at octahedral sites (Figure 44). The Mössbauer spectrum of samarskite from the Ross mine, North Carolina, its characteristics differ from the previous one (Table 22).

The analysis was performed for the metamictic samarskite sample, and the spectrum obtained can be interpreted according to two models: 1. The first model contains three doublets, two of which are associated with Fe^{2+} and one with Fe^{3+}; 2. The second possible model includes two doublets: one attributed to Fe^{2+} divalent iron, the other to Fe^{3+} trivalent iron. Depending on the calculation, the Fe^{3+} content is 34.7% or 33.25%, respectively. Malczewski et al.[2008] proposed that all iron is in octahedral positions. Five years ago, Britvin and co-authors [2019] deciphered the structure of samarskite on natural crystals and revealed that the coordination of trivalent iron is AO_8 square antiprism. Therefore, the question arises as to where Fe2+ is located. It can be assumed that Fe^{2+} is contained in both AO_8 and MO_6 (A = Y, Ln, Th, U^{4+}, Ca, Fe; M = Fe^{3+}, Mn^{2+}) polyhedra simultaneously. Another assumption is that Fe^{2+} occupies only one of these two positions.

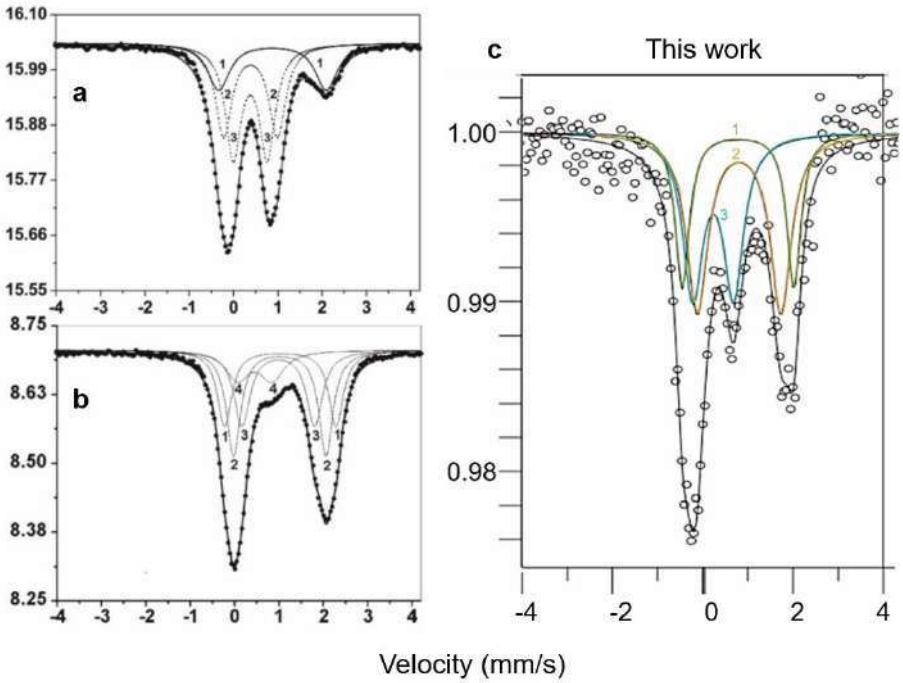

Figure 44. Mössbauer spectrum of metamict samarskite Centennial Cone, Colorado (a), from the Ross mine, North Carolina (b) and from the Black Cloud Mine, Colorado, USA (c).

Table 22. Data on the Mössbauer spectrum of samarskite and comparison with literature parameters.

Sample	χ^2	№ doublets	IS (mm/s)	QS (mm/s)	Γ (mm/s)	Assignment	Wt.%
Samarskite from Centennial Cone, Colorado	1.6	1	0.88 (2)	2.43 (2)	0.3 (2)	Fe^{2+} (oct.)	24 (16)
		2	0.382 (5)	1.21 (3)	0.22 (2)	Fe^{3+} (oct.)	35(3)
		3	0.379 (3)	0.77 (3)	0.21 (1)	Fe^{3+} (oct.)	41(3)
Samarskite from the Ross mine, North Carolina	2.3	1	1.038 (4)	2.51 (3)	0.19 (1)	Fe^{2+} (oct.)	23(3)
		2	1.031 (3)	2.08 (2)	0.19 (3)	Fe^{2+} (oct.)	34(4)
		3	0.994 (6)	1.63 (2)	0.22 (1)	Fe^{2+} (oct.)	28(3)
		4	0.39 (2)	0.92 (3)	0.31 (2)	Fe^{3+} (oct.)	15(1)
MS (in this work)		1-st model (with two doublets of Fe2+)					
		1-1	0.74(1)	2.47 (5)	0.38 (7)	Fe^{2+}	24.0(6)
		1-2	0.76(2)	1.85 (7)	0.56 (6)	Fe^{2+}	41.2(4)
		1-3	0.19(3)	0.90 (5)	0.53 (5)	Fe^{3+}	34.7(1)
		2-nd model (with one doublet of Fe2+)					
		2-1	0.722(8)	2.20 (2)	0.61 (2)	Fe^{2+}	66.7(5)
		2-2	0.24 (1)	0.80 (2)	0.55 (5)	Fe^{3+}	33.2(5)

3.4.4 Raman spectroscopy

Figure 45 shows Raman spectrum of metamict samarskite **MS**. Three spectral curves were obtained respectively from the main, intermediate and altered zones in the sample. Raman bands at 3500 and 1500 cm^{-1} are only observed in the altered zone, indicating the presence of water.

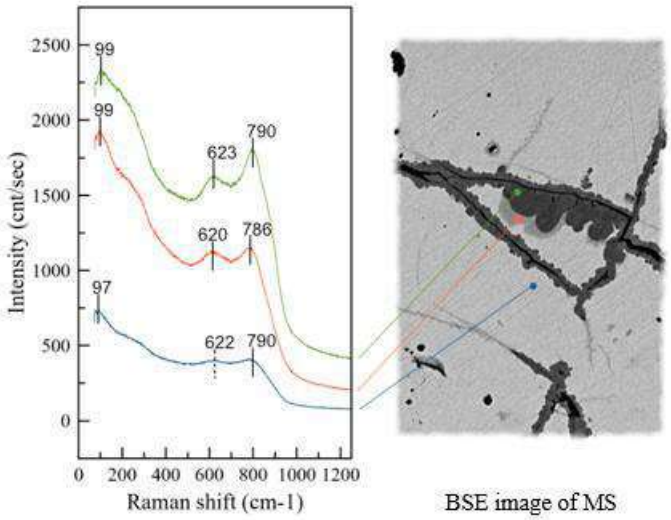

Figure 45. Raman spectra of **MS** and its collect point in BSE images.

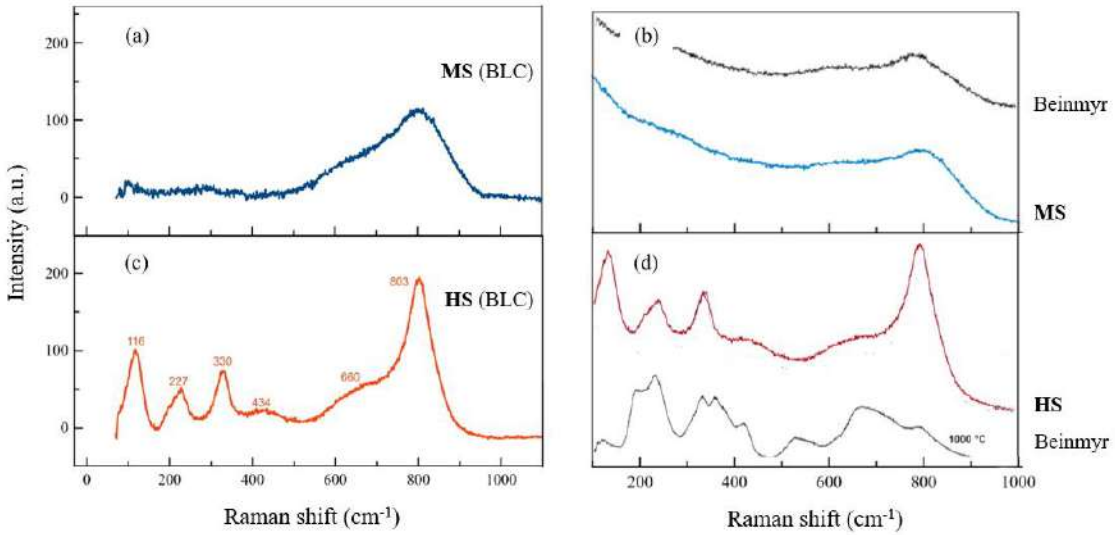

Figure 46. Baseline corrected Raman spectra of metamict (a) and heated samarskite (c). The obtained spectra were compared with metamict samarskite from Beinmyr (b) and its heated sample (d).

Table 23. Raman bands position in samarskite.

Raman bands		Interpretation
MS (см$^{-1}$)	**HS** (см$^{-1}$)	
97	116	
	230	
	324	Bending vibrations O-Ti-O, O-Ta-O and valence vibrations Ti-O
	434	Symmetric *A*-O and *M*-O vibrations
623	660	Antisymmetric *B*-O vibrations
792	803	Symmetric *B*-O vibrations

After heating, sharp peaks appeared in the Raman spectrum: 116, 230, 325, 434, 660 and 803 cm^{-1}. (Figure 46c). Comparing with published data on samarskite from the Beinmyr granite pegmatite [Tomašić et al., 2010], a number of similarities can be noted. The Raman spectrum taken from the Beinmyr samarskite, which was heated to 1000 °C in air, is demonstrated in Figure 46d. According to Tomašić, the peak at 810 cm^{-1} is associated with symmetric B-O stretching vibrations, the peak around 660 cm^{-1} is associated with antisymmetric B-O stretching vibrations and the peak at 430 cm^{-1} is associated with symmetric A-O and W-O stretching vibrations [Tomašić et al., 2010]. Raman bands from 200 to 450 cm^{-1} usually correspond to bending vibrations of O-Ti-O, O-Ta-O and Ti–O

stretching vibration (Table 23) [Tomašić et al., 2004].

3.4.5 Thermal recrystallization

The X-ray powder diffraction was carried out under low vacuum in a Rigaku Ultima IV diffractometer (CoKα). The heating attachment allows reaching a temperature of 1200 °C. The diffraction data is registered at every 100 °C upon heating from room temperature to 600 °C. Temperature step was then set to 25 °C in the temperature range of 625-1200 °C. The average rate is 60°/hour.

As XRD of **MS** show in Figure 47, the diffraction peaks firstly appear above 650°, the wide FWHM (full width at half maxima) indicating that the phase is formed with low crystallinity. The phase can be indexed as a columbite-Fe ($FeNb_2O_6$, ICSD-47187) or as a srilankite (α-PbO_2, ICSD-31311).

At temperatures above 950 °C, the crystallized phase decomposed to two structures: tapiolite-Fe ($Nb_{0.2}Ta_{1.8}O_6$, 28233-ICSD) and β-fergusonite ($YNbO_4$, 100176-ICSD). Note that α-fergusonite is tetragonal and exists at high temperatures. α-fergusonite transforms to β-fergusonite after cooling, which is monoclinic.

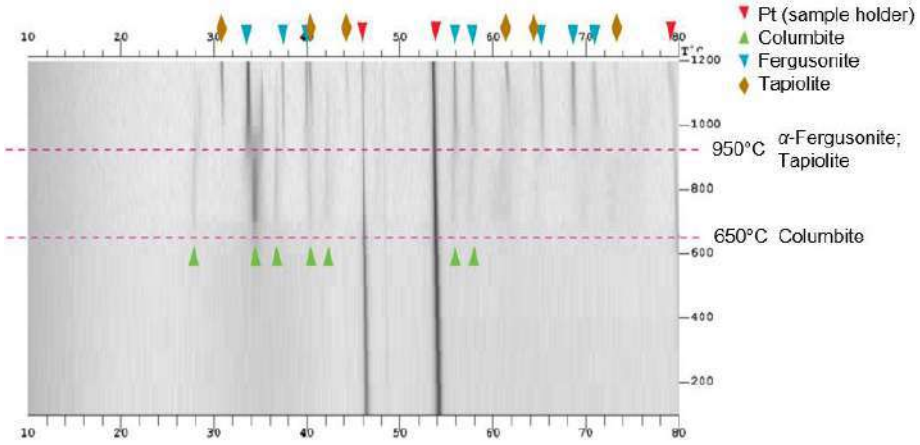

Figure 47. X-ray diffraction perform on metamict samarskite **MS** at temperatures ranging from 25 to 1200°C.

The matamict samarskite underwent simultaneous thermal analysis three times, each under different temperature and atmosphere conditions: 1) heating up to 1300°C in an air flow; 2) also heating to 1300°C, but in an argon atmosphere; 3) from room temperature to 800°C in argon flow. The heating rate was 20°C/min.

Figure 48 shows the TG and DSC curves of **MS** heated in air flow. In the range from 84 to 203°C, an endothermic effect was observed on the DSC curve with a maximum at 134°C, which corresponded to the first stage of mass loss of 0.45 % in the TG curves, suggesting a water loss. With further heating in the range from 203 to 550 °C, two stages of mass loss of 0.62 % is observed on TG without any noticeable thermal effects on DSC. In these intervals, release of water is still the main activity.

When a temperature is increased from 550 to 705°C, a 0.17% mass gain appears noted on the

TG curve. Within this temperature range, the DSC curve exhibited three exothermic peaks, peaking at 677, 705, and 750°C, indicating crystallization of various phases. Interestingly, these crystallization events did not coincide with any observable mass changes. In the range from 1107 to 1300°C, a mass loss step of 0.38% was observed on the TG curves.

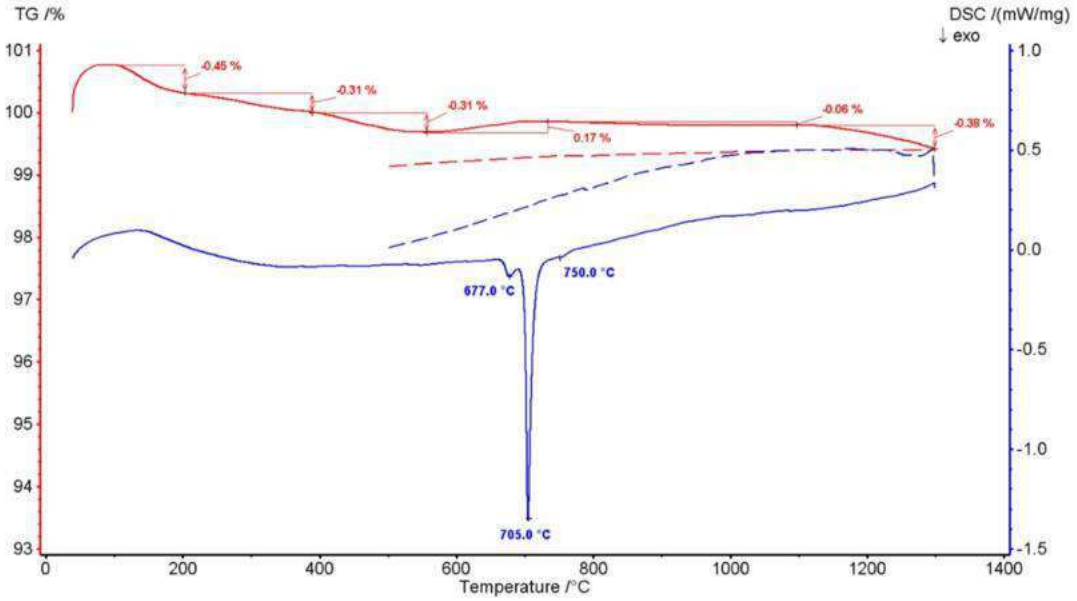

Figure 48. TG and DSC curves of metamict samarskite heated in air atmosphere.

Figure 49 and Figure 50 present the outcomes of two thermal analyses conducted under argon atmosphere. The former covered at 40 to 1300°C temperature range, while the latter covered temperatures below 800°C. Dehydration primarily occurred before reaching 400°C. Subsequently, exothermal effects were observed at 544 and 667°C in both experiments. Notably, thermal treatment in argon led to faster crystallization, with exothermic peaks occurring at lower temperatures compared to heating in an airflow (where crystallization peaked at 677 and 785°C). Between 1075 and 1218°C, a small endothermic effect appeared on the DSC curve, reaching its peak at 1184°C. This suggests a partial melting of a certain phase, which did not be observed in heating circle in airflow.

Comparing the thermal experiments in air and argon, one can conclude that heat treatment in argon accelerates crystallization and melting, while if the samples are heated in air the crystallization is slower, probably due to the consumption of part of the energy in redox reactions.

An X-ray examination of two samples that had undergone thermal analysis experiments revealed that heating the samples to 800 and 1300 °C produced different products. The sample heated to 800°C in argon produced a phase with low crystallinity, which was initially indexed as an α-PbO_2 structure. By contrast, samples heated to 1300 °C contained crystalline tapiolite and fergusonite. This result is consistent with the two crystallization stages in HTXRD experiments.

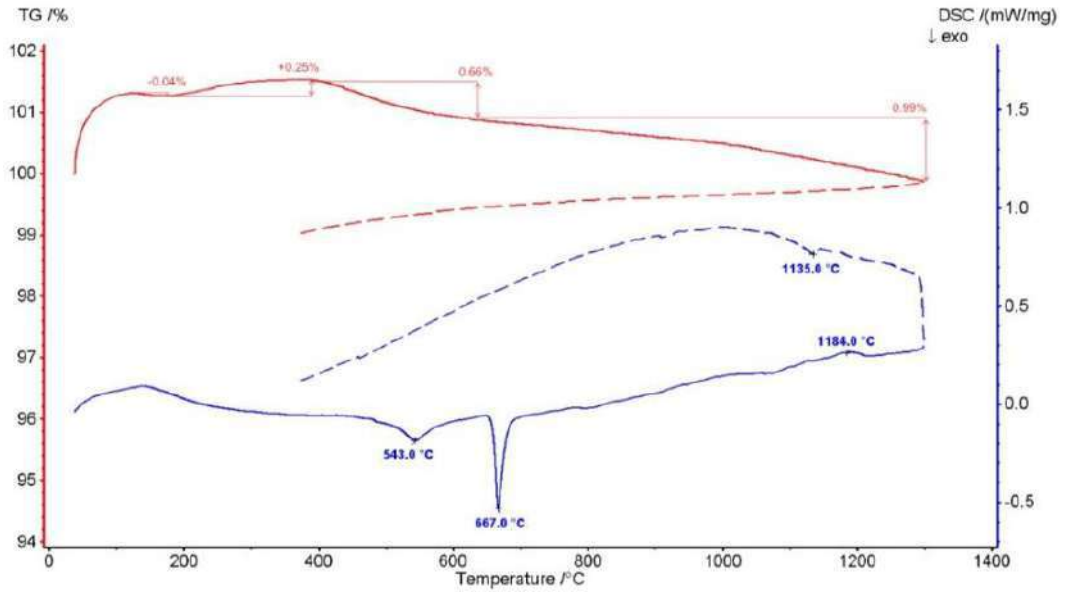

Figure 49. TG and DSC curves of metamict samarskite heated in argon atmosphere.

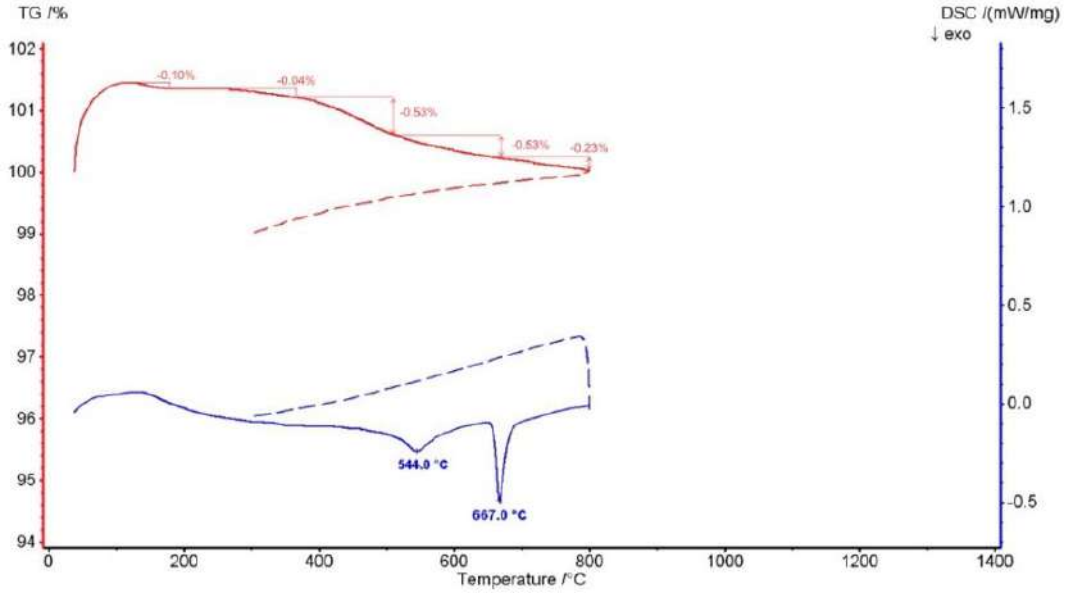

Figure 50. TG and DSC curves when heating metamict samarskite to 800 °C in argon atmosphere.

3.4.6 Concluding remarks

According to Britvin et al., [2019]Britvin et al., [2019]Britvin et al., [2019], the metamict samarskite was expected to thermally recrystallize into α-PbO_2 structure and then into samarskite. But in our experiments, the monoclinic samarskite failed to crystallize.

Chemical composition and Raman spectroscopy strongly indicate that the sample **MS** is samarskite. The chemical composition of the samples corresponds to the empirical mineral formula for samarskite. The BSE image of metamict sample shows its chemical homogeneity. The Raman spectra of **MS** and **HS** are nearly identical to that of samarskite from the Beinmyr granite pegmatite [Tomašić et al., 2010].

The annealing products, produced in various temperature and atmosphere, are summarized in Table 24. The experiments show similar recrystallization pattern. The sample **MS** states crystallize at 650 °C, a phase with a α-PbO_2 structure type can be identified, the phase has low crystallinity. Once the experimental temperature goes higher than 950 °C, the phase decomposes to fergusonite

and tapiolite.

On one hand, the failure of recrystallization of samarskite may due to heavy alteration and hydration, which damaged its structure severely. On the other hand, there was no significant difference in the heating rates and calcination durations, although different experimental temperatures and atmospheres were used. In future experiments, it is recommended that the samples be heated to a temperature slightly below their decomposition temperature (~950 °C) and kept at this temperature for more than 10 hours to enable the crystals to have sufficient time to increase crystallinity.

Table 24. Metamict samarskite crystallized into distinct phases under varying heating conditions.

Atmosphere	Experimental setting	Phase crystallized at respective temperature	
		>800 °C	>1200°C
Air	Heat and X-ray	825 °C #1-str. α-PbO_2 #2-Oxides of REE and U	1200 °C #1-Fergusonite #2-Str. α-PbO_2 #3-Tapiolite or Rutile
	After DSC experiments		1300 °C #1-Fergusonite #2-Tapiolite
Argon	After DSC experiments	800 °C #1-str. α-PbO_2	1300 °C #1-Fergusonite #2-Tapiolite
Weak vaccum	High-temperature XRD *in-situ*	875 °C #1-str. α-PbO_2	1200 °C #1-Fergusonite #2-Tapiolite

3.5 Zirconolite[13]

In this study we have used O.M. Rimskaya-Korsakova and N.I. Krasnova collection of heavy minerals fraction from southern carbonatites and phoscorites-carbonatites from southwestern part of Kovdor. The studied samples are (i) euhedral tabular crystals (southern carbonatites), (ii) euhedral cubic crystals (southern carbonatites), and (iii) euhedral to subhedral prismatic crystals, fragments of broken crystals and anhedral crystals (southwestern phoscorite-carbonatites with tetraferriphlogopite). All studied zirconolite crystals are metamict and in the text below, we refer to them as **MZ** (metamict zirconolite), and recrystallized zirconolite crystals obtained by heating of metamict crystal as **HZ** (recrystallized zirconolite).

3.5.1 Internal zoning and composition

The studied zirconolite crystals are classified into four groups based on their morphology and internal zoning. **MZ-A** group is represented by euhedral tabular (platy) crystals from southern carbonatites. Morphologically, they are similar to some of zirkelite crystals from Seblyavr phoscorites and carbonatites described by [Bulakh et al., 1998]. On backscattered electron images (BSE) all crystal is characterized by well-developed zoning with brighter core and darker rim (Figure 51a). Crystal rim always show rhythmic-type zonation with concentric strips that are parallel to the crystal edges. One of the studied zirconolite crystals is characterized by well-developed sector- and

[13] The structure of zirconolite is characterized by hexagonal tungsten bronze (HTB) layers and the way in which they are stacked in the unit cell. The crystal structures of zirconolite-2*M* and zirconolite-3*T* are shown in Figure 5.

rhythmic-type zoning (**MZ-A^{A}**, Figure 51b).

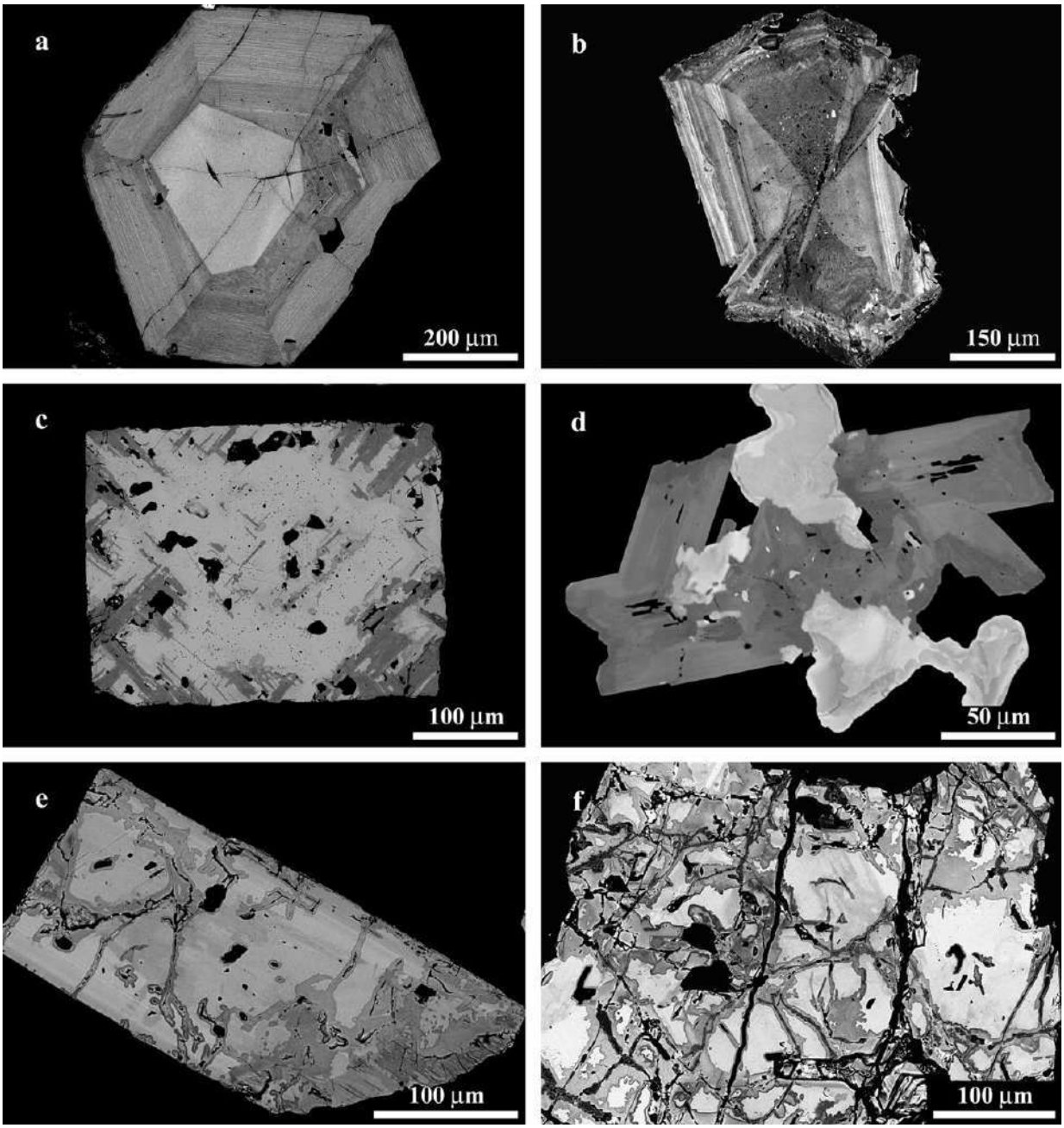

Figure 51. Morphology and internal texture of studied zirconolite: (a) euhedral tabular crystal with rhythmic-type zoning (**MZ-A** group), (b) euhedral crystal with rhythmic- and sector- type zoning (**MZ-A^{A}** group), (c) cubic crystal with pyrochlore and zirconolite (**MZ-B** group), (d) zirconolite- pyrochlore intergrowth (**MZ-C** group), (e) euhedral crystal showing variable degree of mineral alteration (dark grey areas) (**MZ-D** group), and (f) internal texture of highly altered (grey and dark grey) subhedral crystal. Back-scattered electron images.

The second group, denoted as **MZ-B**, is represented by euhedral cubic zirconolite crystals also occurring in southern carbonatites. BSE images of all studied crystals, however, show that they are consist of two minerals, pyrochlore and zirconolite (Figure 51c). Observed intergrowth of zirconolite and pyrochlore explain high sodium content in cubic zirconolite crystals analyzed by Osokin [1979]. Presence of Na in zirconolite from Kovdor phoscorite (0.7 wt% Na_2O) was also reported by Kukharenko et al., [1965].

Zirconolite groups three (**MZ-C**) and four (**MZ-D**) are from phoscorites and carbonatites containing tetraferriphlogopite from southwestern part of the complex. MZ-C is zirconolite occurring in association with pyrochlore and rarely baddeleyite (Figure 51d, see also Fig. 1a in Williams, 1996,

and Fig. 8 in Zaitsev et al., 2015). It occurs as euhedral to subhedral prismatic crystals and BSE images often show heterogeneous internal structure and composition. Compositional differences are probably related to different crystal grown zones (sector-type zoning, Figure 51d), and some crystals show late-stage alteration of mineral.

MZ-D zirconolite occurs as euhedral to subhedral prismatic crystals and fragments of broken crystals. All studied crystals of this group exhibit microcrack and BSE images suggest significant alteration in the mineral composition (Figure 51e, f). Similar alteration textures previously were observed for zirconolite from Afrikanda [Bulakh, Nesterov, Williams, 2006].

Selected zirconolite composition and calculated atoms per formula units (apfu) values are presented in Table 25 and Table 26.

Limited published data for Kovdor zirconolite (wet chemistry method in Kukharenko et al., 1965, microprobe data in Williams, 1996 and Zaitsev et al., 2015) show highly variable composition of mineral and our new data confirm zirconolite composition variability. The studied zirconolite is strongly enriched in Nb (10.8-24.1 wt% Nb_2O_5), contains essential amount of Fe (7.9-9.0 wt% Fe_2O_3), Th (1.0-8.7 wt% ThO_2), Ta (0.5-5.3 wt% Ta_2O_5), REE (2.1-5.0 wt% REE_2O_3) and minor U (0.1-1.9 wt% UO_2). As expected, Ti shows negative correlation with Nb+Ta and Fe (Figure 52a, b), and Ca apfu values negatively correlates with REE (Figure 52c).

Strong enrichment of carbonatititc zirconolite carbonatites in Nb and Fe has been discussed by [Sharygin, Doroshkevich, Khromova, 2016] in their study of Fe-Nb-rich zirconolite from Belaya Zima calcite carbonatites. They suggested that such mineral variety is typical for intrusive carbonatites and new mineral, within zirconolite group, with ideal formula $CaZr(TiNb_{0.5}Fe^{3+}_{0.5})O_7$ could be established. In fact, in studied zirconolite Ti is the dominant component in only 61 of 128 spot analyses (Figure 52d).

Composition of zirconolite from different studied localities at Kovdor (southern carbonatites and southwestern phoscorites + carbonatites) and groups (**MZ-A**, **A1**, **B**, **C** and **D**) partly overlaps (Figure 52), however, there are some differences in compositions. For example, zirconolite (groups **MZ-A**, **B** and **C**) is enriched in Nb, Ta and Fe and depleted in Th (Figure 52e) compared to mineral from group **MZ-D**; data points for zirconolite group **MZ-A** form a distinct field on Ca vs REE plot.

Alteration of zirconolite (group **MZ-D**, Table 26) led to enrichment in Si (up to 9.2 wt% SiO_2), Ba (up to 2.9 wt% BaO), Sr (up to 2.6 wt% SrO), Al (up to 1.0 wt% Al_2O_3), and rarely P (3.4 wt% P_2O_5 in single spot analysis). Content of CaO, ZrO_2 and Fe_2O_3 is decreasing (up to 1.7, 17.8 and 1.5 wt% respectively). Analytical totals are low and range between 89.7 and 96.1 wt%.

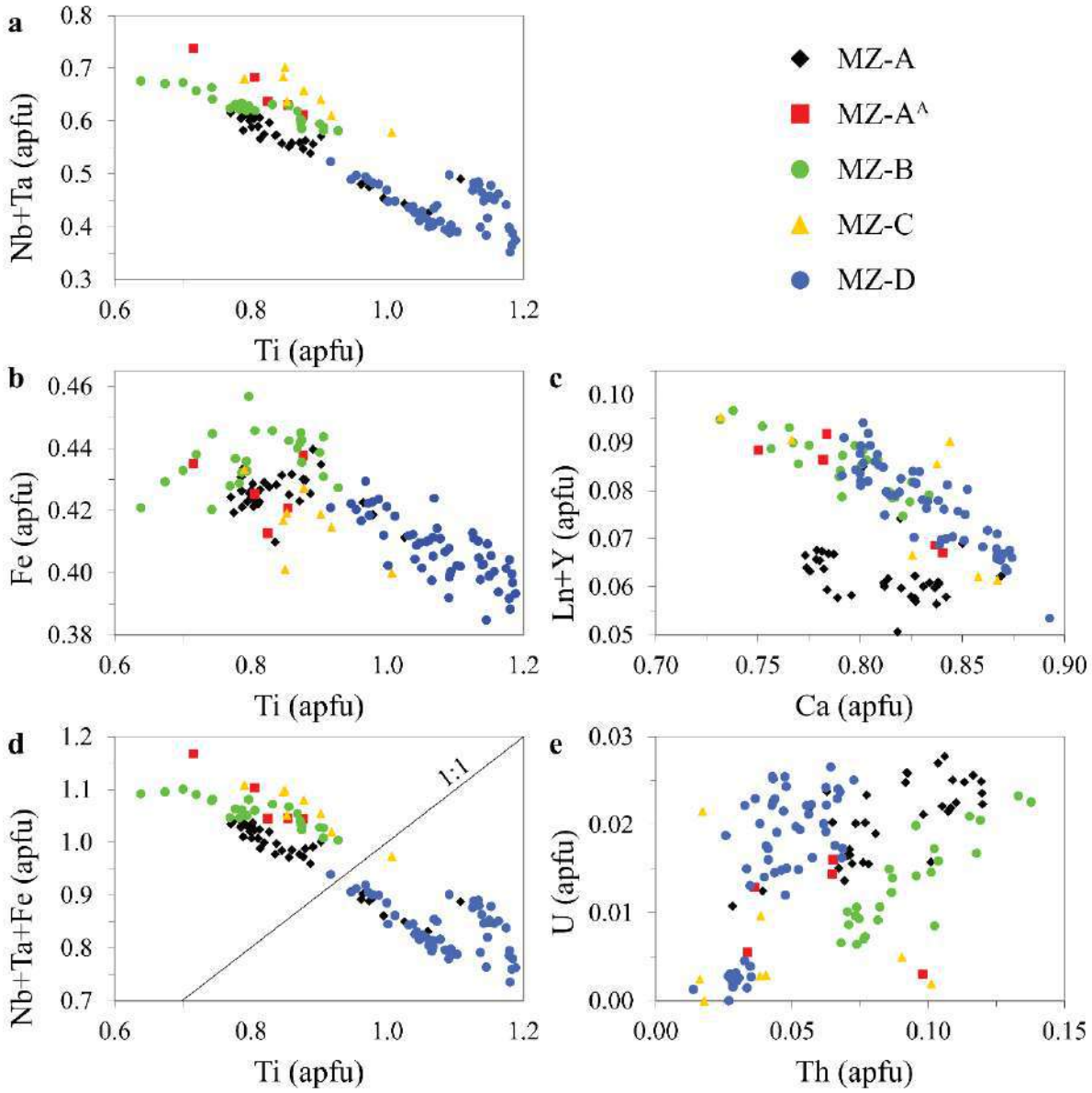

Figure 52. Compositional variations of zirconolite, apfu - atoms per formula unit.

3.5.2 Composition of recrystallized zirconolite

The selected chemical composition and formula coefficients of heated samples are presented in Table 27. The compositional zoning in **MZ-A** is significantly erased after heating (Figure 53). Microcrystals of zirconolite can be observed in enlarged BSE image of **HZ-A** (Figure 54a), where a set of unoriented dark crystals is formed within a brighter matrix. The darker crystals (2-5 μm) in Figure 54a exhibit lower U, REE, and higher Mg, Fe content (Table 27, point 861-862).

The intergrowth texture of zirconolite in pyrochlore persist after heating, as illustrated in Figure 53.The crystallized zirconolite in **HZ-B**, akin to **HZ-A**, manifests a prolonged form with crystal size in the range of 2-5 μm. Other phases are also detected (Figure 54b, c). Based on their chemical composition (Table 27), zirconolite, zircon and baddeleyite can be identified.

The microcrystals of zirconolite can be identified in **HZ-D**, where compositional zoning is also eliminated after heating. The redistribution of elements in thus formed crystallites cannot be studied in detail because of the limitations of the microprobe analysis. Brighter phases congregate around cracks, displaying lower Fe and higher U content.

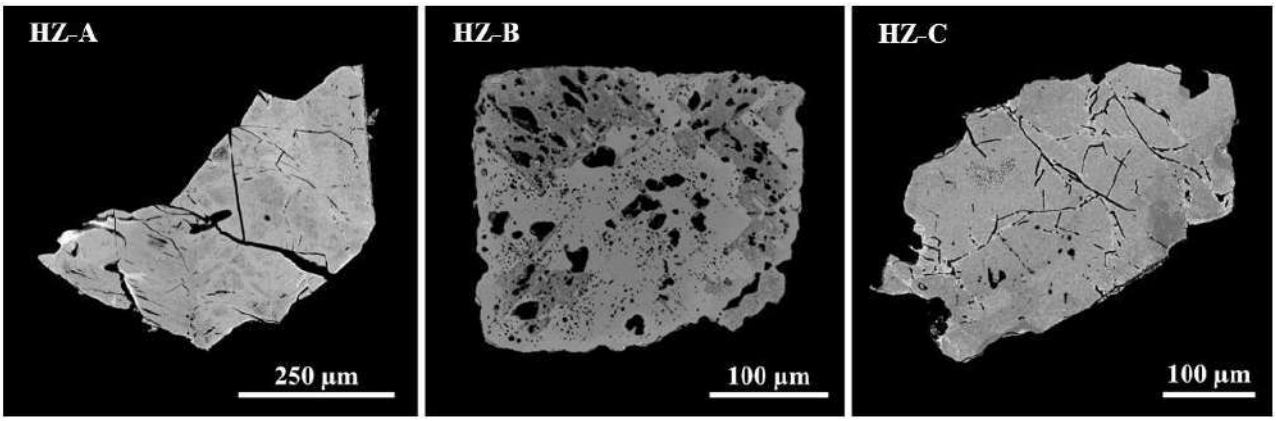

Figure 53. Selected grains of **HZ** samples.

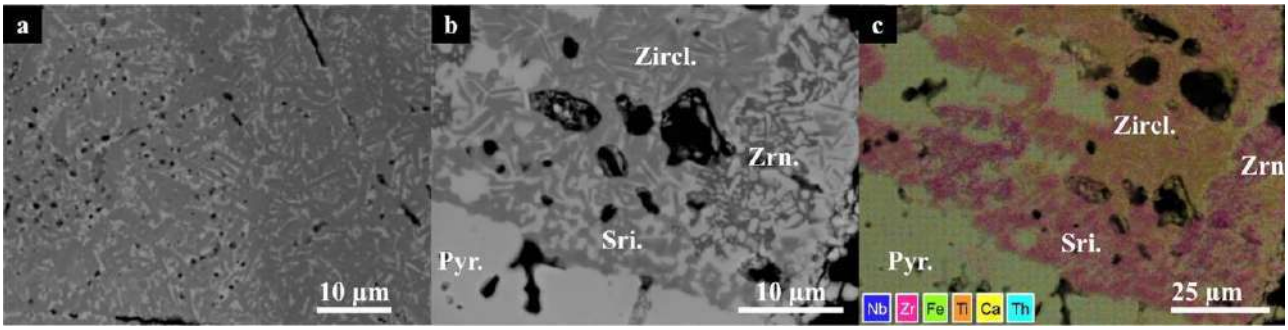

Figure 54. Dark crystals within a brighter matrix of zirconolite composition are observed in sample **HZ-A** (a). Zirconolite, zircon, and srilankite crystallized within pyrochlore in sample **HZ-B** (b). The element mapping of the selected region is presented in (c). The chemical composition is given in Table 27.

Table 25. Chemical composition and atom per formula unit (apfu) of metamict zirconolite grains (**MZ**).

Type	**MZ-A**				**MZ-A^{A}**		**MZ-B**				
Sample	65/a		04850		421		1066/4		1066/3	208/12	
Position	core	core	core	rim			core	rim	rim	core	
Point	1	6	37	39	60	61	29	30	82	91	115
Na_2O						0.17			0.14	0.07	
MgO	0.82	0.73	0.50	0.30	0.48	0.73	0.53	0.47	0.36	1.17	0.67
Al_2O_3	0.18	0.16	0.08	0.10						0.20	0.11
CaO	10.60	10.90	11.48	12.79	12.18	11.12	11.30	11.63	11.70	9.85	11.17
TiO_2	15.39	17.03	19.67	22.23	18.18	14.46	16.70	17.71	18.20	12.14	15.77
MnO	0.51	0.48	0.34	0.22	0.24	0.32	0.49	0.50	0.40	0.70	0.52
Fe_2O_3	8.36	8.45	8.51	8.50	8.97	8.69	8.85	8.87	8.75	7.90	8.49
Y_2O_3	0.13	0.13	0.17	0.17	0.16	0.13	0.14	0.13	0.14	0.12	0.14
ZrO_2	30.39	30.26	32.00	33.92	31.49	29.34	29.52	29.96	29.19	29.31	30.02
Nb_2O_5	15.68	15.73	14.93	13.59	20.71	24.05	19.46	18.64	18.22	19.12	18.62
La_2O_3	0.25	0.24	0.34	0.30	0.32	0.39	0.35	0.32	0.33	0.33	0.34
Ce_2O_3	1.04	0.97	1.41	0.98	1.11	1.64	1.46	1.30	1.36	1.60	1.43
Pr_2O_3	0.20	0.11	0.24	0.15	0.18	0.27	0.22	0.23	0.26	0.28	0.23
Nd_2O_3	0.69	0.67	1.01	0.72	0.79	1.00	1.13	0.96	1.01	1.10	1.00
Sm_2O_3	0.15	0.15	0.20	0.21	0.18	0.22	0.21	0.20	0.18	0.23	0.21
Gd_2O_3	0.09	0.11	0.15	0.12	0.16	0.14	0.12	0.13	0.09	0.09	0.11
HfO_2	0.38	0.43	0.53	0.56	0.61	0.50	0.25	0.29	0.31	0.33	0.33
Ta_2O_5	5.35	4.46	2.51	2.10	0.66	1.23	2.73	2.91	2.91	3.75	3.27
ThO_2	7.73	6.88	4.24	1.95	2.31	4.32	5.07	4.95	4.70	8.65	5.70
UO_2	1.47	1.48	1.64	0.76	0.39	0.98	0.48	0.44	0.69	1.45	0.94
Total	99.52[1]	99.37	99.96	99.66	99.12	99.71	99.06[2]	99.60	98.93	98.54[3]	99.08

Table 25 (Continued)

Type	**MZ-A**				**MZ-A[A]**		**MZ-B**				
Sample	65/a		04850		421		1066/4		1066/3	208/12	
Position	core	core	core	rim			core	rim	rim	core	
Point	1	6	37	39	60	61	29	30	82	91	115
Structural formulae calculated on the basis of 7 O											
Ca	0.774	0.784	0.801	0.869	0.837	0.784	0.802	0.816	0.825	0.738	0.801
Th	0.120	0.105	0.063	0.028	0.034	0.065	0.076	0.074	0.070	0.138	0.087
U	0.022	0.022	0.024	0.011	0.005	0.014	0.007	0.006	0.010	0.023	0.014
Y	0.005	0.005	0.006	0.006	0.005	0.005	0.005	0.004	0.005	0.005	0.005
La	0.006	0.006	0.008	0.007	0.008	0.010	0.009	0.008	0.008	0.009	0.008
Ce	0.026	0.024	0.034	0.023	0.026	0.039	0.035	0.031	0.033	0.041	0.035
Pr	0.005	0.003	0.006	0.003	0.004	0.007	0.005	0.005	0.006	0.007	0.006
Nd	0.017	0.016	0.024	0.016	0.018	0.024	0.027	0.023	0.024	0.027	0.024
Sm	0.004	0.004	0.005	0.004	0.004	0.005	0.005	0.005	0.004	0.006	0.005
Gd	0.002	0.002	0.003	0.003	0.003	0.003	0.003	0.003	0.002	0.002	0.002
Na						0.021			0.018	0.009	
Total	0.982[1]	0.970	0.973	0.970	0.944	0.976	0.974[2]	0.974	1.005	1.006[3]	0.987
Zr	1.009	0.990	1.017	1.048	0.984	0.941	0.953	0.957	0.937	0.999	0.980
Hf	0.007	0.008	0.010	0.010	0.011	0.009	0.005	0.005	0.006	0.007	0.006
Total	1.017	0.999	1.027	1.058	0.996	0.950	0.958	0.962	0.943	1.006	0.986
Ti	0.789	0.860	0.965	1.060	0.877	0.716	0.832	0.872	0.901	0.639	0.794
Nb	0.483	0.477	0.440	0.389	0.600	0.715	0.582	0.552	0.542	0.604	0.563
Fe^{3+}	0.429	0.427	0.418	0.405	0.433	0.430	0.441	0.437	0.434	0.416	0.428
Ta	0.099	0.081	0.045	0.036	0.012	0.022	0.049	0.052	0.052	0.071	0.060
Mg	0.084	0.073	0.048	0.028	0.046	0.071	0.052	0.046	0.035	0.122	0.067
Mn	0.030	0.027	0.018	0.012	0.013	0.018	0.028	0.028	0.022	0.041	0.030
Total	1.912	1.946	1.934	1.931	1.980	1.972	1.983	1.986	1.987	1.894	1.941

Including (1) 0.11 wt% PbO (0.002 apfu), (2) 0.04 wt% PbO (0.001 apfu), (3) 0.13 wt% PbO (0.002 apfu). Si, K, P, Sr, Ba, Dy, Er, Yb, W, F and Cl – below detection limit. Blanks in the Table – content of the element is below detection limit.

Table 25. (Continued.)

Type	**MZ-C**			**MZ-D**							
Sample	04774			4 (2)				10c/534			
Position	core	core	rim	core		rim	rim	core	mantle		rim
Point	139	145	146	163	166	151	155	50	57	59	60
Na_2O	0.11	0.19	0.27								0.08
MgO	0.75	0.44	0.35	0.45	0.40	0.18	0.10	0.47	0.45	0.39	0.17
Al2O3				0.09	0.08	0.14	0.11	0.06		0.07	0.06
CaO	10.66	12.68	12.63	11.71	11.69	12.27	13.12	11.73	11.66	11.97	12.91
TiO_2	15.66	18.80	21.12	21.99	22.81	24.78	24.59	19.85	19.90	20.46	23.27
MnO	0.30	0.19	0.21	0.25	0.26	0.21	0.25	0.33	0.29	0.32	0.31
Fe_2O_3	8.48	8.61	8.28	8.10	8.21	8.09	8.42	8.70	8.49	8.52	8.59
Y_2O_3	0.16	0.11	0.10	0.18	0.19	0.21	0.21	0.15	0.15	0.16	0.17
ZrO_2	28.54	30.39	30.35	33.74	32.89	31.72	31.29	31.68	31.82	32.01	30.81
Nb_2O_5	21.10	19.44	18.24	12.45	12.22	11.78	15.81	15.52	15.08	14.75	17.22
La_2O_3	0.31	0.24	0.28	0.36	0.37	0.35	0.29	0.33	0.30	0.36	0.33
Ce_2O_3	1.39	0.97	1.05	1.46	1.38	1.22	1.02	1.25	1.23	1.22	1.15
Pr_2O_3	0.24	0.16	0.21	0.23	0.22	0.19	0.12	0.23	0.27	0.24	0.16
Nd_2O_3	1.18	0.83	0.82	1.08	1.21	0.97	0.89	1.03	0.96	0.94	0.91
Sm_2O_3	0.27	0.18	0.21	0.23	0.26	0.21	0.19	0.19	0.21	0.20	0.16
Gd_2O_3	0.14	0.12		0.14	0.14	0.15	0.14	0.13	0.15	0.12	0.13
HfO_2	0.43	0.58	0.66	0.44	0.45	0.35	0.28	0.50	0.42	0.45	0.32
Ta_2O_5	2.20	4.59	3.24	2.22	2.03	2.01	0.59	2.24	2.09	2.06	0.76
ThO_2	5.91	1.23	1.12	2.98	3.62	3.17	1.91	4.46	4.59	3.89	2.36
UO_2	0.33		0.17	1.60	1.36	1.05	0.19	1.22	1.12	1.13	0.11
Total	98.15	99.75	99.31	99.71	99.78	99.04	99.49	100.06	99.18	99.25	100.08[1]

Table 25. (Continued)

Type	**MZ-C**			**MZ-D**							
Sample	04774			4 (2)				10c/534			
Position	core	core	rim	core		rim	rim	core	mantle		rim
Point	139	145	146	163	166	151	155	50	57	59	60
Structural formulae calculated on the basis of 7 O											
Ca	0.766	0.867	0.858	0.808	0.805	0.838	0.874	0.815	0.817	0.833	0.862
Th	0.090	0.018	0.016	0.044	0.053	0.046	0.027	0.066	0.068	0.057	0.033
U	0.005		0.002	0.023	0.019	0.015	0.003	0.018	0.016	0.016	0.001
Y	0.006	0.004	0.003	0.006	0.007	0.007	0.007	0.005	0.005	0.006	0.006
La	0.008	0.006	0.007	0.009	0.009	0.008	0.007	0.008	0.007	0.009	0.008
Ce	0.034	0.023	0.024	0.034	0.032	0.028	0.023	0.030	0.029	0.029	0.026
Pr	0.006	0.004	0.005	0.005	0.005	0.004	0.003	0.006	0.006	0.006	0.004
Nd	0.028	0.019	0.018	0.025	0.028	0.022	0.020	0.024	0.022	0.022	0.020
Sm	0.006	0.004	0.005	0.005	0.006	0.005	0.004	0.004	0.005	0.004	0.004
Gd	0.003	0.003		0.003	0.003	0.003	0.003	0.003	0.003	0.003	0.003
Na	0.014	0.023	0.033								0.010
Total	0.967	0.970	0.972	0.963	0.967	0.977	0.970	0.977	0.980	0.984	0.979[1]
Zr	0.934	0.946	0.938	1.060	1.031	0.986	0.948	1.001	1.014	1.013	0.937
Hf	0.008	0.011	0.012	0.008	0.008	0.006	0.005	0.009	0.008	0.008	0.006
Total	0.942	0.957	0.950	1.068	1.039	0.992	0.953	1.011	1.022	1.022	0.942
Ti	0.790	0.903	1.007	1.066	1.103	1.188	1.150	0.968	0.979	1.000	1.091
Nb	0.640	0.561	0.522	0.362	0.355	0.339	0.444	0.455	0.446	0.433	0.485
Fe^{3+}	0.428	0.414	0.395	0.392	0.397	0.388	0.394	0.424	0.418	0.416	0.403
Ta	0.040	0.080	0.056	0.039	0.036	0.035	0.010	0.040	0.037	0.036	0.013
Mg	0.075	0.042	0.033	0.044	0.038	0.017	0.009	0.045	0.044	0.038	0.016
Mn	0.017	0.010	0.011	0.013	0.014	0.011	0.013	0.018	0.016	0.017	0.016
Total	1.991	2.010	2.024	1.917	1.943	1.979	2.021	1.950	1.939	1.940	2.024

Including (1) 0.10 wt% Dy_2O_3 (0.002 apfu). Si, K, P, Sr, Ba, Pb, Er, Yb, W, F and Cl – below detection limit. Blanks in the Table – content of the element is below detection limit.

Table 26. Selected compositions of altered zirconolite.

Type	**MZ-D**					
Sample						
Position			core	rim	rim	rim
Point	14	43	161	27	158	182
Na_2O	0.08		0.17			0.60
MgO	0.10	0.06	0.10	0.34	0.06	0.16
Al_2O_3	0.09	0.10	0.09	1.05		
SiO_2	0.22	0.47		8.27	9.21	3.35
P_2O_5				3.37		
K_2O	0.13		0.16	0.12	0.20	0.16
CaO	7.78	9.44	2.45	3.46	3.22	6.90
TiO_2	25.40	24.02	23.24	19.98	19.68	19.24
MnO	0.21	0.23	0.23		0.11	0.30
Fe_2O_3	4.31	5.59	2.44	3.74	1.52	5.06
SrO	0.14	0.11	0.46	0.19	2.58	0.07
Y_2O_3	0.16	0.18	0.16	0.10		0.17
ZrO_2	31.32	30.70	36.12	17.78	27.03	29.56
Nb_2O_5	18.31	16.03	13.91	22.12	16.26	14.86
BaO			0.55	1.70	2.92	0.18
La_2O_3	0.31	0.28	0.36	0.27	0.24	0.29
Ce_2O_3	0.99	0.99	1.49	0.65	0.94	1.14
Pr_2O_3	0.15	0.14	0.08			0.12
Nd_2O_3	0.80	0.82	1.13	0.33	0.76	0.85
Sm_2O_3	0.15	0.20	0.17			0.18
Gd_2O_3	0.09	0.11	0.16		0.09	0.12
HfO_2	0.35	0.30	0.47	0.30	0.29	0.28
Ta_2O_5	0.61	0.54	2.39	2.65	2.42	3.18
ThO_2	2.26	2.47	2.93	3.04	4.19	4.65
UO_2	0.43	0.37	1.84	0.29	1.19	1.74
Total	94.38	93.15	91.11	89.74	92.93	93.15

Dy, Er, Yb, W, F and Cl – below detection limit. Blanks in the Table – content of the element is below detection limit.

Table 27. Selected compositions of recrystallized zirconolite, pyrochlore, srilankite and zircon in samples **HZ**.

	HZ-A			**HZ-B**				**HZ-D**		
Assu.Minerals	Zirconolite			Pyrochlore	Zircl.	Srilankite	Zircon	Zirconolite		Zircon
Ideal formula	ABM_2O_7			$A_2M_2O_7$	ABM_2O_7	$ZrTiO_4$	$ZrSiO_4$	ABM_2O_7		$ZrSiO_4$
Position		Crystals	Matrix			Crystals		Crack	Matrix	Crack
Colour BSE		Dark	Bright	Bright	Grey	Grey	Dark	bright	Grey	dark
Point	850	861	862	881	882	888	890	994	1003	1027
Na_2O		0.22			0.14	0.13			0.15	
MgO	0.78	0.7	0.41	0.28	0.56	0.46			0.18	
Al_2O_3	0.16	0.14	0.2	0.12	0.2	0.24	0.24	0.22	0.33	
SiO_2				1.1	0.65	0.35	24.31	0.91		28.15
CaO	11.33	11.97	9.2	15.22	10.29	4.54	3.72	8.7	13.52	1.69
TiO_2	15.47	18.55	12.74	15.36	16.95	17.29	4.42	23.6	26.56	3.35
ZrO_2	30.27	29.84	39.22	3.01	28.63	38.53	45.41	28.92	30.52	56.21
Nb_2O_5	17.78	15.7	15.41	30.26	17.2	18.52	6.66	19.31	15.22	3.79
La_2O_3	0.75			1.32	0.65	0.68	0.49	0.75	0.88	
Ce_2O_3	1.09	0.93	1.3	2.52	1.04	0.98	0.91	2.15	1.01	0.73
Nd_2O_3	0.73	0.9	0.8	0.54	1.42	0.46		1.28	1.15	
Sm_2O_3					0.63			0.29		
Gd_2O_3								0.38		
Dy_2O_3							0.39			
Er_2O_3	0.53									
HfO_2							0.83	0.45		0.73
Ta_2O_5	4.82	4.99	4.15	5.21	2.26	2.2		1.86	0.94	
ThO_2	6.03	5.82	6.5	12.82	6.27	3.05	5.62	5.15	2.17	2.79
UO_2	1.95	0.61	1.93	10.53	3.52	3.27	5.73	3.22	0.73	1.61
MnO	0.62	0.45	0.48	0.18	0.62	0.23		0.3	0.47	
Fe_2O_3	7.42	8.97	5.25	1.97	9.02	9.2	1.01	4.32	7.41	0.28
Total	99.73	99.78	97.58	100.45	100.06	100.14	99.74	101.82	101.25	99.34

Table 27. (Continued)

Apfu calculated on the basis of *n* O										
Ca	0.818	0.840	0.692	1.162	0.734	0.182	0.134	0.593	0.883	0.058
La	0.019			0.035	0.016	0.010	0.006	0.018	0.020	
Ce	0.027	0.022	0.033	0.066	0.025	0.014	0.011	0.050	0.023	0.009
Nd	0.018	0.021	0.020	0.014	0.034	0.006		0.029	0.025	
Sm					0.014			0.006		
Gd								0.008		
Dy							0.004			
Er	0.011									
Th	0.092	0.087	0.104	0.208	0.095	0.026	0.043	0.074	0.030	0.020
U	0.029	0.009	0.030	0.167	0.052	0.028	0.043	0.046	0.010	0.011
Na		0.028			0.018	0.010			0.018	0.000
Total	1.014	1.007	0.879	1.651	0.988	0.272	0.241	0.824	1.009	0.098
Zr	0.994	0.953	1.342	0.105	0.929	0.700	0.743	0.896	0.908	0.874
Hf							0.008	0.008	0.000	0.007
Total	0.994	0.953	1.342	0.105	0.929	0.700	0.751	0.905	0.908	0.881
Ti	0.784	0.914	0.672	0.823	0.849	0.484	0.112	1.129	1.219	0.080
Si				0.078	0.043	0.014	0.816	0.058		0.898
Mg	0.078	0.068	0.043	0.030	0.056	0.026			0.016	
Mn	0.035	0.025	0.029	0.011	0.035	0.008	0.000	0.016	0.024	
Fe^{3+}	0.376	0.442	0.277	0.106	0.452	0.258	0.026	0.207	0.340	0.007
Al	0.013	0.011	0.017	0.010	0.016	0.010	0.009	0.016	0.024	
Nb	0.541	0.465	0.489	0.975	0.517	0.312	0.101	0.555	0.420	0.055
Ta	0.088	0.089	0.079	0.101	0.041	0.022		0.032	0.016	
Total	1.916	2.014	1.606	2.134	2.008	1.132	1.064	2.013	2.058	1.040
O=	7	7	7	7	7	4	4	7	7	4

K, P, Sr, Ba, Y, Pr, Yb, W, Pb, F and Cl – below detection limit. Blanks in the Table – content of the element is below detection limit.

3.5.3 Raman spectroscopy

Raman spectra of all metamict zirconolite shows the absence of H_2O molecule and OH group (Figure 55 a). Because of the crystal structure damage, the Raman spectra obtained only show rough molecular vibrational structures. The peaks with large half-width are observed at around 110, 610 and 780 cm^{-1}.

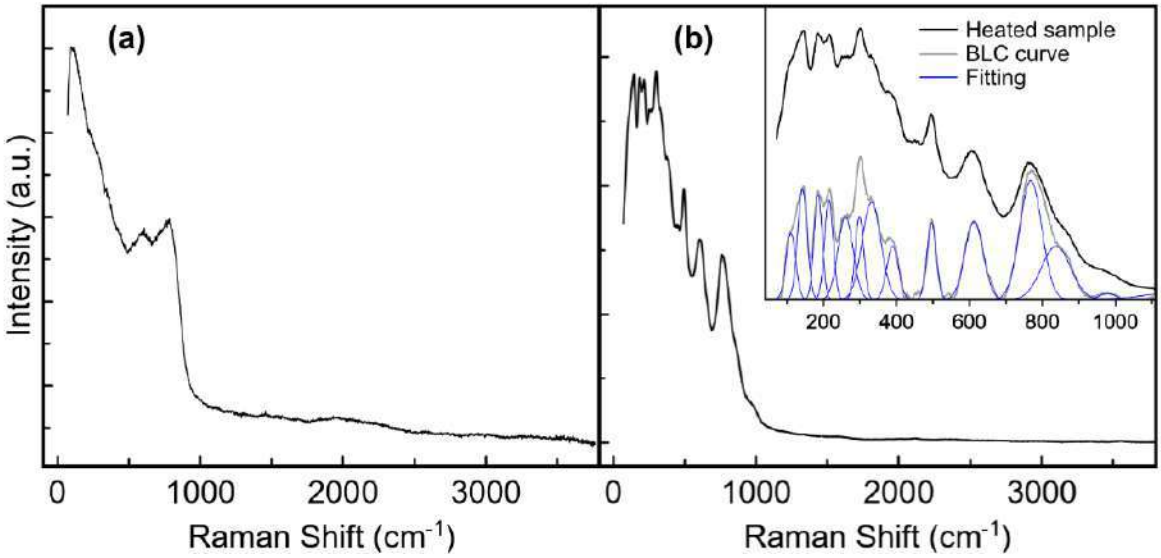

Figure 55**.** Raman spectra of MZ-D (**a**) and crystalline **HZ-D** (**b**). laser is 532 nm.

Table 28. Raman shift (cm^{-1}) of bands observed in crystalized zirconolite.

HZ-A	HZ-B	HZ-D
102	102	110
138	138	142
184	181	185
210	204	214
255	279	260
294	298	298
310	332	331
382	389	389
438	450	-
497	498	496
612	609	612
779	777	768
852	858	837
-	-	978
1175	-	-

There are more Raman bands appear on the spectra and they become sharper after crystallization of samples Figure 55. The main peaks are observed around 142, 185, 298, 496, 612 and 768 cm^{-1}, other weak shoulder bands are located at 110, 214, 260, 331, 389, 837 cm^{-1} [Chukanov et al., 2014; Chukanov et al., 2018]. The observed vibrations are in agreement with that of previously reported zirconolite-related minerals and synthetic zirconolite [Blackburn et al., 2020; Salamat et al., 2013; Thompson et al., 2021; Zhang et al., 2018]. The vibrational mode at 770 cm^{-1} is assigned to the symmetric excitation of TiO_6 octahedra. The bands in the range of 400–800 cm^{-1} correspond to

lower intensity TiO_6 internal vibrations, whereas those below 400 cm^{-1} attributed to vibrations of CaO_8 and ZrO_7 polyhedra [Blackburn et al., 2020; Chukanov et al., 2018]. Table 28 listed the peak positions observed in heated samples **HZ-A**, **-B** and **-D**.

3.5.4 Recrystallization of the metamict zirconolite

The metamict powder sample MZ-D was heated to 1200 °C, its diffraction pattern at each 30 °C shows the phase evolution during recrystallization in Figure 56. Sample from group **D** is contaminated by mineral inclusions such like hydroxyapatite. The X-ray diffraction pattern of **MZ-D** at room temperatures only shows amorphous halo, except a few of impurity peaks. Upon heating, dehydration of hydroxyapatite proceeds, which accompanied by decomposition above 750°.

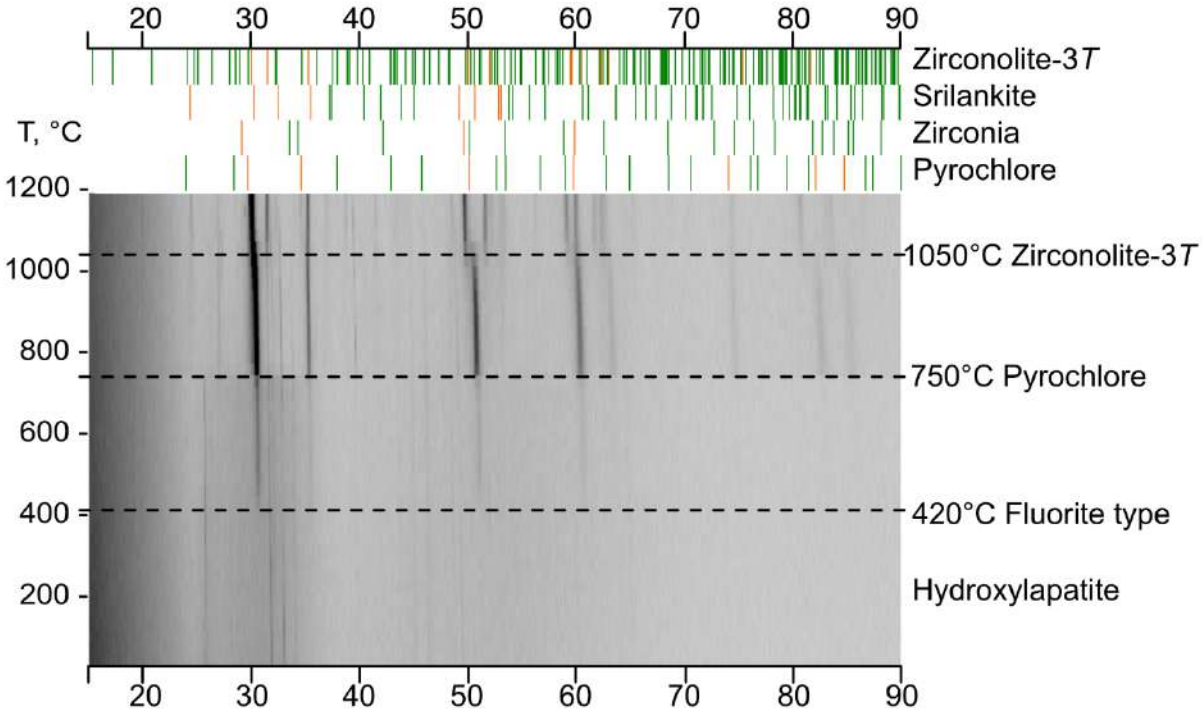

Figure 56. Phase evolution in **MZ-D** with increasing temperature.

The crystallization of a pyrochlore phase can be identified at 750 °C. A fluorite structure phase ($Zr_{0.9}Mg_{0.1}O_2$, ICSD62995), which shows similar reflections as pyrochlore, is firstly observed at 420 °C. The pyrochlore phase significantly increases the intensity of peaks.

The appearance of reflection (006) at 2θ=31.8° indicate that zirconolite crystallized at 1050 °C. A lot of studies on the incorporation in zirconolite reveal the occurrence of polytypes such as 3T, 3O, and 4M with increasing levels of substitution on the Ca, Zr, and Ti sites [Gilbert et al., 2010; Ji et al., 2020]. The polytype 2*M* is characterized by a small unit cell and is more common in zirconolite with relatively pure composition [Vance et al., 2002]. Due to the structure similarity, these polytypes have a lot of X-ray diffraction peak coincided, including the most intensive reflection at around 2θ=30.1°, that resulted in misleading in phase identification.

The empirical formula of sample **HZ-D** derived from Electron Microprobe analysis is $(Ca_{0.81}, REE_{0.08}, Th_{0.04}, U_{0.02})_{\Sigma 0.97}$ $(Zr_{0.96}, Hf_{0.002})_{\Sigma 0.96}$ $(Ti_{1.13}, Nb_{0.37}, Ta_{0.03})_{\Sigma 1.53}$ $Fe_{0.34}$ $Mn_{0.02}$ $Al_{0.04}$ $Si_{0.05}$ O_7.

Ca is substituted by Th, U, and rare earth elements, while Nb and Ta likely occupy some of the Ti sites. The structure-2*M* likely less stable for the composition with such a big amount of substitution elements. Figure 57 compares reflection positions with reference patterns. The reflections at 50.2 (220), 59.7 (042), and 60.6 (226) are assigned to zirconolite-3T, with no strong reflections exclusively belonging to other polytypes.

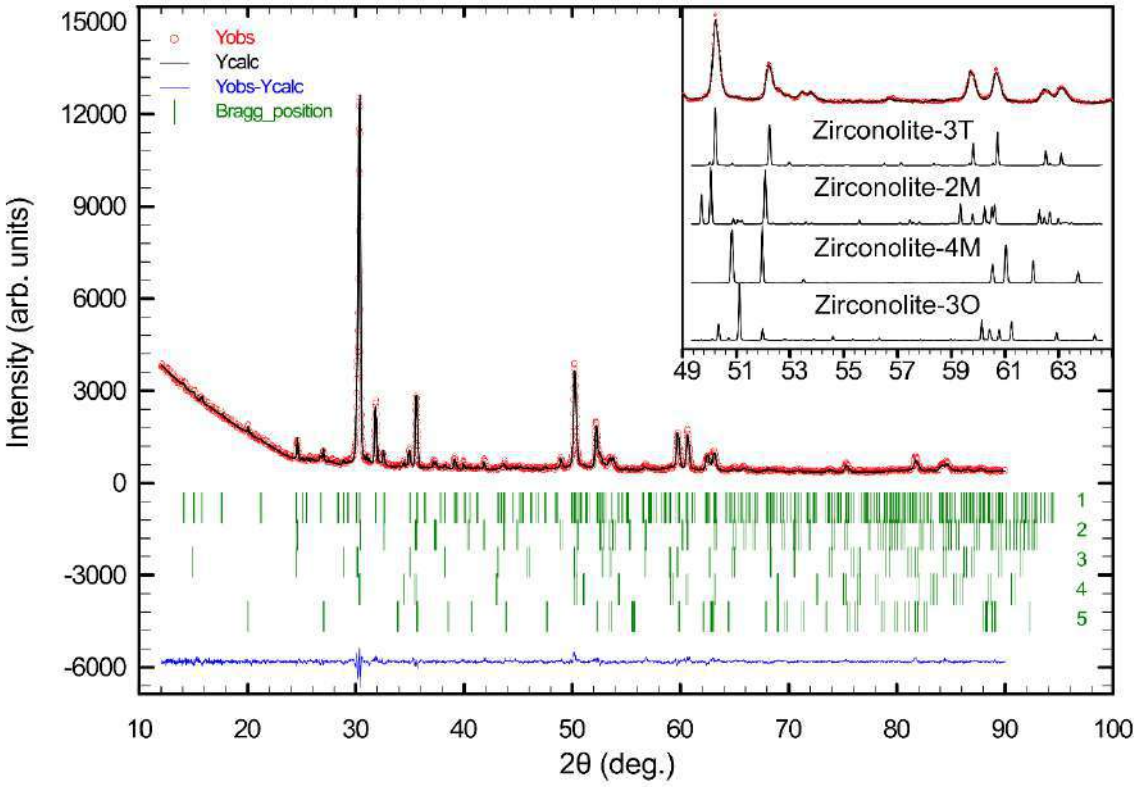

Figure 57**.** X-ray diffraction spectrum of **HZ-D**: nine identified phases listed in Table 29. The focused view (zoomed in 49°-65°) displays the distinctive reflections from polytype 3T, in comparison with other polytypes. Used reference patterns: zirconolite-3*T* [Zubkova et al., 2018], -2*M* [Whittle et al., 2012], -4*M* [Coelho, Cheary, Smith, 1997], -3*O*[Chukanov et al., 2019].

Table 29. Crystallization of zirconolite-3T and associated phases evidenced by Rietveld analysis of sample **HZ-D**.

R-factors	χ^2	2.19	
	Rp	3.66	
	Rwp	4.98	
	Rexp	3.36	
Phase	Name	Wt.%	Reference
1	Zirconolite-3*T*	53.55(51)	[Zubkova et al., 2018]
2	Srilankite	24.64(37)	[Siggel, Jansen, 1990]
3	Pyrochlore	14.58(23)	[Lewandowski et al., 1992]
4	Zirconia	4.98(3)	[Hunter, Howard, Kim, 1998]
5	Zircon	2.25(6)	[Hazen et al., 1987]

Table 29 lists the phases identified in the heated sample and their weight percentage. The major phases crystallized in structures of zirconolite-3*T* (53 wt.%), srilankite (24 wt.%), pyrochlore (14 wt.%) and zircon (2 wt.%), which agree with chemical analyses of heated samples. In the meanwhile, minor phases such as zirconia (5 wt.%) and perovskite are observed, possibly crystallized from certain

non-formula composition or originating from the mineral inclusions in the initial samples.

3.5.5 Thermal expansion of zirconolite-3*T*

Figure 58 shows the temperature dependence of unit cell parameters. The recrystallized sample **HZ-D** is used to exam the thermal expansion of zirconolite-3T. Upon heating to 1200 °C, zirconolite-3T shows very little thermal expansion. Its unit cell parameter *a* and *b* change in a very small range of 7.26 - 7.34 Å, while *c* increases from 16.87 to 17.04 Å. The CTE values obtained are given in Table 30. Coefficients of thermal expansion (CTE) were obtained by fitting a quadratic polynomial to the temperature dependence of unit cell parameters in a range of 25-1200°C:

$a(T) = b(T) = 7.26240(12) + 0.00005634(47)\cdot T + 0.00000000737(37)\ T^2$

$c(T) = 16.86206(78) + 0.0001322(30)\cdot T + 0.0000000156(24)\ T^2$

$V(T) = 770.201(41) + 0.01795(16)\cdot T + 0.00000249(13)\ T^2$

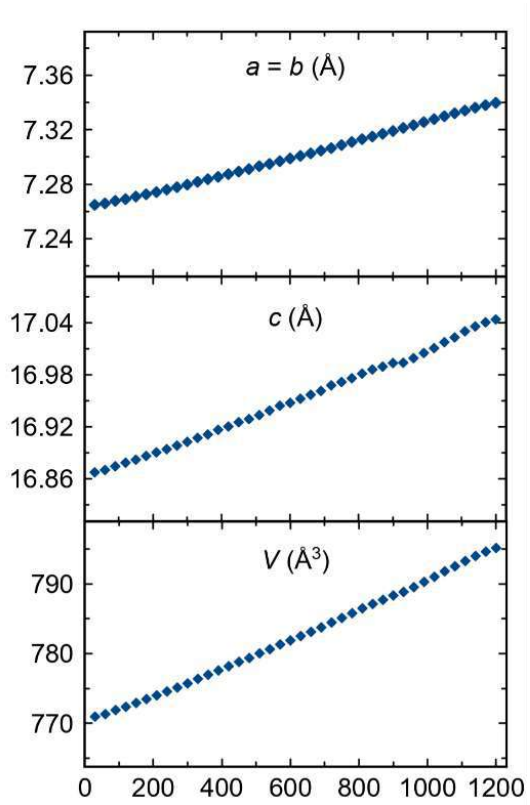

Figure 58**.** Temperature dependence of unit cell parameters of trigonal zirconolite.

Table 30**.** Coefficients of thermal expansion of zirconolite-3*T*.

T, °C	$\alpha_{11}=\alpha_{22}=\alpha_a=\alpha_b$	$\alpha_{33}=\alpha_c$	α_V
25	7.807(62)	7.89(17)	23.50(20)
200	8.151(45)	8.20(12)	24.50(14)
400	8.543(26)	8.555(73)	25.640(85)
600	8.932(15)	8.909(43)	26.773(50)
800	9.319(25)	9.262(68)	27.900(80)
1000	9.704(42)	9.61(12)	29.02(14)
1200	10.087(62)	9.96(17)	30.13(20)

Values of expansion tensor coefficients, multiplied by 10^{-6}

Figure 59 illustrates the expansion on principal axes via ellipsoids. The thermal expansion

within the *ab* plane is isotropic constrained by the symmetry. The average CTE values within the temperature range of 25-1200 °C are as follows: $\overline{\alpha_a} = \overline{\alpha_b} = \overline{\alpha_{11}} = \overline{\alpha_{22}} = 8.95 \cdot 10^{-6}$ °C^{-1}. Similarly, thermal expansion along the c-axis yields a comparable value: $\overline{\alpha_a} = \overline{\alpha_b} = 8.93 \cdot 10^{-6}$ °C^{-1}, indicating nearly isotropic thermal expansion in zirconolite-3*T*.

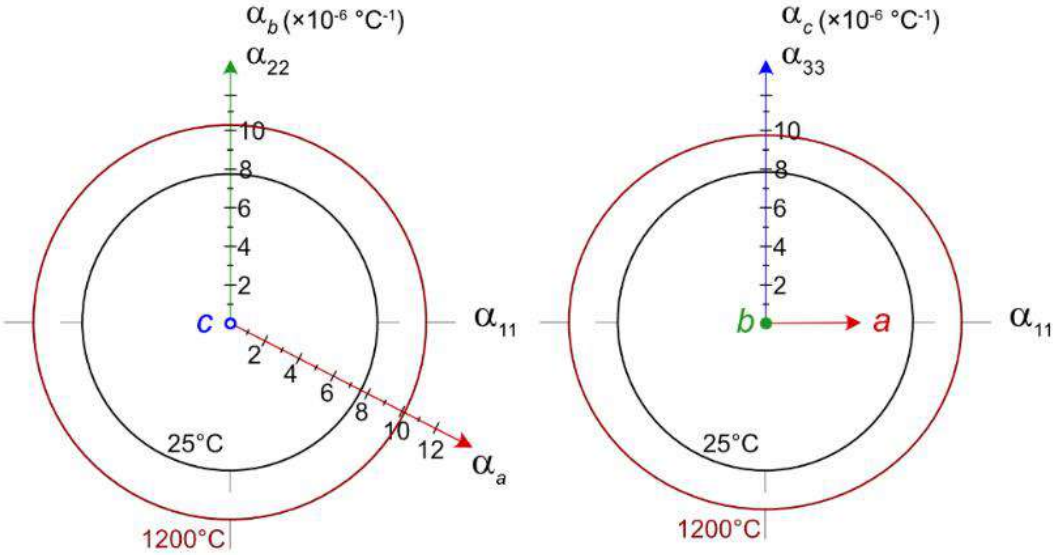

Figure 59. Ellipsoids of coefficients of thermal expansion for zirconolite-3*T*.

3.5.6 Remarks for subsection

In this study, three groups of zirconolites were morphologically characterized and chemically analyzed. The metamict zirconolite samples from the Kovdor massif exhibit notable concentrations of Nb_2O_3, lanthanides, and actinides.

The natural zirconolite-3*T* recrystallizes at 1050°C. The pyrochlore-type and fluorite-type phases precede the recrystallization of zirconolite-3*T* (Figure 56). This observation is in agreement with previous studies when the precursor powder with the composition of zirconolite is heated, the first compound formed has the fluorite-type structure[Vance et al., 1990]. A reverse sequence of phase evolution was observed for zirconolite damaged by radiation. Ewing and Headley [Ewing, Headley, 1983] have reported that upon the radiation damage the crystalline zirconolite first transforms into a mixture fluorite-type phases, eventually becoming completely amorphous. In addition, the formation of pyrochlore may point to the decomposition of the solid solution of zirconolite. As previous research shows that the zirconolite is gradually replaced by pyrochlore, when actinides gradually substitute in Zr-site [Vance et al., 2002; Zhang et al., 2018].

In general, the CTE obtained for zirconolite-3*T* mineral sample with complex composition agrees well with previous studies. Ball et al. [1992] reported CTE values of 10.05(19) ×10^{-6} °C^{-1} and 9.83(15) ×10^{-6} °C^{-1} for 3*T* and 2*M* polytypes, respectively. The lower CTE value observed in our study for zirconolite-3*T* may be attributed to the complex chemistry and polyphase nature of the studied material. This observation suggests that matrix materials may reduce CTE in polyphase ceramics compared to their monophasic counterparts. Zirconolite-3*T* almost isotropic thermal expansion with a volume CTE a_V in the range 23.50(20) to 30.13(20) 10^{-6} °C^{-1}confirms the remarkable

properties of these phases for the use in complex and multicomponent ceramics for the immobilization of HLW.

3.6 Davidite-(La)[14]

Sample origin. Mineral sample, shown in Figure 60, originates from the Radium Hill mine, Australia [Ludwig, Cooper, 1984; Whittle, 1959]. It was stored in the previously existed collection of the radioactive minerals at the department of the Mineral Deposits, Saint-Petersburg State University, Russia.

The initial metamict davidite grains, labeled Dav.1-Dav.5, were hand-picked from the host rock. Dav.4 and Dav.5 grains were each placed into a Pt crucible and kept at 1200 °C for 24 h in air in a Nabertherm furnace followed by cooling to 25 °C with a cooling rate of 5 °C/min. In the text below, we refer to metamict davidite-(La) as **MD** and recrystallized davidite-(La) obtained by heating a metamict sample as **HD**.

Figure 60. Metamict davidite-(La) (**MD**) in the host rock and grains selected for the study.

3.6.1 Chemical composition

The results of electron microprobe analysis are presented in Table 31. Based on 38 O atoms per formula unit, the following formula was calculated (17 points) for the **MD** sample: $(La_{0.48}, Ce_{0.36}, Ca_{0.09})_{\Sigma 0.93}$ $(U_{0.29}, Th_{0.01}, Pb_{0.02}, Y_{0.37}, Nb_{0.03}, Nd_{0.01}, Sm_{0.01}, Gd_{0.01}, Dy_{0.05}, Er_{0.04}, Yb_{0.07})_{\Sigma 0.91}$ $(Mn^{2+}_{0.05}, Fe^{2+}_{1.97})_{\Sigma 2.02}$ $(V_{0.20}, Cr_{0.24}, Fe^{3+}_{5.32})_{\Sigma 5.75}$ $Ti_{12.14}$ $(O_{36.69}, H_2O_{1.31})_{\Sigma 38}$. The water content is determined from the mass difference revealed by the TG analysis.

The backscattered electron (BSE) image in Figure 61 reveals that MD grains exhibit zoning. The brighter zones in BSE correspond to higher U and Th contents but lower Y and rare earth elements (REE). The darker zones in BSE exhibit the lower U and Th but higher Y and REE contents. This zonal distribution of chemical elements may indicate changes in the crystallization conditions. However, this pattern may also be linked to the subsequent post-crystallization processes. Previous studies have indicated that rocks containing davidite-(La) at Radium Hill underwent at least two stages of isotope redistribution [Ludwig, Cooper, 1984].

[14] Davidite-(La) is a specie of crichtonite group, see 1.1.6. It has trigonal structure $R\bar{3}$ (Figure 6).

Table 31. Chemical composition (wt.%) of the metamict (**MD**) (grains Dav.1, Dav.2, Dav.3) and heat-treated (**HD**) (grains Dav.4, Dav.5) davidite-(La). The water content is calculated by the mass difference determined via TG analysis. The *a.p.f.u.* is calculated based on O = 38.

	Initial metamict sample **MD**			Heat-treated **HD**		
Oxides	Average	Range	e.s.d.	Average	Range	e.s.d.
CaO	0.28	0.22-0.37	0.04	0.35	0.26-0.69	0.15
TiO_2	51.66	50.73-52.55	0.43	51.47	47.29-53.32	2.10
V_2O_5	0.95	0.77-1.16	0.12	0.87	0.62-1.07	0.15
Cr_2O_3	0.95	0.68-1.19	0.14	0.92	0.8-1.08	0.08
MnO	0.18	0-0.37	0.11	0.22	0.12-0.3	0.06
Total Fe	30.19	29.78-30.62	0.25	25.57	24.11-28.37	1.54
Fe_2O_3	22.65			17.90		
FeO	7.55			7.67		
Y_2O_3	2.24	1.85-2.45	0.13	1.98	1.41-3.59	0.78
Nb_2O_5	0.23	0-0.39	0.09	0.09	0-0.51	0.19
La_2O_3	4.15	3.97-4.56	0.15	4.26	3.6-4.91	0.48
Ce_2O_3	3.11	2.85-3.34	0.13	3.15	2.85-3.47	0.25
Nd_2O_3	0.06	0-0.49	0.13	0.14	0-0.56	0.22
Sm_2O_3	0.03	0-0.28	0.09	0.06	0-0.36	0.13
Gd_2O_3	0.10	0-0.31	0.14	0.04	0-0.26	0.10
Dy_2O_3	0.54	0-0.84	0.24	0.42	0-0.73	0.31
Er_2O_3	0.42	0-0.66	0.20	0.55	0-1.11	0.42
Yb_2O_3	0.78	0.44-1.13	0.18	0.97	0.61-1.57	0.31
PbO	0.18	0-0.4	0.14	0.23	0-0.37	0.12
ThO_2	0.15	0-0.38	0.13	0.08	0-0.26	0.12
UO_2	4.15	3.64-5.04	0.41	6.34	3.8-8.68	1.48
Total	100.36	98.69-101.71	0.88	97.69	97.09-98.41	0.52
H_2O	1.26					

a.p.f.u.	Initial	Heated
O^{2-}	38	38
La^{3+}	0.48	0.51
Ce^{3+}	0.36	0.38
Ca^{2+}	0.09	0.12
(La,Ce,Ca)	0.93	1.01
U^{4+}	0.29	0.46
Th^{4+}	0.01	0.01
Pb^{2+}	0.02	0.02
Y^{3+}	0.37	0.34
Nb^{5+}	0.03	0.01
Nd^{3+}	0.01	0.02
Sm^{3+}	0.01	0.02
Gd^{3+}	0.01	0.00
Dy^{3+}	0.05	0.04
Er^{3+}	0.04	0.06
Yb^{3+}	0.07	0.10
(U,Y,REE)	0.91	1.07
Mn^{2+}	0.05	0.06
Fe^{2+}	1.97	2.09
(Mn^{2+},Fe^{2+})	2.02	2.15
V^{5}+	0.20	0.19
Cr^{3+}	0.24	0.24
Fe^{3+}	5.32	4.38
(Fe^{3+},Cr^{3+})	5.75	4.80
Ti^{4+}	12.14	12.59
H_2O	1.31	0

Heat treated grains Dav. 4, 5 (i.e., **HD**) have the formula: $(La_{0.51}, Ce_{0.38}, Ca_{0.12})_{\Sigma 1.01}$ $(U_{0.46}, Th_{0.01}, Pb_{0.02}, Y_{0.34}, Nb_{0.01}, Nd_{0.02}, Sm_{0.02}, Gd_{0.00}, Dy_{0.04}, Er_{0.06}, Yb_{0.10})_{\Sigma 1.07}$ $(Mn^{2+}{}_{0.06}, Fe^{2+}{}_{2.09})_{\Sigma 2.15}$ $(V_{0.19}, Cr_{0.24}, Fe^{3+}{}_{4.38})_{\Sigma 4.80}$ $Ti_{12.59}$ O_{38}. BSE image of two heat-treated davidite grains is shown in Figure 62, where the mineral grains exhibit a porous texture. There is an irregular-shaped inclusion with a diameter of about 10 μm in Dav. 5, which has a chemical composition of uraninite UO_2. Bright spots with a diameter smaller than 1 μm can be observed (Figure 62). However, due to their extremely small size, the chemical composition of these spots cannot be determined unambiguously. These small grains have a higher U and Y content comparing to the grayish "background", but a lower Fe and Ca content. As can be seen from the BSE images acquired before and after the heating, there is a redistribution of elements. Other phases have crystallized in addition to davidite. (see below).

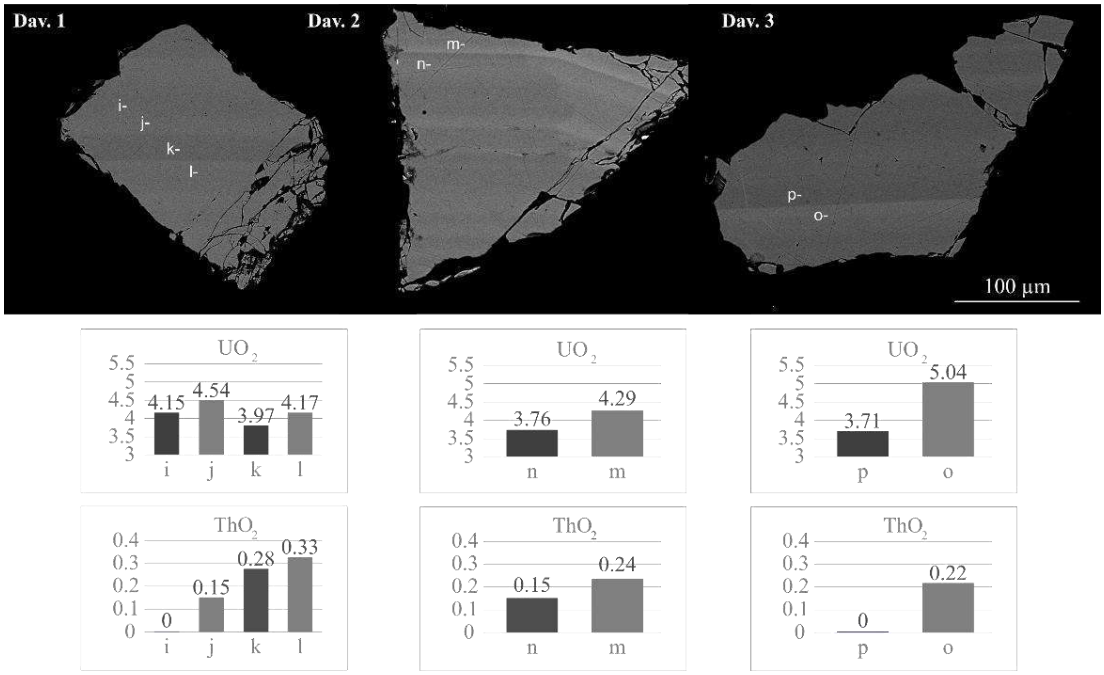

Figure 61. BSE images of the metamict davidite-(La) grains (i.e., **MD**). The BSE bright and dark areas differ due to the different uranium and thorium content.

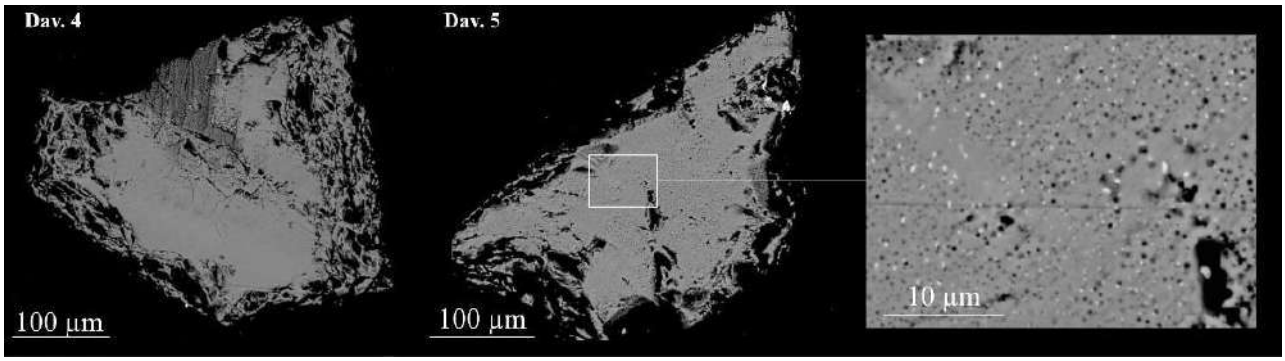

Figure 62. BSE images of the heat-treated sample grains (i.e., **HD**). The porous texture is shown to the right. Many bright dots with a size of less than 1 µm can be seen.

3.6.2 Raman spectroscopy

Raman spectra of the **MD** and **HD** are represented in Figure 63. The vibration modes in both spectra are not pronounced. Baseline (BL) correction using Crystal-Sleuth software was applied. Gaussian function peak fitting was done.

Obtained spectra for both initial and heat-treated sample show typical bands for the crichtonite-group minerals in the regions of 100-200 cm^{-1}, 300-450 cm^{-1}, and 700-800 cm^{-1}[Alifirova et al., 2020]. We have compared the collected spectra with those of davidite-(La) [Frost, Reddy, 2011a], and other mineral species of the crichtonite group [Alifirova et al., 2020]. Despite the fact that one of the samples studied earlier by Frost and Reddy [2011a] is also from the Radium Hill, its Raman spectrum slightly differs. The peak at 641 cm^{-1} has an increased intensity, while the bands at 732 and 809 cm^{-1} have lower intensity. The difference in Raman spectra depends on the distribution of cations in *T*, *C*1-*C*3 sites (general formula of davidite $^{XII}A\,^{VI}B\,^{IV}T_2\,^{VI}C1_6\,^{VI}C2_6\,^{VI}C3_6\,O_{38}$) [Alifirova et al., 2020].

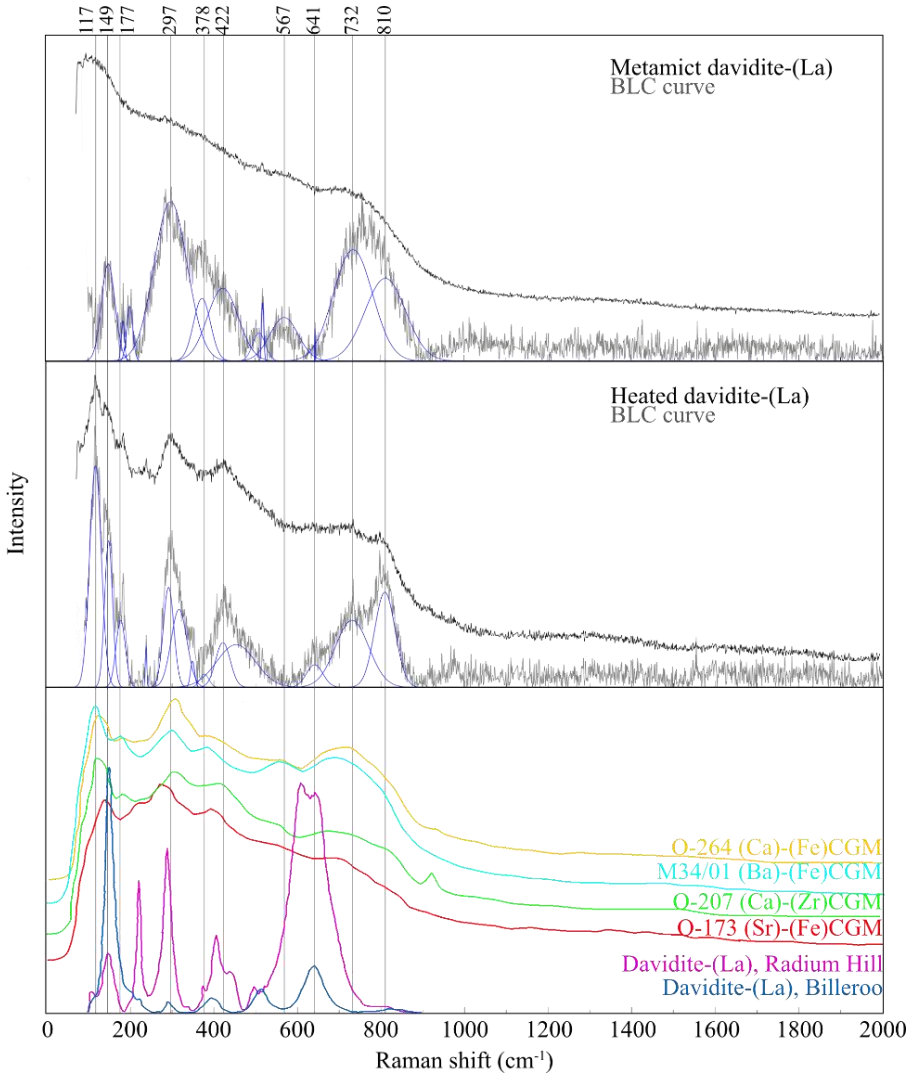

Figure 63. Raman spectra of **MD** and **HD**. Baseline correction (BLC) was performed using the program CrystalSleuth. Four published spectra [Alifirova et al., 2020] and davidite-(La) from Radium Hill and Billeroo [Frost, Reddy, 2011a] are given for comparison.

The Raman spectrum of **MD** shows broad and low-intensity bands. The strongest Raman bands are observed at 149, 297, 378, 422, 732, and 810 cm^{-1}. Other weaker bands can be detected at 177, 199, 508, and 567 cm^{-1}. Bands can be assigned according to Frost and Reddy [2011a]. Bands below 220 cm^{-1} can be tentatively assigned to molecular deformation and lattice modes. The 238-274 cm^{-1} and 300-560 cm^{-1} bands may correspond to U-O vibrations. The bands at 600-650 cm^{-1} are assigned to the Ti-O stretching vibrations. The bands at 732 and 811 cm^{-1} are due to the symmetric stretching vibration of $(UO_2)^{2+}$.

Raman spectra of the **HD** sample represent many inten sive bands: 117, 149, 177, 238, 297, 317, 350, 378, 422, 454, 642, 732 and 810 cm^{-1}. Raman bands splitting is observed in the range 100-500 cm^{-1}. The vibration mode at 567 cm^{-1} observed for the **MD** sample is not registered for the **HD**.

3.6.3 Thermal analysis

Figure 64 displays the TG and DSC curves. The mineral undergoes a color change and exhibits a porous texture after heating to 1300 °C. The TG curve reveals five stages of the mass loss.

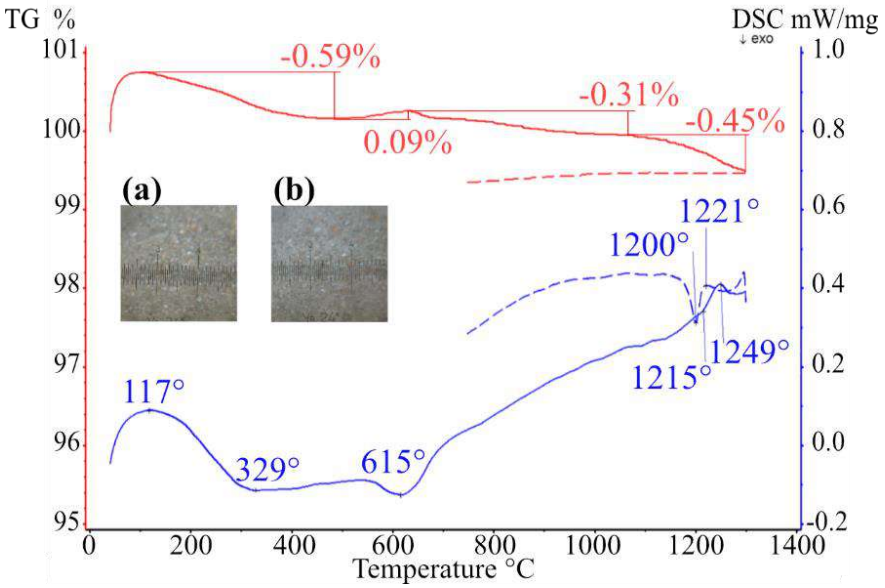

Figure 64. TG and DSC curves for the **MD** and photographs of the sample before (**a**) and after (**b**) the heating/cooling cycle (5 × 5 mm). Note the color change of the probe during the experiment.

The first endothermic effect with a peak at 121 °C corresponds to the loss of 0.42 wt.% due to the release of the adsorption water. A notable exothermic slope appeared in the DSC curve in the range of 529–747 °C. Notably, the mass has increased in the range 529–617 °C but returned to its decreasing trend after reaching 617 °C. The combination of the mass increase and exothermic effect suggests the possibility of the oxidation process for iron and other elements.

In the range 747–1215 °C, the TG curve exhibits a 0.38 wt.% mass loss. The DSC curve reveals an endothermic peak at 1248 °C. This effect is accompanied by a 0.26 wt.% mass loss in the TG curve. The shape of the endothermic peak suggests a partial melting of the sample. During the subsequent cooling, the DSC curve showed an exothermic peak at 1201 °C due to the crystallization of the partially melted material.

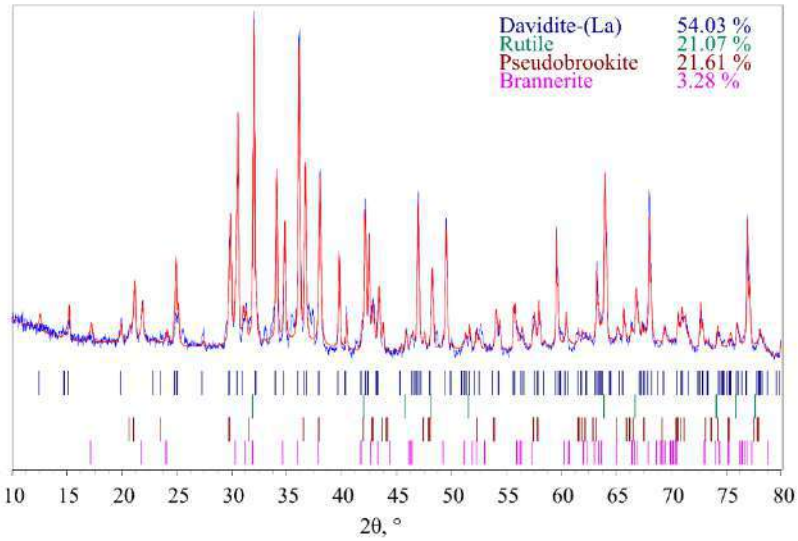

Figure 65. Powder X-ray diffraction pattern (R_{wp} = 4.4%) for the Dav.1 sample, obtained after the thermal analysis.

Figure 65 shows the X-ray powder pattern obtained for the sample after the thermal analysis. The following ICSD cards were employed: #100554 davidite-(La), #62679 rutile #291617 pseudobrookite, and #30670 ilmenite. The dominant phase in the sample is davidite-(La). Ilmenite

(10.91 wt.%), rutile (2.22 wt.%) and pseudobrookite (2.66 wt.%) are the main decomposition products after the partial melting of the sample.

3.6.4 High-temperature X-ray diffraction of MD

Figure 66 a show the evolution of the PXRD patterns of the **MD** in the range of 25–1200 °C. The peaks corresponding to davidite-(La) (ICSD #100554) gradually appear in the range 600–700 °C. Figure 67 shows the pattern obtained after the complete cooling of the crystallized davidite-(La) with the following phases identified: davidite-(La) 84.19 wt %, rutile 2.22 wt %, pseudobrookite 2.66 wt % and ilmenite 10.91 wt. %.

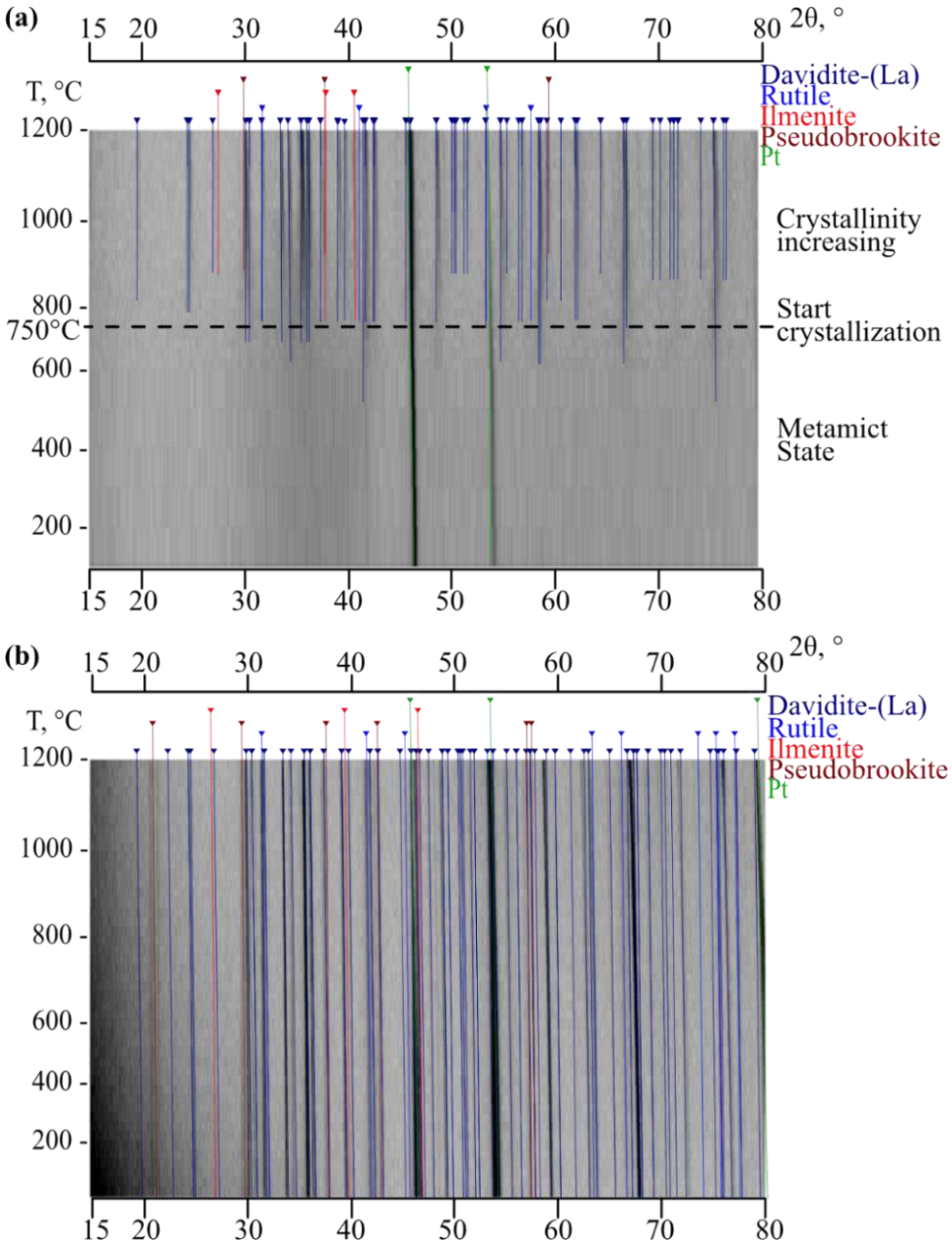

Figure 66. Evolution of the powder diffraction patterns of the **MD** (**a**) and **HD** (**b**) as a function of temperature.

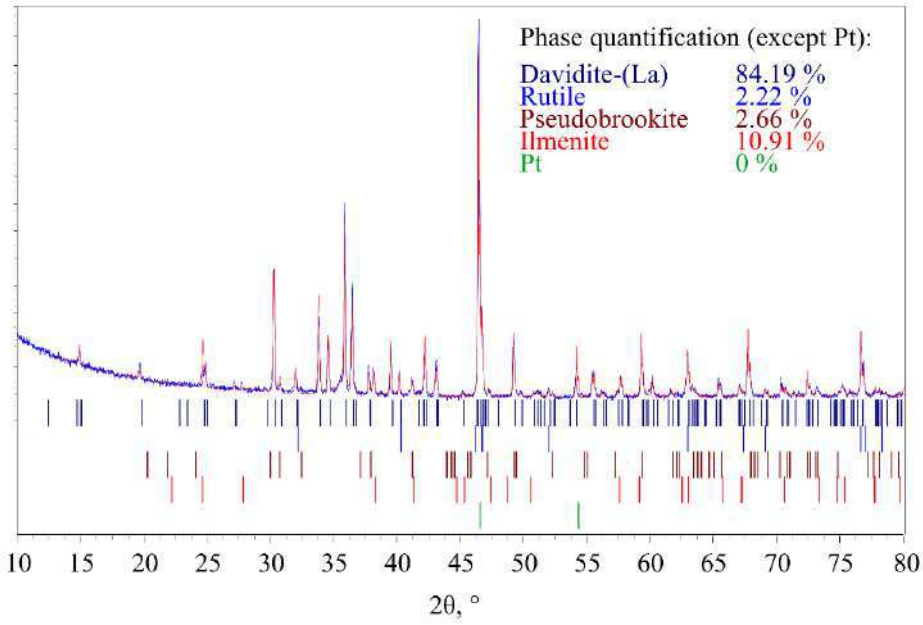

Figure 67. X-ray powder diffraction pattern (Rwp = 7.4%) obtained after the high-temperature X-ray diffraction measurements shown in Figure 66 a.

3.6.5 The thermal expansion of HD

The **HD** unit-cell was refined at each temperature, employing the hexagonal lattice of the space group $R\bar{3}$, instead of the rhombohedral setting ($R\bar{3}$:R). The R_{wp} value increases with the temperature rise from 9.88% to 12.74%, and the goodness-of-ft (GoF) increases from 1.63 to 1.94.

The unit-cell parameters of the **HD** almost linearly increase upon heating (Figure 68a). The unit-cell parameter *a* increases in the narrow range 10.364 (1) – 10.491 (1) Å, while the *c* value increases from 20.858 (1) to 21.133 (1) Å. The unit-cell volume increases from 1940.39 (24) to 2014.62 (31) Å^3. The temperature dependence of the lattice parameters in the range of 25–1200 °C was approximated by the following polynomials of the second order:

$a(T) = 10.36332(43) + 0.0847(17)\cdot10^{-3}\cdot T + 0.0159(13)\cdot10^{-6}\cdot T^2$

$c(T) = 20.8546(13) + 0.1709(50)\cdot10^{-3}\cdot T + 0.0463(40)\cdot10^{-6}\cdot T^2$

$V(T) = 1939.69(24) + 47.47(94)\cdot10^{-3}\ T + 10.98(76)\cdot10^{-6}\cdot T^2$

Table 32 provides the thermal expansion coefficients (TEC) for **HD**. The average CTE along the *a* and *b* axes is $\bar{\alpha}_a = \bar{\alpha}_b$ =9.96 (3) × 10^{-6} ºC^{-1}, while the CTE along the c axis is somewhat more pronounced: $\bar{\alpha}_c$ =10.79 (4) × 10^{-6} ºC^{-1}. The observed character of the thermal expansion (Figure 68b) is in agreement with the structure of davidite-(La) characterized by layers stacked along the *c* axis. The volume coefficient α_V was calculated as follows: $\alpha_V = \alpha_{11} + \alpha_{22} + \alpha_{33} = \alpha_a + \alpha_b + \alpha_c$. It increases from 23.03(31) × 10^{-6} to 35.08(32) × 10^{-6} ºC^{-1} in the temperature range 25–1200 °C [Chen et al., 2024b].

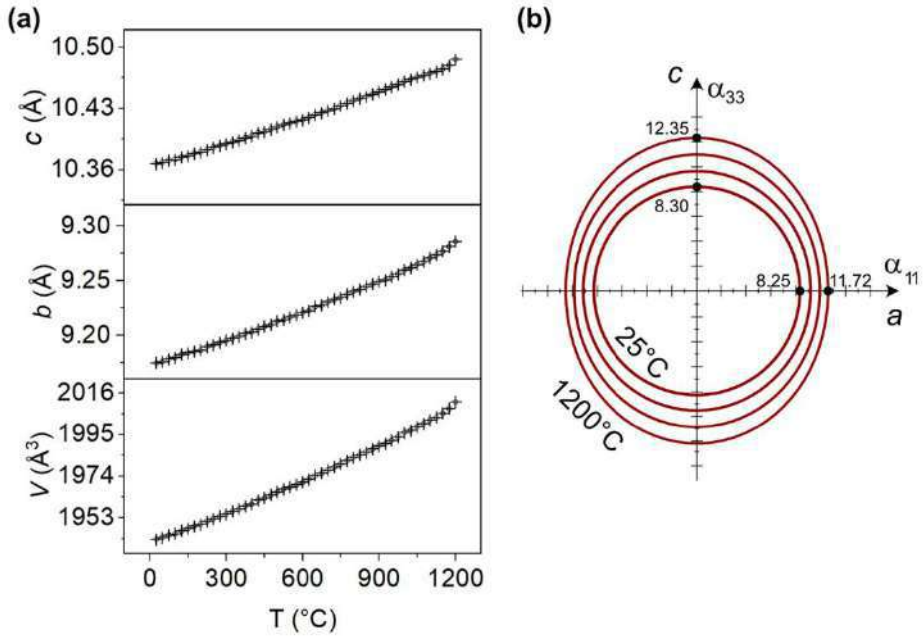

Figure 68. Temperature dependence of the unit-cell parameters for **HD** (**a**). The main sections of the thermal expansion tensor (**b**). Values of the TEC are multiplied by 10^{-6} ($°C^{-1}$)

Table 32. CTE for davidite-(La) (**HD**) at different temperatures.

T, ºC	CTE, × 10^{-6} ºC^{-1}			
	$\alpha_{11} = \alpha_a$	$\alpha_{22} = \alpha_b$	$\alpha_{33} = \alpha_c$	α_V
25	7.86(12)	7.86(12)	7.30(23)	23.03(31)
100	8.08(11)	8.08(11)	7.65(20)	23.81(27)
200	8.363(87)	8.363(87)	8.12(16)	24.85(22)
300	8.647(68)	8.647(68)	8.59(13)	25.89(17)
400	8.931(51)	8.931(51)	9.057(96)	26.92(13)
500	9.214(37)	9.214(37)	9.522(70)	27.950(94)
600	9.496(31)	9.496(31)	9.986(58)	28.979(79)
700	9.778(37)	9.778(37)	10.449(69)	30.004(95)
800	10.058(51)	10.058(51)	10.910(95)	31.03(13)
900	10.338(68)	10.338(68)	11.37(13)	32.05(17)
1000	10.617(87)	10.617(87)	11.83(16)	33.06(22)
1100	10.89(11)	10.89(11)	12.28(20)	34.07(27)
1200	11.17(13)	11.17(13)	12.74(23)	35.08(32)

3.6.6 Remarks for subsection

The recrystallization of the metamict davidite-(La) (**MD**) was determined by the HTXRD is between 600 and 700 °C, while the DSC curve exhibits an exothermal peak at 615 °C. The **MD** has a massive texture, in contrast to the **HD** having a porous texture due to volume change. HTXRD results indicate that the unit-cell volume of the **HD** increases by 73.23 $Å^3$ within the temperature range of 25–1200 ºC.

Furthermore, the DSC curve exhibits an endothermic effect at 1215 °C, suggesting a partial melting of the **HD** and the formation of minor phases. Following the heating process, the **HD** exhibits an inhomogeneous distribution of elements. It has been found that certain elements are partially or completely excluded from the **MD** structure after heating, thus forming relatively stable phases: ilmenite, rutile and pseudobrookite. Previously, it was reported that pseudobrookite is a common by-

product phase that arises as a result of the hydrothermal synthesis of “uranium davidite $(U,Fe,Ti)_{21}O_{39}$” [Korolev, Gaidukova, Rumyantseva, 1977].

To the best of our knowledge, our study presents the first report on the thermal expansion of the crystalline davidite- (La) (**HD**) with a high content of various radionuclides. Our findings indicate that davidite-(La) exhibits a low coefficient of thermal expansion (CTE) α_V = 23.0(3)- 35.1(3) × 10^{-6} $^oC^{-1}$ in the temperature range 25–1200 °C, indicating its thermophysical stability in contrast to many other phases utilized for nuclear waste immobilization. Furthermore, it exhibits an almost isotropic thermal expansion. All thermal expansion coefficients exhibit a linear increase with the increase in temperature. Despite the limitation of the experiment temperature to 25–1200 °C, the trends of the unit-cell parameters, expressed as derived polynomials, can be utilized to simulate the CTE at higher temperatures.

Chapter 4. New synthetic compounds related to minerals of the crichtonite group

A number of minerals are archetypes for new materials with unusual magnetic properties. An example of such an archetype mineral is the well-known perovskite group. From the position of "from minerals to materials" approach the minerals of the crichtonite group have received much less attention, despite their very high isomorphic capacity and a huge range of elements capable of entering the crystal structure. This prompted us to perform systematic studies on the synthesis of various compounds related to crichtonite and to study the magnetic properties.

4.1 Feasibility of synthesis

The titanium framework in crichtonite, as observed in its natural form, is achievable via laboratory synthesis. This was evidenced by Peterson and Grey [1995], who successfully prepared Ti^{3+}-containing lindsleyite, $BaMn_3Ti_{18}O_{38}$, albeit without magnetic properties characterization. Inspired by their methodology, the author undertook the synthesis of crichtonite titanites and subsequently conducted magnetic property assessments.

The general formula for synthetic crichtonite is $^{XII}A\,^{VI}B\,^{IV}T2_2\,^{VI}C1_6{}^{VI}C2_6{}^{VI}C3_6\,O_{38}$, where the Roman numerals indicate coordination with oxygen atoms. In our work, the *C*-site is occupied by Ti^{4+} and Ti^{3+}, Fe^{3+} or Cr^{3+}, while *B*-sites accommodate Mn^{2+}, the *A*-site accommodates larger cations such as REE^{3+}, Ca^{2+}, Sr^{2+} and Ba^{2+}.

The structure comprises two different R and O layers in a $(ROR^*)_3$ rhombohedral sequence, with R* related to R by an inversion center. Layer R is characterised by 6-member rings, which consists of *C*2,3 octahedra (TiO_6 or FeO_6) sharing edges. The rings are linked together by *T*-site tetrahedra (MnO_4) and 12-coordinated *A* (big cations), as shown in Figure 6. Layer O involves twelve *C*1 octahedra (TiO_6) forming a larger hexagonal ring with a *B* octahedron (MnO_6) at the center. The linkage between R and O layers occur only through vertices, while between T and T* is through *C*1–*C*2 edges.

The framework $AMn_3Ti_{18}O_{38}$ has been successfully synthesized for divalent cations Ca^{2+}, Sr^{2+} and Ba^{2+} in the A-site. Characterization of the magnetic properties of these crichtonites may reveal insights into the impact of ionic radii of cations into the material.

Rare earth elements (REE) are of significant interest in magnetic materials due to their unique electron configurations, offering various possibilities for magnetic interactions. In our study, we attempted synthesis with trivalent REE: Y, La, Ce, Nd, Sm, and Gd. Only three systems, $REEMn_3Ti_{18}O_{38}$ with *REE*= La, Ce, Nd, exhibited a crichtonite phase exceeding 90 %. For Y-Mn-Ti-O, only 10 % of crichtonite was crystallized from the stoichiometric precursor. In the cases of Sm-Mn-Ti-O and Gd-Mn-Ti-O, the percentage of crystallized crichtonite decreased gradually to 85 % and 62 %, respectively. Failure in synthesis occurred as a result of the inability of Sm and Gd to fully occupy the A-site, attributable to their small ionic radii.

Synthetic crichtonite in this work, $A^{2+}(RE^{3+})Mn_3Ti_{18}O_{38}$, with titanium in the C-site, exhibited a mixed state comprising fourteen (thirteen) nonmagnetic Ti^{4+} and four (five) Ti^{3+}. Ti^3 ([Ar]3d^1) with one unpaired electron and Mn^{2+} ([Ar]3d^5) with 5 free electrons were the major contributors to magnetic interaction in the studied compounds.

Apart from substituting the A-site, substitution for B- and C-sites also affects magnetic properties and material performance. Fe^{3+}, with similar ionic radii to Ti^{3+}, has five unpaired electrons ([Ar]3d^5), promise for successful synthesis and enhanced magnetic properties. Substitution of Fe^{3+} for Ti^{3+} was achieved in $LaMn_3Ti_{13}Fe_5O_{38}$ and $SrMn_3Ti_{14}Fe_4O_{38}$, which are detailed later.

The author also explored other possibilities of the crichtonite structure. Uma and Sleight [Uma, Sleight, 2002] synthesized $BiMg_{2.5}V_{18.5}O_{38}$ in the crichtonite structure, providing insight into its potential. We repeated their synthesis route for various vanadate in crichtonite structure, but the results showed limited crystallization (see Table 3), with the aimed phase crichtonite reaching only up to 50%, accompanied by impurities such as V_4O_7 and V_6O_{11}, hindering further magnetic measurements.

4.2 Synthetic crichtonite with rare-earth elements (La^{3+}, Ce^{3+}, Nd^{3+})

Inspired by davidite, we successfully produced the crichtonites with the A-site filled by La^{3+}, Ce^{3+}, and Nd^{3+}. The synthesis utilized chemicals with purities exceeding 99%, including La_2O_3, CeO_2, Nd_2O_3, MnO, and TiO_2 (anatase).

4.2.1 $LaMn_3Ti_{18}O_{38}$

XRD refinement

X-ray diffraction (XRD) analysis confirmed the formation of the desired crichtonite $LaMn^{2+}{}_3Ti^{4+}{}_{13}Ti^{3+}{}_5O_{38}$ (LaMTO) with phase content of 90.54(45) wt.%. Additionally, impurities consisting of 7.64(12) % pseudobrookite, 1.49(7) % rutile, and 0.33(6) % MnO_2 were detected (Figure 69). The phase content in the sample and unit cell parameters of crichtonite were refined using Rietveld method and are provided in Table 34.

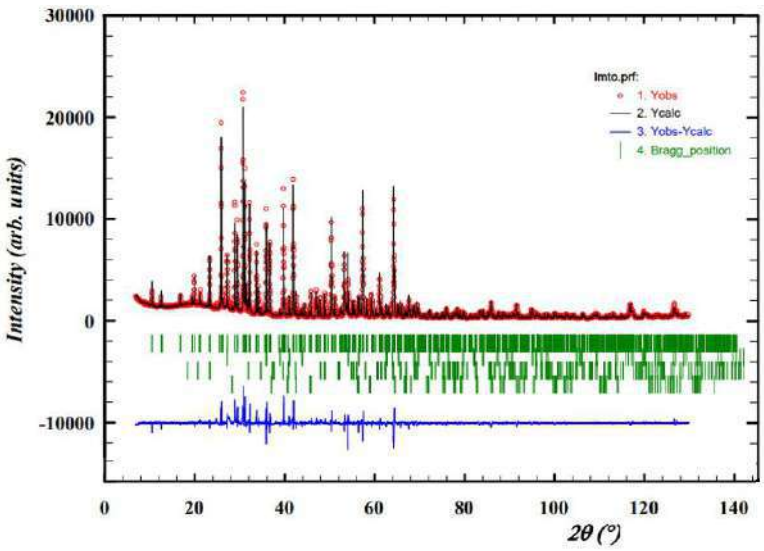

Figure 69. The diffraction spectrum and refinement of LaMTO.

DC magnetic measurements

Figure 70a illustrates magnetic susceptibility of LaMTO, which increases dramatically as the temperature decreases, indicating the onset of magnetic ordering at 4.4 K. There is no significant ZFC-FC divergence observed under 0.1 T applied field. It reaches highest susceptibility of 10.5 emu mol^{-1} at 2K.

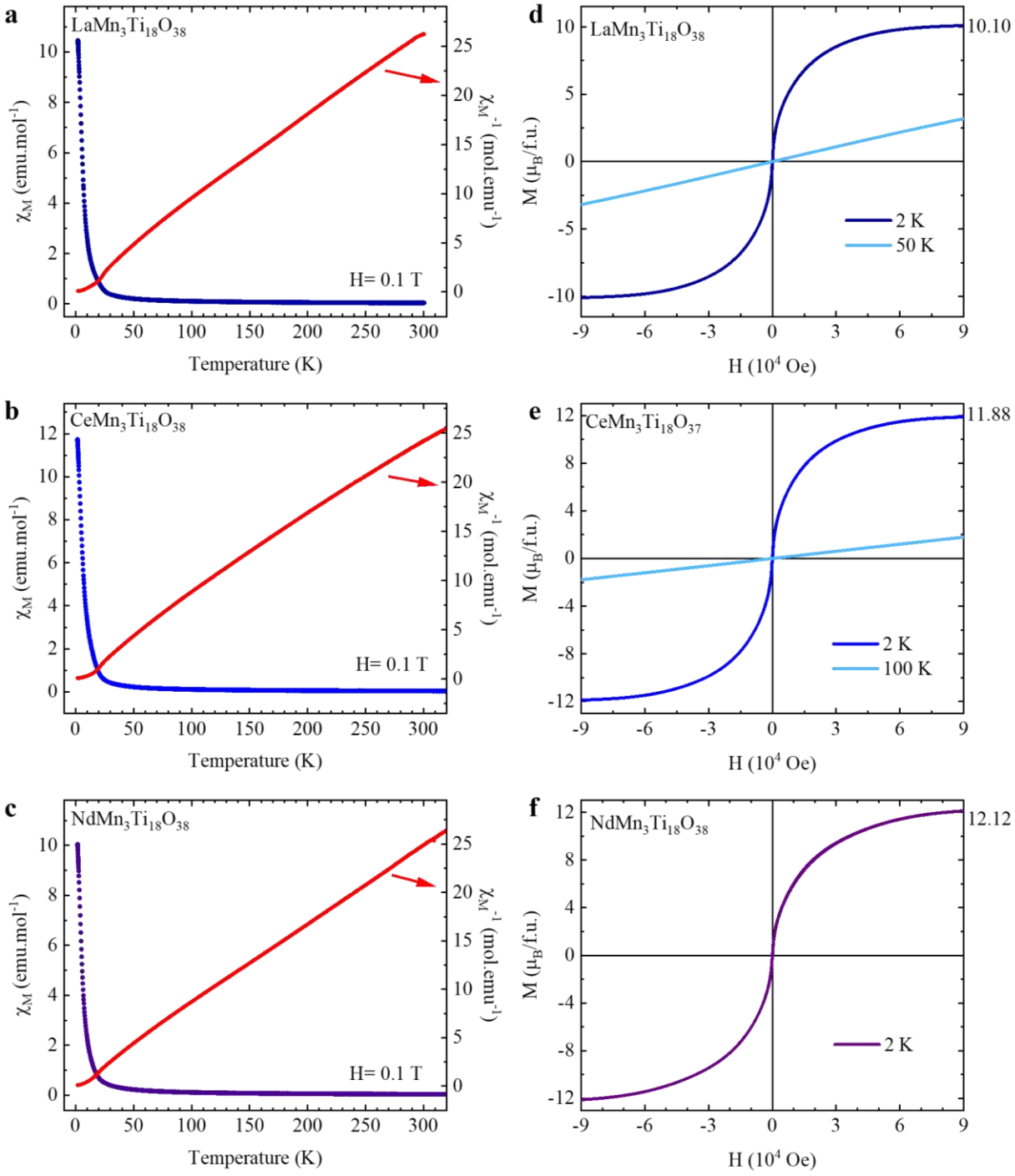

Figure 70. Temperature dependence of magnetic susceptibility (χ_M) and its reciprocal (χ_M^{-1}) for LaMTO (a), CeMTO (b) and NdMTO (c). Field dependent magnetization at different temperatures of LaMTO (d), CeMTO (e) and NdMTO (f).

The reciprocal curves of zero-field-cooled (ZFC) and field-cooled (FC) susceptibility exhibit near-linearity with slight divergence at elevated temperatures (above 100 K).

Within the temperature range of 200-290 K, the inverse susceptibility aligns well with the

Curie–Weiss law. From the fit, an effective moment μ_{eff} = 9.72 μ_B and Weiss Temperature (θ_W) of -7.22 K were determined. The negative Weiss temperature indicates a predominant antiferromagnetic (AFM) interaction, originated by the magnetic moments of Mn^{2+} and Ti^{3+} ions.

The theoretical magnetic moment can be calculated using the expression $\mu_{\text{theor.(LMTO)}} = \sqrt{3 \cdot \mu_{B\,(Mn^{2+})}{}^2 + 5 \cdot \mu_{B\,(Ti^{3+})}{}^2}$ with effective magnetic moments of 5.92 μ_B for Mn^{2+} and 1.73 μ_B for Ti^{3+}, the calculated theoretical magnetic moment for LaMTO is 10.96 μ_B, slightly higher than its magnetic moment determined from the Curie-Weiss fit. This difference between two values may arise from a potential overestimation of sample mass due to impurities present in the sample.

Figure 70d presents the isothermal magnetization of LaMTO measured at temperatures of 2, 10, 20, 30, 40, and 50 K. The curve illustrates that a maximum magnetization of 10.10 μ_B/f.u. is attained under a maximum applied field of 9 T. At 2 K, a narrow hysteresis is observed, with a remnant magnetization of 0.12 μ_B/f.u., indicating the presence of ferromagnetic components. However, hysteresis is absent at temperatures of 10 K and higher.

The expected Mn and Ti spin moments ($2S_{Mn}$ = 5 μ_B and $2S_{Ti}$ = 1 μ_B) in a Ferrimagnetic (FiM) configuration, wherein 15 μB arises from three Mn^{2+} ions while being offset by -5 μB from five Ti^{3+} ions, explain the observed 10.10 μB under a 9 T field.

AC magnetic Measurements

Alternating current (AC) magnetic susceptibility was subsequently measured and revealed a spin-glass behavior of LaMTO, see Figure 71a.

The freezing temperature T_f varies according to the Vogel–Fulcher equation (Figure 71b).

$$\omega = \omega_0 \exp\left(-E_a/k_B \cdot (T_f - T_0)\right)$$

where ω is the frequency, $\frac{1}{\omega_0}$ is the intrinsic relaxation time (t_0), E_a is the activation energy, k_B is the Boltzmann constant and T_0 is the Vogel–Fulcher temperature. After modification of the above equation, one can obtain a simple relation between T_f and ω: $\frac{E_a}{k_B} = \ln(t_0\omega) \cdot (T_0 - T_f)$, with three fitting parameters: T_0, E_a and t_0. The intrinsic relaxation time ($\tau_0 = \frac{1}{\omega_0}$) can vary from 10^{-7} s, found in $Co_{0.2}Zn_{0.8}Fe_2O_4$ cluster-glass compound [Bhowmik, Ranganathan, 2002], to 10^{-13} s typical for spin-glass compounds [Tholence, 1980].

The fittings were made considering the two extremes t_0 values for spin-glass compounds $10^{-9}s \leq t_0 \leq 10^{-13}s$, obtaining $\frac{E_a}{k_B}$ = 0.24(1) and 0.46(4) with T_0 = 2.83(2) and 2.74(3) K, respectively. The very low activation energy in LaMTO is in the typical range of (0.2−2) for cluster spin glasses [Kearins et al., 2021]. Both values are much smaller than obtained for spin-glass compounds[Klimczuk et al., 2009]: e.g. Fe_2TiO_5 (3.4) [Tholence et al., 1986], and is also smaller than estimated for cluster-glass compounds: U_2IrSi_3 (1.6)[Li et al., 2003], $Co_{0.2}Zn_{0.8}Fe_2O_4$ (0.77) [Bhowmik, Ranganathan, 2002]. This comparison strongly suggests the formation of the FM cluster-

glass state in LaMTO below the freezing temperature.

The very low activation energies in LaMTO reflect that T_f changes only 0.09 K when the frequency changes four orders of magnitude. This magnitude of change is three times smaller than LaMTFO (See 4.2.2). For spin-glasses, the relative shift per frequency decade, $\delta T_f = \Delta T_f / [T_f \Delta \log(\omega)]$, is often calculated. In LaMTO we estimate $\delta T_f = 0.007$, which is two order of magnitude smaller than those reported for noninteracting ideal superparamagnetic systems (δ = 0.1) [Dormann, Bessais, Fiorani, 1988], but comparable to 0.005 reported for cluster-glass U_2IrSi_3 [Li et al., 2003] and CuMn, which is an example of a canonical spin-glass compound [Mydosh, 1993].

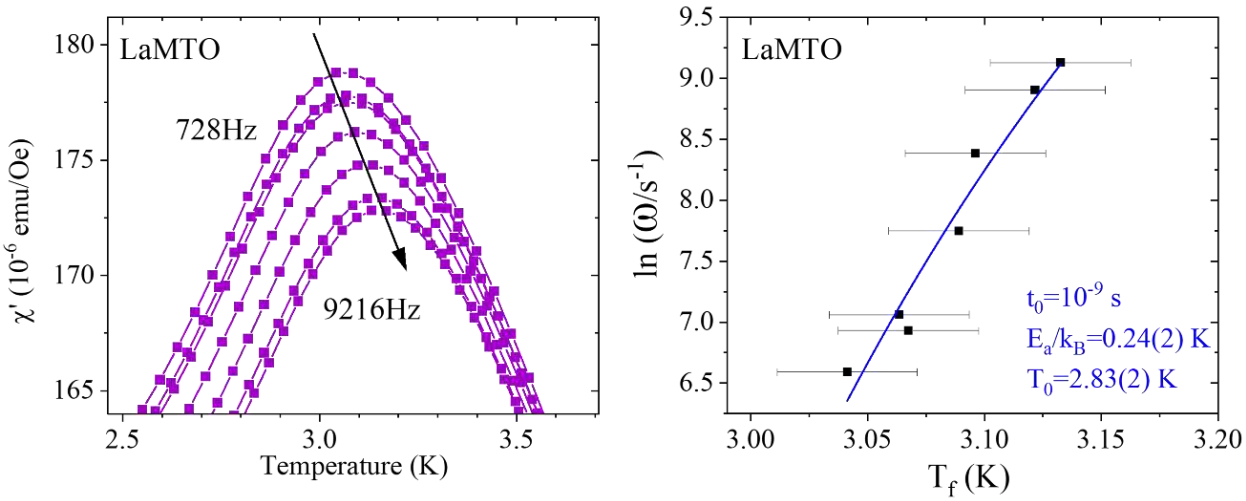

Figure 71. LaMTO's temperature dependence of χ' in alternating current field (a). The change of freezing temperature T_f is fitted well with the Vogel Fulcher equation.

4.2.2 $LaMn_3Ti_{13}Fe_5O_{38}$

XRD refinements

Substitution of Ti^{3+} by Fe^{3+} in LaMTO resulted in a less stable phase. Rietveld analysis proved that the sample contains 78.92(17) wt.% of crichtonite phase, associated with 19.87(13) wt.% of pseudobrookite and ilmenite of 1.21(09) wt.% (Figure 72). Due to the decreased ionic radii of Fe^{3+}, compared with Ti^{3+}, the unit cell of LaMTFO (with a=10.4085(1)Å c=20.8052(2) Å), are smaller than those of LaMTO, a=10.41777(3)Å and c=20.81982(11) Å (Table 34).

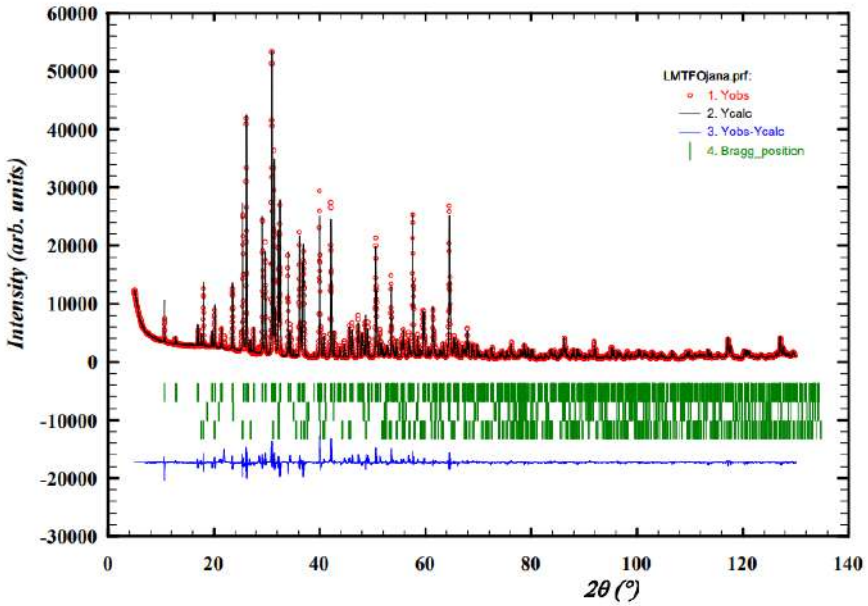

Figure 72. Rietveld refinement of LaMTFO. XRD wavelength λ=1.54 Å.

DC magnetic measurements

The zero-field-cooled (ZFC) and field-cooled (FC) susceptibility curves of LaMTFO indicates a magnetic transition below 12.2(1) K. Subsequently, the curves display a decreasing trend in the temperature from 8 to 2 K, as depicted in Figure 73a. This decrease is accompanied by ZFC-FC divergence, with ZFC susceptibility peaking at 0.93 emu mol^{-1} at 7.6 K, and FC susceptibility reaching its maximum of 0.96 emu mol^{-1} at 5.9 K. Figure 73a illustrates curvature in the reciprocal plots of ZFC and FC susceptibility. Analysis using Curie–Weiss fit across the temperature span of 210-290 K reveals a Weiss temperature (θ_W) of -111.4(2) K, indicating antiferromagnetic interaction.

The magnetization of the LaMTFO sample, as depicted in Figure 73b, exhibits a slow response to the applied field at both 2 K and 10 K. At 2 K, the presence of a narrow hysteresis with a remnant magnetization of 0.15 μ_B/f.u. suggests the presence of ferromagnetic components, which diminishes notably at 10 K. The maximum magnetization of LaMTFO reaches 6.06 μ_B/f.u. at 2 K under an external field of 9 T. The applied field not being sufficiently strong to achieve saturation magnetization. This maximum magnetization deviates from the expected magnetic moment, assuming any colinear arrangement of Mn^{2+} (5 μ_B, 3 *a.p.f.u.*) and Fe^{3+} (5 μ_B, 5 *a.p.f.u.*) spins. In addition, the discrepancy between the actual and expected atom per fomular unit may lead to misestimation of the magnetic moment.

AC magnetic measurements

The alternating-current (AC) susceptibility revealed a spin-glass behavior of LaMTFO, as shown in Figure 73,c. χ' represent the real (in-phase) components of the susceptibility. At different frequencies varying from 193 to 9216 Hz, all χ' measured reach peaks at temperature around 10.5 K, in general agreement with the magnetic transition temperature determined from direct-current (DC) susceptibility measurement, $T_{f(dc)}$=12.2(1) K. The peak temperature is identified with the spin-glass

freezing temperature $T_{f(ac)}$. The freezing temperature changes only 0.30 K when frequency changes four orders of magnitude. The relative variation in freezing temperature per decade of frequency (δ) can be calculated by considering $\delta = \frac{\Delta T_f}{T_f \Delta \log(\omega)}$ [Klimczuk et al., 2009; Marcano et al., 2019], yield δ = 0.007 , which is similar to that of LaMTO – an order of magnitude smaller than for canonical spin-glass systems and thus suggests the formation of an FM cluster-glass state.Click or tap here to enter text.Click or tap here to enter text.Click or tap here to enter text.

The freezing temperature T_f shifts to higher temperature with increasing frequency, the correlation is in accordance with the Vogel–Fulcher equation, $\omega = \omega_0 \exp\left(\frac{-E_a}{k_B(T_f - T_0)}\right)$. The fittings were made considering the two edge values of intrinsic relaxation time: 10^{-7} s ≤ τ_0 ≤ 10^{-13} s, obtaining E_a/k_B = 0.35(3) and 1.13(8) with Vogel-Fulcher temperature (T_0) of 10.05(3) and 9.71(6) K, respectively (Figure 73d). The very low activation energy in LaMTFO is in the typical range of (0.2−2)T_f for cluster spin glasses [Kearins et al., 2021] and suggests the formation of the FM cluster-glass state in LaMTFO below T_f.

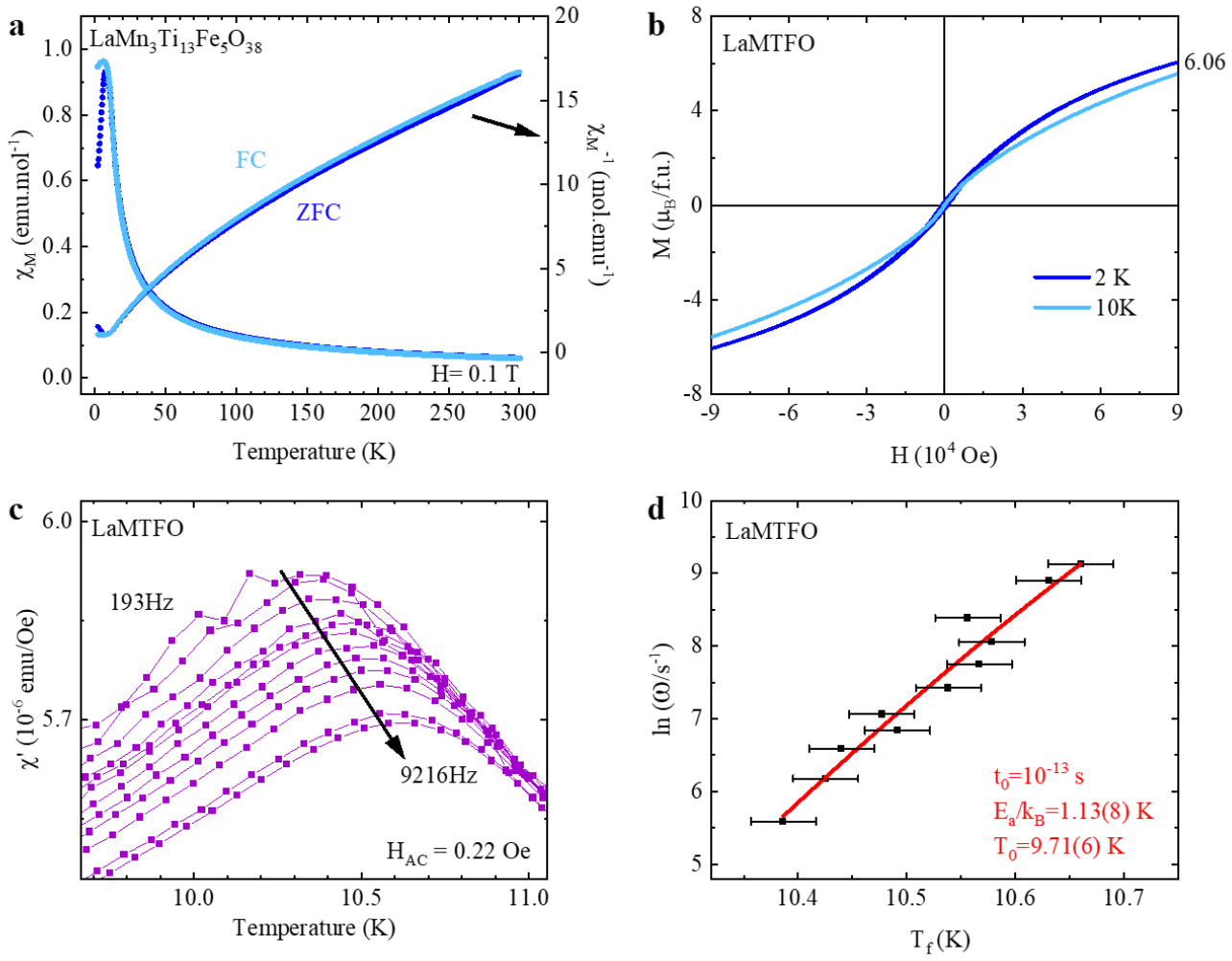

Figure 73. Magnetic measurements for LaMTFO: Temperature Dependence of DC magnetic susceptibility (χ_M) and its reciprocal (χ_M^{-1}) (a), Field-Dependent Magnetization (b), and temperature dependence of the real part of the AC susceptibility (c). The freezing temperature correlates with the AC frequency, consistent with the Vogel-Fulcher description (d).

4.2.3 $CeMn_3Ti_{18}O_{38}$

XRD refinement

Following the synthesis with La, we attempted to replicate the crichtonite framework using Ce instead. The resulting sample comprises 97.78(71) wt.% of crichtonite, accompanied by 1.75(11) wt.% of ilmenite phase ($MnTiO_3$) and 0.47(3) wt.% of pyrophanite (proposed chemical formula: Ce_2TiO_5) (Figure 74).

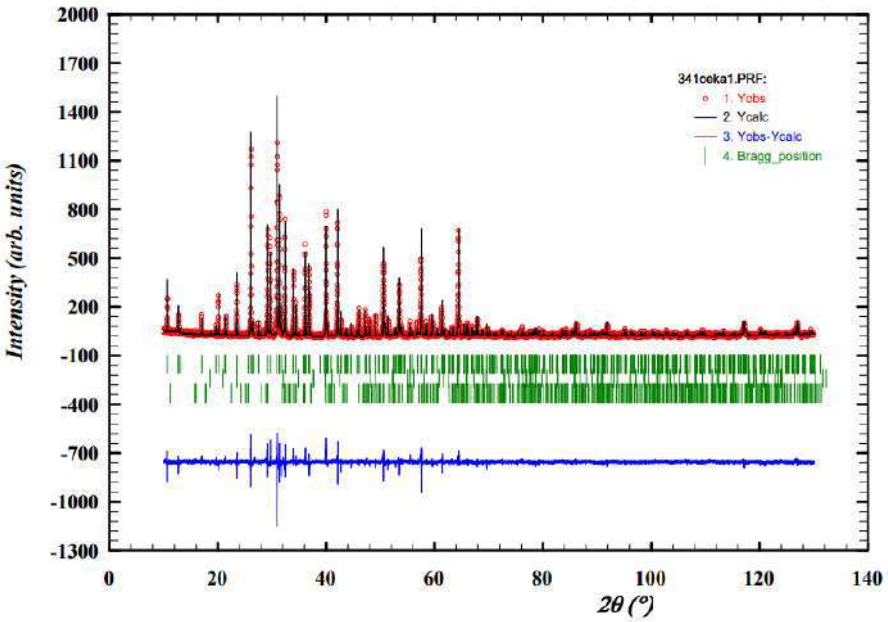

Figure 74. Rietveld refinement of CeMTO. XRD wavelength λ=1.54 Å. Chi2=1.5.

DC magnetic measurements

$CeMn_3Ti_{18}O_{38}$ (CeMTO) exhibits magnetic behavior similar to that of LaMTO (Figure 70b, e). Both ZFC and FC susceptibilities experience a sudden increase as temperature decreases, with a transition occurring at 3.62 K. Applying the Curie-Weiss fit to the inverse susceptibility within the temperature range of 200-290 K yielded a Curie constant of 13.62 and a Weiss temperature of -30.73 K. The negative Weiss temperature suggests the presence of antiferromagnetic interaction in CeMTO.

Theoretical calculation of the magnetic moment of this compound varies depending on the possible oxidation states of cerium (+3, +4), resulting in μ_{theor} values of 11.24 μ_B/f.u. for $Ce^{3+}Mn^{2+}{}_3Ti^{4+}{}_{13}Ti^{3+}{}_5O_{38}$, and 11.09 μ_B/f.u. for $Ce^{4+}Mn^{2+}{}_3Ti^{4+}{}_{12}Ti^{3+}{}_6O_{38}$, respectively. However, the calculated magnetic moment from the Curie-Weiss fit ($\mu_{calc.}$) is 10.44 μ_B/f.u. and lower than both theoretical values.

The magnetization of CeMTO reaches a maximum value of 11.88 μ_B/f.u. under a 9-Tesla field at 2 K, which is near saturation magnetization. At this temperature, a hysteresis loop is evident with a residual magnetization of 0.07 μ_B/f.u.

AC magnetic measurements

Alternating current (AC) magnetic susceptibility revealed spin-glass behavior in CeMTO (Figure 75). The freezing temperature shifts to higher temperatures as the frequency increases, with a shift magnitude of 0.07 K. The relative shift per frequency decade for CeMTO, δT_f, is calculated to

be 0.006, which is similar to the value for LaMTO, LaMTFO and suggests a cluster-glass state.

Vogel–Fulcher fittings were performed on the freezing temperature T_f as a function of frequency. Considering the two extremes t_0 values for spin-glass compounds $10^{-9}s \leq t_0 \leq 10^{-13}s$, we obtained $\frac{E_a}{k_B} = 0.25(2)$ and 0.47(3), with T_0 = 2.74(2) K and 2.64(2) K, respectively.

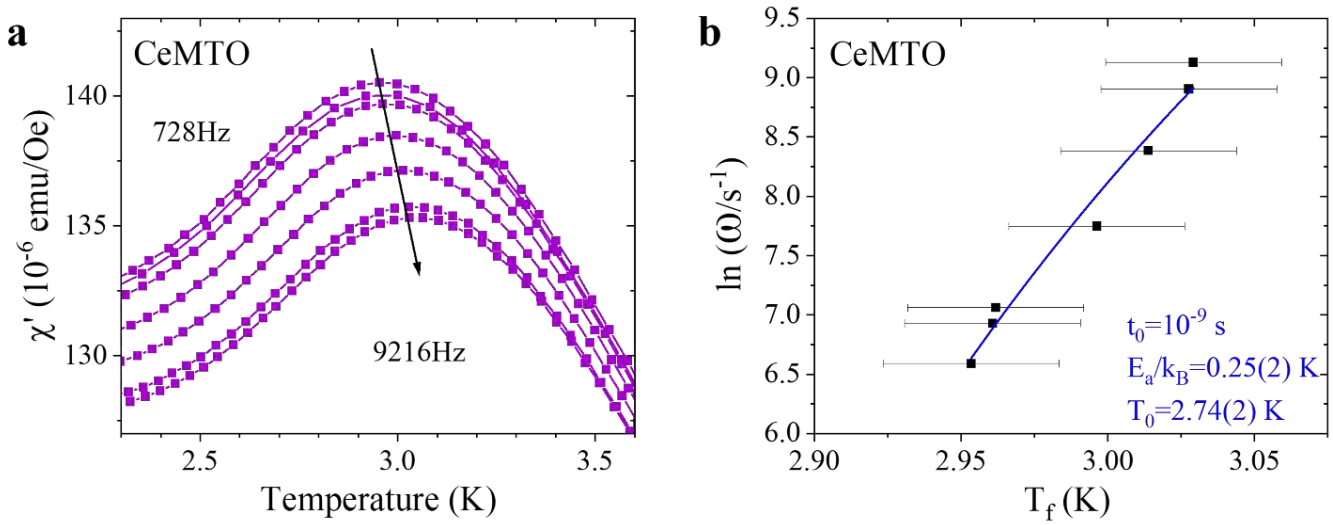

Figure 75. AC susceptibility of CeMTO and the frequency dependent freezing temperature.

4.2.4 $NdMn_3Ti_{13}Ti_5O_{38}$

Nd^{3+} possesses a higher number of free electrons compared to La^{3+}, Ce^{4+} and Ce^{3+}, suggesting that compounds containing $Nd^{3+}Mn^{2+}{}_3Ti^{4+}{}_{13}Ti^{3+}{}_5O_{38}$ (NdMTO) are likely to exhibit stronger magnetic behavior than LaMTO and CeMTO.

NPD refinements

The synthetic powder sample was found to consist of 96.2(9) wt.% of crichtonite phase, with minor impurity phases Ti_3O_5 crystallized (3.8(2) wt.%), the Neutron powder spectra is shown in Figure 76, the phase content is summarized in Table 34.

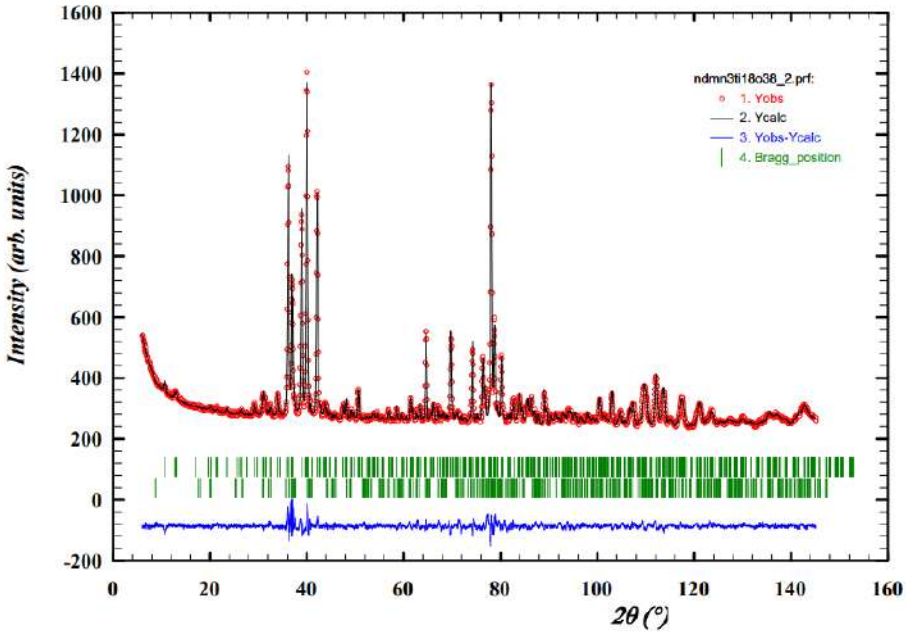

Figure 76. Rietveld refinement of NdMTO. NPD wavelength λ=1.50 Å. Chi2=4.1.

The structural parameters obtained from the Rietveld analysis are detailed in Table 33. Bond Valence Sum (BVS) of each atom $\Sigma(s_{ij})$ were obtained considering the relation $s_{ij} = \exp[(r_0 - r_{ij})/b$, where r_{ij} are the bond lengths, $b = 0.37$ and r_0 is an empirical parameter [Brown, 2020]. The bond valence sum calculation confirms the mix valence state of Ti^{4+} and Ti^{3+} in the C3 site. Notably, the oxidation state of neodymium exhibits only 2.15(1).

Table 33. Structural parameters obtained from the Rietveld fitting made to the NPD (λ = 1.50 Å) patterns for NdMTO compounds at 280 K.

NdMTO					
Atom	Site	x	y	z	BVS
Nd	3a	0.66667(0)	0.33333(0)	0.33333(0)	2.154(13)
Mn1	3b	0(0)	0(0)	0.5(0)	1.881(16)
Mn2	6c	0.66666(0)	0.33333(0)	0.64705(69)	2.155(29)
Ti1	18f	0.23755(143)	0.32032(122)	0.39768(35)	4.039(66)
Ti2	18f	0.32557(95)	0.08659(26)	0.39484(0)	4.127(48)
Ti3	18f	0.61778(0)	0.14383(0)	0.49503(0)	3.595(110)
O1	18f	0.19092(75)	0.13029(82)	0.43467(29)	1.894(42)
O2	6c	0.66666(0)	0.33333(0)	0.54380(51)	2.020(70)
O3	18f	0.72209(76)	0.53955(61)	0.67117(31)	2.347(36)
O4	18f	0.40428(92)	0.44401(89)	0.45118(26)	2.264(93)
O5	18f	0.35563(85)	0.25730(81)	0.55920(29)	2.040(45)
O6	18f	0.37199(73)	0.27011(77)	0.34292(24)	1.728(28)
O7	18f	0.49924(77)	0.20596(90)	0.43831(30)	2.206(68)

The powder sample NdMTO was examined using a neutron beam line with a wavelength of 2.42 Å at temperatures of 1.5 K and 30 K. The diffraction results are illustrated in Figure 77. No additional magnetic reflections appear upon cooling, suggesting the spin-glass behavior of NdMTO.

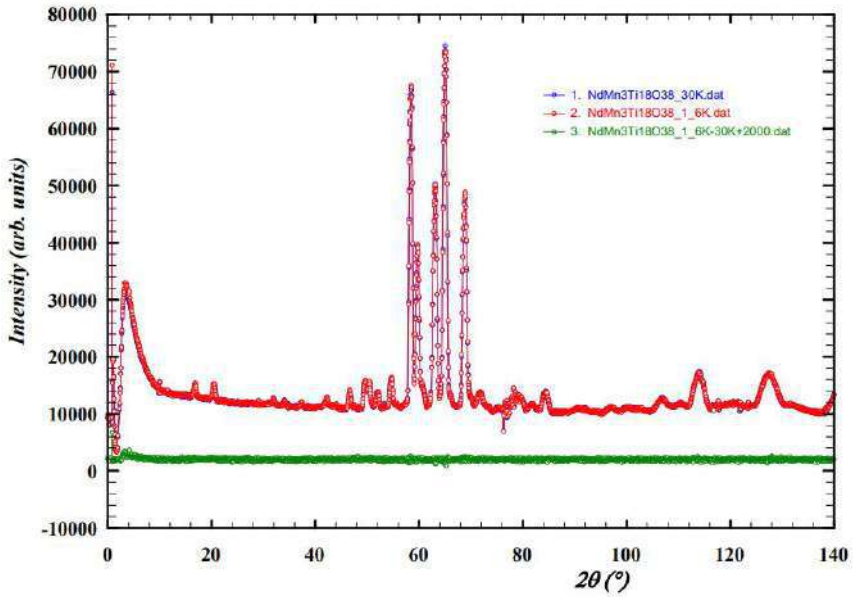

Figure 77. Neutron diffraction spectra of NdMTO obtained at temperatures of 1.5 K (blue) and 30 K (red) (λ=2.42Å). The difference is illustrated by the green curve, showing that the two spectra are nearly identical.

DC magnetic measurements

The results of DC magnetic measurements of neodymium crichtonite are illustrated in Figure 70d, f. The transition temperature was determined as 3.98 K from the susceptibility curve. The divergence between the inverse susceptibility curves occurred due to the technical error. The Curie-Weiss fit is applied to the inverse susceptibility curves between 200 and 290 K. The Curie constant is 12.24 and negative Weiss temperature θ_W = -4.24 K suggests the similar antiferromagnetic behavior like the former two compounds.

The field-dependent magnetization of NdMTO was measured in 2 K, which reveals that this compound exhibits 12.12 μ_B/f.u. when a field of 9 Tesla is applied, this value should be less than but very close to the saturation magnetization. There is hysteresis observed on NdMTO with a remnant magnetization of 0.06 μ_B/f.u.

4.2.5 Subsection summary

The results of Rietveld refinement and magnetic measurements are summarized in Table 34 and Table 35, respectively. The compounds of *RE*$Mn_3Ti_{18}O_{38}$, were synthesized with *RE* = La^{3+}, Ce^{3+} and Nd^{3+}. The unit cell parameters are decreasing in agreement with the ionic radii of the cation.

Table 34. The phase content and unit cell parameters of synthetic crichtonite with rare-earth elements La, Ce and Nd.

	LaMTO	LaMTFO	CeMTO	NdMTO
Diffraction wavelength	XRD (λ=1.54Å)	XRD (λ=1.54Å)	XRD (λ=1.54Å)	NPD (λ=1.50Å)
Crichtonite(wt.%)	90.54(45)	78.92(17)	97.78(71)	96.23(93)
Pseudobrookite(wt.%)	—	19.87(13)	—	—
Ilmenite (wt.%)	1.49(07)	1.21(09)	1.75(11)	—
TiO_2(wt.%)	7.64(12)	—	—	—
Ti_3O_5(wt.%)	—	—	—	3.77(17)
a(Å)	10.41777(3)	10.4085(1)	10.41482(6)	10.3891(2)
c(Å)	20.81982(11)	20.8052(2)	20.80754(15)	10.3891(2)
Volume(Å^3)	1956.85(6)	1952.64(1)	1954.59(2)	20.79181(61)
R_{wp}	10.1	7.63	19.4	2.24
R_{exp}	3.17	2.95	15.72	1.1
χ^2	10.2	3.6	1.52	4.13

The results of the neutron powder diffraction (NPD) on NdMTO confirmed the absence of magnetic reflections from room temperature down to 1.5 K. Through detailed AC measurements and neutron diffraction at low temperatures, four compounds were confirmed to exhibit spin-glass behavior. However, three titanates—LaMTO, CeMTO, and NdMTO—behave differently from the iron-substituted compound, LaMTFO. In DC magnetic measurements, the three titanates exhibited similar magnetic transitions and magnetization at 2K and 9 T, contrasting with the behavior of the Fe-substituted compound.

Table 35. The magnetic measurements result of synthetic crichtonite with REE.

Sample name		LMTO	CeMTO		NMTO
A-site cation		La^{3+}	Ce^{3+}	Ce^{4+}	Nd^{3+}
Electron Configuration		$[Xe]6s^0$	$[Xe]6s^1$	$[Xe]6s^0$	$[Xe]4f^3$
Ionic radii	(Å)	1.36	1.34	1.14	1.27
Unit cell parameters	a (Å)	10.41777(3)	10.41482(6)		10.3891(2)
	c (Å)	20.81982(11)	20.80754(15)		10.3891(2)
Sample purity	(%)	90.54(45)	97.78(71)		93.03(84)
Transition temperature	(K)	4.4	3.62		3.98
Maximum magnetization	(μ_B/f.u.)	10.10	11.88		12.12
at which temperature		2 K	2 K		3 K
Remnant magnetization	(μ_B/f.u.)	0.12	0.07		0.06
Curie Constant	C (a.u.)	11.91	13.62		12.24
Weiss temperature	θ_W (K)	-9.35(6)	-30.73(19)		-4.23(11)
Calc. magnetic moment	$\mu_{cal.}$(μ_B)	9.76	10.45		9.89
Theor. magnetic moment	$\mu_{theo.}$(μ_B)	10.95	11.24	11.09	11.67

4.3 Synthetic crichtonite with divalent cations (Ca^{2+}, Sr^{2+} and Ba^{2+})

Expanding upon the achievements seen with lanthanides crichtonite, we are motivated to experiment with modifying the A-site cation to non-magnetic divalent elements such as Ca, Sr, and Ba. The chemicals $CaCO_3$, $SrCO_3$, $BaCO_3$, MnO and TiO_2 (anatase) were used.

4.3.1 $CaMn_3Ti_{18}O_{38}$

NPD refinements

The sample obtained, $CaMn^{2+}{}_3Ti^{4+}{}_{14}Ti^{3+}{}_4O_{38}$ (CaMTO), consists of 87.66(75)% crichtonite phase, with impurities comprising 7.96(8)% rutile and 4.39(11)% magnetic ilmenite (chemical formula $MnTiO_3$). Neutron powder diffraction data and Rietveld refinements are shown in Figure 78.

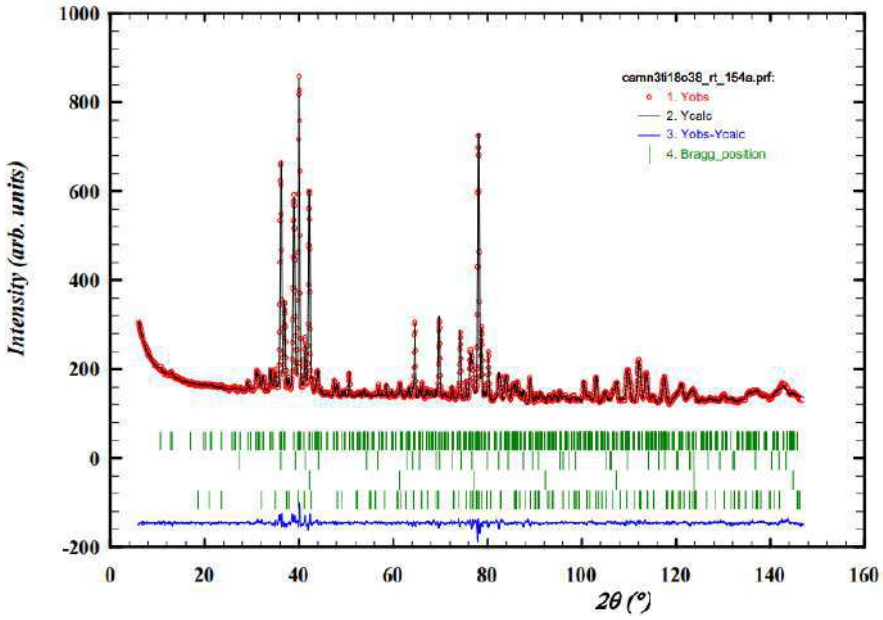

Figure 78. Rietveld refinement of neutron diffraction spectrum for CaMTO. Wavelength λ=1.54 Å. Chi2=3.1.

In this compound, the A-site is fully occupied by Ca^{2+}. However, the B1-site shows a slight Ca doping and it is occupied by 0.73(4) Mn and 0.27(4) Ca. This distribution is further supported by Bond Valence Sum (BVS) calculations.

The BVS confirms that the oxidation state of B1 site equals to 1.87/3.01 when assuming that it is fully occupied by Mn/Ca^{2+}. The lower BVS of 1.36(1) at this site is attributed to the small size of Ca^{2+} for the dodecahedron, creating a sizable cavity. The remaining sites are as follows: B2 by Mn^{2+}, C1 and C2 by Ti^{4+}, and C3 by Ti^{3+}. Detailed atomic parameters are provided in Table 36.

Table 36. Atomic parameters obtained from the Rietveld refinement made to the NPD (l=1.54Å) patterns for CaMTO compounds at 300K. [a] Refined site occupancy for Mn1/Ca2 is 0.73(4)/0.27(4).

CaMTO					
Atom	Site	x	y	z	BVS
Ca1	3a	0.66667(0)	0.33333(0)	0.33333(0)	1.361(7)
Mn1/Ca2[a]	3b	0(0)	0(0)	0.5(0)	1.867(13)/3.012(21)
Mn2	6c	0.66666(0)	0.33333(0)	0.64603(65)	2.120(30)
Ti1	18f	0.24011(119)	0.30978(122)	0.39958(34)	3.980(64)
Ti2	18f	0.32852(87)	0.08823(120)	0.39188(40)	4.075(57)
Ti3	18f	0.52338(73)	0.37554(93)	0.49891(47)	3.614(44)
O1	18f	0.19175(61)	0.13182(72)	0.43526(23)	2.054(49)/2.245(49)
O2	6c	0.66666(0)	0.33333(0)	0.5436(46)	2.300(36)
O3	18f	0.71948(66)	0.53874(55)	0.67182(25)	2.129(36)
O4	18f	0.4013(68)	0.44172(70)	0.45028(23)	2.135(38)
O5	18f	0.36269(75)	0.26501(68)	0.55835(24)	1.925(39)
O6	18f	0.3687(65)	0.2666(67)	0.34163(27)	1.889(41)
O7	18f	0.49765(61)	0.203(68)	0.43959(22)	2.015(32)

Magnetic structure determined by neutron diffraction

Neutron powder diffraction experiments were conducted on CaMTO (λ=2.41Å) at temperatures of 2K and 30K Figure 79. By comparing the patterns obtained at these temperatures, magnetic reflections were distinctly identified, as illustrated in the inset of Figure 79. The peaks (101) and (110) are the major magnetic reflections, increase in intensity at 2 K. This reflection can be indexed in a primitive unit cell with the same lattice parameter. As the size of the magnetic and crystallographic unit cell is coincident, the propagation vector is **k**= [0 0 0]. The magnetic structure has been determined from the 2 K data. The final Rietveld refinement was obtained with Fullprof with the mΓ1+ irreducible representation with the rhombohedral magnetic space group $R\bar{3}$ (#148). A satisfactory solution was found by modeling a colinear ferrimagnetic arrangement between Mn and Ti spins along z axis (Figure 80). The ordered magnetic moments determined at 2K are 3.90(1) μ_B for Mn1 and Mn2, the Ti3 exhibits magnetic moment of 0.17(1) μ_B ($R_{mag.}$ =11.1). The Mn1 and Mn2 were refined separately, and the obtained value are nearly identical, their magnetic moments therefore were constrained to be same to reduces errors.

$MnTiO_3$, an impurity crystallized in the ilmenite structure, demonstrates magnetic behavior. The magnetic structure of $MnTiO_3$, described by Shirane, J. Pickart, and Ishikawa in [Shirane, J. Pickart, Ishikawa, 1959], with a magnetic space group denoted as R-3', #148.19, is refined to suit this

phase. Its magnetic structure is also demonstrated in Figure 79.

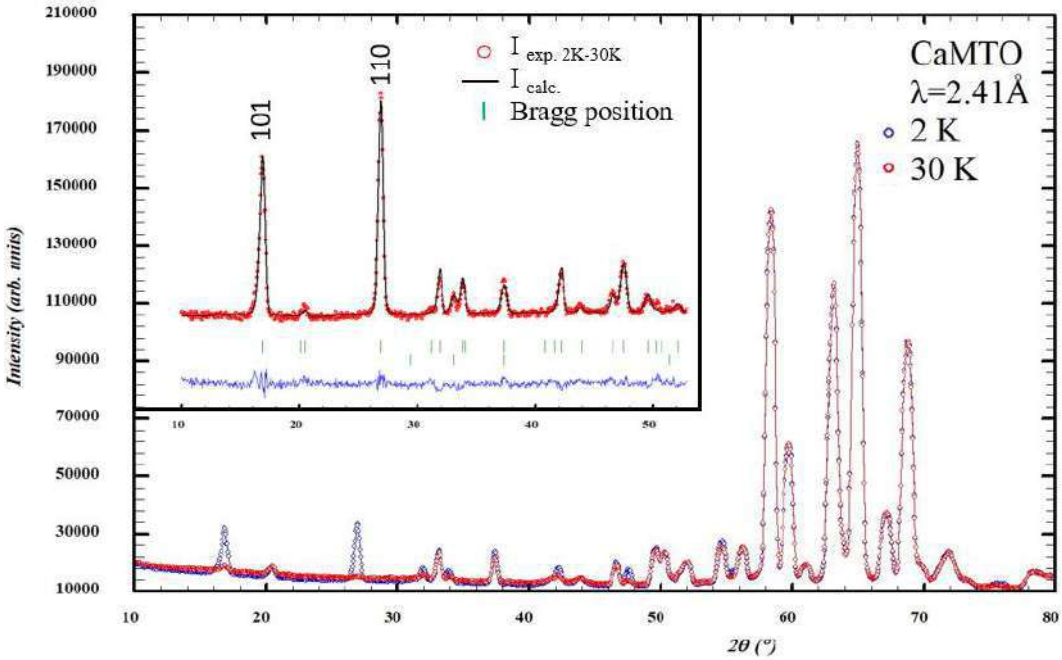

Figure 79. Magnetic reflections of CaMTO are illustrated by the difference between neutron diffraction patterns at 2K and 30K, the Bragg position of magnetic structures of CaMTO and $MnTiO_3$ are both demonstrated (green lines).

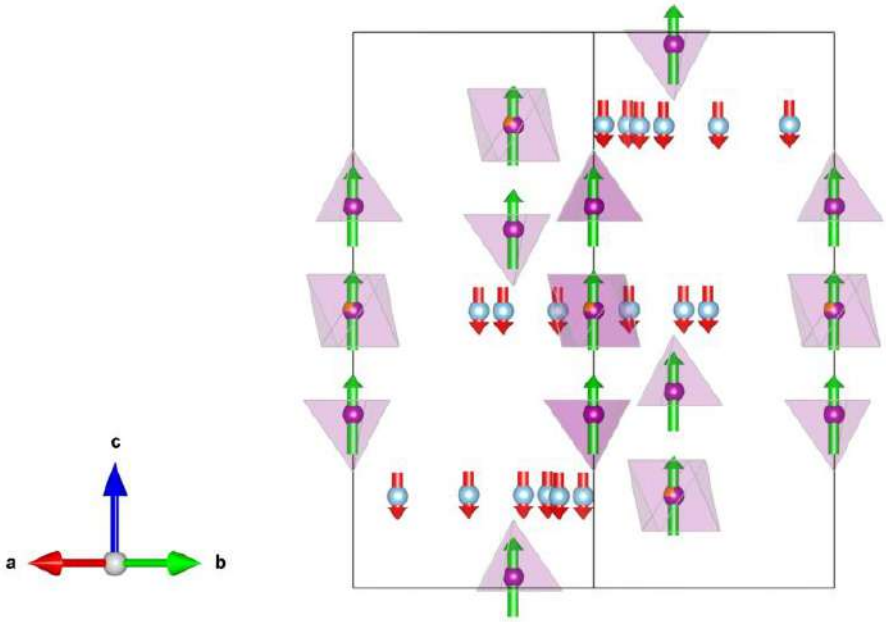

Figure 80. Schematic graphic of ferrimagnetic arrangement between Mn (green arrow) and Ti (red arrow) spins along the z axis.

DC magnetic measurements

Analysis of the magnetic susceptibility measurements reveals that the transition temperature of CaMTO occurs at 14.37(1) K, with no discernible divergence between the ZFC and FC curves under 0.1 T external field (Figure 81a). Curie-Weiss fit on the inverse susceptibility curve within the temperature range of 230-290 K was performed, the obtained Curie constant and Weiss temperature are indicative of antiferromagnetic interactions, with θ_W=-7.58(19) K. From the Curie constant C = 11.831(8), the calculated magnetic moment $\mu_{calc.}$ is 9.729(1) μ_B. The theoretical magnetic moment, determined by $\mu_{theor.(CaMTO)} = \sqrt{3 \cdot \mu_{B\,(Mn^{2+})}{}^2 + 4 \cdot \mu_{B\,(Ti^{3+})}{}^2}$ =11.41 μ_B.

At 3 K, the saturation magnetization of CaMTO is observed in a field of 9 Tesla (Figure 81d). A narrow hysteresis loop is evident at this temperature, exhibiting a remnant magnetization of 0.17 μ_B/f.u. As the temperature increases, the contribution of ferromagnetic components gradually diminishes. By 20 K, the hysteresis has reduced with a residual magnetization reduced of 0.02 μ_B/f.u.

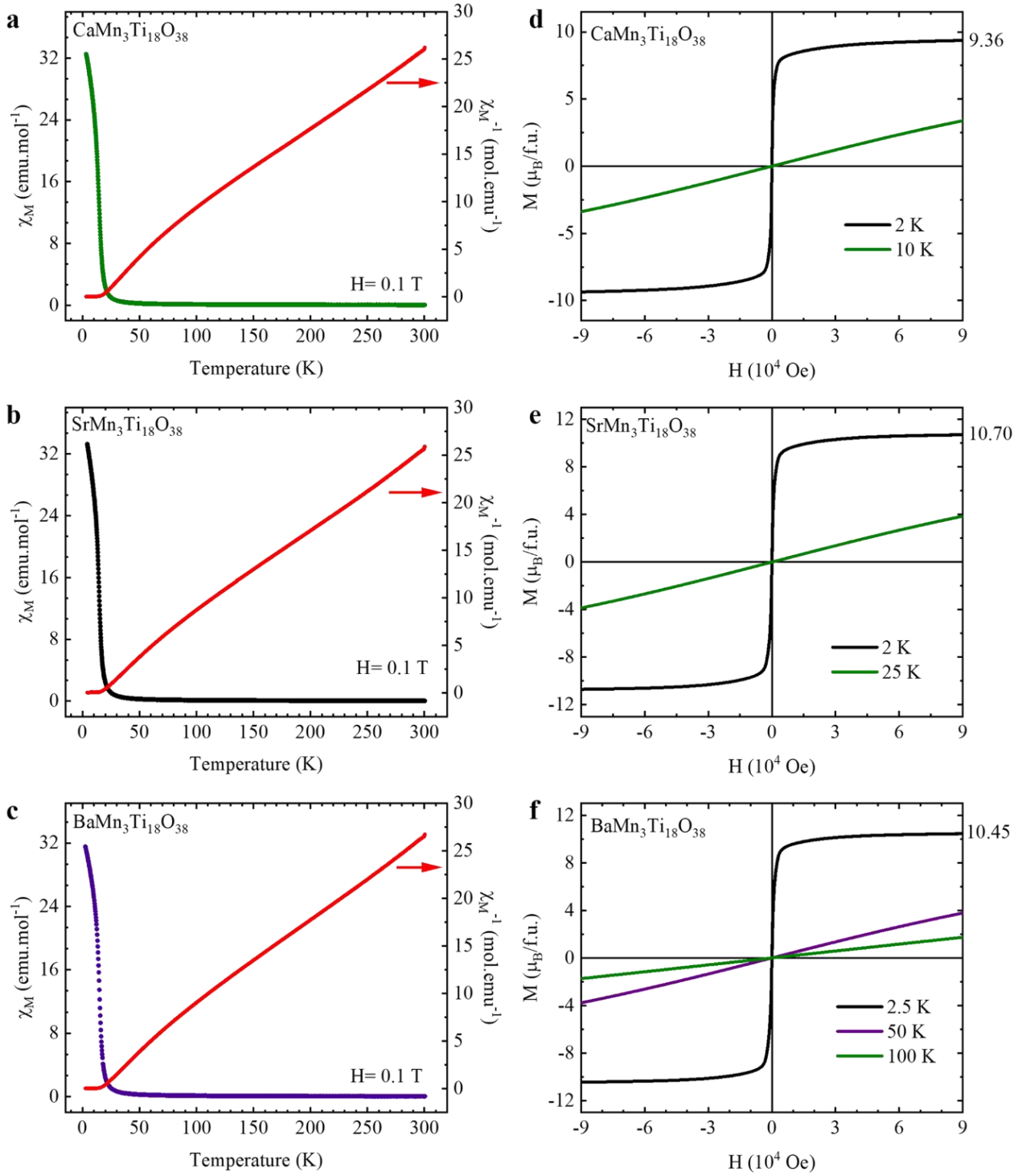

Figure 81. Magnetic susceptibility and its reciprocal χ^{-1} as a function of temperature for CaMTO (a), SrMTO (b) and BaMTO (c); the Curie Weiss law fitted at high temperature is shown with a black straight line. Field dependent magnetization of CaMTO (d), SrMTO (e) and BaMTO (f) at different temperatures.

4.3.2 $Ca_2Fe_2Ti_{18}O_{38}$

NPD refinements

Neutron diffraction obtained at 306 K (λ = 1.54 Å) confirmed the crystallization of the crichtonite phase in the CaFTO sample, even though it only constitutes 55.0(1) wt.% with 45.0(1) wt.% of rutile, see Figure 82. The unit cell parameters are a = 10.3852(2) Å, c = 20.922(5) Å, V = 1954.17(7) Å^3.

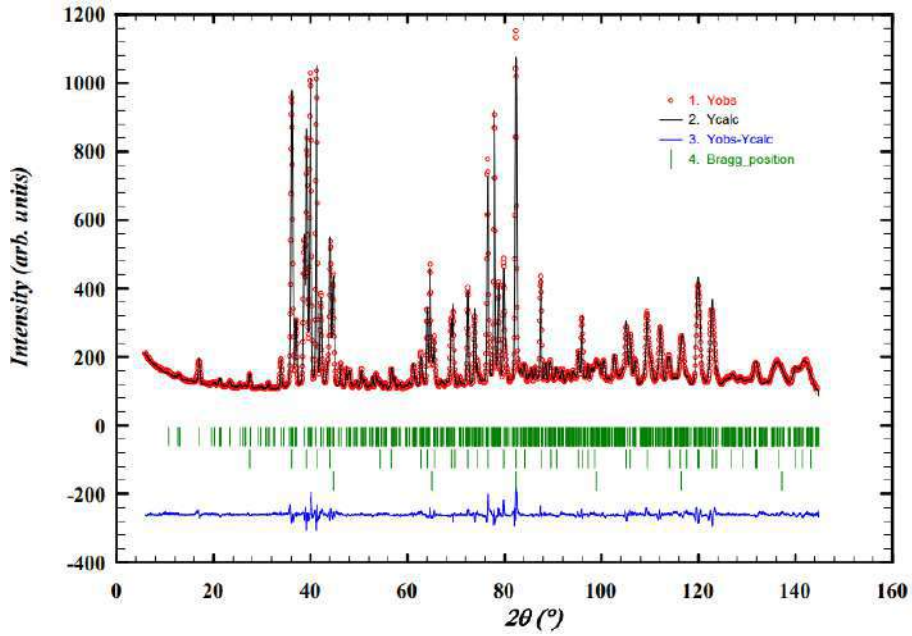

Figure 82. Rietveld refinement of neutron diffraction spectrum for CaFTO. Wavelength λ=1.54 Å. Chi2=5.8.

After several trials of refinement considering iron at different sites, we have refined the crystal structure of CaFTO in detail (Table 37). In CaFTO, calcium occupies not only the dodecahedral *A*1 site but also the octahedral *B*1 site, while the tetrahedral sites are fully occupied by divalent iron. The remaining octahedral *C*1-*C*3 sites are primarily occupied by titanium. Notably, Ti^{4+} in the Ti3 site is confirmed to be partially substituted by Fe^{3+}, with a ratio of 0.825(3) Ti^{4+} to 0.185(3) Fe^{3+}.

Table 37. Atomic parameters for CaFTO compounds obtained from the Rietveld refinement made to the NPD (λ=1.54Å) patterns at 306K. [a] Refined site occupancy for Ti3/Fe3 is 0.825(3)/0.185(3).

CaFTO					
Atom	Site	x	y	z	BVS
Ca1	3a	0.66667	0.33333	0.33333	1.34(6)
Ca2	3b	0	0	0.5	2.584(15)
Fe2	6c	0.66666	0.33333	0.64460(20)	1.933(18)
Ti1	18f	0.2377(12)	0.3154(11)	0.3987(3)	3.984(55)
Ti2	18f	0.3248(10)	0.0866(12)	0.3906(4)	4.08(54)
Ti3/Fe3 [a]	18f	0.533(3)	0.386(3)	0.5009(13)	3.698(129)/3.179(111)
O1	18f	0.1991(5)	0.1373(6)	0.43530(20)	2.171(44)
O2	6c	0.66666	0.33333	0.5471(4)	2.312(78)
O3	18f	0.7201(7)	0.5376(5)	0.67230(20)	2.204(33)
O4	18f	0.4025(7)	0.4411(8)	0.45120(20)	2.235(79)
O5	18f	0.3610(6)	0.2614(6)	0.56000(20)	1.922(48)
O6	18f	0.3717(6)	0.2658(6)	0.34100(20)	1.811(34)
O7	18f	0.4965(5)	0.2081(6)	0.44200(20)	1.856(57)

Magnetic structure

The neutron diffraction (λ=2.41Å) perform on CaFTO at 1.6K and 20K separately. The difference between these two spectra shown in Figure 83b is caused by magnetic transformation.

After following the same procedure for refining magnetic reflections as done previously, the magnetic structure of CaFTO was determined. The magnetic atoms are located at the Fe2 and Ti3/Fe3 positions, with magnetic moments of 0.95(3) and -0.22(2) μ_B, respectively. The negative sign indicates that the magnetic moment of Fe2 is oriented opposite to the magnetic moment of Ti3/Fe3. The schematic magnetic structure is shown in Figure 84.

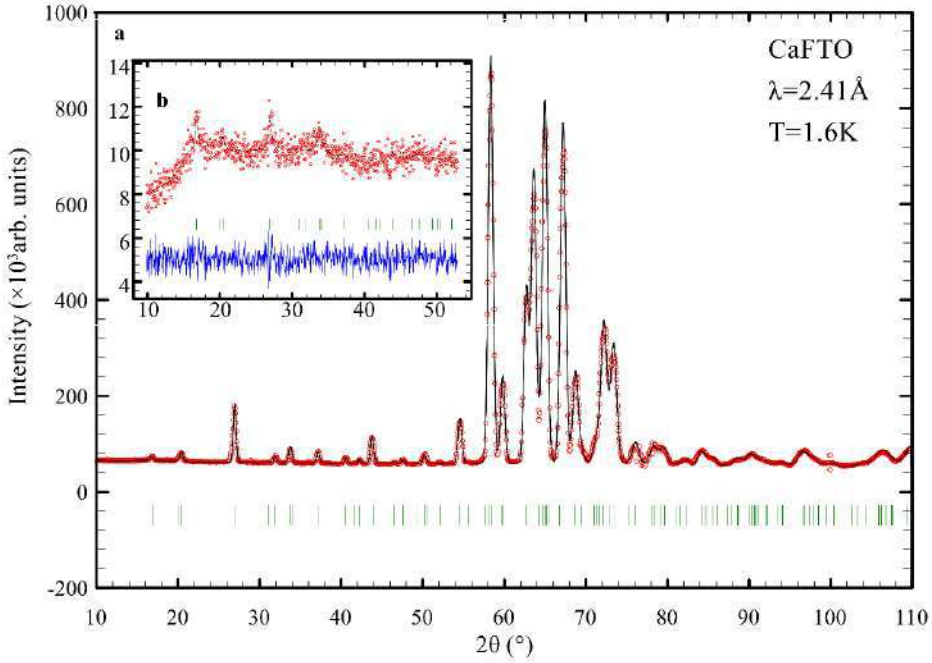

Figure 83. Neutron diffraction (λ = 2.41 Å) of CaFTO obtained at 1.6 K (a). The difference between spectra at 1.6K and 20K shows the magnetic reflections (b).

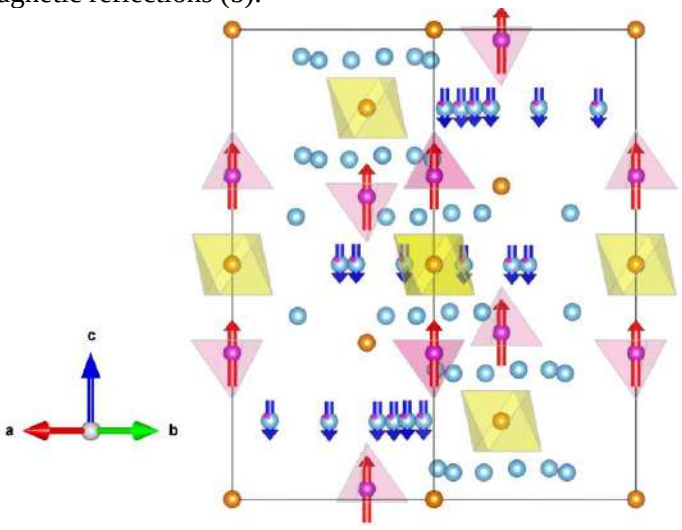

Figure 84. In CaFTO, the magnetic moments are determined 0.95(3) and -0.22(2) μ_B for Fe2 (red arrow) and Ti3/Fe3 (blue arrow), respectively.

DC magnetic measurements

The magnetic transition upon cooling in CaFTO is evident in the magnetic susceptibility curve, which shows a dramatic increase at 6.49(4) K (Figure 85a). The plot of reciprocal susceptibility χ^{-1} versus temperature exhibits a positive curvature. Due to the high content of non-magnetic impurity,

specifically 45.0(1) wt.% of rutile, the Curie-Weiss law is not applicable to this data.

The magnetic moment rapidly increases to 3.5 μ_B per formula unit at 1.3 T, with a slower increasing trend observed up to 9 T. The maximum magnetization, measured at a field of 9 T, reaches 5.30 μ_B per formula unit (Figure 85b).

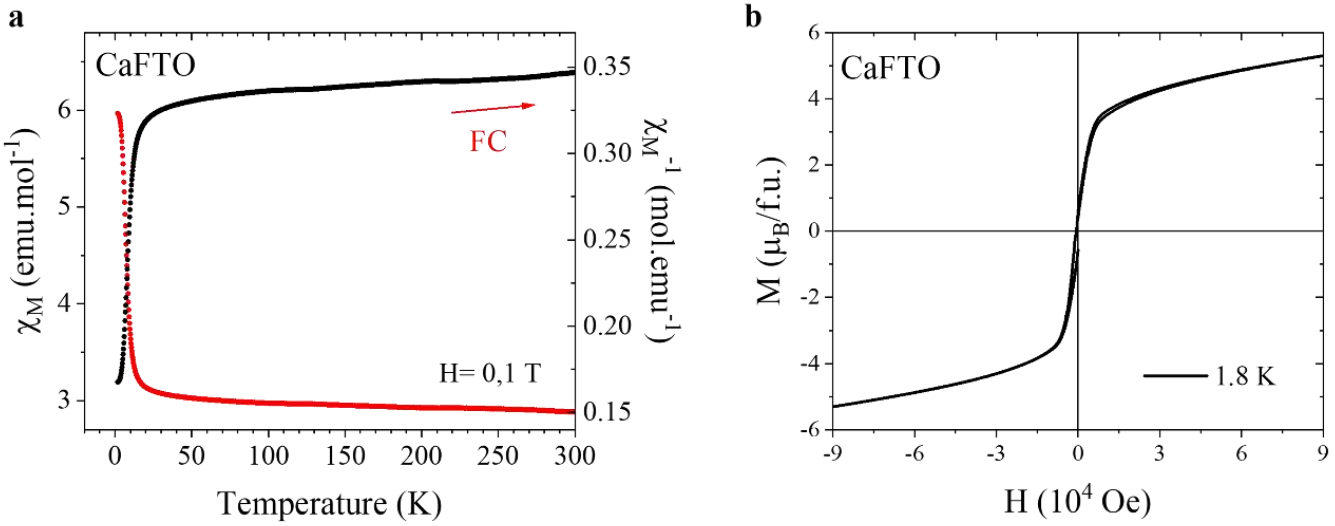

Figure 85. Magnetic susceptibility and its reciprocal χ^{-1} as a function of temperature for CaFTO (a), Field dependent magnetization at different temperatures (b).

4.3.3 $SrMn_3Ti_{18}O_{38}$

NPD refinements

The $SrMn^{2+}{}_3Ti^{4+}{}_{14}Ti^{3+}{}_4O_{38}$ (SrMTO) sample shows a small amount of TiO_2 precursor [7.2(4) wt%], the neutron diffraction spectrum obtained at room temperature is included in Figure 86.

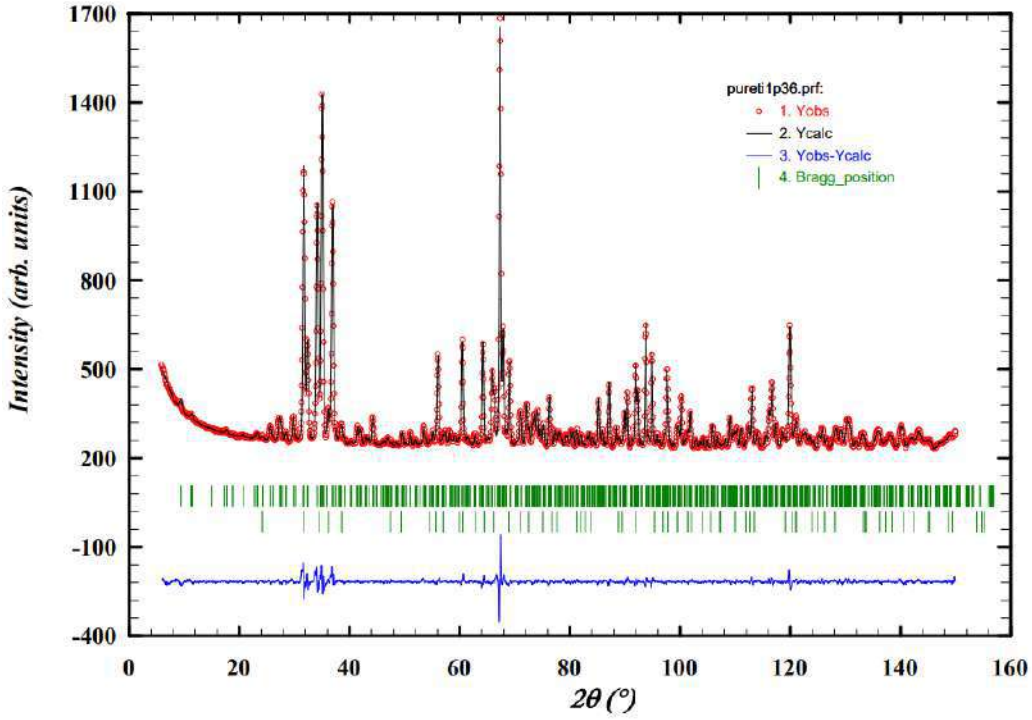

Figure 86. Rietveld refinement of neutron diffraction spectrum for SrMTO. Wavelength λ=1.36 Å. Chi2=4.6.

Rietveld refinements yield the phase content and unit cell parameters, which are summarized in Table 42 with other samples' parameters. The cell parameters for SrMTO (a=10.4282(1)Å, c=20.8410(3)Å) are larger in comparison with SrMTFO (see 4.3.3, a=10.4200(1)Å, c=20.8147(4)Å)

due to the different ionic radii and this suggests that Fe^{3+} (0.645 Å) substitutes Ti^{3+} (0.67Å) and not Ti^{4+}(0.605Å).

Refined structural parameters of SrMTO are listed in Table 38. Bond valence sum (BVS) calculations for SrMTO confirm a 4+ oxidation state for Ti1 and Ti2. However, the Ti3 site shows a lower BVS of 3.52(3), indicating a mixed-valence state of Ti^{4+} and Ti^{3+} at this site.

Table 38. Structural parameters obtained from the Rietveld fitting made to the NPD (λ = 1.36 Å) patterns for SrMTO 300 K.

SrMTO					
Atom	Wyckoff	x	y	z	BVS
Sr1	3a	0	0	0	1.83(6)
Mn1	6c	0	0	1/2	1.87(8)
Mn2	3b	2/3	1/3	0.6454(4)	2.07(1)
Ti1	18f	0.2394(7)	0.3142(7)	0.3985(2)	4.08(4)
Ti2	18f	0.3278(6)	0.0841(7)	0.3928(2)	3.93(3)
Ti3	18f	0.5222(5)	0.3754(6)	0.4970(3)	3.52(3)
O1	18f	0.1922(4)	0.1324(4)	0.4358(2)	1.88(2)
O2	18f	2/3	1/3	0.5450(3)	2.12(2)
O3	18f	0.7211(4)	0.5409(3)	0.6711(2)	2.21(2)
O4	18f	0.4009(4)	0.4388(4)	0.4494(1)	2.12(2)
O5	18f	0.3611(4)	0.2612(4)	0.5589(1)	1.99(2)
O6	18f	0.3647(4)	0.2649(4)	0.3411(1)	1.84(2)
O7	6c	0.4973(4)	0.2039(5)	0.4418(2)	2.10(2)

DC magnetic measurements

Temperature dependence of the magnetic susceptibility (χ) of SrMTO shows a magnetic transition at T_N=15K without any FC-ZFC divergence under 0.1 T applied field, see Figure 81b. The fit of the reciprocal susceptibility to the Curie–Weiss law above 210K suggests predominant ferromagnetic (FM) interactions with θ_{CW} = 5.0(1) K. The calculated effective magnetic moment of 9.6(1) μ_B/f.u. is slightly reduced from the expected value of 10.82 μ_B for 3 Mn^{2+} (S=5/2) and 4 Ti^{3+} (S=1/2); this could be due to the small amount of unreacted TiO_2 and thus an error in the considered mass, but it could also be due to an orbital contribution from the t_{2g} degeneracy of the $3d^1$ electrons in Ti^{3+} or to a reduced fitted range.

Field dependent magnetization measurements at 2 and 50K are shown in Figure 81e. No hysteresis was detected, in accordance with the χ(T) behavior. At low temperature, a sharp increase of the magnetization can be observed and it can access 9 μ_B with only 0.4 T and reaches 10.7 μ_B at 9 T.

Magnetic structure determined by neutron diffractions

NPD patterns of SrMTO at low temperature revealed the appearance of magnetic peaks below 15 K, see Figure 87a. These extra reflections coincide with the crystal structure and can be indexed with a **k** = [0 0 0] propagation vector (Γ point of the first Brillouin zone). ISODISTORT was used to determine the possible magnetic structures and space groups [Campbell et al., 2006]. The final Rietveld refinement was obtained with Fullprof with the mΓ1+ irreducible representation with the

rhombohedral magnetic space group $R\bar{3}$ (#148). Figure 87b shows the full pattern with both crystal and magnetic structures at 1.5 K. The appearance of magnetic reflections is evidenced by the intensity contrast between 1.5 and 50 K in Figure 87a.

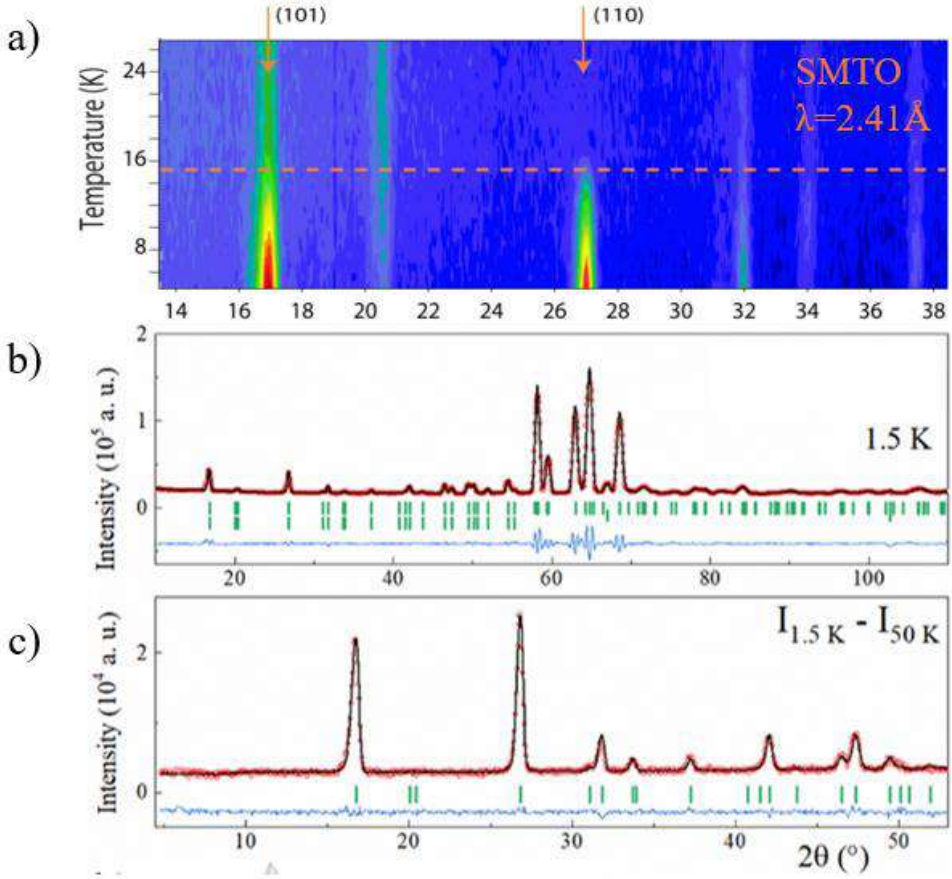

Figure 87. NPD of SrMTO: over varying temperature ranges from 5K to 27K (a), and at 1.5 K showing the Bragg positions (green lines) of both the crichtonite structure and the magnetic structure (b); The magnetic reflections is discernible from the intensity difference between 1.5 and 50 K (c).

The magnetic structure shown in Figure 88a consists of a ferrimagnetic arrangement between Mn and Ti spins along the z axis. The refined moments at 1.5 K converged to 4.11(2) μ_B and 0.30(2) μ_B for Mn^{2+} and Ti^{3+} respectively (R_{mag} = 3.02%, χ^2 = 1.48). Attempts to refine only Mn moments resulted in fits of lower quality (R_{mag} = 4.93%, χ^2 = 2.09), thus proving the contribution of the titanium to the model. The slightly reduced moments from the expected $2S_{Mn}$ =5 μ_B and $2S_{Ti}$ =1 μ_B possibly reflect the disorder of the 3+/4+ mixed valency state in the Ti3 position. However, the ideal FiM disposition of 11 μ_B from 3 × Mn^{2+} with 15 μ_B against 4 μ_B from the 4 × Ti^{3+} explains the values of 10.7 μ_B at 9 T observed in the M vs. H curve at 2K. The temperature evolutions of the Mn and Ti moments are shown in Figure 88b, they follow a critical law $\mu(T) = \mu_1\left[1 - \left(\frac{T}{T_N}\right)\right]^{\beta}$ with μ_1=0.29(3) μ_B and 4.37(5) μ_B for Ti and Mn, T_N=14.68(1) K and β=0.39(1). The critical exponent is close to the theoretical value of β= 0.367 for a 3D Heisenberg magnet, which is appropriate for the structure described before. Observation of unsaturated moments is common in Mn^{2+} oxides as observed for instance in Mn_2FeReO_6 (3.5 μ_B) or $MnTiO_3$ (3.9 μ_B) [Arévalo-López, Attfield, 2013; Arévalo-López, McNally, Attfield, 2015].

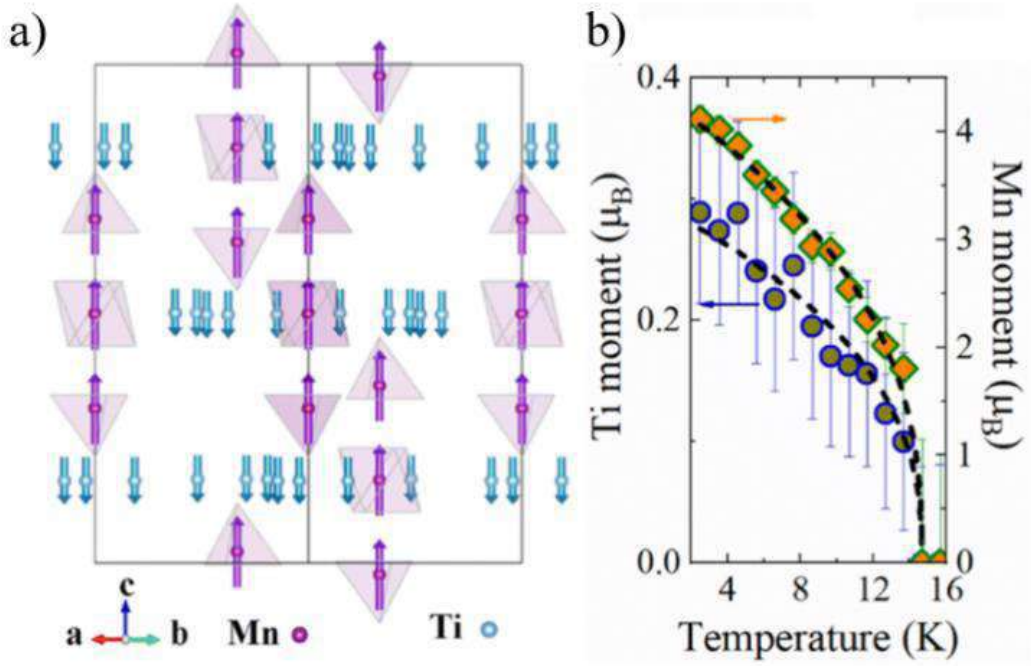

Figure 88. (a) Schematic magnetic structure of SrMTO. (b) Temperature evolutions of the Mn and Ti moments in SrMTO [Rosas-Huerta et al., 2023].

Magnetic heat capacity

Heat capacity measurements without applying a magnetic field (black curve in Figure 89a) exhibit a distinct transition of SrMTO at 15K, consistent with its FiM transition temperature. The curves of temperature-dependent heat capacity exhibit a feature that appears at around 10-30 K, see Figure 89a. The features flatten, broaden and move to higher temperatures when a magnetic field is applied. This was attributed to a Schottky anomaly and its contribution was calculated through the equation:

$$C_{Sch} = NR(\Delta/k_BT)^2 e^{\Delta/k_BT}/\left(1+e^{\Delta/k_BT}\right)^2$$

where R is the ideal gas constant (R=8.314 J mol^{-1} K^{-1}) and Δ is the Schottky gap. Δ/k_BT showed a value of 16.38 K at 2K. This value reflects a linear relation with the applied field, see inset of Figure 89a, well-known for a magnetic Schottky term caused by orphan or magnetic impurities [Zhu et al., 2023].

The heat capacity is composed by magnetic contribution and lattice (or phonon) contributions $C_p = C_m + C_{latt}$. The lattice contribution is modeled by the Debye and Einstein equation[15] and demonstrated in Figure 89a as a red curve.

Magnetic entropy contribution in SrMTO is obtained by integration of the magnetic heat capacity divided by temperature $S = \frac{C_m}{T}$ (J mol^{-1} K^{-1}). After the lattice (phonon) contribution was subtracted, the magnetic entropy released of 47.65 J mol^{-1} K^{-1} (see Figure 89b), which accounts for around 70% of the theoretical value S =R(3ln(2S_{Mn}+1)+4ln(2S_{Ti}+1))=67.74 J mol^{-1} K^{-1} for three Mn^{2+}

[15] $C_{latt} = 9\mathrm{C_D N}k_B\left(\frac{T}{\theta_D}\right)^3\int_{\theta_D/T}^{0}\frac{x^4e^x}{(e^x-1)^2}dx + 3\mathrm{N}k_B\mathrm{C_E}\left(\frac{\theta_E}{T}\right)^2\frac{e^{\theta_E/T}}{\left(e^{\theta_E/T}-1\right)^2}$,
where N is the Avogadro's number (6.023×10^{23} mol^{-1}), C_D, θ_D, C_E and θ_E are the weighting factor and Debye/Einstein temperature, and values of θ_D = 330(2) K, θ_E = 697(3) K, C_D = 0.7374 and C_E = 5 were used in the fitting.

(S_{Mn}=5/2) and four Ti^{3+} (S_{Ti}=1/2).

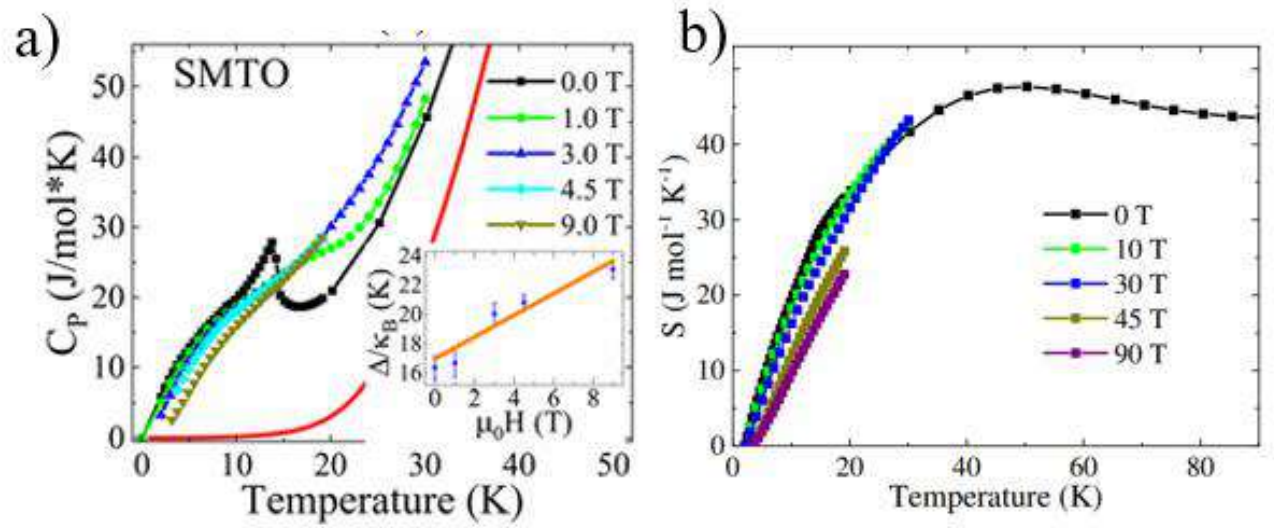

Figure 89. (a) Heat capacity C_p in dependence of temperature for SrMTO, the lattice contribution C_{latt} is demonstrated by the red curve. (b) Magnetic entropy contribution in SrMTO as function of the applied field.

4.3.4 $SrMn_3Ti_{14}Fe_4O_{38}$

NPD refinements

The synthesized $SrMn^{2+}{}_3Ti^{4+}{}_{14}Fe^{3+}{}_4O_{38}$ (SrMTFO) is pure, whithout any unreacted presursora or impurities. For this composition, the large *A*1 position is occupied in this case by Sr^{2+}, whereas Mn^{2+} is located at the *B*1 and *B*2 positions in octahedral and tetrahedral coordination, respectively. Ti^{3+}(Fe^{3+}) cations are located in the *C*1–3 octahedral positions. The neutron diffraction spectrum of SrMTFO and Rietveld refinement is shown in Figure 90.

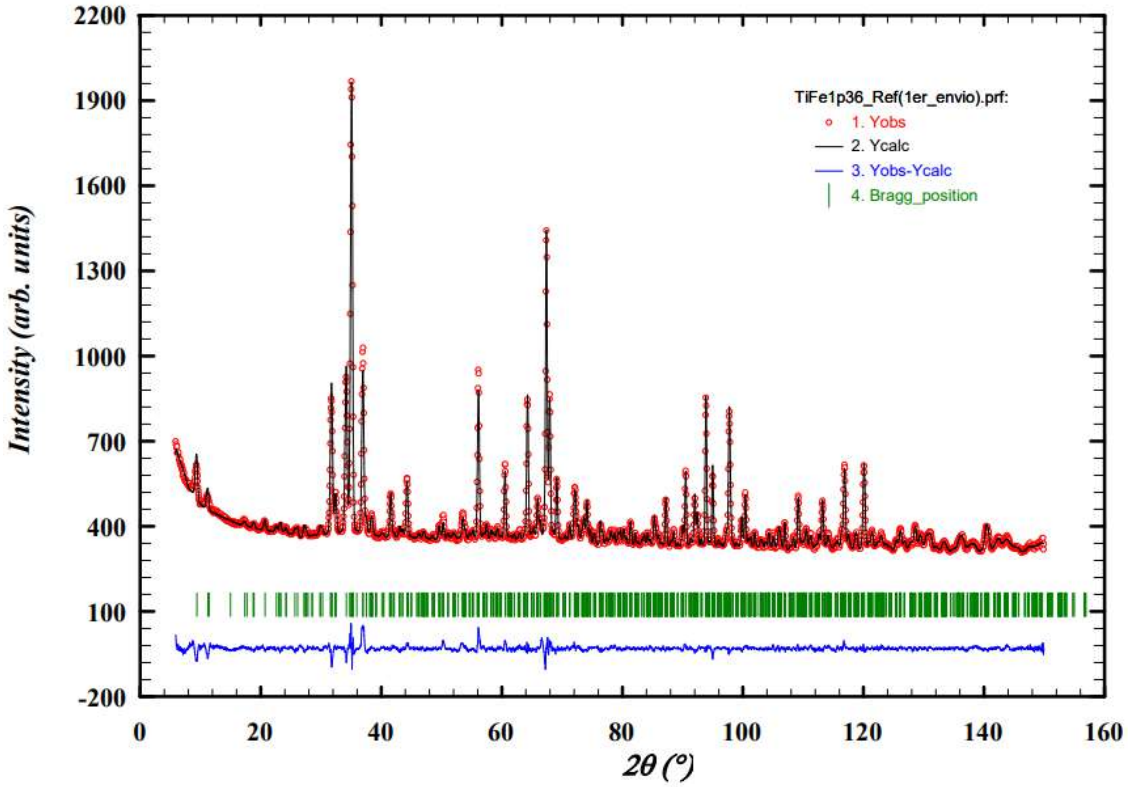

Figure 90. Rietveld refinement of neutron diffraction spectrum for SrMTFO. Wavelength λ=1.36 Å. Chi2=5.2.

The cell parameters for SrMFTO were refined *a*=10.4200(1) Å, *c*=20.8147(4) Å (Table 42). Neutron diffraction refinements confirmed the preferential occupation of Fe into the Ti3 position after several trials considering Fe in the other available positions, the obtained atomic parameters are shown in Table 39. This distribution aligns with bond valence sum (BVS) calculations, Ti1 and Ti2 positions confirm a 4+ oxidation state but a smaller ~ 3.5+/3.1+ for Ti3/Fe3. Thus, the nominal formula results $Sr^{2+}Mn_3^{2+}Ti_{14}^{4+}Fe_4^{3+}O_{38}$ for SMTFO, with a Ti3(Fe3) 4^+:3^+ mixed valence position in a 1:2 ratio [Rosas-Huerta et al., 2023].

Table 39. Structural parameters obtained from the Rietveld fitting made to the NPD (λ = 1.36 Å) patterns for SrMTFO compounds at 300 K. [a] Refined site occupancy factors for Ti3/Fe3 were 0.548(3)/0.451(3).

SrMTFO					
Atom	Wyckoff	x	y	z	BVS
Sr1	3a	0	0	0	1.788(8)
Mn1	6c	0	0	1/2	1.98(1)
Mn2	3b	2/3	1/3	0.6456(5)	2.29(3)
Ti1	18f	0.2446(1)	0.3163(1)	0.4014(3)	4.10(6)
Ti2	18f	0.3335(9)	0.0867(1)	0.3908(4)	3.90(5)
Ti3/Fe3[a]	18f	0.5250(1)	0.3740(2)	0.4989(7)	3.56/3.06(6)
O1	18f	0.1923(5)	0.1318(6)	0.4375(2)	1.78(4)
O2	18f	2/3	1/3	0.5453(4)	2.26(3)
O3	18f	0.7202(7)	0.5364(5)	0.6709(3)	2.04(3)
O4	18f	0.4052(6)	0.4378(7)	0.4503(2)	2.13(4)
O5	18f	0.3570(6)	0.2538(6)	0.5594(2)	1.95(4)
O6	18f	0.3671(6)	0.2704(6)	0.3414(2)	1.99(8)
O7	6c	0.4939(6)	0.2045(7)	0.4426(2)	2.09(3)

DC magnetic measurements

The magnetic susceptibility presents a transition at 8.0(5) K with a FC-ZFC divergence, pointing towards a canted AFM or spin-glass behavior, see Figure 91a. Curie–Weiss fit to the inverse susceptibility above 210 K results in θ_W= -82.6(4) K supporting strong AFM interactions. The calculated effective moment of 13.1(1) μ_B per f.u. is reduced from the expected moment of 15.65 μ_B for 3 Mn^{2+} (S = 5/2) and 4 Fe^{3+} (S = 5/2). It also shows a large frustration index of $f = \frac{|\theta|}{T} = 10.25$.

The neutron powder diffraction (NPD) patterns of SMTFO (λ=2.41Å) at 2K and 50K are nearly identical (Figure 91c), suggesting the absence of new magnetic structure in low temperature.

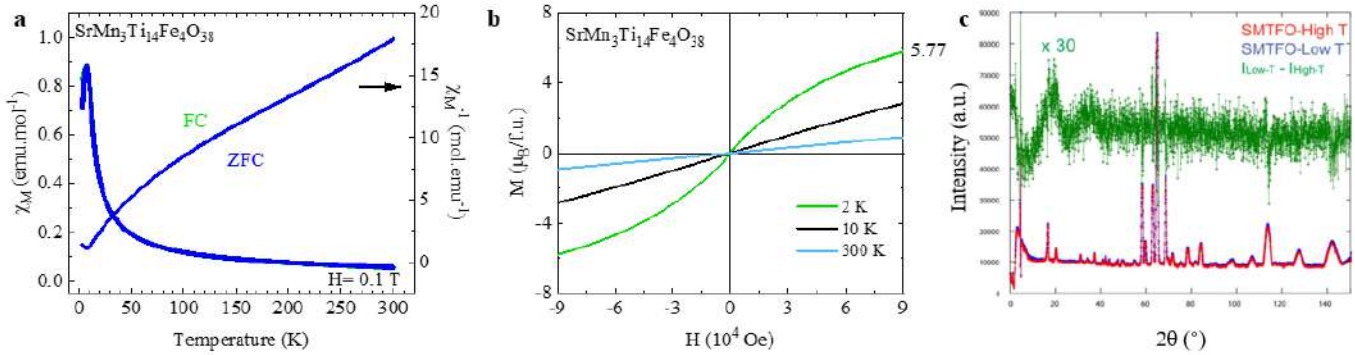

Figure 91. Magnetic susceptibility and its inverse curves of SMTFO (a). Field dependent magnetization at 2K, 10K and 300K (b). High-resolution powder diffraction patterns for the SMTFO compound at 50K (red line) and 2K (blue line) (c). The difference is depicted multiplied by 30 and shown in the green line.

AC magnetic measurements

Alternating current (AC) magnetic susceptibility was subsequently measured and revealed a spin-glass behavior of SMTFO, see Figure 92a. The freezing temperature T_f varies according to the Vogel–Fulcher equation $\omega = \omega_0 \exp\left(-E_a/k_B \cdot (T_f - T_0)\right)$ (Figure 92b). The fittings were made considering the two extremes t_0 values for spin-glass compounds $10^{-9}s \leq t_0 \leq 10^{-13}s$, obtaining $\frac{E_a}{k_B} = 0.5$ and 1 with T_0 =8.22 and 8.02 K, respectively. The very low activation energies in SMTFO reflect that T_f changes only 0.25 K when the frequency changes four orders of magnitude. For spin-glasses, the relative shift per frequency decade, $\delta T_f = \Delta T_f/[T_f \Delta \log(\omega)]$, is often calculated. In SMTFO we estimate $\delta T_f = 0.007$, which is an order of magnitude smaller than for canonical spin-glass systems and thus suggests the formation of an FM cluster-glass state.

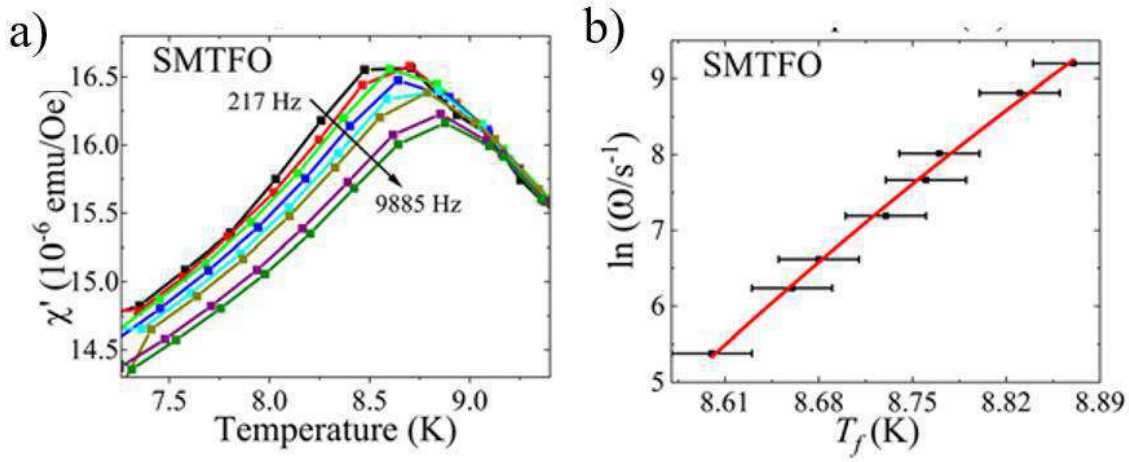

Figure 92. (a) Temperature dependence of χ' in AC field. (b) the change of freezing temperature T_f is fitted well with the Vogel Fulcher equation.

4.3.5 $SrFe_3Ti_{18}O_{38}$

NPD refinement

Neutron powder diffraction has confirmed the crystallization of crichtonite (55.0(2) wt.%) with 45.0(1) wt.% of rutile in the sample SrFTO. The spectrum and refinement are shown in Figure 93.

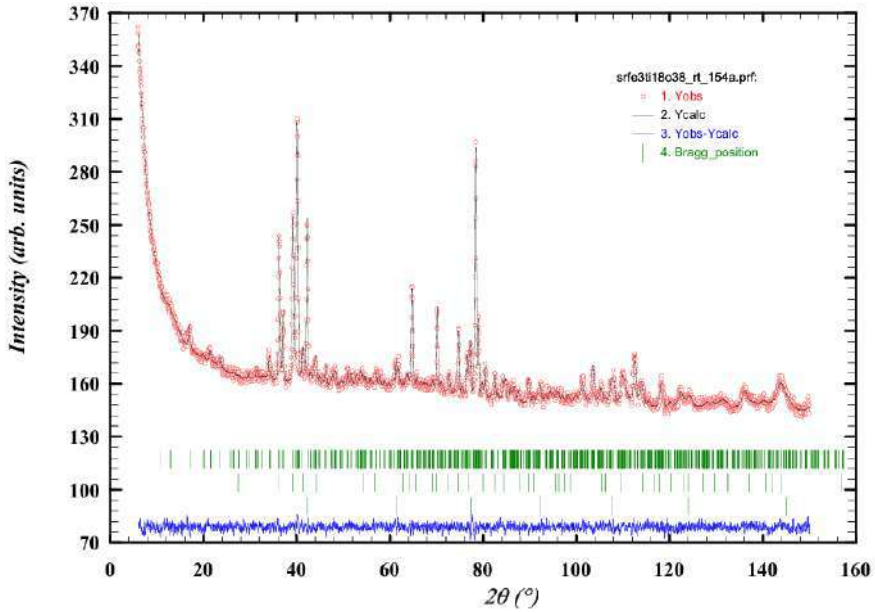

Figure 93. Rietveld refinement of neutron diffraction spectrum for SrFTO. Wavelength λ=1.54 Å. Chi2=1.3.

The refined unit cell parameters are a = 10.3831(5) Å, c = 20.681(1) Å, and V = 1930.9(2) Å^3, which are smaller than those of SrMTFO. The obtained structural parameters are estimated and provided in Table 40. According to the BVS calculation, the tetrahedra are fully occupied by Fe^{2+}, and the octahedral B-sites are occupied by Fe^{2+} and Ti^{4+} in a ratio of 0.64(3)/0.36(3).

Table 40. Structural parameters obtained from the Rietveld fitting made to the NPD (λ = 1.54 Å) patterns for SrFTO 300 K. [a] Refined site occupancy for Fe1/Ti is 0.64(3)/0.36(3).

SrFTO					
Atom	Wyckoff	x	y	z	BVS
Sr1	3a	0.67	0.33	0.33	1.761(21)
Fe1/Ti[a]	3b	0.00	0.00	0.50	1.847(32)/2.149(37)
Fe2	6c	0.67	0.33	0.6421(5)	2.440(62)
Ti1	18f	0.226(3)	0.293(2)	0.3979(8)	4.439(180)
Ti2	18f	0.326(2)	0.080(3)	0.3917(9)	3.842(136)
Ti3	18f	0.525(2)	0.3610(15)	0.5021(11)	3.691(109)
O1	18f	0.1869(16)	0.1334(15)	0.4359(6)	2.362(147)
O2	6c	0.67	0.33	0.5488(10)	2.913(96)
O3	18f	0.7180(16)	0.5329(12)	0.6716(6)	2.225(86)
O4	18f	0.4039(17)	0.4378(16)	0.4510(6)	1.563(66)
O5	18f	0.3695(15)	0.2595(16)	0.5593(6)	2.188(107)
O6	18f	0.3630(15)	0.2695(16)	0.3421(6)	1.954(95)
O7	18f	0.4937(14)	0.1997(15)	0.4422(6)	2.133(84)

Magnetic structure

Neutron diffraction (λ=2.41 Å) on SrFTO was performed at 2 K and 30 K, revealing the appearance of magnetic reflections (Figure 94a). During the analysis of the magnetic structure of SrFTO at 2K, the ferromagnetic arrangement of the magnetic moments of the Fe1,2 and Ti3 sites was again found to be a satisfactory solution (Figure 94b). The magnetic moments at the Fe1 and Fe2 sites are 2.45(2) μ_B, while that at the Ti3 site is 0.19(2) μ_B ($R_{mag.}$= 3.86%, χ^2=1.12).

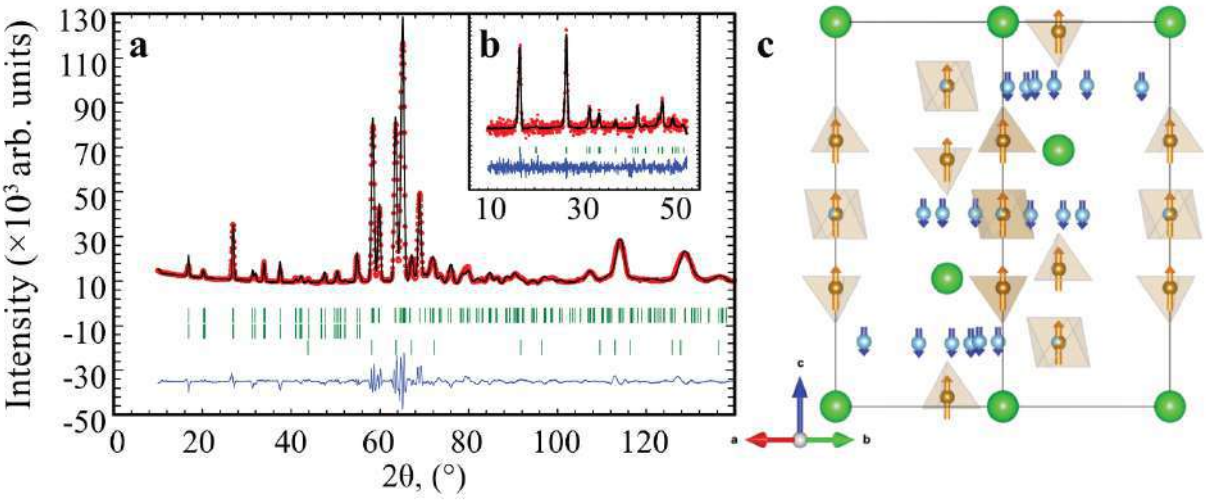

Figure 94. The neutron diffraction spectrum (λ=2.41Å) of SrFTO at 2K (a). The difference between two spectra obtained at 2K and 30K (b). The schematic ferrimagnetic arrangement of Fe1,2 and Ti3 magnetic moments is represented by yellow and blue arrows, respectively.

DC magnetic measurements

The magnetic susceptibility in field cooling mode increases dramatically with decreasing temperature, presenting a distinct transition at 11.7(5) K. The plot of the χ^{-1} exhibits a positive curvature, which is likely due to a temperature independent contribution χ_{ip}. In this case the modified form of the Curie-Weiss law is:

$$\chi^{-1} = \frac{1}{\frac{C}{T - \theta_{CW}} + \chi_{ip}}$$

The modified Curie-Weiss law was applied to the temperature range of 140-293 K. The obtained Curie constant is C = 10.2(1), the Curie-Weiss temperature is θ_{CW} = -16.7(11) K, and the temperature-independent coefficient is χ_{ip} = 0.4980(4). The magnetic moment, derived from the Curie constant, is $\mu_{eff.}$ = 9.02(2) μ_B, which is very close to the theoretic magnetic moment $\mu_{calc.}$ = 9.17 μ_B. The theoretical magnetic moment can be calculated using $\mu_{calc.} = \sqrt{3\mu_{Fe^{2+}}{}^2 + 4\mu_{Ti^{4+}}{}^2}$.

The maximum magnetization, measured at a field of 9 T, differs significantly between 2 K and 400 K. At 2 K and 9 T, the magnetization reaches 6.47 μ_B per formula unit, whereas at 400 K and 9 T, it is only 0.73 μ_B/f.u.

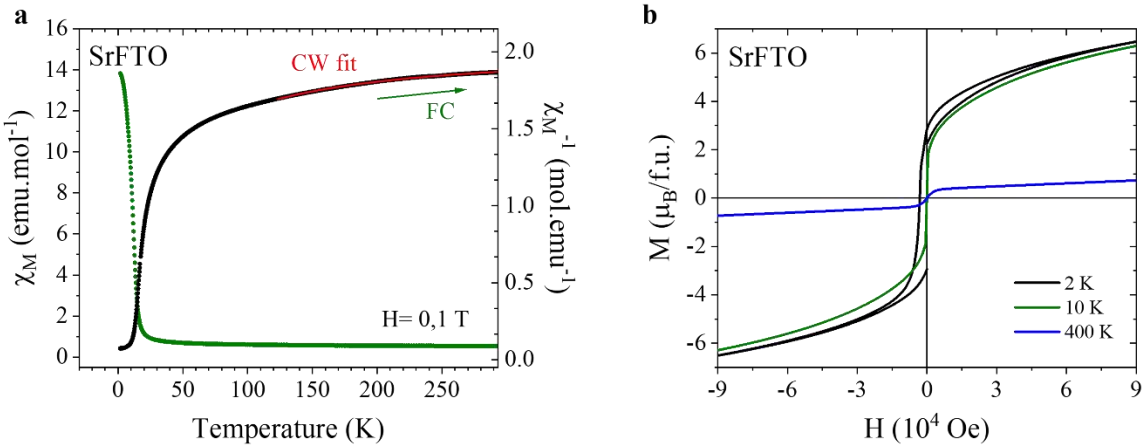

Figure 95. Magnetic susceptibility and its reciprocal χ^{-1} as a function of temperature for SrFTO (a), Field dependent magnetization at different temperatures.

4.3.6 $BaMn_3Ti_{18}O_{38}$

NPD refinement

The synthetic powder sample of $BaMn^{2+}{}_3Ti^{4+}{}_{13}Ti^{3+}{}_5O_{38}$ (BaMTO) was examed using neutron diffraction (λ=1.54Å), see Figure 96. The sample consists of 93.9(4) % crichtonite phase, along with impurities comprising 3.02(6) % rutile and 3.02(7) % hollandite (Table 42). It's worth noting that hollandite is commonly found alongside minerals of the crichtonite group in nature. This association is reflected in its ideal formula, $BaMn_8O_{16}$, which is approximately half of the crichtonite formula $AB_3C_{18}O_{38}$.

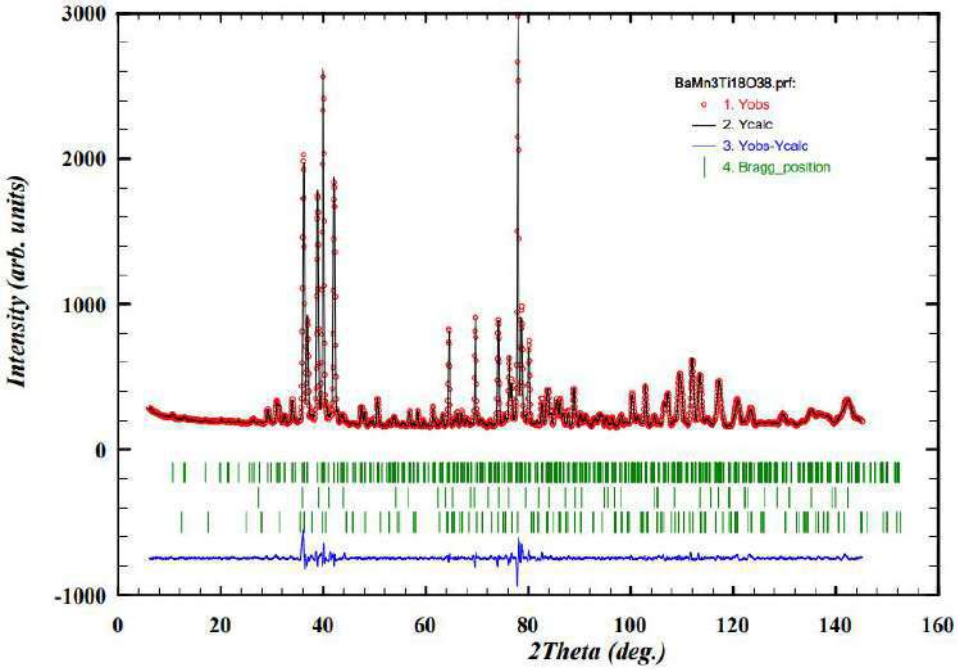

Figure 96. Rietveld refinement of neutron diffraction spectrum for BaMTO. Wavelength λ=1.54 Å. Chi2=5.8.

The unit cell parameters of BaMTO are a = 10.4016(1)Å, c = 20.8151(4)Å, V = 1950.32(5)Å^3. The refined structural parameters are listed in Table 41.

Table 41. Atomic parameters of BaMTO, obtained from NPD refinement (λ=1.54Å, T=230K).

BaMTO					
Atom	Wyckoff	x	y	z	BVS
Ba1	3a	0.6667(0)	0.3333(0)	0.33333(0)	2.678(7)
Mn1	3b	0 (0)	0 (0)	0.50000(0)	2.021(8)
Mn2	6c	0.66666(0)	0.33333(0)	0.64506(34)	2.077(14)
Ti1	18f	0.24135(62)	0.31480(71)	0.39872(19)	4.099(33)
Ti2	18f	0.32393(52)	0.08348(63)	0.39309(20)	3.999(28)
Ti3	18f	0.62184(54)	0.14599(53)	0.49839(26)	3.591(26)
O1	18f	0.19007(34)	0.13125(36)	0.43676(14)	1.917(23)
O2	6c	0.6666(0)	0.3333(0)	0.54430(25)	2.231(20)
O3	18f	0.72166(32)	0.54059(30)	0.67182(15)	2.233(18)
O4	18f	0.40325(39)	0.44009(38)	0.44922(12)	2.211(22)
O5	18f	0.36016(38)	0.26010(35)	0.55936(14)	2.006(23)
O6	18f	0.36251(34)	0.26439(36)	0.34093(14)	1.919(19)
O7	18f	0.49300(36)	0.20183(38)	0.44294(13)	2.135(19)

DC magnetic measurements

The significant increase of susceptibility of BaMTO (See Figure 81c) indicates an onset of magnetic ordering at T = 14.77 K. However, it should be noted that the inverse susceptibilities of the ZFC and FC curves display a divergence in the temperature range of 298-100 K, likely due to equipment error. Despite this discrepancy, both curves conform to the Curie-Weiss description within the temperature range of 220-300 K. The fits yield distinct values for the Weiss temperature, with θ_W =3.29(27) K for the ZFC curve and -27.33(27) K for the FC curve. Considering that the ZFC susceptibility measurements are obtained during cooling, while the FC data is collected during heating, it is reasonable to consider the ZFC data as more precise.

The magnetization measurements reveal that BaMTO exhibits a magnetic moment of 9.13

μ_B/f.u. at 2.5 K under an external field of 0.5 Tesla (Figure 81f). Upon increasing the applied magnetic field to 9 Tesla, the sample approaches saturation magnetization, with a magnetic moment of 10.45 μ_B/f.u. observed. Notably, a small hysteresis is only observed at 2.5 K, with a remnant magnetic moment of 0.04 μ_B/f.u. However, no similar magnetic contribution is observed at temperatures of 10 K and above.

Magnetic structure determined by neutron diffractions

NPD patterns (λ=2.42Å) of BaMTO at low temperature revealed the appearance of magnetic peaks (see Figure 97a), which were also seen in CaMTO and SrMTO. Following the same procedures that applied for processing the data of CaMTO and SrMTO, the propagation vector **k** = [0 0 0] (Γ point of the first Brillouin zone), the mΓ1+ irreducible representation and the rhombohedral magnetic space group $R\bar{3}$ (#148) were applied in refinement of BaMTO magnetic structure. Figure 97b shows the full pattern with both crystal and magnetic structures at 1.6 K. The appearance of magnetic reflections is evidenced by the intensity contrast between 1.6 and 20 K in Figure 97c.

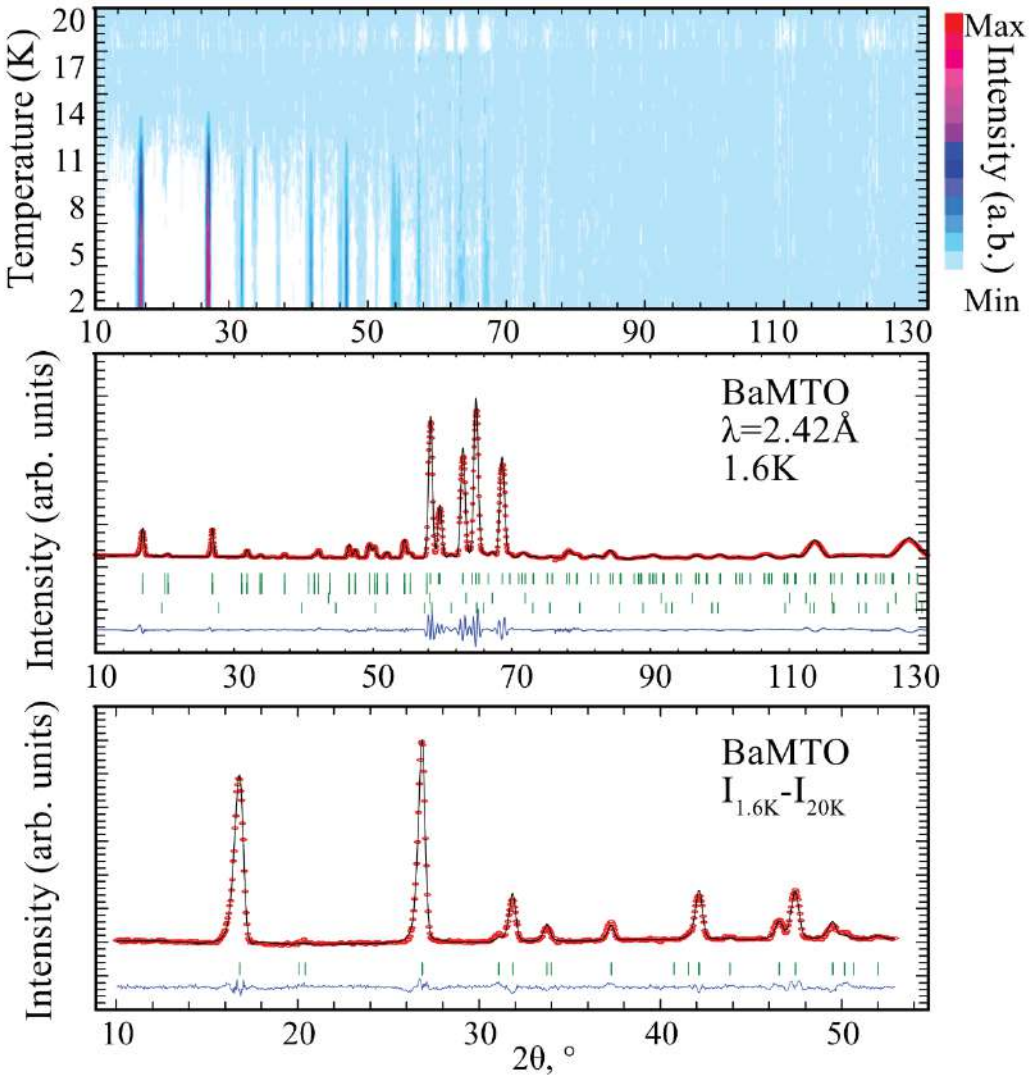

Figure 97. Neutron powder diffraction patterns evaluating in temperature range of 20K-1.6K. Refinement results at 1.6K (below). The refinement of NPD at 1.6K, the Bragg positions of BaMTO, its magnetic structure, rutile and hollandite are shown in green lines. The difference between two spectra at 1.6K and 20K shows the magnetic reflection.

Alike the magnetic structure of CaMTO and SrMTO, the BaMTO's magnetic structure shown in Figure 98a consists of a ferrimagnetic arrangement between Mn and Ti spins along the z axis. The refined moments at 1.6 K converged to 4.36(1) μ_B and 0.24(1) μ_B for Mn1, Mn2 and Ti5 respectively (R_{mag} = 7.64%, χ^2 = 1.52). They are less than the expected values $2S_{Mn}$ =5 μ_B and $2S_{Ti}$ =1 μ_B. The evolutions of the Mn and Ti moments in dependence of temperatures are shown in Figure 98b.

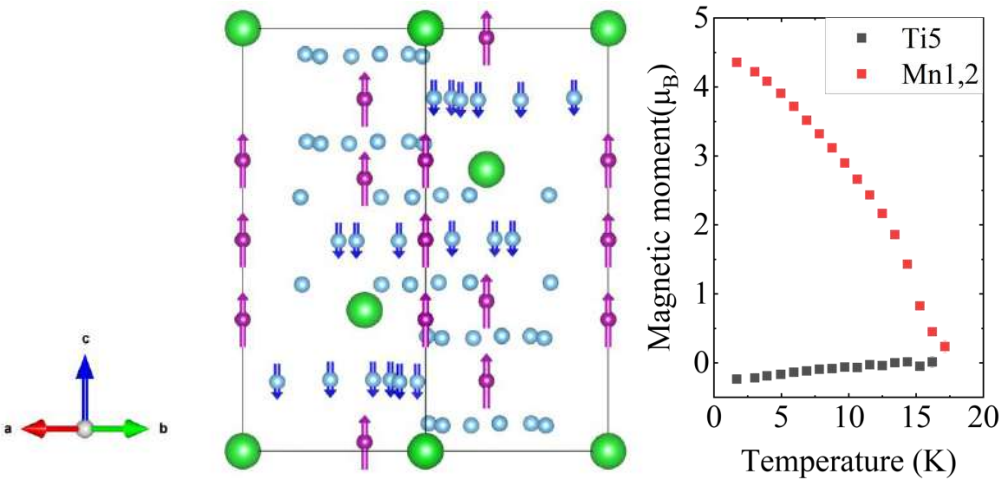

Figure 98. The schematic magnetic structure of BaMTO at 1.6K (a) and the temperature dependence of Mn, Ti magnetic moments in range of 1.6K – 20K (b).

4.3.7 Subsection summary

The results of Rietveld analysis are shown in Table 42. The data for CaMTO, SrMTO, SrMTFO and BaMTO are summarized in Table 43.

Table 42. The phase content and unit cell parameters of synthetic crichtonite with divalent cations Ca, Sr and Ba.

	CaMTO	CaFTO	SrMTO	SrMTFO	SrFTO	BaMTO
Diffraction wavelength	NPD (λ=1.54Å)	NPD (λ=1.54Å)	NPD (λ=1.36Å)	NPD (λ=1.36Å)	NPD (λ=1.54Å)	NPD (λ=1.54Å)
Crichtonite(wt.%)	87.66(75)	54.98(16)	92.8(7)	100(0)	55.0(2)	93.95(37)
TiO_2(wt.%)	7.96(8)	45.02(13)	7.2(4)	—	45.0(1)	3.02(6)
Ilmenite (wt.%)	4.39(11)	—	—	—	—	—
Hollandite (wt.%)	—	—	—	—	—	3.02(7)
a(Å)	10.4041(2)	10.3852(1)	10.4282(1)	10.4200(1)	10.3852(1)	10.4029(1)
c(Å)	20.8157(6)	20.9221(4)	20.8410(3)	20.8147(4)	20.9221(4)	20.8181(1)
Volume($Å^3$)	1951.33(3)	1954.17(5)	1962.78(4)	1957.17(5)	1954.17(5)	1951.10(50)
R_{wp}(%)	1.77	2.57	7.61	11.1	2.6	3.25
R_{exp}(%)	1.01	1.09	3.56	4.77	1.1	1.34
χ^2 (%)	3.07	5.51	4.57	5.38	5.5	5.85

Since all three samples contain the same magnetic ions - three Mn^{2+} and four Ti^{3+} per formular unit - and the A-site cations have no unpaired electrons, the theoretic magnetic moment of three samples should be the same – 11.41 μB. However, the calculated values of the magnetic moments, derived from the Curie-Weiss fit, are smaller than the theoretical values and show a decreasing trend with the increase of the ion radius.

Neutron Powder Diffraction (NPD) analysis conducted in the absence of a magnetic field confirms the ferrimagnetic (FiM) arrangement arrangement in CaMTO, CaFTO, SrMTO and BaMTO.

The ordered magnetic moments in these compounds have been determined.

Specifically, when the spins of Mn^{2+} and Ti^{3+} ions are fully aligned in three compounds *A*MTO (*A*=Ca, Sr, Ba) at low temperatures, it is observed that the ordered magnetic Moment of Mn^{2+} in compound increases with increasing cation radii, whereas the magnetic moment of Ti^{4+} does not a clear correlation (Table 43).

Table 43. Summarizing the results of magnetic measurements for crichtonite with divalent cation.

Sample name		CaMTO	SrMTO	BaMTO
A-site cation		Ca^{2+}	Sr^{2+}	Ba^{2+}
Electron Configuration		$[Ar]4s^0$	$[Kr]5s^0$	$[Xe]6s^0$
Ionic radii	(Å)	1.44	1.34	1.61
Unit cell parameters	*a* (Å)	10.4041(2)	10.4282(1)	10.4324(1)
	c (Å)	20.8157(6)	20.8410(3)	20.8765(1)
Sample purity	(%)	90.54(45)	97.78(71)	93.90(58)
Transition temperature	(K)	14.37	14.4	14.77
Saturation magnetization	(μ_B/f.u.)	9.36	10.71	10.45
at which temperature		3 K	2 K	2.5 K
Curie Constant	C (a.u.)	11.83(1)	11.63(1)	11.19(1)
Weiss temperature	θ_W (K)	-7.58(19)	2.86(22)	3.29(27)
	$\mu_{cal.}(\mu_B)$	9.728(1)	9.646(2)	9.462(2)
	$\mu_{theo.}(\mu_B)$		11.41	
Magnetic moments				
Mn1,2	(μ_B)	3.90(1)	4.11(2)	4.36(1)
Ti3	(μ_B)	0.17(1)	0.30(2)	0.24(1)

In the sample CaFTO and SrFTO, the substitution of Mn^{2+} by Fe^{3+} at the *B*, *T* -site has been achieved. Compared to Mn^{2+} in the previous *A*MTO compounds, this replacement at the *B* and *T* sites does not disrupt the magnetic ordering. Moreover, the magnetic moment values of Ti^{4+} at the *C*3 site do not change significantly, being 0.19(2) μ_B for SrFTO and 0.22(2) μ_B for CaFTO. However, Fe^{3+} in the tetrahedral site exhibits a reduced magnetic moment: 2.45(2) μ_B for SrFTO and only 0.95(3) μ_B for CaFTO, despite that Fe^{3+} ($[Ar]3d^5$) possesses more unpaired electrons compared to Ti^{3+} ($[Ar]3d^1$).

In addition, Fe^{3+} in CaFTO also enters in *C*3 site, partially substituting Ti3, which does not disrupt the magnetic ordering. Contracting that, the full substitution of Ti^{3+} in *C*3 position by Fe^{3+} has been achieved in sample SrMTFO. However, the disorder between Ti and Fe breaks the long-range magnetic order and SMTFO shows spin glass behavior.

Conclusion

Minerals containing radioactive elements can simulate high-level radioactive waste within a crystalline matrix. At the same time, the synthesis of materials containing radioactive elements is associated with relatively high risk. Therefore, studying naturally occurring radioactive minerals is an effective way to investigate the long-term stability of nuclear waste.

In this study, six radioactive minerals were examined. Figure 99 summarizes the behavior of these metamict minerals under high temperature. Structural damage in brannerite and davidite was successfully restored. Fergusonite and thorite also exhibited crystallization during heating, which accompanied by a phase transition between their respective modifications. Observations of metamict zirconolite showed a transition from disorder to a supergroup structure, which ultimately resulted in the formation of the zirconolite-3*T* structure.

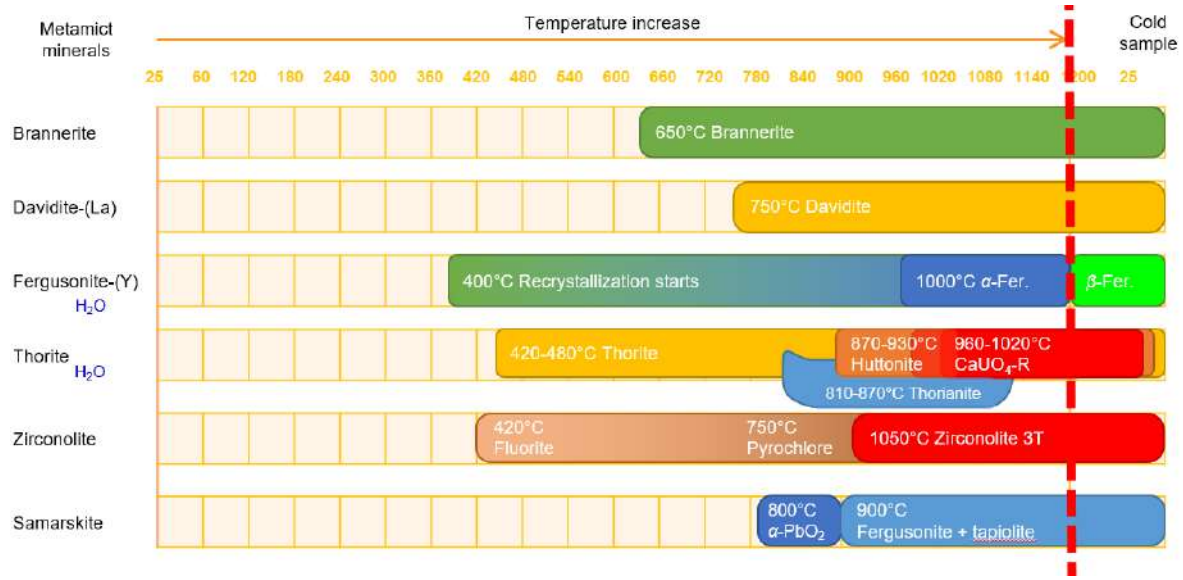

Figure 99. Phase evolution of four studied minerals under high temperature

Successful recrystallization was observed for brannerite, davidite, and fergusonite, as evidenced by the weight percentage of the crystallized target phase (Table 44). During the recrystallization of thorite and zirconolite, a number of by-product phases were observed. Additionally, heating these minerals resulted in element redistribution, manifested as a mosaic texture.

As part of this work, a systematic study of the thermal expansion of five structures was also conducted. The thermal expansion and in-situ recrystallization of brannerite and davidite were studied for the first time. The results are presented in Table 45, arranged in order from the smallest to the largest volumetric thermal expansion. The difference between the maximum and minimum values of the coefficient of thermal expansion (CTE) is also provided to show the anisotropy of thermal expansion of each structure.

Table 44. Summary of the recrystallization results of the studied minerals.

	Wt.% in metamict sample				Start temperature of crystallization	Crystalline target phase (Wt. %) in the sample after heating to 1200 ºC and subsequent cooling.
	Ln	*Ac* [1]	Y_2O_3	H_2O, F, Cl		
Brannerite	-	61.5(9)	-	-	650°C	90.5(6)
Davidite-(La)	9.4(2)	4.3(2)	2.2(1)	<1.26(1) [3]	750°C	84.2(3)
β-Fergusonite-(Y)	12.1(1)	3.6(4)	25.4(1)	6.42(1) [3]	400°C	88.3(3)
Thorite	-	59.7(5) – 78.0(4)	-	1.9(8) – 14.5(5) [2]	420°C	67(1)-92(1) [4]
Zirconolite	3.1(4)	2.3(5) – 7.3(6)	0.15(3)	<1.4(3) [2]	420°C	52.9(5)
Samarskite	4.9(1)	11.0(3)	13.1(3)	<1.34(1) [3]	800°C	0(0)

[1] UO_2 + ThO_2

[2] Evaluated by analytical sum of Electron Micro-Probe Analysis.

[3] Estimated by the weight difference of the sample after thermogravimetric analysis.

[4] Huttonite + thorite

Table 45. Summary of the coefficient of thermal expansion (CTE) calculations.

Mineral	$\bar{\alpha}_{11}$	$\bar{\alpha}_{22}$	$\bar{\alpha}_{33}$	$\bar{\alpha}_{max}$-$\bar{\alpha}_{min}$	$\bar{\alpha}_V$
Thorite	3.47(17)	$\bar{\alpha}_{11}$	5.54(18)	2.07(35)	12.49(12)
Huttonite	8.37(17)	5.76(12)	6.44(13)	2.61(30)	20.57(11)
Brannerite	15.44(16)	4.54(5)	5.19(12)	10.9(42)	25.17(26)
Zirconolite-3*T*	8.93(15)	$\bar{\alpha}_{11}$	8.91(13)	0.02(28)	26.78(15)
Davidite-(La)	9.96(3)	$\bar{\alpha}_{11}$	10.79(4)	0.83(7)	30.73(8)
α-fergusonite [2]	14.36(16)	$\bar{\alpha}_{11}$	8.83(14)	5.53(30)	32.02(17)
β-fergusonite [1]	33.39(31)	12.31(20)	-13.62(20)	47.01(51)	32.09(51)

Average CTE of studied minerals in a temperature range of 25-1200 °C. ([1] 25-500 [2] 800-1200 °C). CTE values are multiplied by × 10^{-6} $°C^{-1}$.

Among the structures examined, both thorite and huttonite, especially thorite, exhibit small volume expansion and minimal anisotropy. These two minerals are isostructural with zircon and monazite, respectively. In fact, the excellent thermal expansion properties exhibited by thorite are also common to zircon-type orthosilicates. Zircon and monazite have been applied in nuclear waste management due to their remarkable properties. The study on thorite and huttonite enriches the database, considering them endmembers in zircon and monazite family.

Another promising matrix for immobilizing radionuclides is brannerite. While thermal expansion of brannerite-type vanadates [Bobiński, Ziółkowski, 1991] and wolframites [Chernorukov et al., 2011] has been studied previously, this work represents the first thermal study of the aristotype of brannerite - a uranium-bearing titanite. Compared to other structures, brannerite exhibits a relatively low volumetric coefficient of thermal expansion (CTE), yet its anisotropy is relatively high.

The obtained CTE for zirconolite-3*T* are consistent with reference data [Ball, Thorogood, Vance, 1992]. While the 2*M* polytype of zirconolite has been extensively studied, our investigation into the 3*T* polytype contributes new insights to existing knowledge. Note that our work is the first detailed mineralogical study of zirconolite from Kovdor.

Davidite exhibits a relatively large volumetric thermal expansion, comparable to perovskite and pyrochlore [Ball, Thorogood, Vance, 1992; Kutty et al., 1994], yet it expands nearly isotropically. Another advantage of davidite is its nearly isotropic expansion.

Fergusonite, particularly the *β*-polymorph, shows the highest volumetric expansion and anisotropy. Thermal deformation arising from phase transitions may compromise the stability of ceramic waste forms.

Table 46 summarizes the identified properties of the studied lanthanide and actinoid oxide minerals.

Table 46. Summarizing the identified properties of oxide minerals with lanthanides and actinoids

	Thermal expansion	$\bar{\alpha}_{max}$-$\bar{\alpha}_{min}$	Content of Ac, Ln and Y	The presence of phase transitions with ↑T°C	Novelty of study
Thorite	Low	Low anisotropic	Very high	+	1. First thermal expansion study on natural sample 3. First study of recrystallization products by EBSD method.
Huttonite	Low	Low anisotropic	Very high	+	
β-fergusonite	Very high	Strongly anisotropic	High	+	1. Determination of temperatures of phase transitions, by-products during recrystallization 2. First study of thermal expansion on mineral samples.
α-fergusonite	Very high	Medium anisotropy	High	+	
Zirconolite-3*T*	Medium	Isotropic	Low	-	1. First detailed mineralogical study of zirconolites from Kovdor. 2. Thermal expansion study on natural samples.
Davidite-(La)	Medium	Almost isotropic	Very high	-	1. First thermal expansion study on natural sample. 2. First in-situ study of the recrystallization. 3. Synthesis of a series of new compounds with structural type of crichtonite. Detailed study of magnetic properties. It is possible to consider crichtonites as a promising class of materials with a variety of magnetic properties.
Brannerite	Medium	Anisotropic	Very high	-	1. First thermal expansion study on natural sample 2. First in-situ study of the recrystallization

The structure of crichtonite with a very high isomorphic capacity motivated our study and work on the synthesis of new compounds of this family. A series of compounds were synthesized by systematic substitution of different cations. Despite its potential, the magnetic properties of materials with a crichtonite structure are relatively underexplored, providing good perspectives for research. The study reveals ferrimagnetic properties in manganese-based crichtonites.

A series of compounds with a crichtonite structure have been synthesized with the most basic framework being $AMn_3Ti_{18}O_{38}$ (*A*MTO), where *A* represents La, Ce, Nd, Ca, Sr, or Ba, and Ti is in 3+/4+ mix-valence state. Base on this framework, new compounds LaMTFO, SrMTFO, SrFTO and CaFTO were synthesized by replacing Mn, Ti with Fe partially or totally.

These compounds $AMn_3Ti_{18}O_{38}$ exhibit similar magnetic properties revealed by magnetic measurement. Neutron powder diffraction has confirmed the a ferrimagnetic arrangement of Mn^{2+} and Ti^{3+} spins in CaMTO, SrMTO and BaMTO.

However, the LaMTO, CeMTO and NdMTO are proved to be spin-glass. Summarized this observation, one can conclude that the rare earth elements in the dodecahedron positions can break

the ferrimagnetic arrangement in crichtonite with *A*MTO framework. In addition, observations on samples LaMTFO and SrMTFO reveals that substituting Ti^{3+} with Fe^{3+} in the Ti3 site also disrupts the magnetic ordering, leading to spin glass behavior.

CaFTO and SrFTO proved that even if Mn is fully replaced, the ferrimagnetic arrangement is still exist between *T* and *C* site atoms.

Table 47 summarizes the revealed magnetic properties in new compounds. In conclusion, our study demonstrates a ferrimagnetic arrangement of Mn^{2+} and Ti^{3+} spins in CaMTO, SrMTO, BaMTO, CaFTO and SrFTO. Conversely, LaMTO, CeMTO, NdMTO, LaMTFO and SrMTFO exhibit spin-glass behavior. These observations suggest that the incorporation of rare earth elements in the dodecahedral positions and iron in octahedra *C* positions disrupts the ferrimagnetic order within the crichtonite *A*MTO framework.

Table 47. The magnetic behavior of synthesized new compounds

New compounds	Magnetic behavior	Max magnetization at 9T field (μ_B/f.u.)
$LaMn_3Ti_{18}O_{38}$	Spin-glass	10.10
$LaMn_3Ti_{13}Fe_5O_{38}$	Spin-glass	6.06
$CeMn_3Ti_{18}O_{38}$	Spin-glass	11.88
$NdMn_3Ti_{18}O_{38}$	Spin-glass	12.12
$CaMn_3Ti_{18}O_{38}$	Ferrimagnetic arrangement	9.36
$CaFe_3Ti_{18}O_{38}$	Ferrimagnetic arrangement	5.30
$SrMn_3Ti_{18}O_{38}$	Ferrimagnetic arrangement	10.71
$SrMn_3Ti_{14}Fe_4O_{38}$	Spin-glass	5.87
$SrFe_3Ti_{18}O_{38}$	Ferrimagnetic arrangement	6.20
$BaMn_3Ti_{18}O_{38}$	Ferrimagnetic arrangement	10.45

Table of figures

.

Tables

Reference

1. Adler H. H., Puig J. A. Observations on the Thermal Behavior of Brannerite // The American Minerologist. 1961. Vol. 46.

2. Alifirova T., Rezvukhin D., Nikolenko E., Pokhilenko L., Zelenovskiy P., Sharygin I., Korsakov A., Shur V. Micro-Raman study of crichtonite group minerals enclosed into mantle garnet // Journal of Raman Spectroscopy. 2020. Vol. 51. № 9. P. 1493–1512.

3. Arévalo-López A. M., Attfield J. P. Weak ferromagnetism and domain effects in multiferroic $LiNbO_3$-type $MnTiO_3$-II // Physical Review B. 2013. Vol. 88. № 10. P. 104416.

4. Arévalo-López A. M., McNally G. M., Attfield J. P. Large Magnetization and Frustration Switching of Magnetoresistance in the Double-Perovskite Ferrimagnet Mn_2FeReO_6 // Angewandte Chemie International Edition. 2015. Vol. 54. № 41. P. 12074–12077.

5. Asuvathraman R., Kutty K. V. G. Thermal expansion behaviour of a versatile monazite phase with simulated HLW: A high temperature x-ray diffraction study // Thermochimica Acta. 2014. Vol. 581. P. 54–61.

6. Bain G. A., Berry J. F. Diamagnetic Corrections and Pascal's Constants // Journal of Chemical Education. 2008. Vol. 85. № 4. P. 532.

7. Balek V., Vance E. R., Zeleňák V., Málek Z., Šubrt J. Use of emanation thermal analysis to characterize thermal reactivity of brannerite mineral // Journal of Thermal Analysis and Calorimetry. 2007. Vol. 88. № 1. P. 93–98.

8. Ball C. J., Thorogood G. J., Vance E. R. Thermal expansion coefficients of zirconolite ($CaZrTi2O_7$) and perovskite ($CaTiO_3$) from X-ray powder diffraction analysis // Journal of Nuclear Materials. 1992. Vol. 190. № C. P. 298–301.

9. Bellatreccia F., Ventura G. Della, Caprilli E., Williams C. T., Parodi G. C. Crystal-chemistry of zirconolite and calzirtite from Jacupiranga, São Paulo (Brazil) // Mineralogical Magazine. 1999. Vol. 63. № 5. P. 649–660.

10. Bellatreccia F., Ventura G. Della, Williams C. T., Lumpkin G. R., Smith K. L., Colella M. Non-metamict zirconolite polytypes from the feldspathoid-bearing alkalisyenitic ejecta of the Vico volcanic complex (Latium, Italy) // European Journal of Mineralogy. 2002. Vol. 14. № 4. P. 809–820.

11. Belogub E. V., Bazhenov A. G. Ilmenskie Mountains - a journey into mineralogical paradise. 1997. 21-24 p. [in Russian]

12. Bhowmik R. N., Ranganathan R. Anomaly in cluster glass behaviour of $Co_{0.2}Zn_{0.8}Fe_2O_4$ spinel oxide // Journal of Magnetism and Magnetic Materials. 2002. Vol. 248. № 1. P. 101–111.

13. Biagioni C., Orlandi P., Pasero M., Nestola F., Bindi L. Mapiquiroite, $(Sr,Pb)(U,Y)Fe_2(Ti,Fe^{3+})_{18}O_{38}$, a new member of the crichtonite group from the Apuan Alps, Tuscany, Italy // European Journal of Mineralogy. 2014. Vol. 26. № 3. P. 427–437.

14. Blackburn L. R., Sun S., Gardner L. J., Maddrell E. R., Stennett M. C., Hyatt N. C. A systematic investigation of the phase assemblage and microstructure of the zirconolite $CaZr_{1-x}Ce_xTi_2O_7$ system // Journal of Nuclear Materials. 2020. Vol. 535. P. 1–11.

15. Blasse G. Vibrational spectra of yttrium niobate and tantalate // Journal of Solid State Chemistry. 1973. Vol. 7. № 2. P. 169–171.

16. Bobiński W., Ziółkowski J. Anisotropy of thermal expansion of the brannerite-type MnV_2O_6: Effect of doping with MoO_3 and Li_2O; theoretical predictions, verification, new rules // Journal of Solid State Chemistry. 1991. Vol. 91. № 1. P. 82–97.

17. Borodin L. S., Nazarenko I. I., Rikhter T. L. The new mineral zirconolite — a complex oxide of the AB_3O_7 type // Dokl. Akad. Nauk SSSR., 1956. P. 845–848.

18. Brauer G., Gradinger H. On heterotypic mixed phases in rare earth oxides. I. // Zeitschrift fuer Anorganische und Allgemeine Chemie. 1950. Vol. 276. № 5–6. P. 209–226. [in German]

19. Britvin S. N., Pekov I. V., Krzhizhanovskaya M. G., Agakhanov A. A., Ternes B., Schüller W., Chukanov N. V. Redefinition and crystal chemistry of samarskite-(Y), $YFe^{3+}Nb_2O_8$: cation-ordered niobate structurally related to layered double tungstates // Physics and Chemistry of Minerals. 2019. Vol. 46. № 7. P. 727–741.

20. Brown I. D. Bond valence parameters [E-resource]. URL: https://www.iucr.org/resources/data/datasets/bond-valence-parameters.

21. Bubnova R. S., Firsova V. A., Filatov S. K. Software for determining the thermal expansion tensor and the graphic representation of its characteristic surface (theta to tensor-TTT) // Glass Physics and Chemistry. 2013. Vol. 39. № 3. P. 347–350.

22. Bubnova R. S., Firsova V. A., Volkov S. N., Filatov S. K. RietveldToTensor: Program for Processing Powder X-Ray Diffraction Data under Variable Conditions // Glass Physics and Chemistry. 2018. Vol. 44. № 1. P. 33–40.

23. Bulakh A. G., Nesterov A. R., Williams C. T. Zirconolite, $CaZrTi_2O_7$, re-examined from its type locality at Afrikanda, Kola Peninsula, Russia and some Synroc implications // Neues Jahrbuch fur Mineralogie, Abhandlungen. 2006. Vol. 182. № 2. P. 109–121.

24. Bulakh A. G., Nesterov A. R., Williams C. T., Anisimov I. S. Zirkelite from the Sebl'yavr carbonatite complex, Kola Peninsula, Russia: an X-ray and electron microprobe study of a partially metamict mineral // Mineralogical Magazine. 1998. Vol. 62. № 6. P. 837–846.

25. Burakov B. E., Ojovan M., Lee W. E. Crystalline Materials for Actinide Immobilisation.: Imperical college press, 2011.

26. Campbell B. J., Stokes H. T., Tanner D. E., Hatch D. M. ISODISPLACE: a web-based tool for exploring structural distortions // Journal of Applied Crystallography. 2006. Vol. 39. № 4. P. 607–614.

27. Cao Q., Krivovichev S. V., Burakov B. E., Liu X., Liu X. Natural metamict minerals as analogues of aged radioactive waste forms // Journal of Radioanalytical and Nuclear Chemistry. 2015. Vol. 304. № 1. P. 251–255.

28. Capitani G. C., Mugnaioli E., Guastoni A. What is the actual structure of samarskite-(Y)? A TEM investigation of metamict samarskite from the garnet codera dike pegmatite (Central Italian Alps) // American Mineralogist. 2016. Vol. 101. № 7. P. 1679–1690.

29. Cartz L., Karioris F. G., Gowda K. A. Metamict states of $ThSiO_4$. dimorphs, huttonite and thorite // Radiation Effects. 1982. Vol. 67. № 3. P. 83–85.

30. Caurant D., Majérus O. Glasses and glass-ceramics for nuclear waste immobilization // Encyclopedia of Materials: Technical Ceramics and Glasses.: Elsevier, 2021. P. 762–789.

31. Černý P., London D., Novák M. Granitic Pegmatites as Reflections of Their Sources // Elements. 2012. Vol. 8. № 4. P. 289–294.

32. Chakhmouradian A. R., Williams C. T. Mineralogy of high-field-strength elements (Ti, Nb, Zr, Ta, Hf) in phoscoritic and carbonatitic rocks of the Kola Peninsula, Russia // Phoscorites and carbonatites from mantle to mine: the key example of the Kola alkaline province / под ред. F. Wall, A. N. Zaitsev.: Mineralogical Society of Great Britain and Ireland, 2004.

33. Chakhmouradian A. R., Zaitsev A. N. Afrikanda: an association of ultramafic, alkaline and alkali-silica-

rich carbonatitic rocks from mantle-derived melts // Phoscorites and carbonatites from mantle to mine: the key example of the Kola alkaline province / под ред. F. Wall, A. N. Zaitsev.: Mineralogical Society of Great Britain and Ireland, 2004.

34. Chakhmouradian A. R., Zaitsev A. N. Calcite-amphibole-clinopyroxene rock from the Afrikanda complex, Kola Peninsula, Russia: mineralogy and a possible link to carbonatites. I. Oxide minerals // The Canadian Mineralogist. 1999. Vol. 37. P. 177–198.

35. Chakhmouradian A. R., Zaitsev A. N. Calcite-amphibole-clinopyroxene rock from the Afrikanda, Kola Peninsula, Russia: Mineralogy and a possible link to carbonatites. III. Silicate minerals // The Canadian Mineralogist. 2002. Vol. 40. P. 1347.

36. Chapman N., Hooper A. The disposal of radioactive wastes underground // Proceedings of the Geologists' Association. 2012. Vol. 123. № 1. P. 46–63.

37. Charalambous F. A., Ram R., Pownceby M. I., Tardio J., Bhargava S. K. Chemical and microstructural characterisation studies on natural and heat treated brannerite samples // Minerals Engineering. 2012. Vol. 39. P. 276–288.

38. Cheary R. W., Coelho A. A. A site occupancy analysis of zirconolite CaZrxTi3-xO7 // Physics and Chemistry of Minerals. 1997. Vol. 24. № 6. P. 447–454.

39. Chen R., Siidra O. I., Firsova V. A., Arevalo-Lopez A., Colmont M., Ugolkov V. L., Bocharov V. N. The Chemistry, Recrystallization and Thermal Expansion of Brannerite from Akchatau, Kazakhstan // Materials. 2023. Vol. 16. № 4. P. 1719.

40. Chen R., Siidra O. I., Firsova V. A., Ugolkov V. L., Vlasenko N. S., Bocharov V. N., Arevalo-Lopez A. M., Colmont M., Tokarev I. V. Thermal evolution of the metamict fergusonite-(Y) // Physics and Chemistry of Minerals. 2024a. Vol. 51. № 1. P. 8.

41. Chen R., Siidra O. I., Ugolkov V. L., Firsova V. A., Vlasenko N. S., Arevalo-Lopez A. M., Colmont M., Bocharov V. N. Thermal evolution of metamict davidite-(La) from the Radium Hill, Australia: recrystallization and thermal expansion // Physics and Chemistry of Minerals. 2024b. Vol. 51. № 2. P. 12.

42. Chernikov A. A., Dorfman M. D. Mineral composition of rare metal uranium, beryllium with emerald and other deposits in endo and exocontacts of the kuu granite massif (central kazakhstan) // New Data on Minerals. M. 2004. Vol. 39. P. 71–79.

43. Chernorukov N. G., Knyazev A. V, Kuznetsova N. Yu., Ladenkov I. V. Investigation of phase transitions and thermal expansion of some complex tungsten-containing oxides // Physics of the Solid State. 2011. Vol. 53. № 2. P. 292–298.

44. Chukanov N. V, Vigasina M. F. Vibrational (Infrared and Raman) Spectra of Minerals and Related Compounds.: Springer Cham, 2020. 1376 p.

45. Chukanov N. V, Zubkova N. V, Pekov I. V, Vigasina M. F., Polekhovsky Y. S., Ternes B., Schüller W., Britvin S. N., Pushcharovsky D. Yu. Stefanweissite, $(Ca,REE)_2Zr_2(Nb,Ti)(Ti,Nb)_2Fe^{2+}O_{14}$, a new zirconolite-related mineral from the Eifel paleovolcanic region, Germany // Mineralogical Magazine. 2019. Vol. 83. № 4. P. 607–614.

46. Chukanov N. V., Krivovichev S. V., Pakhomova A. S., Pekov I. V., Schäfer C., Vigasina M. F., Van K. V. Laachite, $(Ca,Mn)_2Zr_2Nb_2TiFeO_{14}$, a new zirconolite-related mineral from the Eifel volcanic region, Germany // European Journal of Mineralogy. 2014. Vol. 26. № 1. P. 103–111.

47. Chukanov N. V., Rastsvetaeva R. K., Kazheva O. N., Ivanov O. K., Pekov I. V., Agakhanov A. A., Van K. V., Shcherbakov V. D., Britvin S. N. Saranovskite, $SrCaFe^{2+}{}_2(Cr_4Ti_2)Ti_{12}O_{38}$, a new crichtonite-group mineral // Physics and Chemistry of Minerals. 2020. Vol. 47. № 11.

48. Chukanov N. V., Zubkova N. V., Britvin S. N., Pekov I. V., Vigasina M. F., Schäfer C., Ternes B., Schüller W., Polekhovsky Y. S., Ermolaeva V. N., Pushcharovsky D. Y. Nöggerathite-(Ce),

$(Ce,Ca)_2Zr_2(Nb,Ti)(Ti,Nb)_2Fe^{2+}O_{14}$, a new zirconolite-related mineral from the eifel volcanic region, Germany // Minerals. 2018. Vol. 8. № 10. P. 1–14.

49. Clausen K., Hayes W., MacDonald J. E., Schnabel P., Hutchings M. T., Kjems J. K. Neutron scattering investigation of disorder in UO_2 and ThO_2 at high temperatures // High Temperatures - High Pressures. 1983. Vol. 15. P. 383–390.

50. Clavier N., Szenknect S., Costin D. T., Mesbah A., Poinssot C., Dacheux N. From thorite to coffinite: A spectroscopic study of $Th_{1-x}U_xSiO_4$ solid solutions // Spectrochimica Acta - Part A: Molecular and Biomolecular Spectroscopy. 2014. Vol. 118. P. 302–307.

51. Coelho A. A., Cheary R. W., Smith K. L. Analysis and Structural Determination of Nd-Substituted Zirconolite-4*M* // Journal of Solid State Chemistry. 1997. Vol. 129. № 2. P. 346–359.

52. Colella M., Lumpkin G. R., Zhang Z., Buck E. C., Smith K. L. Determination of the uranium valence state in the brannerite structure using EELS, XPS, and EDX // Physics and Chemistry of Minerals. 2005. Vol. 32. № 1. P. 52–64.

53. Dachille F., Roy R. Effectiveness of Shearing Stresses in Accelerating Solid Phase Reactions at Low Temperatures and High Pressures // The Journal of Geology. 1964. Vol. 72. № 2. P. 243–247.

54. Davey W. P. Precision measurements of the lattice constants of twelve common metals // Physical Review. 1925. Vol. 25. № 6. P. 753–761.

55. Dill H. G. Pegmatites and aplites: Their genetic and applied ore geology // Ore Geology Reviews. 2015. Vol. 69. P. 417–561.

56. Dixon Wilkins M. C., Mottram L. M., Maddrell E. R., Stennett M. C., Corkhill C. L., Kvashnina K. O., Hyatt N. C. Synthesis, Characterization, and Crystal Structure of Dominant Uranium(V) Brannerites in the $UTi_{2-x}Al_xO_6$ System // Inorganic Chemistry. 2021. Vol. 60. № 23. P. 18112–18121.

57. Dormann J. L., Bessais L., Fiorani D. A dynamic study of small interacting particles: superparamagnetic model and spin-glass laws // Journal of Physics C: Solid State Physics. 1988. Vol. 21. № 10. P. 2015.

58. Ercit T. S. Identification and alteration trends of granitic-pegmatite-hosted (Y,REE,U,Th)-(Nb,Ta,Ti) oxide minerals: A statistical approach // Canadian Mineralogist. 2005. Vol. 43. № 4. P. 1291–1303.

59. Ewing R. C. The crystal chemistry of complex niobium and tantalum oxides. IV. The metamict state: Discussion // American Mineralogist. 1975. Vol. 60. № 7–8. P. 728–733.

60. Ewing R. C. The metamict state: 1993 - the centennial // Nuclear Inst. and Methods in Physics Research, B. 1994. Vol. 91. № 1–4. P. 22–29.

61. Ewing R. C., Chakoumakos B. C., Lumpkin G. R., Murakami T. The Metamict State // MRS Bulletin. 1987. Vol. 12. № 4. P. 58–66.

62. Ewing R. C., Haaker R. F. The metamict state: Implications for radiation damage in crystalline waste forms // Nuclear and Chemical Waste Management. 1980. Vol. 1. № 1. P. 51–57.

63. Ewing R. C., Headley T. J. Alpha-recoil damage in natural zirconolite ($CaZrTi_2O_7$) // Journal of Nuclear Materials. 1983. Vol. 119. № 1. P. 102–109.

64. Ewing R. C., Lutze W. High-level nuclear waste immobilization with ceramics // Ceramics International. 1991. Vol. 17. № 5. P. 287–293.

65. Eyal Y., Lumpkin G. R., Ewing R. C. Natural annealing of alpha-recoil damage in metamict minerals of the thorite group // MRS Online Proceedings Library (OPL). 1986. Vol. 84. P. 635–643.

66. Faria D. L. A. de, Lopes F. N. Heated goethite and natural hematite: Can Raman spectroscopy be used to differentiate them? // Vibrational Spectroscopy. 2007. Vol. 45. № 2. P. 117–121.

67. Ferguson R. B. The crystallography of synthetic $YTaO_4$ and fused fergusonite // The Canadian Mineralogist. 1955. Vol. 6. № 1. P. 72–77.

68. Filatov S. K. High-temperature crystal chemistry. Leningrad, Russia: Nedra, 1990. 288 p. [in Russian]

69. Filho L. A. D. M., Chukanov N. V, Rastsvetaeva R. K., Aksenov S. M., Pekov I. V, Chaves M. L. S. C., Richards R. P., Atencio D., Brandão P. R. G., Scholz R., Krambrock K., Moreira R. L., Guimarães F. S., Romano A. W., Persiano A. C., Oliveira L. C. A. de, Ardisson J. D. Almeidaite, $Pb(Mn,Y)Zn_2(Ti,Fe^{3+})_{18}O_{36}(O,OH)_2$, a new crichtonite-group mineral, from Novo Horizonte, Bahia, Brazil // Mineralogical Magazine. 2015. Vol. 79. № 2. P. 269–283.

70. Finch C. B., Harris L. A., Clark G. W. The thorite → huttonite phase transformation as determined by growth of synthetic thorite and huttonite single crystals // The American Mineralogist. 1964. Vol. 49. P. 782–785.

71. Firsova V. A., Bubnova R. S., Volkov S. N., Filatov S. K. RietveldToTensor (RTT) // Institute of Silicate Chemistry of Russian Academy of Sciences, St Petersburg, Russia. 2015.

72. Förster H. J., Harlov D. E., Milke R. Composition and Th-U-total Pb ages of huttonite and thorite from Gillespie's Beach, South Island, New Zealand // The Canadian Mineralogist. 2000. Vol. 38. № 3. P. 675–684.

73. Frost R. L., Čejka J., Weier M. L., Martens W. N. Raman spectroscopy study of selected uranophanes // Journal of Molecular Structure. 2006. Vol. 788. № 1. P. 115–125.

74. Frost R. L., Reddy B. J. The effect of metamictization on the Raman spectroscopy of the uranyl titanate mineral davidite $(La,Ce)(Y,U,Fe^{2+})(Ti,Fe^{3+})_{20}(O,OH)_{38}$ // Radiation Effects and Defects in Solids. 2011a. Vol. 166. P. 133–136.

75. Frost R. L., Reddy B. J. Raman spectroscopic study of the uranyl titanate mineral brannerite $(U,Ca,Y,Ce)_2(Ti,Fe)_2O_6$: Effect of metamictisation // Journal of Raman Spectroscopy. 2011b. Vol. 42. № 4. P. 691–695.

76. Fuchs L. H., Gebert E. X-ray studies of synthetic coffinite, thorite and uranothorites // The American Mineralogist. 1958. Vol. 43. P. 243–248.

77. Fuchs S., Schumann D., Martin R. F., Couillard M. The extensive hydrocarbon-mediated fixation of hydrothermal gold in the Witwatersrand Basin, South Africa // Ore Geology Reviews. 2021. Vol. 138. P. 104313.

78. Garg A. B., Liang A., Errandonea D., Rodríguez-Hernández P., Muñoz A. Monoclinic-Triclinic Phase Transition Induced by Pressure in Fergusonite-type $YbNbO_4$ // Journal of Physics: Condensed Matter., 2022. Vol. 34. № 17. P. 22408–22418.

79. Gatehouse B. M., Grey I. E., Hill R. J., Rossell H. J. Zirconolite, $CaZr_xTi_{3-x}O_7$; structure refinements for near-end-member compositions with x= 0.85 and 1.30 // Acta Crystallographica, Section B: Structural Crystallography and Crystal Chemistry. 1981. Vol. 37. P. 306–312.

80. Gatehouse B. M., Grey I. E., Smyth J. R. Structure Refinement of Mathiasite, $(K_{0.62}Na_{0.14}Ba_{0.14}Sr_{0.10})_{\Sigma 1.0}[Ti_{12.90}Cr_{3.10}Mg_{1.53}Fe_{2.15}Zr_{0.67}Ca_{0.29}(V,Nb,Al)_{0.36}]_{\Sigma 21.0}O_{38}$ // Acta Crystallographica. 1983. Vol. C39. P. 421–422.

81. Gatehouse Bryan. M., Grey I. E., Campbell I. H., Kelly P. R. The crystal structure of loveringite – a new member of the crichtonite group // American Mineralogist. 1978. Vol. 63. № 1–2. P. 28–36.

82. Gatehouse Bryan. M., Grey I. E., Kelly P. R. The crystal structure of davidite // American Mineralogist. 1979. Vol. 64. P. 1010–1017.

83. Ge X., Fan G., Li G., Shen G., Chen Z., Ai Y. Mianningite, $(\square,Pb,Ce,Na)\ (U^{4+},Mn,U^{6+})\ Fe^{3+}{}_2(Ti,Fe^{3+})_{18}O_{38}$, a new member of the crichtonite group from Maoniuping REE deposit, Mianning county, southwest

Sichuan, China // European Journal of Mineralogy. 2017. Vol. 29. № 2. P. 331–338.

84. George D. R. Thorite from California, a New Occurrence and Variety // American Mineralogist. 1951. Vol. 36. № 1–2. P. 129–132.

85. Gibb F. G. F. High-temperature, very deep, geological disposal: a safer alternative for high-level radioactive waste? // Waste Management. 1999. Vol. 19. № 3. P. 207–211.

86. Gieré R., Lumpkin G. R., Smith K. L. 11. Titanate ceramics for high-level nuclear waste immobilization / под ред. S. Heuss-Aßbichler, G. Amthauer, M. John. : De Gruyter, 2018. P. 223–242.

87. Gieré R., Williams C. T., Lumpkin G. R. Chemical characteristics of natural zirconolite // Bulletin suisse de minéralogie et pétrographie. 1998. Vol. 78. P. 433–459.

88. Gilbert M. R., Selfslag C., Walter M., Stennett M. C., Somers J., Hyatt N. C., Livens F. R. Synthesis and characterisation of Pu-doped zirconolites – $(Ca_{1-x}Pu_x)Zr(Ti_{2-2x}Fe_{2x})O_7$ // IOP Conference Series: Materials Science and Engineering. 2010. Vol. 9. P. 012007.

89. Giletti B. J., Kulp J. L. Radon leakage from radioactive minerals // American Mineralogist. 1955. Vol. 40. № 5–6. P. 481–496.

90. Glagovskii É. M., Kuprin A. V, Pelevin L. P., Konovalov É. E., Starkov O. V, Levakov E. V, Postnikov A. Y., Lisitsa F. D. Immobilization of high-level wastes in stable mineral-like materials in a self-propagating high-temperature synthesis regime // Atomic Energy. 1999. Vol. 87. № 1. P. 514–518.

91. Gong W. L., Ewing R. C., Wang L. M., Xie H. S. Crichtonite structure type ($AM_{21}O_{38}$ and $A_2M_{19}O_{36}$) as a host phase in crystalline waste form ceramics // Materials Research Society Symposium - Proceedings. 1994. Vol. 353. P. 807–815.

92. Gorzhevskaya S. A., Sidorenko G. A., Smorchkov I. E. A new modification of fergusonite: β-fergusonite // Geologiya Mestorozhdenii Redkikh Elementov. 1961. Vol. 9. P. 28–29.

93. Graham J., Thornber M. R. The crystal chemistry of complex niobium and tantalum oxides IV. The metamict state // American Mineralogist. 1974. Vol. 59. № 9–10. P. 1047–1050.

94. Grey I. E., Gatehouse B. M. The crystal structure of landauite, $Na[MnZn_2(Ti,Fe)_6Ti_{12}]O_{38}$ // Canadian Mineralogist. 1978. Vol. 16. P. 63–68.

95. Grey I. E., Lloyd D. J. The crystal structure of senaite // Acta Crystallographica Section B. 1976. Vol. 32. № 5. P. 1509–1513.

96. Grey I. E., Lloyd D. J., White J. S. The structure of crichtonite and its relationship to senaite // American Mineralogist. 1976. Vol. 61. P. 1203–1212.

97. Guastoni A., Cámara F., Nestola F. Arsenic-rich fergusonite-beta-(Y) from Mount Cervandone (Western Alps, Italy): Crystal structure and genetic implications // American Mineralogist. 2010. Vol. 95. № 4. P. 487–494.

98. Guastoni A., Secco L., Škoda R., Nestola F., Schiazza M., Novák M., Pennacchioni G. Non-metamict aeschynite-(Y), polycrase-(Y), and samarskite-(Y) in NYF pegmatites from arvogno, vigezzo valley (central alps, Italy) // Minerals. 2019. Vol. 9. № 5. P. 1–23.

99. Haggerty S. E., Smyth J. R., Erlank A. J., Rickard R. S., Danchin R. V. Lindsleyite (Ba) and mathiasite (K): two new chromium-titanates in the crichtonite series from the upper mantle. // American Mineralogist. 1983. Vol. 68. № 5–6. P. 494–505.

100. Haidinger W. XIX. Description of Fergusonite, a New Mineral Species // Earth and Environmental Science Transactions of The Royal Society of Edinburgh. 1826. Vol. 10. № 2. P. 271–278.

101. Hanson S. L., Simmons W. B., Falster A. U. Nb-Ta-Ti oxides in granitic pegmatites from the Topsham

pegmatite district, southern Maine // The Canadian Mineralogist. 1998. Vol. 36. № 2. P. 601–608.

102. Hanson S. L., Simmons W. B., Falster A. U., Foord E. E., Lichte F. E. Proposed nomenclature for samarskite-group minerals: new data on ishikawaite and calciosamarskite // Mineralogical Magazine. 1999. Vol. 63. № 1. P. 27–36.

103. Hatch L. P. Ultimate Disposal of Radioactive Wastes // American Scientist. 1953. Vol. 41. № 3. P. 410–421.

104. Hazen R. M., Finger L. W., Agrawal D. K., McKinstry H. A., Perrotta A. J. High-temperature crystal chemistry of sodium zirconium phosphate (NZP) // Journal of Materials Research. 1987. Vol. 2. № 3. P. 329–337.

105. Hess F. L., Wells R. C. Brannerite, a new uranium mineral // Journal of the Franklin Institute. 1920. Vol. 189. № 2. P. 225–237.

106. Ho T. C., Kuo T. H., Hopper J. R. Thermodynamic study of the behavior of uranium and plutonium during thermal treatment under reducing and oxidizing modes // Waste Management. 2000. Vol. 20. № 5–6. P. 355–361.

107. Hunter B. A., Howard C. J., Kim D.-J. Neutron Diffraction Study of Tetragonal Zirconias containing Tetravalent Dopants // Australian Journal of Physics. 1998. Vol. 51. № 3. P. 539–545.

108. Hutchings M. T., Withers P. J., Holden T. M., Lorentzen T. Introduction to the Characterization of Residual Stress by Neutron Diffraction. : CRC Press, 2005. Вып. 1 st ed.

109. Jadli T., Mleiki A., Rahmouni H., Khirouni K., Hlil E. K., Cheikhrouhou A. Investigation of physical properties of manganite on example of $Sm_{0.}35Pr_{0.2}Sr_{0.45}MnO_3$ // Physica B: Condensed Matter. 2021. Vol. 600. P. 412548.

110. James J. D., Spittle J. A., Brown S. G. R., Evans R. W. A review of measurement techniques for the thermal expansion coefficient of metals and alloys at elevated temperatures // Measurement Science and Technology. 2001. Vol. 12. № 3. P. R1.

111. Jégou C., Caraballo R., Peuget S., Roudil D., Desgranges L., Magnin M. Raman spectroscopy characterization of actinide oxides $(U_{1-y}Pu_y)O_2$: Resistance to oxidation by the laser beam and examination of defects // Journal of Nuclear Materials. 2010. Vol. 405. № 3. P. 235–243.

112. Ji S., Liao C.-Z., Chen S., Zhang K., Shih K., Chang C.-K., Sheu H., Yan S., Li Y., Wang Z. Higher valency ion substitution causing different fluorite-derived structures in $CaZr_{1-x}Nd_xTi_{2-x}Nb_xO_7$ ($0.05 \leq x \leq 1$) solid solution // Ceramics International. 2021. Vol. 47. № 2. P. 2694–2704.

113. Ji S., Su M., Liao C., Ma S., Wang Z., Shih K., Chang C. K., Lee J. F., Chan T. S., Li Y. Synchrotron x-ray spectroscopy investigation of the Ca1−xLnxZrTi2−x(Al, Fe)xO7 zirconolite ceramics (Ln = La, Nd, Gd, Ho, Yb) // Journal of the American Ceramic Society. 2020. Vol. 103. № 2. P. 1463–1475.

114. Jin G. B., Soderholm L. Solid-state syntheses and single-crystal characterizations of three tetravalent thorium and uranium silicates // Journal of Solid State Chemistry. 2015. Vol. 221. P. 405–410.

115. Kapustin Y. L. Occurrence of nepheline-bearing rocks at carbonatite contacts // Academia Nauka SSSR. 1976. Vol. 25. P. 166–170. [in Russian]

116. Kawakami S., Takeda N., Dr. S. K., Tsutsui F., Harada J., Arai M., Mitome M., Ohmura K., Yubuta K., Shishido T. Synthesis and magnetic properties of fergusonite-structured $La(NbVMn)O_4$ // Emerging Materials Research. 2013. Vol. 2. № EMR4. P. 191–197.

117. Kearins P., Solana-Madruga E., Ji K., Ritter C., Attfield J. P. Cluster Spin Glass Formation in the Double Double Perovskite CaMnFeTaO6 // The Journal of Physical Chemistry C. 2021. Vol. 125. № 17. P. 9550–9555.

118. Kessoft S. E., Sinclair W. J., Ringwood A. E. Solid solution limits in synroc zirconolite // Nuclear and

Chemical Waste Management. 1983. Vol. 4. № 3. P. 259–265.

119. Kesson S. E., Ringwood A. E. Immobilization of sodium in synroc // Nuclear and Chemical Waste Management. 1981. Vol. 2. № 1. P. 53–55.

120. Kim B. H., Ghosh T. K., Lee Y. B., Prelas M. A. Thermal and X-ray diffraction analysis studies during the decomposition of ammonium uranyl nitrate // Journal of Radioanalytical and Nuclear Chemistry. 2012. Vol. 292. № 3. P. 1075–1083.

121. Kimber S. A. J., Attfield J. P. Disrupted antiferromagnetism in the brannerite MnV_2O_6 // Physical Review B. 2007. Vol. 75. № 6. P. 64406.

122. Kimura T. Magnetoelectric Hexaferrites // Annual Review of Condensed Matter Physics. 2012. Vol. 3. № Volume 3, 2012. P. 93–110.

123. Klimczuk T., Zandbergen H. W., Huang Q., McQueen T. M., Ronning F., Kusz B., Thompson J. D., Cava R. J. Cluster-glass behavior of a highly oxygen deficient perovskite, $BaBi_{0.28}Co_{0.72}O_{2.2}$ // Journal of Physics: Condensed Matter. 2009. Vol. 21. № 10. P. 105801.

124. Knyazev A. V., Komshina M. E., Savushkin I. A. Synthesis and high-temperature X-ray diffraction study of thorium orthosilicate // Radiochemistry. 2017. Vol. 59. № 3. P. 225–228.

125. Kolesov B. Raman investigation of H_2O molecule and hydroxyl groups in the channels of hemimorphite // American Mineralogist. 2006. Vol. 91. № 8–9. P. 1355–1362.

126. Komkov A. I. the Structure of Natural Fergusonite, and of a Polymorphic Modification // Kristallografiya. 1959. Vol. 4. № 6. P. 836–841.

127. Korolev K. G., Gaidukova V. S., Rumyantseva G. V. Structural and morphological features and composition of davidite // Textures and structures of uranium ores of endogenous deposits. Moscow: Moscow Atomizdat, 1977. P. 51–57. [in Russian]

128. Kukharenko A. A., Orlova M. P., Bulakh A. G., Bagdasarov E. A., Rimskaya-Korsakova O. M., Nefedov E. I., Ilingsky G. A., Sergeev A. S., Abakumova N. B. The Caledonian Complexes of Ultrabasic-Alkaline and Carbonatite Rocks on Kola Peninsula and in Northern Karelia (Geology,Petology, Mineralogy and Geochemistry). Moscow, Russian: Nedra, 1965. [In Russian]

129. Kutty K. V. G., Rajagopalan S., Mathews C. K., Varadaraju U. V. Thermal expansion behaviour of some rare earth oxide pyrochlores // Materials Research Bulletin. 1994. Vol. 29. № 7. P. 759–766.

130. Lafuente B., Downs R. T., Yang H., Stone N. The power of databases: The RRUFF project // Highlights in Mineralogical Crystallography / под ред. T. Armbruster, R. M. Danisi.: De Gruyter (O), 2016. P. 1–30.

131. Langreiter T., Kahlenberg V. TEV—A Program for the Determination of the Thermal Expansion Tensor from Diffraction Data // Crystals (Basel). 2015. Т. 5. № 1. P. 143–153.

132. Li D. X., Nimori S., Shiokawa Y., Haga Y., Yamamoto E., Onuki Y. Ferromagnetic cluster glass behavior in U2IrSi3 // Physical Review B. 2003. Vol. 68. № 17. P. 172405.

133. Liegeois-Duyckaerts M. Infrared and Raman spectrum of $CaUO_4$: New data and interpretations // Spectrochimica Acta Part A: Molecular Spectroscopy. 1977. Vol. 33. № 6–7. P. 709–713.

134. Lima-de-Faria J. Heat treatment of metamict euxenites, polymignites, yttrotantalites, samarskites, pyrochlores, and allanites // Mineralogical Magazine and Journal of the Mineralogical Society. 1958. Vol. 31. № 242. P. 937–942.

135. Lin J., Dahan I., Valderrama B., Manuel M. V. Structure and properties of uranium oxide thin films deposited by pulsed dc magnetron sputtering // Applied Surface Science. 2014. Vol. 301. P. 475–480.

136. Loopstra B. O., Rietveld H. M. The structure of some alkaline-earth metal uranates // Acta

Crystallographica Section B Structural Crystallography and Crystal Chemistry. 1969. Vol. 25. № 4. P. 787–791.

137. los Reyes M. de, Aughterson R. D., Gregg D. J., Middleburgh S. C., Zaluzec N. J., Huai P., Ren C., Lumpkin G. R. Ion beam irradiation of ABO4 compounds with the fergusonite, monazite, scheelite, and zircon structures // Journal of the American Ceramic Society. 2020. Vol. 103. № 10. P. 5502–5514.

138. Lottermoser B. G., Ashley P. M. Environmental review of the Radium Hill mine site, South Australia Umwelt-Revision des Radium-Hill- Uranbergbaugeländes, Südaustralien // 2005. Vol. 57. № 2. P. 2–6.

139. Ludwig K. R., Cooper J. A. Geochronology of Precambrian granites and associated U-Ti-Th mineralization, northern Olary province, South Australia // Contributions to Mineralogy and Petrology. 1984. Vol. 86. № 3. P. 298–308.

140. Lumpkin G. R. Ceramic waste forms for actinides // Elements. 2006. Vol. 2. № 6. P. 365–372.

141. Lumpkin G. R., Blackford M. G., Colella M. Chemistry and radiation effects of davidite // American Mineralogist. 2013. Vol. 98. № 1. P. 275–278.

142. Lumpkin G. R., Chakoumakos B. C. Chemistry and radiation effects of thorite-group minerals from the Harding pegmatite, Taos County, New Mexico // American Mineralogist. 1988. Vol. 73. № 11–12. P. 1405–1419.

143. Lumpkin G. R., Ewing R. C., Foltyn E. M. Thermal recrystallization of alpha-recoil damaged minerals of the pyrochlore structure type // Journal of Nuclear Materials. 1986. Vol. 139. № 2. P. 113–120.

144. Lumpkin G. R., Gao Y., Gieré R., Williams C. T., Mariano A. N., Geisler T. The role of Th-U minerals in assessing the performance of nuclear waste forms // Mineralogical Magazine. 2014. Vol. 78. № 5. P. 1071–1095.

145. Lumpkin G. R., Leung S. H. F., Ferenczy J. Chemistry, microstructure, and alpha decay damage of natural brannerite // Chemical Geology. 2012. Vol. 291. P. 55–68.

146. Lumpkin G. R., Smith K. L., Blackford M. G. Heavy ion irradiation studies of columbite, brannerite, and pyrochlore structure types // Journal of Nuclear Materials. 2001. Vol. 289. № 1–2. P. 177–187.

147. Lutze W., Ewing R. C. Radioactive waste forms for the future. Netherlands: North Holland, 1988. 791 p.

148. Malczewski D., Grabias A. 57Fe Mössbauer spectroscopy and X-ray diffraction study of complex metamict minerals. Part II // Hyperfine Interactions. 2008. Vol. 186. № 1–3. P. 75–81.

149. Malczewski D., Grabias A., Dercz G. 57Fe Mössbauer spectroscopy of radiation damaged samarskites and gadolinites // Hyperfine Interactions. 2010. Vol. 195. № 1. P. 85–91.

150. Marcano N., Algarabel P. A., Barquín L. F., Araujo J. P., Pereira A. M., Belo J. H., Magén C., Morellón L., Ibarra M. R. Cluster-glass dynamics of the Griffiths phase in $Tb_{5-x}La_xSi_2Ge_2$ // Physical Review B. 2019. Vol. 99. № 5. P. 54419.

151. Markkula M., Arevalo-Lopez A. M., Paul Attfield J. Neutron diffraction study of monoclinic brannerite-type CoV_2O_6 // Journal of Solid State Chemistry. 2012. Vol. 192. P. 390–393.

152. Markovich V., Wisniewski A., Szymczak H. Chapter One - Magnetic Properties of Perovskite Manganites and Their Modifications // Handbook of Magnetic Materials / под ред. K. H. J. Buschow.: Elsevier, 2014. P. 1–201.

153. Mazeina L., Ushakov S. V., Navrotsky A., Boatner L. A. Formation enthalpy of ThSiO4 and enthalpy of the thorite → huttonite phase transition // Geochimica et Cosmochimica Acta. 2005. Vol. 69. № 19. P. 4675–4683.

154. McCarthy G. J., White W. B., Pfoertsch D. E. Synthesis of nuclear waste monazites, ideal actinide hosts for geologic disposal // Materials Research Bulletin. 1978. Vol. 13. № 11. P. 1239–1245.

155. Meldrum A., Boatner L. A., Zinkle S. J., Wang S. X., Wang L. M., Ewing R. C. Effects of dose rate and temperature on the crystalline-to-metamict transformation in the ABO_4 orthosilicates // Canadian Mineralogist. 1999a. Vol. 37. № 1. P. 207–221.

156. Meldrum A., Zinkle S. J., Boatner L. A., Ewing R. C. Heavy-ion irradiation effects in the ABO4 orthosilicates: decomposition, amorphization, and recrystallization // Physical Review B - Condensed Matter and Materials Physics. 1999b. Vol. 59. № 6. P. 3981–3992.

157. Mills S. J., Bindi L., Cadoni M., Kampf A. R., Ciriotti M. E., Ferraris G. Paseroite, $PbMn^{2+}(Mn^{2+},Fe^{2+})_2(V^{5+},Ti,Fe^{3+},\square)_{18}O_{38}$, a new member of the crichtonite group // European Journal of Mineralogy. 2012. Vol. 24. № 6. P. 1061–1067.

158. Momin A. C., Mirza E. B., Mathews M. D. High temperature X-ray diffractometric studies on the lattice thermal expansion behaviour of UO_2, ThO_2 and $(U_{0.2}Th_{0.8})O_2$ doped with fission product oxides // Journal of Nuclear Materials. 1991. Vol. 185. № 3. P. 308–310.

159. Mtougui S., Khalladi R., Mekkaoui N. El, Housni I. El, Idrissi S., Bahmad L., Ziti S., Labrim H. Study of the magnetic properties of the perovskite $CeFeO_3$: Monte Carlo Simulations // Computational Condensed Matter. 2018. Vol. 17. P. e00329.

160. Mugiraneza S., Hallas A. M. Tutorial: a beginner's guide to interpreting magnetic susceptibility data with the Curie-Weiss law // Communications Physics. 2022. Vol. 5. № 1. P. 95.

161. Murakami T. Metamictization of Minerals. // Journal of the Mineralogical Society of Japan. 1993. Vol. 22. № 1. P. 3–20.

162. Mydosh J. A. Spin glasses: an experimental introduction. London: Taylor & Francis, 1993.

163. Ni Y., Hughes J. M., Mariano A. N. Crystal chemistry of the monazite and xenotime structures // American Mineralogist. 1995. Vol. 80. № 1–2. P. 21–26.

164. Olivier V., André-Mayer A. S., Diondoh M., Aurélien E., Maryse O., Moussa I., Michel C., Marc P., Marieke V. L. Uranium mineralization associated with late magmatic ductile to brittle deformation and Na–Ca metasomatism of the Pan-African A-type Zabili syntectonic pluton (Mayo-Kebbi massif, SW Chad) // Mineralium Deposita. 2021. Vol. 56. № 7. P. 1297–1319.

165. Omel'yanenko B. I., Livshits T. S., Yudintsev S. V, Nikonov B. S. Natural and artificial minerals as matrices for immobilization of actinides // Geology of Ore Deposits. 2007. Vol. 49. № 3. P. 173–193.

166. Orlandi P., Pasero M., Duchi G., Olmi F. Dessauite, $(Sr,Pb)(Y,U)(Ti,Fe^{3+})_{20}O_{38}$, a new mineral of the crichtonite group from Buca della Vena Mine, Tuscany, Italy // American Mineralogist. 1997. Vol. 82. № 7–8. P. 807–811.

167. Orlandi P., Pasero M., Rotiroti N., Olmi F., Demartin F., Moëlo Y. Gramaccioliite-(Y), a new mineral of the crichtonite group from Stura Valley, Piedmont, Italy // European Journal of Mineralogy. 2004. Vol. 16. № 1. P. 171–175.

168. Osokin A. S. Accessory-rare-metal mineralization in carbonatites of one alkali-ultramafic massif (Kola Peninsula) // Mineralogy and Geochemistry. 1979. Vol. 6. P. 27–38. [in Russian]

169. Pabst A. Brannerite from Califonia // American Mineralogist. 1954. Vol. 39. № 1–2. P. 109–117.

170. Pabst A. The Metamict State // American Mineralogist. 1952. Vol. 37. P. 137–157.

171. Pabst A., Hutton C. O. Huttonite, a new monoclinic thorium silicate // American Mineralogist. 1951. Vol. 5. P. 60–65.

172. Papoutsa A. D., Pe-Piper G. The relationship between REE-Y-Nb-Th minerals and the evolution of an A-type granite, Wentworth Pluton, Nova Scotia // American Mineralogist. 2013. Vol. 98. № 2–3. P. 444–462.

173. Pascal M.-L., Muro A. Di, Fonteilles M., Principe C. Zirconolite and calzirtite in banded forsterite-spinel-calcite skarn ejecta from the 1631 eruption of Vesuvius: inferences for magma-wallrock interactions // Mineralogical Magazine. 2009. Vol. 73. № 2. P. 333–356.

174. Patchettt E. J., Nuffield W. E. The synthesis and crystallography of brannerite, [Part] 10 of Studies of radioactive compounds // The Canadian Mineralogist. 1960. Vol. 6. № 4. P. 483–490.

175. Paufler P., Weber T. On the determination of linear expansion coefficients of triclinic crystals using X-ray diffraction // European Journal of Mineralogy. 1999. Vol. 11. № 4. P. 721–730.

176. Peterson R. C., Grey I. E. Preparation and structure refinement of synthetic Ti^{3+} -containing lindsleyite, $BaMn_3Ti_{18}O_{38}$ // The Canadian Mineralogist. 1995. Vol. 33. № 5. P. 1083–1089.

177. Pieczka A., Szuszkiewicz A., Szełęg E., Ilnicki S., Nejbert K., Turniak K. Samarskite-group minerals and alteration products: an example from the julianna pegmatitic system, piława górna, sw poland // The Canadian Mineralogist. 2014. Vol. 52. № 2. P. 303–319.

178. Piilonen P. C., Rowe R., Poirier G., Grice J. D., McDonald A. M. Discreditation of thorogummite // The Canadian Mineralogist. 2014. Vol. 52. № 4. P. 769–774.

179. Pointurier F., Marie O. Identification of the chemical forms of uranium compounds in micrometer-size particles by means of micro-Raman spectrometry and scanning electron microscope // Spectrochimica Acta Part B: Atomic Spectroscopy. 2010. Vol. 65. P. 797–804.

180. Popova V. I., Churin E. I., Blinov I. A., Gubin V. A. Fergusonite-(Y) and products of its alteration in granite pegmatite from the vein of the Beregovaya Zenkovsky massif in the Urals // Novyye Dannyye o Mineralakh,. 2012. Vol. 47. P. 47–55. [in Russian]

181. Rastsvetaeva R. K., Aksenov S. M., Chukanov N. V, Menezes L. A. D. Crystal structure of almeidaite, a new mineral of the crichtonite group // Doklady Chemistry. 2014. Vol. 455. № 1. P. 53–57.

182. Rastsvetaeva R. R. K. Critchotnite and its family: the story of the discovery of two new minerals // Minerallogy and Crystalloghy. 2020. № 8. P. 39–47.

183. Rezvukhin D. I., Rashchenko S. V, Sharygin I. S., Malkovets V. G., Alifirova T. A., Pautov Leonid. A., Nigmatulina E. N., Seryotkin Y. V. Botuobinskite and mirnyite, two new minerals of the crichtonite group included in Cr-pyrope xenocrysts from the Internatsionalnaya kimberlite // Mineralogical Magazine. 2023. Vol. 87. № 3. P. 433–442.

184. Ringwood A. E. Disposal of high-level nuclear wastes: A geological perspective // Mineral. Mag. 1985. Vol. 49. № 2. P. 159–176.

185. Robinson S. C., Abbey S. Uranothorite from eastern Ontario // The Canadian Mineralogist. 1957. Vol. 14. № 5. P. 1–14.

186. Rodríguez-Carvajal J. Recent advances in magnetic structure determination by neutron powder diffraction // Physica B: Condensed Matter. 1993. Vol. 192. № 1. P. 55–69.

187. Rosas-Huerta J. L., Chen R., Ritter C., Siidra O., Colmont M., Arévalo-López A. M. Ferrimagnetic and spin glass behaviour in $SrMn^{2+}_3Ti^{4+}_{14}M^{3+}_4O_{38}$ (M = Ti and Fe) synthetic crichtonites // Chemical Communications. 2023. Vol. 59. № 88. P. 13199–13202.

188. Salamat A., McMillan P. F., Firth S., Woodhead K., Hector A. L., Garbarino G., Stennett M. C., Hyatt N. C. Structural transformations and disordering in zirconolite ($CaZrTi_2O_7$) at high pressure // Inorganic Chemistry. 2013. Vol. 52. № 3. P. 1550–1558.

189. Sameera S., Prabhakar Rao P., Chandran M. R. Structure and dielectric properties of a new series of pyrochlores in the Ca-Sm-Ti-M-O (M = Nb and Ta) system // Journal of Materials Science: Materials in Electronics. 2011. Vol. 22. № 11. P. 1631–1636.

190. Sarin P., Hughes R. W., Lowry D. R., Apostolov Z. D., Kriven W. M. High-temperature properties and ferroelastic phase transitions in rare-earth niobates ($LnNbO_4$) // Journal of the American Ceramic Society. 2014. Vol. 97. № 10. P. 3307–3319.

191. Seydoux-Guillaume A. M., Montel J. M. Experimental determination of the thorite-huttonite phase transition // EUG IX.: Terra Nova, 1997. P. 421.

192. Seydoux-Guillaume A. M., Wirth R., Nasdala L., Gottschalk M., Montel J. M., Heinrich W. An XRD, TEM and Raman study of experimentally annealed natural monazite // Physics and Chemistry of Minerals. 2002. Vol. 29. № 4. P. 240–253.

193. Shannon R. D. Revised effective ionic radii and systematic studies of interatomic distances in halides and chalcogenides // Acta Crystallographica Section A. 1976. Vol. 32. № 5. P. 751–767.

194. Sharygin V. V., Doroshkevich A. G., Khromova E. A. Nb-Fe-rich zirconolite-group minerals in calcite carbonatites of the Belaya Zima massif (Eastern Sayan) (in Russain) // Mineralogy. 2016. Vol. 4. P. 3–18.

195. Shelly L., Schweke D., Danon A., Rosen B. A., Hayun S. Exploring the Redox Properties of $Ce_{1-x}U_xO_{2\pm\delta}$ ($x \leq 0.5$) Oxides for Energy Applications // Inorganic Chemistry. 2023. Vol. 62. № 29. P. 11456–11465.

196. Shelyug A., Rafiuddin M. R., Mesbah A., Clavier N., Szenknect S., Dacheux N., Guo X., Navrotsky A. Effect of Annealing on Structural and Thermodynamic Properties of $ThSiO_4$-$ErPO_4$ Xenotime Solid Solution // Inorganic Chemistry. 2021. Vol. 60. № 16. P. 12020–12028.

197. Shirane G., J. Pickart S., Ishikawa Y. Neutron Diffraction Study of Antiferromagnetic $MnTiO_3$ and $NiTiO_3$ // Journal of the Physical Society of Japan. 1959. Vol. 14. № 10. P. 1352–1360.

198. Siggel A., Jansen M. $ZrSn_{0.6}Ti_{0.5}O_4$ as a matrix for ceramic colours. Structural investigations on $ZrTiO_4$ and $ZrSn_{0.6}Ti_{0.5}O_4$ // Zeitschrift fuer Anorganische und Allgemeine Chemie. 1990. Vol. 582. P. 93–102.

199. Simmons W. B., Hanson S. L., Falster A. U. Samarskite-(Yb): A new species of the samarskite group from the Little Patsy pegmatite, Jefferson County, Colorado // Canadian Mineralogist. 2006. Vol. 44. № 5. P. 1119–1125.

200. Smith K. L., Lumpkin G. R., Blackford M. G., Day R. A., Hart K. P. The durability of synroc // Journal of Nuclear Materials. 1992. Vol. 190. P. 287–294.

201. Staatz M. H., Adams J. W., Wahlberg J. S. Brown, yellow, orange, and greenish-black thorites from the Seerie pegmatite, Colorado // Journal of Research of the US Geological Survey. 1976. Vol. 4. № 5. P. 575–582.

202. Stark M., Noller M. Spectral variability of the uranyl silicates uranophane-α and uranophane-β: polymorphism and luminescence // Physics and Chemistry of Minerals. 2022. Vol. 50. № 1. P. 2.

203. Strzelecki A. C., Barral T., Estevenon P., Mesbah A., Goncharov V., Baker J., Bai J., Clavier N., Szenknect S., Migdisov A., Xu H., Ewing R. C., Dacheux N., Guo X. The Role of Water and Hydroxyl Groups in the Structures of Stetindite and Coffinite, $MSiO_4$ (M = Ce, U) // Inorganic Chemistry. 2021. Vol. 60. № 2. P. 718–735.

204. Sugitani Y., Suzuki Y., Nagashima K. Polymorphism of samarskite and its relationship to other structurally related Nb–Ta oxides with the α-PbO_2 structure // American Mineralogist. 1985. Vol. 70. № 7–8. P. 856–866.

205. Szymanski J. T., Scott J. D. A Crystal Structure Refinement of Synthetic Brannerite, UTi_2O_6, and its Bearing on Rate of Alkaline-Carbonate Leaching of Brannerite in Ore // Canadian Mineralogist. 1982. Vol. 20. P. 271–279.

206. Taira N., Wakeshima M., Hinatsu Y., Tobo A., Ohoyama K. Magnetic structure of pyrochlore-type $Er_2Ru_2O_7$ // Journal of Solid State Chemistry. 2003. Vol. 176. № 1. P. 165–169.

207. Taylor M., Ewing R. C. The crystal structures of the $ThSiO_4$ polymorphs: huttonite and thorite // Acta Crystallographica Section B Structural Crystallography and Crystal Chemistry. 1978. Vol. 34. № 4. P. 1074–1079.

208. Tholence J. L. On the frequency dependence of the transition temperature in spin glasses // Solid State Communications. 1980. Vol. 35. № 2. P. 113–117.

209. Tholence J. L., Yeshurun Y., Kjems J. K., Wanklyn B. Spin dynamics and low temperature properties of the anisotropic spin glass Fe_2TiO_5 // Journal of Magnetism and Magnetic Materials. 1986. Vol. 54–57. P. 203–204.

210. Thompson N. B. A., Frankland V. L., Bright J. W. G., Read D., Gilbert M. R., Stennett M. C., Hyatt N. C. The thermal decomposition of studtite: analysis of the amorphous phase // Journal of Radioanalytical and Nuclear Chemistry. 2021. Vol. 327. № 3. P. 1335–1347.

211. Tomašić N., Bermanec V., Gajović A., Linarić M. R. Metamict minerals: An insight into a relic crystal structure using XRD, raman spectroscopy, SAED and HRTEM // Croatica Chemica Acta. 2008. Vol. 81. № 2. P. 391–400.

212. Tomašić N., Bermanec V., Plodinec M., Gajović A. Samarskite high-temperature modification recrystallisation: vibrational spectroscopy probing.: 7th European Conference on Mineralogy and Spectroscopy, 2011. P. 2011.

213. Tomašić N., Gajović A., Bermanec V., Linarić M., Rajić Su D. Š. koda. Preservation of the samarskite structure in a metamict ABO_4 mineral: a key to crystal structure identification // European Journal of Mineralogy. 2010. Vol. 22. № 3. P. 435–442.

214. Tomašić N., Gajović A., Bermanec V., Rajić M. Recrystallization of metamict Nb-Ta-Ti-REE complex oxides: A coupled X-ray-diffraction and Raman spectroscopy study of aeschynite-(Y) and polycrase-(Y) // Canadian Mineralogist. 2004. Vol. 42. № 6. P. 1847–1857.

215. Tomašić N., Gajović A., Bermanec V., Su D. S., Rajić Linarić M., Ntaflos T., Schlogl R., Recrystallization, Ntaflos T., Schlögl R. Recrystallization mechanisms of fergusonite from metamict mineral precursors // Physics and Chemistry of Minerals. 2006. Vol. 33. № 2. P. 145–159.

216. Tumurugoti P., Clark B. M., Edwards D. J., Amoroso J., Sundaram S. K. Cesium incorporation in hollandite-rich multiphasic ceramic waste forms // Journal of Solid State Chemistry. 2017. Vol. 246. P. 107–112.

217. Turuani M., Choulet F., Eglinger A., Goncalves P., Machault J., Mercadier J., Seydoux-Guillaume A.-M., Reynaud S., Baron F., Beaufort D., Batonneau Y., Gouy S., Mesbah A., Szenknect S., Dacheux N., Chapon V., Pagel M. Geochemical fingerprints of brannerite (UTi_2O_6): an integrated study // Mineralogical Magazine. 2020. Vol. 84. № 2. P. 313–334.

218. Tyupina E. A., Kozlov P. P., Krupskaya V. V. Application of Cement-Based Materials as a Component of an Engineered Barrier System at Geological Disposal Facilities for Radioactive Waste—A Review // Energies. 2023. Vol. 16. № 2.

219. Uher P., Ondrejka M., Konečný P. Magmatic and post-magmatic Y-REE-Th phosphate, silicate and Nb-Ta-Y-REE oxide minerals in A-type metagranite: an example from the Turčok massif, the Western Carpathians, Slovakia // Mineralogical Magazine. 2009. Vol. 73. № 6. P. 1009–1025.

220. Uma S., Sleight A. W. A New Bismuth Magnesium Vanadate with Reduced Vanadium: BiMg2.5V18.5O38 // Journal of Solid State Chemistry. 2002. Vol. 164. № 1. P. 138–143.

221. Vance E. R., Ball C. J., Blackford M. G., Cassidy D. J., Smith K. L. Crystallisation of zirconolite from

an alkoxide precursor // Journal of Nuclear Materials. 1990. Vol. 175. № 1. P. 58–66.

222. Vance E. R., Lumpkin G. R., Carter M. L., Cassidy D. J., Ball C. J., Day R. A., Begg B. D. Incorporation of uranium in zirconolite ($CaZrTi_2O_7$) // Journal of the American Ceramic Society. 2002. Vol. 85. № 7. P. 1853–1859.

223. Vance E. R., Watson J. N., Carter M. L., Day R. A., Begg B. D. Crystal Chemistry and Stabilization in Air of Brannerite, UTi_2O_6 // Journal of the American Ceramic Society. 2001. Vol. 84. № 1. P. 141–144.

224. Ventura G. Della Della, Bellatreccia F., Williams C. T. Zirconolite with significant $REEZrNb(Mn,Fe)O_7$ from a xenolith of the Laacher See eruptive center, Eifel volcanic region, Germany // Canadian Mineralogist. 2000. Vol. 38. № 1. P. 57–65.

225. Waitzinger M., Sorger D., Paar W. H., Finger F. Geochronological constraints on uranium mineralization within the Hüttenberg siderite deposit (Eastern Alps, Austria) // Geochemistry. 2021. Vol. 81. № 1. P. 125678.

226. Wang F., Fan G., Li T., Gg X., Wu Y., Wang T., Yao J. Haitaite-(La), $LaU^{4+}Fe^{3+}{}_2(Ti_{13}Fe^{2+}{}_4Fe^{3+})_{\Sigma 18}O_{38}$, a New Member of the Crichtonite Group // Acta Geologica Sinica - English Edition. 2022. Vol. 96. № 6. P. 2007–2014.

227. Wang S. X., Begg B. D., Wang L. M., Ewing R. C., Weber W. J., Govidan Kutty K. V. Radiation stability of gadolinium zirconate: A waste form for plutonium disposition // Journal of Materials Research. 1999a. Vol. 14. № 12. P. 4470–4473.

228. Wang S. X., Wang L. M., Ewing R. C., Was G. S., Lumpkin G. R. Ion irradiation-induced phase transformation of pyrochlore and zirconolite // Nuclear Instruments and Methods in Physics Research, Section B: Beam Interactions with Materials and Atoms. 1999b. Vol. 148. № 1–4. P. 704–709.

229. Weber W. J., Navrotsky A., Stefanovsky S., Vance E. R., Vernaz E. Materials Science of High-Level Nuclear Waste Immobilization // MRS Bulletin. 2009. Vol. 34. № 1. P. 46–53.

230. Whittle A. W. G. The nature of davidite // Economic Geology. 1959. Vol. 54. № 1. P. 64–81.

231. Whittle K. R., Hyatt N. C., Smith K. L., Margiolaki I., Berry F. J., Knight K. S., Lumpkin G. R. Combined neutron and X-ray diffraction determination of disorder in doped zirconolite-2*M* // American Mineralogist. 2012. Vol. 97. № 2–3. P. 291–298.

232. Williams C. T. The occurrence of niobian zirconolite, pyrochlore and baddeleyite in the Kovdor carbonatite complex, Kola Peninsula, Russia // Mineralogical Magazine. 1996. Vol. 60. № 401. P. 639–646.

233. Williams C. T., Gieré R. Zirconolite: A Review of Localities Worldwide, and a Compilation of its Chemical Compositions // Bulletin of the Natural History Museum London. 1996. Vol. 52. № 1. P. 1–24.

234. Wolten G. M. The structure of the M'-phase of YTaO4, a third Fergusonite polymorph // Acta Crystallographica. 1967. Vol. 23. № 6. P. 939–944.

235. Wu F. Y., Yang Y. H., Mitchell R. H., Bellatreccia F., Li Q. L., Zhao Z. F. In situ U-Pb and Nd-Hf-(Sr) isotopic investigations of zirconolite and calzirtite // Chemical Geology. 2010. Vol. 277. № 1–2. P. 178–195.

236. Wülser P.-A., Meisser N., Brugger J., Schenk K., Ansermet S., Bonin M., Bussy F. Cleusonite, $(Pb,Sr)(U^{4+},U^{6+})(Fe^{2+},Zn)_2(Ti,Fe^{2+},Fe^{3+})_{18}(O,OH)_{38}$, a new mineral species of the crichtonite group from the western Swiss Alps // European Journal of Mineralogy. 2006. Vol. 17. № 6. P. 933–942.

237. Xu Y., Meier M., Das P., Koblischka M. R., Hartmann U. Perovskite manganites: potential materials for magnetic cooling at or near room temperature // Crystal Engineering. 2002. Vol. 5. № 3–4. P. 383–389.

238. Yang H.-C., Eun H.-C., Lee D.-G., Oh W.-Z., Lee K.-W. Behavior of radioactive elements during

thermal treatment of nuclear graphite waste thermodynamic model analysis // Journal of Nuclear Science and Technology. 2005. Vol. 42. № 10. P. 869–876.

239. Yang K., Chen L., Wu F., Zheng Q., Li J., Song P., Wang Y., Liu R., Feng J. Thermophysical properties of $Yb(Ta_xNb_{1-x})O_4$ ceramics with different crystal structures // Ceramics International. 2020. Vol. 46. № 18. P. 28451–28458.

240. Yashima M., Lee J. H., Kakihana M., Yoshimura M. Raman spectral characterization of existing phases in the Y_2O_3-Nb_2O_5 system // Journal of Physics and Chemistry of Solids. 1997. Vol. 58. № 10. P. 1593–1597.

241. Yefimov A. V., Borodayev Y. S., Mozgova N. N., Nenasheva S. N. Bismuth mineralization of the akchatau molybdenum-tungsten deposit, central Kazakhstan // International Geology Review. 1990. Vol. 32. № 10. P. 1017–1027.

242. Yudintsev S. V. Isolation of Separated Waste of Nuclear Industry // Radiochemistry. 2021. Vol. 63. № 5. P. 527–555.

243. Yudintsev S. V., Nickolsky M. S., Ojovan M. I., Stefanovsky O. I., Nikonov B. S., Ulanova A. S. Zirconolite Polytypes and Murataite Polysomes in Matrices for the REE—Actinide Fraction of HLW // Materials. 2022. Vol. 15. № 17.

244. Yudintsev S. V., Stefanovskii S. V., Kir'yanova O. I., Lian J., Ewing R. Radiation resistance of fused titanium ceramic for actinide immobilization // Atomic Energy. 2001. Vol. 90. № 6. P. 487–494.

245. Zaitsev A. N., Chakhmouradian A. R. Calcite-amphibole-clinopyroxene rock from the Afrikanda complex, Kola Peninsula, Russia: mineralogy and a possible link to carbonatites. II. Oxysalt minerals // The Canadian Mineralogist. 2002. Vol. 40. P. 103–120.

246. Zaitsev A. N., Chakhmouradian A. R., Siidra O. I., Spratt J., Williams C. T., Stanley C. J., Petrov S. V, Britvin S. N., Polyakova E. A. Fluorine-, yttrium- and lanthanide-rich cerianite-(Ce) from carbonatitic rocks of the Kerimasi volcano and surrounding explosion craters, Gregory Rift, northern Tanzania // Mineralogical Magazine. 2011. Vol. 75. № 6. P. 2813–2822.

247. Zaitsev A. N., Terry Williams C., Jeffries T. E., Strekopytov S., Moutte J., Ivashchenkova O. V, Spratt J., Petrov S. V, Wall F., Seltmann R., Borozdin A. P. "Rare earth elements in phoscorites and carbonatites of the Devonian Kola Alkaline Province, Russia: Examples from Kovdor, Khibina, Vuoriyarvi and Turiy Mys complexes" // Ore Geology Reviews. 2015. Vol. 64. P. 477–498.

248. Zhang P., Feng Y., Li Y., Pan W., Zong P. an, Huang M., Han Y., Yang Z., Chen H., Gong Q., Wan C. Thermal and mechanical properties of ferroelastic $RENbO_4$ (RE = Nd, Sm, Gd, Dy, Er, Yb) for thermal barrier coatings // Scripta Materialia. 2020. Vol. 180. P. 51–56.

249. Zhang Y. B., Wang J., Wang J. X., Huang Y., Luo P., Liang X. F., Tan H. Bin. Phase evolution, microstructure and chemical stability of $Ca_{1-x}Zr_{1-x}Gd_{2x}Ti_2O_7$ ($0.0 \leq x \leq 1.0$) system for immobilizing nuclear waste // Ceramics International. 2018. Vol. 44. № 12. P. 13572–13579.

250. Zhang Y., Karatchevtseva I., Qin M., Middleburgh S. C., Lumpkin G. R. Raman spectroscopic study of natural and synthetic brannerite // Journal of Nuclear Materials. 2013. Vol. 437. № 1–3. P. 149–153.

251. Zhang Y., Lumpkin G. R., Li H., Blackford M. G., Colella M., Carter M. L., Vance E. R. Recrystallisation of amorphous natural brannerite through annealing: The effect of radiation damage on the chemical durability of brannerite // Journal of Nuclear Materials. 2006. Vol. 350. № 3. P. 293–300.

252. Zhang Y., Mir A. H. A review of brannerite structured materials for nuclear waste management // Journal of Nuclear Materials. 2023. Vol. 583. P. 154512.

253. Zhu T., Zhu B., Mentré O., Lee S., Chen D., Jin Y., Zhu W., Arévalo-López Á. M., Minaud C., Choi K.-Y., Lü M. $Cu_3Te_2O_5(OH)_4$: A Frustrated Two-Dimensional Quantum "Magnetic Raft" as a Possible Pathway to a Spin Liquid // Chemistry of Materials. 2023. Vol. 35. № 10. P. 3951–3959.

254. Zozulya D., Macdonald R., Bagiński B. REE fractionation during crystallization and alteration of fergusonite-(Y) from Zr-REE-Nb-rich late- to post-magmatic products of the Keivy alkali granite complex, NW Russia // Ore Geology Reviews. 2020. Vol. 125. P. 103693.

255. Zubkova N. V, Chukanov N. V, Pekov I. V, Ternes B., Schüller W., Ksenofontov D. A., Pushcharovsky D. Yu. The crystal structure of nonmetamict Nb-rich zirconolite-3*T* from the Eifel paleovolcanic region, Germany // Zeitschrift für Kristallographie - Crystalline Materials. 2018. Vol. 233. № 7. P. 463–468.